論文 / 著書情報
Article / Book Information

題目(和文)	
Title(English)	Roles of water in subduction zone dynamics and mantle chemical evolution
著者(和文)	中尾篤史
Author(English)	Atsushi Nakao
出典(和文)	学位:博士(理学), 学位授与機関:東京工業大学, 報告番号:甲第10413号, 授与年月日:2017年3月26日, 学位の種別:課程博士, 審査員:岩森 光,中島 淳一,横山 哲也,上野 雄一郎,太田 健二
Citation(English)	Degree:Doctor (Science), Conferring organization: Tokyo Institute of Technology, Report number:甲第10413号, Conferred date:2017/3/26, Degree Type:Course doctor, Examiner:,,,,
学位種別(和文)	博士論文
Type(English)	Doctoral Thesis

Ph.D. Thesis

Roles of water in subduction zone dynamics and mantle chemical evolution

Atsushi Nakao

Department of Earth and Planetary Sciences,
Graduate School of Science and Engineering,
Tokyo Institute of Technology

March 2017

Abstract

In Chapter I, geophysical and geochemical approaches for investigating water in the Earth's interior are briefly reviewed. The aim of this study is to consistently characterize the roles of water in these processes, especially subducting slab physics and mantle geochemical evolution, based on these approaches.

In Chapter II, the effects of water on subduction dynamics, e.g., the plate migration rate, slab geometry, stress field, and back-arc spreading, are investigated using a 2-D self-consistent model for lithosphere subduction and whole-mantle convection. Here, the author models water transportation coupled with hydrous mineral phase changes. Interactions of mantle flows and water transportation are simulated using constitutive and state equations for hydrous rocks. The model has successfully reproduced water distribution in a mantle wedge and along the slab with sufficient resolution comparable to that of previous models focused on mantle wedge structure. Lower density of the subducting slab due to hydration decreases subduction rates, back-arc spreading, and slab stagnation at the phase boundary at 660-km depth. In contrast, low viscosity owing to hydration enhances rapid subduction, trench migration, and slab stagnation. Thus, water is capable of generating two opposite situations in terms of the stress field of the overlying lithosphere and the subduction rate, depending on the temporo-spatial distribution of density and viscosity variations. Therefore, the geodynamic effects of water may generate a broad range of subduction structures and dynamics, as observed in actual subduction zones such as Tonga and Mariana. Variation in buoyancy corresponding to the water content of the mantle wedge and slab surface, from relatively dry to several thousand parts per million, may account for the observed variations, although extremely buoyant cases do not seem to occur in nature. Water in the mantle is therefore key to better understanding whole-mantle-scale slab dynamics as well as island-arc volcanic processes.

In Chapter III, the fractionation, advection, and radioactive decay of U, Th, Pb, Rb, Sr, Sm, Nd, and several imaginary trace elements in both the solid and aqueous fluid phases are incorporated into the numerical model described in Chapter II. The simulation results reproduce the dehydration of oceanic crust and the overlying serpentinite, as well as the corresponding extraction of hydrophile elements in the mantle wedge. Aqueous fluids bearing the incompatible elements ascend toward the base of the overlying

continental plate. However, the spatial distribution of chemical heterogeneity with variable degrees of depletion generated in this process is limited to the region around the subducting slab. The depleted materials sink to and accumulate at the bottom of the mantle because of their high density and viscosity. This process may be the origin of the hidden reservoir with extremely high Pb isotopic ratios. In contrast, the simulation shows that the dehydration of hydrous ringwoodite just below the 660-km discontinuity causes efficient propagation of hydrophilic heterogeneity. The boundary functions as a filter for water and hydrophiles carried by penetrating oceanic slabs, and causes accumulation of hydrous ringwoodite enriched in hydrophiles along the bottom of the transition zone. In contrast, depleted residues are continuously generated at 660 km and sink into the lower mantle. Because the chemical heterogeneity around 660 km is located in a hotter, less viscous region, it can propagate widely within a short period of time. The hydrous ringwoodite bodies above 660 km occasionally generate hydrophile-rich wet plumes because of the low density of the hydrous ringwoodite. We consider wet plumes from the 660-km discontinuity during continental convergence as a possible origin of hemispherical isotopic heterogeneity because continental collision, i.e., trench advance, and slab penetration at 660 km depth tend to occur simultaneously. This study shows that simultaneous modeling of geodynamics and geochemistry is a powerful approach for relating multiple observations.

In Chapter IV, the conclusions of this research are summarized. These findings emphasize the importance of integrating geodynamics and geochemistry.

Contents

Chapter I.

Chapter II.

Chapter IV.

Chapter I.

Geodynamics and geochemistry in a water planet

Tectonics of our hydrous planet and other planets

Abundant liquid water, which is regarded as a requirement for a planet to be habitable (e.g., Ulmschneider, 2005), is characteristic of the Earth. Liquid sea water can react extensively with ocean-floor rocks where sufficient thermal energy is supplied from within the planet, such as along a mid-oceanic ridge (Ranero & Sallarès, 2004) or where an oceanic plate bends (Peacock, 2001; Mével, 2003). Such rock–water reactions cause lithosphere weakening, which leads to oceanic plate subduction (Regenauer-Lieb et al., 2001; Van der Lee et al., 2008) and enhanced thermal convection (Nakagawa et al., 2015; Mallard et al., 2016). Subduction of the ocean floor maintains the youth of the Earth's surface. Thus, liquid water is an important trigger for active plate tectonics and the efficient thermal convection of the Earth.

In contrast, such active lateral tectonics is not observed on other planets such as Venus. For example, lateral forces induced by thermal convection in the mantle of Venus generate compressional ridge belts (e.g., Rusalka Planitia) and decompressional grabens (e.g., Devana Chasma; Miyamoto et al., 2008). If sufficient liquid water were present, such compressional or decompressional force would create plate boundaries, i.e., subduction zones and mid-oceanic ridges, as observed on the Earth. Moreover, based on the distribution of craters on Venus, the planet experienced global resurfacing several hundred million years ago (Schaber et al., 1992; Strom et al., 1994). For these reasons, it is likely that the tectonics of non-hydrous planets differ greatly from the tectonics of the Earth.

Roles of water in the planetary interior

Active plate tectonics leads to the transportation of hydrous rocks into the interior of the planet. As water changes the elastic, viscous, plastic, and frictional parameters of mantle minerals (e.g., Jacobsen et al., 2008; Karato & Jung, 2003), various dynamic phenomena are triggered over various time scales. At the second to minute scale, aqueous fluid released from the subducting oceanic crust may cause intermediate-depth earthquakes (Yamasaki & Seno, 2003; Faccenda et al., 2012). Water along a megathrust boundary may function as a lubricant during large earthquakes (e.g., via thermal pressurization; Bizzarri & Cocco, 2006; Yagi et al., 2012). At the annual scale, hydrous rock contributes to rapid post-seismic viscoelastic deformation in island arc regions; a great deal of recent research is focused on simulating such processes after large earthquakes using GPS (Global Positioning System) observations (Sun et al., 2014; Masuti et al., 2016). At the million-year scale, hydrous rock affects the evolution of subduction zones, such as the thermal structure of the mantle wedge (Arcay et al., 2005) and the formation of the accretionary prism (Gerya & Meilick, 2011). At the billion-year scale, hydrous rocks control heat flux from the planet to space (Nakagawa et al., 2015).

Aqueous fluid release is also essential in the chemical evolution of the Earth. By acting on Si–O–Si bonds in silicate minerals, aqueous fluids decrease the melting points of mantle rocks (Barker, 1983), which generates magmatism in subduction zones. Water seems to be necessary to generate granitic magma, which is thus far only known to exist on the Earth. Because of the buoyancy of continental crust including granite, continental plates have been floating on the Earth's surface through Earth's history ("continental drift"; e.g., Turcotte & Schubert, 2001) and are regarded to be massive reservoirs of incompatible elements. Aqueous fluid and melt phases affect the behavior of trace elements and are necessary to achieve the compositions of volcanic rocks found in island arc regions (e.g., concentration of Pb; Kimura et al., 2009; Ikemoto & Iwamori, 2014). The dehydration process occurring in subduction zones is also regarded as indispensable for the global isotopic evolution recorded in mantle-derived basalts (Chase, 1981; Tatsumi, 2005; Iwamori & Nakamura, 2015).

Discrepancies between previous geochemical models

However, the structures, origins, and evolution of geochemical heterogeneities recorded as the mantle-derived basalts remain enigmatic. In this section, two opposite hypotheses for the chemical evolution of mantle are described:

Isotopic studies of mantle-derived basalt have indicated extremely dehydrated ancient components (High-μ, or HIMU; $\sim$2 Ga; e.g., Tatsumi, 2005). The mechanism to preserve these component for such great lengths of time is somewhat controversial because the estimated mixing time of mantle convection is roughly equivalent to the preservation time (1–3 Gyr; e.g., Gurnis & Davies, 1986; Christensen, 1989; Hoffman & McKenzie., 1985).

One solution is that the high density of the subducting oceanic crust may contribute to its preservation (Nakagawa & Tackley, 2005), which would suggest a layered structure in the Earth's mantle.

In contrast, an independent component analysis of these basalt samples (Iwamori & Nakamura, 2015) has indicated a global hemispherical structure interpreted as the fluid-added signature. Iwamori & Nakamura (2015) propose "top-down hemispherical dynamics" in which subducting slabs concentrated in a continental hemisphere affect both volatile concentration and cooling of the inner core (Tanaka & Hamaguchi, 1997; Cao & Romanowicz, 2004). This vertically divided chemical structure differs greatly from the traditional HIMU-preserving structure. In addition, Iwamori & Nakamura (2012, 2015) propose that this hemispherical structure was generated during a supercontinent era, which suggests a much younger age for the heterogeneities (i.e., several hundreds of Myr, the scale of a supercontinental cycle; e.g., Nance et al., 2014).

Therefore the chemical structure of the mantle (and the corresponding geochemical history) is not clearly delineated, especially at great depths; therefore, geochemical data should be interpreted in conjunction with geophysical observation and processes, as will be described in later sections.

Problems of previous numerical simulations

To evaluate the validity of previously described geochemical models, fluid dynamic numerical simulations that include water transportation are useful. Such simulations have been applied to investigate water distribution and resultant geodynamics, such as rapid post-seismic deformation (Sun et al., 2014), mantle wedge structures (Arcay et al., 2005), and the generation of island arc magma (Horiuchi & Iwamori, 2016). However, almost all previous studies have employed artificial mechanical boundary conditions: i.e., fixed plate geometry and/or fixed plate velocity. With such settings, interactions between water distribution and mantle flows (including plate motion, slab geometry, and the stress fields of island arcs) may not be reproduced appropriately.

Moreover, introducing experimentally derived rheology models of wet materials (e.g., Karato & Wu, 1993) is difficult with some numerical codes; Extreme viscosity contrasts between the cold slab and the wet mantle wedge prevent reaching a stable solution for the equation of motion using an iterative numerical method. Therefore, approximate wet rheology with gradual change in viscosity have been employed in some previous studies.

One of objectives of this thesis is to overcome these weak points of the previous numerical models for water transportation by introducing suitable mechanical boundary conditions, suitable solvers, and the experimentally derived wet rheology.

Approaches for water distribution in the mantle

Although both geophysical and geochemical approaches may be effective to investigate the distribution and roles of water deep in the Earth's mantle, both have advantages and disadvantages. Geophysical approaches (e.g., seismology, GPS, and electrical conductivity) provide high-resolution images of inner structures, but do not provide historical information. In contrast, geochemical approaches provide historical information in the form of geochemical records such as elemental abundances and isotopic ratios, but have limited spatial resolution compared with those offered by geophysical methods. Therefore, a combination of these two approaches is suitable to provide detailed spatiotemporal information about water circulation in the Earth's mantle.

Overview of thesis

In this thesis, the roles of water in both geodynamic and geochemical processes are systematically formulated and discussed. The specific targets of this investigation are subduction zone evolution (time scale of 1 Myr to 1 Gyr) and the isotopic evolution of the mantle. For this purpose, a 2-D fluid dynamic simulation of mantle convection that includes water and element transportation is constructed. An outline of the model is shown in Figure 1. First, the interaction between mantle convection and water distribution is investigated (Chapter II). Secondly, the transportation of trace elements (including isotopic evolution), which is affected by both mantle convection and water transportation, is incorporated into the model (Chapter III). The results of the simulation are expected to relate geophysical observations, e.g., GPS (Lallemand et al., 2005, 2008), seismic velocity (Hafkenscheid et al., 2006; Zhao et al., 2009; Schmandt et al., 2014), and electrical conductivity (Wannamaker et al., 2009; Karato, 2011; Sun et al., 2015) data, with geochemical observations (Hart et al., 1992; Iwamori & Nakamura, 2015).

In Chapter II, the basic equations and numerical schemes of the simulation are described. Water is transported via solid phase flows (red arrow from 'Mantle Convection'

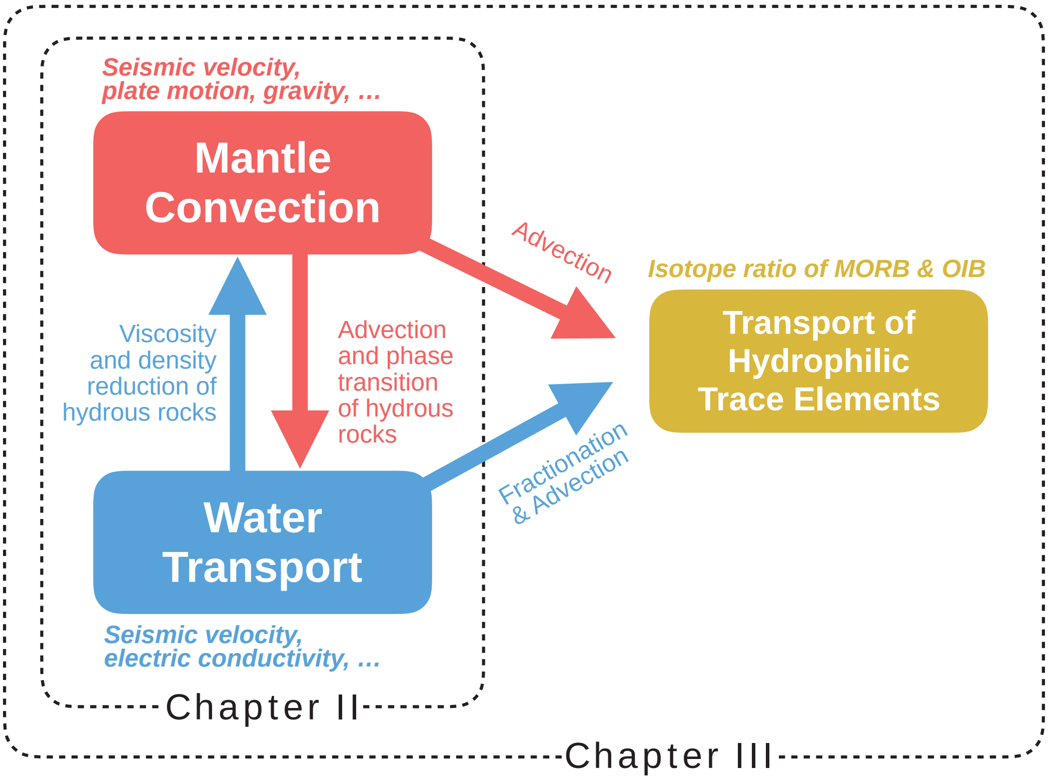

Figure 1: Targets and their relations in this study.

to 'Water Transport' in Figure 1). At the same time, viscosity and density reduction caused by hydration control solid phase flows (blue arrow from 'Water Transport' to 'Mantle Convection' in Figure 1). In the simulation, these changes in the physical properties of hydrous mantle rocks are treated as variable parameters, and the effects of water on subduction zone evolution are evaluated, e.g., in terms of plate velocity, slab geometry, stress field, and back-arc spreading.

In Chapter III, elemental fractionation/transportation and the resultant isotopic evolution are incorporated into the simulation described in Chapter II. Elements are transported via solid phase flows (red arrow from 'Mantle Convection' to 'Transport of Hydrophilic Trace Elements' in Figure 1) and via ascent of the aqueous fluid phase (blue arrow from 'Water Transport' to 'Transport of Hydrophilic Trace Elements' in Figure 1). Dehydration processes in the lower mantle play an important role in the generation and transportation of chemical heterogeneity; however, the relevant physical and chemical parameters are not yet well constrained (e.g., the upward velocity of the aqueous fluid phase, water storage capacity of the lower mantle, and the partition coefficients of trace elements between the solid and fluid phases under lower-mantle conditions). Therefore, these parameters are treated as variable in this chapter. The mechanisms responsible for the global isotopic heterogeneity of the Earth's mantle are discussed based on the results of the simulation.

In Chapter IV, the conclusions of this study are summarized, and the importance of integrating geodynamics and geochemistry is emphasized.

Chapter II.

Effects of water transportation on subduction dynamics: Roles of viscosity and density reduction[1]

1. Introduction

1.1. Possible roles of water in the mantle on geophysical phenomena

It is widely accepted that the Earth's mantle contains water in several tens to several hundreds of parts per million according to electrical conductivity measurements of hydrous minerals and electromagnetic observations (Karato, 2011). Water in rocks causes subduction initiation (Van der Lee et al., 2008), low viscosity of the asthenosphere (Karato & Jung, 1998), magmatism in volcanic arcs (Iwamori, 1998), fault zones (Wannamaker et al., 2009), and deeper earthquakes (Yamasaki & Seno, 2003). Experimental studies have quantified the viscosity and the density of hydrous rocks, both of which are much smaller than those of dry rocks (e.g., Hirth & Kohlstedt, 2003; Inoue et al., 1998). The introduction of constitutive and state equations of hydrous rocks to fluid mechanical simulations enables assessment of the effects of water on mantle dynamics such as thinning of the overlying lithosphere (Arcay et al., 2005), growth of an accretion wedge and back-arc spreading owing to weak hydrous rocks and melts (Gerya & Meilick, 2011), and rapid water transportation by "wet plumes" of buoyant hydrous rocks above stagnant slabs (Richard & Iwamori, 2010).

1.2. Previous numerical simulation for water transportation

These previous numerical studies have provided invaluable insight into the role of water in subduction zones by highlighting the individual physical and chemical influences of water on the wedge mantle and the overriding plate (Table 1). Because of the limitation of the model domains, the influences of water on subduction dynamics including plate motions have been scarcely debated. Numerical and laboratory simulations of free

[1]This chapter is based on the author's published paper: Nakao, A., Iwamori, H., and Nakakuki, T. (2016). Effects of water transportation on subduction dynamics: Roles of viscosity and density reduction. *Earth Planet. Sci. Lett.*, **454**, 178–191.

convection show remarkable acceleration/deceleration of subducting slabs associated with phase transition (e.g., Nakakuki & Mura, 2013; Čížková & Bina, 2013; Schellart, 2008). In addition, seafloor age distribution analysis has revealed that the generation rates of oceanic plates have varied during the past 100 Myr (Conrad & Lithgow-Bertelloni, 2007), indicating inconstant subduction velocities in nature. However, it is still challenging to combine water transportation with a whole-mantle scale model because fine resolution is required to simulate water transportation and to apply actual rheology near the subduction zone.

1.3. Concepts of this chapter

This study seeks to determine the effects of water transportation on the behavior of the sinking and overlying plates integrated into the whole mantle convection. We focus on the velocity of the plates, slab deformation, the stress field of the overlying plate, and back-arc spreading by constructing a numerical model with the following characteristics: (1) free convection of whole-mantle scale without imposing velocity boundary conditions (e.g., Tagawa et al., 2007; Nakakuki & Mura, 2013), (2) phase diagrams of hydrous peridotite and hydrous basalt (Iwamori, 2007) to introduce hydration and dehydration reactions, and (3) properties of hydrous rocks formularized in constitutive and state equations. Introducing (3) makes (1) and (2) interactive. Regarding (3), we apply Arrhenius-type rheology functions for wet crystals determined experimentally (e.g., Hirth & Kohlstedt, 2003; Korenaga & Karato, 2008) and density reduction proportional to its water content (e.g., Richard & Iwamori, 2010; Horiuchi & Iwamori, 2016), both of which have been often simplified or not considered in previous studies (e.g., Rüpke et al., 2004; Arcay et al., 2005; Gerya & Meilick, 2011). Through these effects of hydration on rock properties, our simulation will demonstrate that water is not just a passive tracer in mantle flows but is an important factor in the changes of mantle flows and slab behavior.

2. Numerical settings and basic equations

2.1. Design of 2-D model and initial conditions

The 2-D domain of our model (Figure 3) is 10,000 km in width $\times$ 2,900 km in length and includes phase boundaries at 410-km and 660-km depths, of which the effects on temperature and density are quantified in the energy conservation equation (Section 2.3)

Table 1: Comparison between numerical models for water transportation in Earth's mantle published recently. †Although there are no published description of the solver for mass and momentum conservation equation in Quinquis & Buiter (2014), they pay attention to the convergence of the mechanical solution under a large viscosity gradient. Therefore, the solver seems to be based on an iterative algorithm.

	Density reduction owing to hydration	**Viscosity reduction owing to hydration**	**Yield strength reduction owing to hydration**	**Model domain (width × depth)**	**Boundary condition along plate surface**	**Shape of subducting slab**	**Solver for momentum equation**
This study	Proportional to water content	Arrhenius type	No	10,000 km × 2,900 km	Free slip	Free	Direct method
Horiuchi & Iwamori (2016)	Proportional to water content	Simplified (Arcay et al., 2005)	No	500 km × 300 km	Constant velocity	Fixed	Direct method
Nakagawa et al. (2015)	Proportional to water content	Arrhenius type	No	2-D whole mantle	Free slip	Free	Iterative method (Tackley, 2008)
Quinquis & Buiter (2014)	No	Arrhenius type	No	3,000 km × 670 km	Free slip with constant flow velocity	Free	Iterative method† (Buiter & Ellis, 2012)
Fujita & Ogawa (2013)	No	No	No	(No description) × 2,000 km	Free slip	Free	No description
Faccenda et al. (2012)	Considered	Wet olivine (Ranalli, 1995)	Considered	3,000 km × ~700 km	Free slip/ constant v.	Free	Direct method (Gerya & Yuen, 2007)
Gerya & Meilick (2011)	No	No	Considered	4,000 km × 200 km	Free slip with constant flow velocity	Free	Direct method (Gerya & Yuen, 2007)
Richard & Iwamori (2010)	Proportional to water content	Arrhenius type	No	520 km × 520 km	Free slip / No slip	Fixed	Iterative method (Christensen & Harder, 1991)
Hebert et al. (2009)	pHMELTS	Arrhenius type	No	230.9 ~ 692.8 km × 555 km	Constant velocity	Fixed	Direct method (King et al., 1990)
Arcay et al. (2005)	No	Simplified	No	2,220 km × 200 km	Constant velocity	Fixed	Iterative method (Christensen, 1984)
Rüpke et al. (2004)	No	No	No	1,600 km × 800 km	Constant velocity	Fixed	No description

and the state equation (Section 2.5). Free slip conditions are imposed along top, bottom, and side boundaries so that the plate migration rates are controlled by the balance between the buoyancy and viscous resistance. This enables us to evaluate the effects of water on these rates. Surface temperature is constant at 273 K; therefore, as an oceanic plate migrates toward the right, the plate becomes thick as a result of cooling. Otherwise, no heat flux from the core to the mantle is assumed. In addition, insulating conditions are imposed along the side boundaries. The initial temperature of the lithosphere is determined from a cooling half-space model. The initial age of the oceanic plate is 0 Ma at the mid-ocean ridge and 100 Ma at the trench, and the initial age of the continental plate is 20 Ma. A thin, movable, and deformable weak zone dipping 27° mimicking a plate boundary is initially placed at a location 6,000 km from the left boundary. This segment has low yield strength (Section 2.4) and is transported by mantle flows (Section 2.6). Accordingly, the thickness and the angle of the weak zone change with the passage of time without synthetic forces. Although the segment extends along the slab, it does not reflect the mantle rheology below 240-km depth. Moreover, a 7.5-km-thick slab of mid-ocean ridge basalt (MORB; White et al., 1992) and a 35-km-thick slab of continental crust are placed along the surface, both of which are transported by convection.

The model domain is much larger than that of previous 2-D models (Arcay et al., 2005; Gerya & Meilick, 2011; Horiuchi & Iwamori, 2016). In order to derive fine solution around the subduction zones without consuming extensive computation time, we used a dual grid system developed by Tagawa et al. (2007), which includes a variable grid for equation of motion (Section 2.2) and a uniform grid for heat and marker transportation (Sections 2.3 and 2.6).

2.2. Mass and momentum conservation

All symbols used in the following equations are listed in Table 2.

We assume the mantle to be a 2-D incompressible, highly viscous fluid, the motion of which can be described as

$$\left(\frac{\partial^2}{\partial x^2} - \frac{\partial^2}{\partial z^2}\right)\left[\eta\left(\frac{\partial^2\psi}{\partial x^2} - \frac{\partial^2\psi}{\partial z^2}\right)\right] + 4\frac{\partial^2}{\partial x\partial z}\left(\eta\frac{\partial^2\psi}{\partial x\partial z}\right) = \frac{\partial\rho}{\partial x}g, \tag{1}$$

where stream function ψ is defined by

$$\boldsymbol{v} = (u, w) \equiv \left(\frac{\partial\psi}{\partial z}, -\frac{\partial\psi}{\partial x}\right). \tag{2}$$

Table 2: Physical parameters and variables. The influences of the parameters with daggers (†) are demonstrated in Appendix A.

Symbols	Explanations	Values	Units	References
A	Pre-exponential factor in constitutive laws		$\mathrm{Pa}^{-n}\ \mathrm{s}^{-1}$	
A_1	for dry diffusion creep ($z > 300$ km)	4.3733×10^{-12}	$\mathrm{Pa}^{-1}\ \mathrm{s}^{-1}$	Nakakuki & Mura (2013)
A_2	for wet diffusion creep ($z > 300$ km)	(depends on r)	$\mathrm{Pa}^{-1}\ \mathrm{s}^{-1}$	This study
A_3	for dry dislocation creep ($z < 300$ km)	4.6546×10^{-11}	$\mathrm{Pa}^{-1}\ \mathrm{s}^{-1}$	Nakakuki & Mura (2013)
A_4	for wet dislocation creep ($z < 300$ km)	(depends on r)	$\mathrm{Pa}^{-1}\ \mathrm{s}^{-1}$	This study
c_{Y}	Friction coefficient of intact material	0.3	–	Byerlee (1978)
c_{YF}	Friction coefficient of fractured material	0.004	–	Nakakuki & Mura (2013)
$C_{\mathrm{H_2O}}$	Water content in solid (weight fraction)		$\mathrm{kg\ kg}^{-1}$	
$C_{\mathrm{OH^-}}$	OH^- content in solid (molar ratio)		$\mathrm{ppm\ H\ Si}^{-1}$	
C_p	Specific heat at constant pressure	1.2×10^3	$\mathrm{J\ K}^{-1}\ \mathrm{kg}^{-1}$	c.f., Waples & Waples (2004)
d_{410}	Half thickness of the 410-km boundary	20	km	Nakakuki & Mura (2013)
d_{660}	Half thickness of the 660-km boundary	2	km	Nakakuki & Mura (2013)
E^*	Activation energy		$\mathrm{kJ\ mol}^{-1}$	
E_1^*	for dry diffusion creep ($z > 300$ km)	240	$\mathrm{kJ\ mol}^{-1}$	e.g., Karato & Wu (1993)
E_2^*	for wet diffusion creep ($z > 300$ km)	240	$\mathrm{kJ\ mol}^{-1}$	e.g., Karato & Wu (1993)
E_3^*	for dry dislocation creep ($z < 300$ km)	430	$\mathrm{kJ\ mol}^{-1}$	e.g., Karato & Wu (1993)
E_4^*	for wet dislocation creep ($z < 300$ km)	430	$\mathrm{kJ\ mol}^{-1}$	e.g., Karato & Wu (1993)
g	Gravity acceleration	10	$\mathrm{m\ s}^{-2}$	
h	Thickness of mantle	2,900	km	e.g., Dziewonski & Anderson (1981)
H^{mantle}	Internal heating of mantle	5.44×10^{-12}	$\mathrm{W\ kg}^{-1}$	c.f., Turcotte & Schubert (2001)
H^{MORB}	Internal heating of MORB	5.44×10^{-11}	$\mathrm{W\ kg}^{-1}$	c.f., Turcotte & Schubert (2001)
H^{granite}	Internal heating of granite	5.44×10^{-10}	$\mathrm{W\ kg}^{-1}$	c.f., Turcotte & Schubert (2001)
k	Thermal conductivity	4.68	$\mathrm{W\ m}^{-1}$	c.f. Clauser & Huenges (1995)
n_3	Stress exponent for dry dislocation creep	3.0	–	Karato & Wu (1993)
n_4	Stress exponent for wet dislocation creep	3.0	–	Karato & Wu (1993)
p	Pressure		Pa	
r	Power of the viscosity water dependence		–	
r_{diff}	for wet diffusion creep ($z > 300$ km)	$0 - 1.93$	–	e.g., Hirth & Kohlstedt (2003)
r_{disl}	for wet dislocation creep ($z < 300$ km)	$0 - 1.95$	–	e.g., Hirth & Kohlstedt (2003)
R	Gas constant	8.3145	$\mathrm{J\ mol}^{-1}\ \mathrm{K}^{-1}$	
t	Time		s	
T	Absolute temperature of mantle		K	
T_0	Temperature at the surface ($z = 0$)	273	K	
T_{410}	Temperature at the 410-km boundary	1,691	K	Nakakuki & Mura (2013)
T_{660}	Temperature at the 660-km boundary	1,818	K	Nakakuki & Mura (2013)
$\boldsymbol{v} = (u, w)$	Velocity field of mantle		$\mathrm{m\ s}^{-1}$	

Table 2 (continued).

Symbols	Explanations	Values	Units	References
V^*	Activation volume		$cm^3\ mol^{-1}$	
V_1^*	for dry diffusion creep ($z > 300$ km)	(depends on z)	$cm^3\ mol^{-1}$	Nakakuki & Mura (2013)
V_2^*	for wet diffusion creep ($z > 300$ km)	(depends on z)	$cm^3\ mol^{-1}$	Nakakuki & Mura (2013)
V_3^*	for dry dislocation creep ($z < 300$ km)	15	$cm^3\ mol^{-1}$	Karato & Wu (1993)
V_4^*	for wet dislocation creep ($z < 300$ km)	15	$cm^3\ mol^{-1}$	Karato & Wu (1993)
V_0	at $z = 0$ km to calculate LM viscosity	5	$cm^3\ mol^{-1}$	Karato & Wu (1993)
V_L	at $z = 2000$ km to calculate LM viscosity	4	$cm^3\ mol^{-1}$	Nakakuki & Mura (2013)
x	Lateral coordinate	$0 - 10000$	km	
z	Vertical coordinate	$0 - 2900$	km	
z_{410}	Depth of the 410-km boundary ($T = T_{410}$)	410	km	Dziewonski & Anderson (1981)
z_{660}	Depth of the 660-km boundary ($T = T_{660}$)	660	km	Dziewonski & Anderson (1981)
α	Thermal expansivity	2.5×10^{-5}	K^{-1}	c.f., Schmeling et al. (2003)
β	Density water dependence coefficient	$0 - 2$	–	e.g., Jacobsen et al. (2008)
Γ_{410}	Function for smooth 410-km boundary		–	Christensen & Yuen (1985)
Γ_{660}	Function for smooth 660-km boundary		–	Christensen & Yuen (1985)
Γ_C	Function for smooth crust/mantle boundary		–	
γ_{410}	Clapeyron slope of the 410-km boundary	+3	$MPa\ K^{-1}$	Katsura & Ito (1989) †
γ_{660}	Clapeyron slope of the 660-km boundary	−3	$MPa\ K^{-1}$	Akaogi & Ito (1993) †
$\Delta\rho_C$	Density contrast between granite and mantle	600	$kg\ m^{-3}$	c.f., Waples & Waples (2004)
$\Delta\rho_{410}$	Density contrast at the 410-km boundary	182.5	$kg\ m^{-3}$	Dziewonski & Anderson (1981)
$\Delta\rho_{610}$	Density contrast at the 660-km boundary	194.2	$kg\ m^{-3}$	Dziewonski & Anderson (1981)
$\dot{\varepsilon}, \dot{\varepsilon}_{ij}$	Strain rate		s^{-1}	
$\dot{\varepsilon}_{\mathrm{II}}$	Second invariant of strain rate		s^{-1}	
η	Effective viscosity of mantle		Pa s	
η_{ref}	Reference viscosity at 410-km depth	5×10^{20}	Pa s	e.g., Okuno & Nakada (2001)
σ, σ_{ij}	Stress		Pa	
σ_{II}	Second invariant of stress		Pa	
σ_{Y}	Yield strength		Pa	
σ_{Y0}	Cohesive strength	30	MPa	Byerlee (1978)
σ_{YF}	Cohesive strength at fractured areas		Pa	
σ_{Ymax}	Maximum yield strength	200	MPa	Kohlstedt et al. (1995) †
ψ	Stream function		$m^2\ s^{-1}$	
ρ	Density of mantle		$kg\ m^{-3}$	
ρ_0	Reference density	3,900	$kg\ m^{-3}$	c.f., Dziewonski & Anderson (1981)
ρ_s	Density at the surface to calculate σ_{Y}	3,300	$kg\ m^{-3}$	c.f., Waples & Waples (2004)

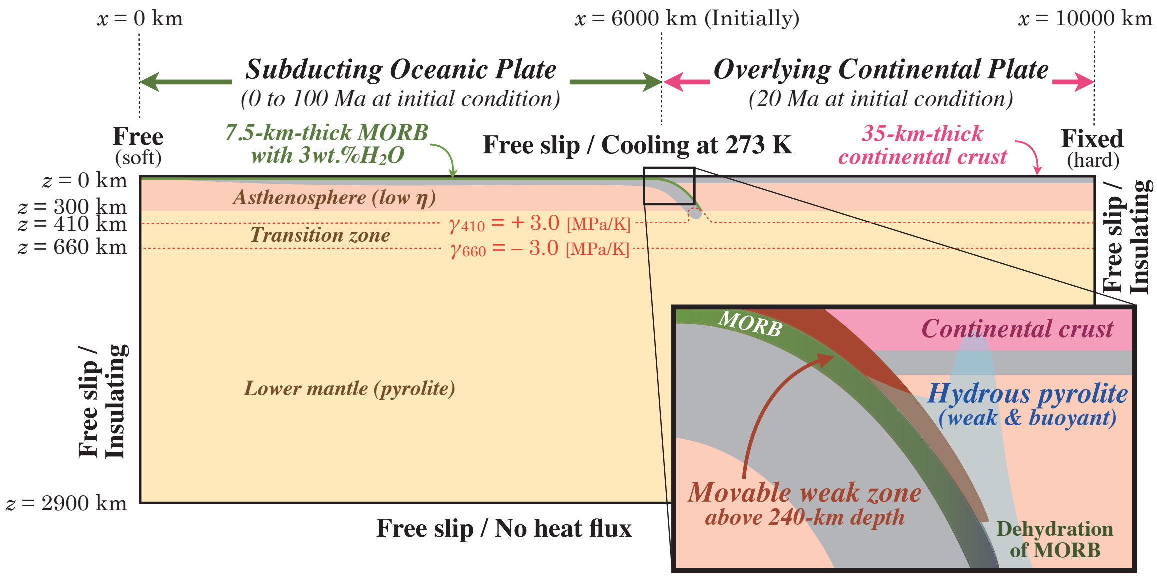

Figure 2: Schematic diagram of the 2-D convection model. Details are described in Section 2.1.

Because we introduce water-dependent viscosity η and density ρ (Sections 2.4 and 2.5), the motion of mantle rocks is affected by hydration-dehydration reactions.

Equation (1) is discretized by a finite volume method into a grid with 1346×306 nodes distributed non-uniformly. Areas with large viscosity or density gradients, e.g., near the plate boundary, hydrous zones, thermal boundary layers, and phase transition boundaries, are divided finely; the others, e.g., mid-lower mantle, are not. The minimum and maximum spacing are taken to be 2.5 km and 25 km, respectively.

One of the difficulties in solving a discretized equation of motion lies in deriving a robust solution under a large viscosity gradient. We applied the modified Cholesky decomposition algorithm, which is a direct solver of linear systems (e.g., Tagawa et al., 2007), although the direct method demands more computer resources than that of an iterative method, which has been often used in previous studies (Table 1).

2.3. Energy conservation

An equation of heat balance includes terms of thermal advection, adiabatic heating, latent heat due to the 410- and 660-km phase boundaries, thermal diffusion, viscous

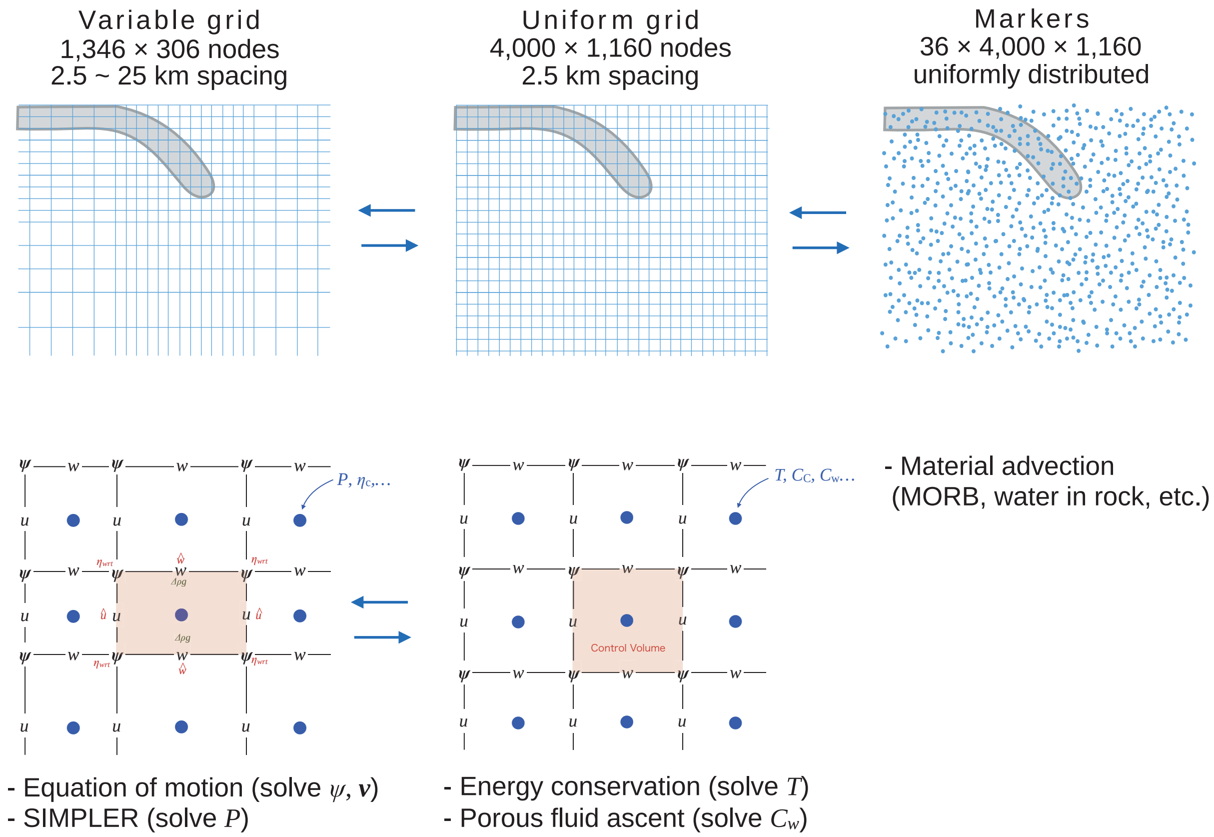

Figure 3: Schematic diagrams of grid and marker systems used in the simulation. A variable, sparse grid (left) is used for solving equation of motion (Section 2.2 and Appendix B) for the sake of rapid computation. A uniform grid (middle) is used for solving heat transportation including advection and diffusion (Section 2.3) and for having aqueous porous flow transported vertically (Section 2.6). Markers floating in the model domain are used for the material transportation including MORB, fault zone, and water in rocks (Sections 2.6 and 2.7) in order to avoid numerical diffusion.

dissipation, and heat generation by radioactive elements,

$$\rho_0 C_p \left(\frac{\partial T}{\partial t} + \boldsymbol{v} \cdot \nabla T - w \frac{\alpha g T}{C_p} \right) + \gamma_{410} \frac{\Delta\rho_{410} T}{\rho_0} \frac{D\Gamma_{410}}{Dt}$$
$$+ \gamma_{660} \frac{\Delta\rho_{660} T}{\rho_0} \frac{D\Gamma_{660}}{Dt} = k\nabla^2 T + 4\eta\dot{\varepsilon}_{\mathrm{II}}^2 + \rho_0 H, \tag{3}$$

where Γ_{410}, Γ_{660}, and $\dot{\varepsilon}_{\mathrm{II}}$ are defined by

$$\Gamma_i \equiv \frac{1}{2}\left[1 + \tanh\left(\frac{p - \rho_0 g z_i + \gamma_i (T - T_i)}{\rho_0 g d_i}\right)\right] \quad (i = 410, 660) \tag{4}$$

$$\dot{\varepsilon}_{\mathrm{II}} \equiv \sqrt{\frac{1}{2}\sum_{i,j=1}^{2} \dot{\varepsilon}_{ij}^2}. \tag{5}$$

Different internal heating H is imposed among the mantle ($\times 1$), oceanic crust ($\times 10$), and continental crust ($\times 100$) based on present-day estimation (Turcotte & Schubert, 2001). To derive the temperature field for successive time steps, Equation (3) is discretized into a uniform grid consisting of 4,000 $\times$ 1,160 square control volumes with a 2.5-km side using a partially upwind finite volume scheme (Clauser & Kiesner, 1987).

2.4. Rheology model

2.4.1. Diffusion and dislocation creep

As suggested by experimental results, we assume that the deformation rate of the dry and wet rocks follows Arrhenius laws (e.g., Korenaga & Karato, 2008),

$$\dot{\varepsilon}_{1(\mathrm{diff,dry})} = A_1 \exp\left(-\frac{E_1^* + pV_1^*}{RT}\right)\sigma \tag{6}$$

$$\dot{\varepsilon}_{2(\mathrm{diff,wet})} = A_2 C_{\mathrm{OH}^-}^{r_{\mathrm{diff}}} \exp\left(-\frac{E_2^* + pV_2^*}{RT}\right)\sigma \tag{7}$$

$$\dot{\varepsilon}_{3(\mathrm{disl,dry})} = A_3 \exp\left(-\frac{2}{n_3 + 1}\frac{E_3^* + pV_3^*}{RT}\right)\sigma \tag{8}$$

$$\dot{\varepsilon}_{4(\mathrm{disl,wet})} = A_4 C_{\mathrm{OH}^-}^{r_{\mathrm{disl}}} \exp\left(-\frac{2}{n_4 + 1}\frac{E_4^* + pV_4^*}{RT}\right)\sigma. \tag{9}$$

Here, grain-size effects on diffusion creep are ignored (included in coefficient A_i). We approximate dislocation creep to linear creep with reduced activation enthalpy according to Christensen (1984). For simplification, the viscosity of MORB is assumed to be the same as that of the mantle.

We applied the values of activation energy E_i^* and activation volume V_i^* of the upper mantle estimated by Karato & Wu (1993) to the whole mantle; however, the viscosity of the lower mantle calculated from Arrhenius laws for olivine is much larger than that observed from postglacial rebound (e.g., Milne et al., 1999; Okuno & Nakada, 2001). In order to reduce the pressure dependence, the activation volume below 300-km depth is assumed to decrease linearly with the depth, i.e.,

$$V_{1,2}^{*} = V_0 + (V_L - V_0)\,\frac{z}{h}. \tag{10}$$

Because deformation in laboratories differs from that in Earth's mantle on both spatial and temporal scales, it is necessary to re-evaluate the viscosity scales A_i. A_1 is determined so that the viscosity calculated from the above constitutive law for dry diffusion creep corresponds to an estimation $\eta_{\mathrm{ref}} = 5 \times 10^{20}$ at the 410-km phase boundary (e.g., Milne et al., 1999; Okuno & Nakada, 2001). A_2 is determined so that the wet diffusion mechanism is dominant ($\dot{\varepsilon}_2 > \dot{\varepsilon}_1$) when the rock contains water above 100 ppm at the 410-km phase transition condition. The formulation is based on the assumption that the viscosity of the present-day mantle transition zone containing 100 ppm H_2O could be realized by both dry and wet diffusion mechanisms. A_3 and A_4, coefficients for dislocation creep, are determined so that dislocation creep becomes dominant ($\dot{\varepsilon}_3 > \dot{\varepsilon}_1$ and $\dot{\varepsilon}_4 > \dot{\varepsilon}_2$) above 300-km depth to reproduce the low viscosity of the asthenosphere.

The values of the water exponent r_{diff} and r_{disl} are treated as variable parameters owing to their uncertainty (Korenaga & Karato, 2008; Hirth & Kohlstedt, 2003; Fei et al., 2013). The meanings and origin of the uncertainty of r are discussed in Section 4.3.

Dry and wet deformation mechanisms simultaneously work on the same material. As $\dot{\varepsilon}_{\mathrm{dry}} \gg \dot{\varepsilon}_{\mathrm{wet}}$ in less-hydrated rocks and $\dot{\varepsilon}_{\mathrm{dry}} \ll \dot{\varepsilon}_{\mathrm{wet}}$ in well-hydrated rocks, the effective strain rate is approximated by the value of the dominant mechanism,

$$\dot{\varepsilon} = \max\left[\dot{\varepsilon}_1, \dot{\varepsilon}_2, \dot{\varepsilon}_3, \dot{\varepsilon}_4\right]. \tag{11}$$

2.4.2. Yielding of highly viscous fluid

In addition to creep mechanisms, in order to reproduce plate-like behavior, we introduce yielding of highly viscous fluid (e.g., Cserepes, 1982; Moresi & Solomatov, 1998; Tackley, 2000). If stress reaches yield strength σ_{Y}, the viscosity significantly decreases, i.e.,

$$\eta = \frac{\sigma_{\mathrm{Y}}}{2\dot{\varepsilon}_{\mathrm{II}}} \quad (\sigma_{\mathrm{II}} = \sigma_{\mathrm{Y}}), \tag{12}$$

where $\dot{\varepsilon}_{\rm II}$ is defined by Equation (5). On the contrary, if the stress acting on the rock is smaller than the yield strength, the creep mechanisms dominate as defined by Equation (11),

$$\eta = \frac{\sigma_{\rm II}}{\dot{\varepsilon}} \quad (\sigma_{\rm II} < \sigma_{\rm Y}). \tag{13}$$

The second invariant of stress is defined by

$$\sigma_{\rm II} \equiv \sqrt{\frac{1}{2}\sum_{i,j=1}^{2}\sigma_{ij}^2}. \tag{14}$$

The yield strength is assumed to increase linearly with the depth z, i.e.,

$$\sigma_{\rm Y} = \min[(\sigma_{\rm Y0} + c_{\rm Y}\rho_s g z), \sigma_{\rm Ymax}]. \tag{15}$$

The maximum yield strength $\sigma_{\rm Ymax}$ is determined as the brittle-ductile transition of the lithosphere (Kohlstedt et al., 1995). Although the larger $\sigma_{\rm Ymax}$ of the overlying lithosphere prevents trench motion and rapid subduction, we regard their effects on the subduction mode as minimal, as discussed in Appendix C. Small values of cohesive strength $\sigma_{\rm YF}$ and friction coefficient $c_{\rm YF}$ are imposed on the fault zone at $x = 6,000$ km and the mid-ocean ridge at $x = 0$ km. Contrary to that reported by Gerya & Meilick (2011), we do not incorporate the decline of lithospheric yield strength owing to hydration.

Finally, the lower and upper limits of the effective viscosity are set to be 10^{17} and 10^{25} Pa s, respectively. Examples of the calculated effective viscosity profiles are shown in Figure 4a.

2.5. State equation

We introduce temperature- and water-dependent density, $\rho = \rho(T, C_{\rm H_2O})$. Thermal expansivity α and hydration expansivity β are defined by

$$\alpha \equiv -\frac{1}{\rho}\left(\frac{\partial\rho}{\partial T}\right)_{C_{\rm H_2O}} \tag{16}$$

$$\beta \equiv -\frac{1}{\rho}\left(\frac{\partial\rho}{\partial C_{\rm H_2O}}\right)_{T}. \tag{17}$$

Since density changes owing to both heating and hydration (i.e., αdT and $\beta dC_{\rm H_2O}$) are typically very small, the total derivative of density can be expressed by

$$\begin{aligned} d\rho &= \left(\frac{\partial\rho}{\partial T}\right)_{C_{\rm H_2O}} dT + \left(\frac{\partial\rho}{\partial C_{\rm H_2O}}\right)_{T} dC_{\rm H_2O} \\ &= -\rho_0\alpha(T - T_0) - \rho_0\beta C_{\rm H_2O}, \end{aligned} \tag{18}$$

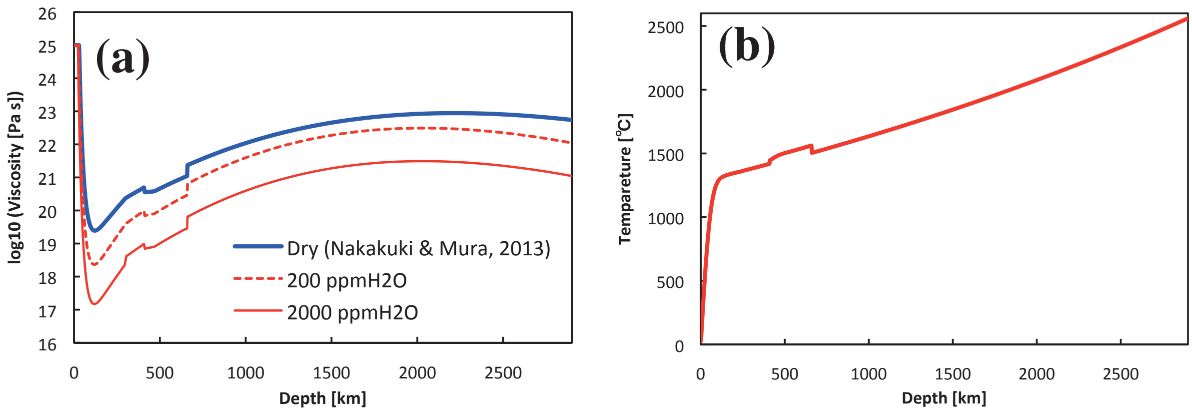

Figure 4: (a) Examples of the viscosity profiles in the simulation in the case of $r_{\mathrm{diff}} = 1.0, r_{\mathrm{disl}} = 1.2$. Viscosity gaps at the depth of 410 and 660 km are caused by temperature gaps. (b) Temperature profile in the simulation. Gaps at the 410- and 660-km discontinuity correspond to latent heat.

where ρ_0 is the reference density, and T_0 is the reference temperature. The reference water content is 0 ppm in this expression.

Besides these thermal and hydration effects, we take into account of phase changes of olivine morphologies and crustal materials for the calculation of the buoyancy term in Equation (1) as

$$\begin{aligned} \rho &= \rho_0 \left[1 - \alpha \left(T - T_0\right) - \beta C_{\mathrm{H_2O}}\right] \\ &+ \Delta\rho_{410}\Gamma_{410} + \Delta\rho_{660}\Gamma_{660} - \Delta\rho_C\Gamma_C. \end{aligned} \tag{19}$$

After Jacobsen et al. (2008), Mao et al. (2008), and Inoue et al. (1998), β $[(\mathrm{kgH_2O/kg})^{-1}]$ are 1.6 for olivine, 1.3 for wadsleyite, and 1.2 for ringwoodite. However, under a high-pressure condition, β is less constrained (Richard & Iwamori, 2010), and the value is treated as a variable. The meanings and origin of the uncertainty of β are discussed in Section 4.3.

The last three terms in Equation (19) are associated with the 410-km phase change, the 660-km phase change, and the continental crust, respectively. Density increases $\Delta\rho_{410}$ and $\Delta\rho_{660}$ are based on the Preliminary Reference Earth Model (PREM; Dziewonski & Anderson, 1981). Although Clapeyron slopes γ_{410} and γ_{660} are somewhat controversial, we verified that their effects on the subduction mode were minimal, as discussed in the supplementary materials. Γ_C is set to be 0 (peridotite) to 1 (continental crust). The density of MORB is assumed to be the same as that of mantle rocks.

2.6. *Transportation of water*

2.6.1. *Solid phase*

We assume that water bonded to or captured in minerals is transported with mantle flows, as expressed by the advection equation:

$$\frac{\partial C_{\mathrm{H_2O}}}{\partial t} + \boldsymbol{v} \cdot \nabla C_{\mathrm{H_2O}} = -\dot{C}_{\mathrm{H_2O}}^{\mathrm{sol}\to\mathrm{aq}}. \tag{20}$$

Here, hydrogen diffusion ($\kappa_{\mathrm{H}} \ll 10^{-6}$ [$\mathrm{m^2/s}$]; Mackwell & Kohlstedt, 1990; Sun et al., 2015) is ignored owing to the short calculation period (< 50 Myr). The advection term is calculated by a Marker-and-Cell method using 4,000 × 1,160 × 36 particles. We assume that MORB containing 3 wt.%H_2O sinks into an initially dry mantle (Rüpke et al., 2004; Horiuchi & Iwamori, 2016). The effects of water distribution in oceanic plates are verified in the supplementary materials: Given 6 wt.%H_2O within the uppermost oceanic crust, similar results were obtained. If $C_{\mathrm{H_2O}}$ in MORB or peridotite reaches the maximum water content determined by p–T phase diagrams of Iwamori (2007), excess aqueous fluid is emitted from the solid phase. Although the water storage capacity of the lower mantle is controversial, we assumed it to be 0.21 wt.% (Murakami et al., 2002) because we mainly simulated slab behavior in the upper mantle. The effect of the water storage capacity of the lower mantle is discussed in Section 3.4 in Chapter III.

2.6.2. *Aqueous fluid phase*

In subduction zones with continuous dehydration, the upward velocity of the fluid flowing through porous media is 10^2 to 10^4 times higher than that of mantle flows (McKenzie, 1984; Horiuchi & Iwamori, 2016). We therefore assume that all water released from the subducting slab is transported instantaneously upward and is absorbed into the overlying rocks that have available water capacity according to the p–T conditions, within one time step, i.e.,

$$\boldsymbol{v}_{\mathrm{aq}} = -\infty. \tag{21}$$

In this way, water transportation can be simulated only by solving the equation of motion for the solid phase. This approximation has been employed by Iwamori & Nakakuki (2013) and Nakagawa et al. (2015). Validity of the approximation is verified by introducing a finite fluid ascent velocity in Section 3.3 in Chapter III.

2.7. Transportation of crust and fracture zone

The transportation of other heterogeneities such as MORB, continental crust, and fault segments (C_i) is also calculated by using the Marker-and-Cell method:

$$\frac{\partial C_i}{\partial t} + \boldsymbol{v} \cdot \nabla C_i = 0. \tag{22}$$

2.8. Time step

The time-step interval Δt of each cycle is variable and is determined so that the maximum value of the Courant number $c_{i,j}$ becomes 0.1, i.e.,

$$c_{i,j} = \left(\frac{u_{i,j}}{\Delta x} + \frac{w_{i,j}}{\Delta z} \right) \Delta t = 0.1 \tag{23}$$

where $u_{i,j}$ and $w_{i,j}$ are velocity components at the (i, j) node. $\Delta x = 2.5$ km and $\Delta z = 2.5$ km are the grid spacing.

Finally, a series of numerical procedures consisting from above basic equations is summarized in Figure 5.

3. Results

In the following parameter study, two physical properties r (exponent of hydration-viscosity coefficient in the constitutive laws; Section 2.4) and β (hydration-density coefficient in the state equation; Section 2.5), are treated as variables; other settings and parameters are equalized. Twelve pairs of the parameters and the corresponding run IDs are listed in Figure 6, and snapshots of all 12 runs are shown in Figure 7.

3.1. Overview of water transportation

An example of the simulated evolution ($r_{\text{diff}} = 1.0, r_{\text{disl}} = 1.2, \beta = 1.0$) is shown in Figure 8. The oceanic plate begins to subduct as a result of its negative thermal buoyancy; correspondingly, the hydrous MORB layer sinks into the deep mantle (5.45 Myr in Figure 8b,c). According to a phase diagram of hydrous basalt (Iwamori, 2007), MORB emits almost all water transforming into eclogite at a depth of about 70 km; accordingly, a layer of hydrous peridotite just above the subducted oceanic crust forms. Because the hydrous ultramafic layer still sinks, according to the phase diagram of hydrous peridotite of Iwamori (2007), dehydration reactions of hydrous minerals occur at about 600°C (Ol + Serp + Chl + Amp → Ol + Opx + Chl + Cpx) and at about 800°C (Ol + Opx +

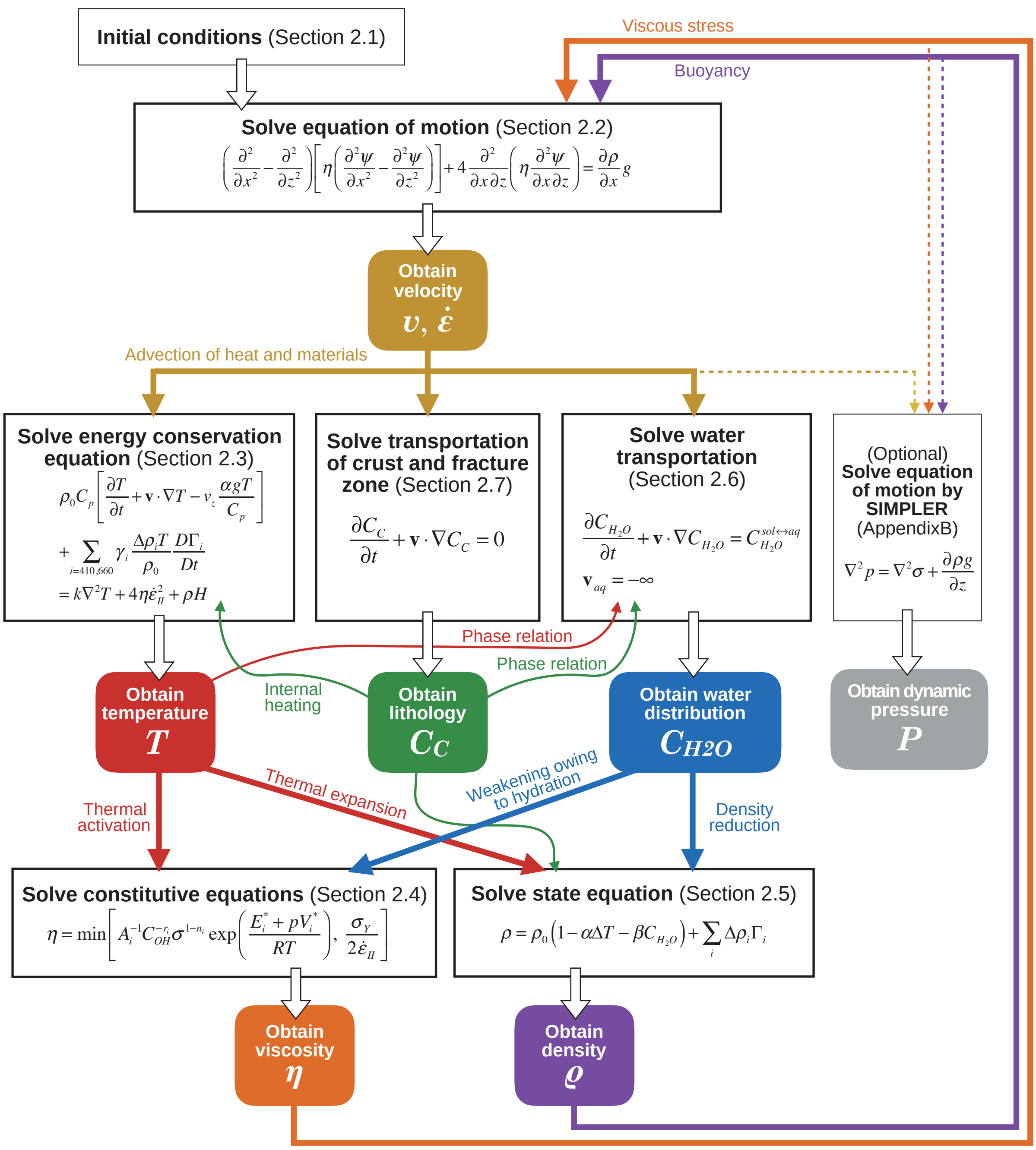

Figure 5: Flow chart of the numerical simulation in this chapter.

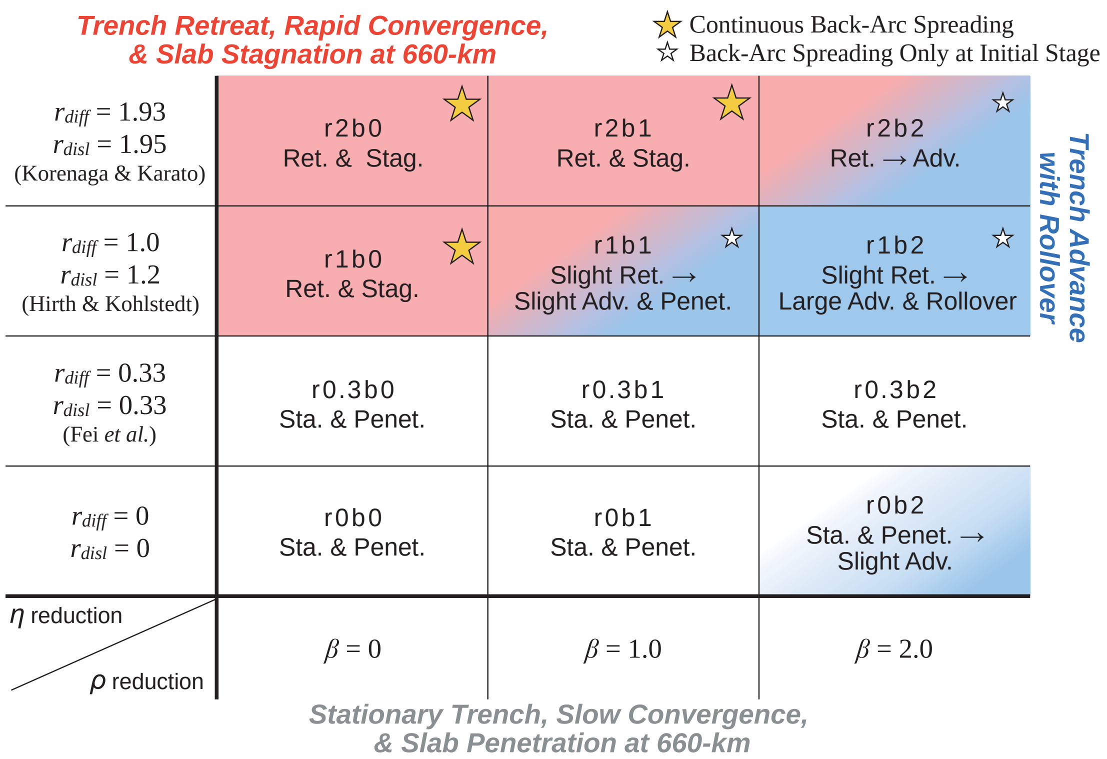

Figure 6: Run list and the corresponding results diagram of all 12 cases with different hydrous weakening r (vertical) and hydrous buoyancy β (lateral).

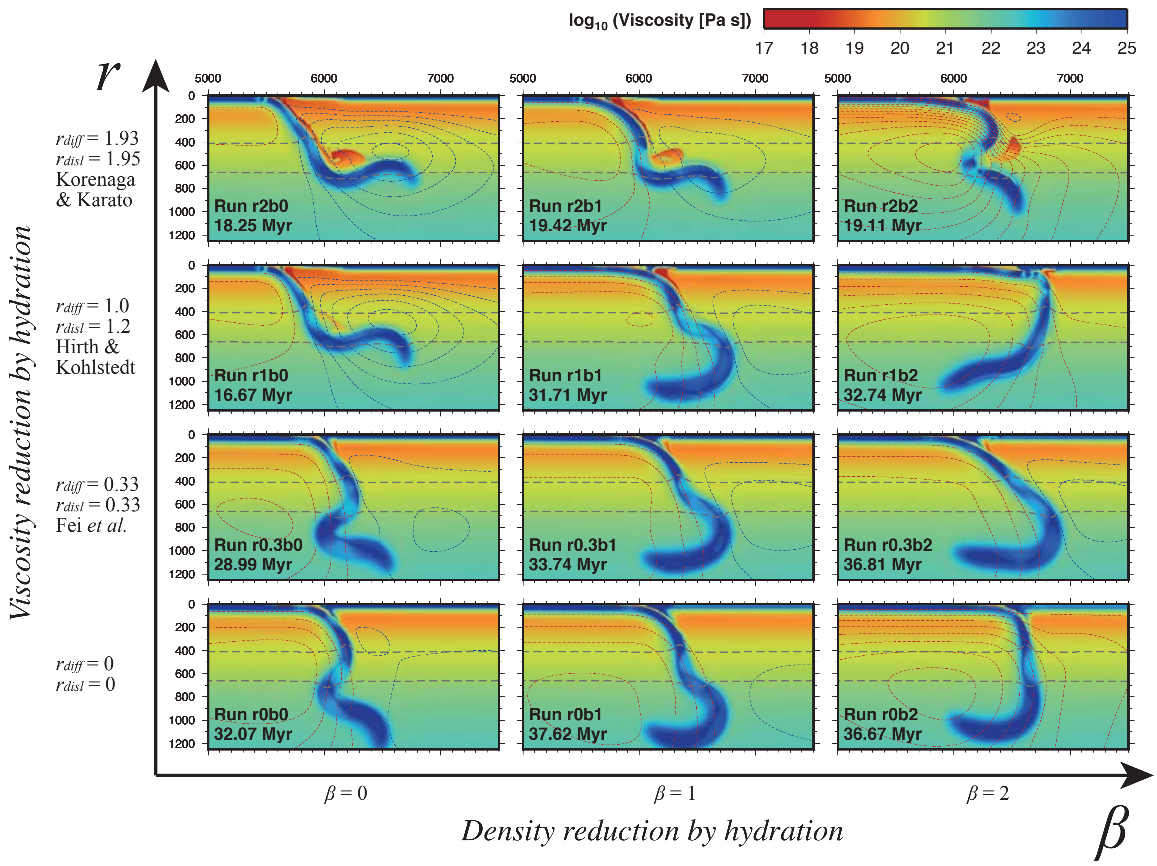

Figure 7: Summary of all 12 runs with different hydrous weakening r (vertically) and hydrous buoyancy β (laterally). The colored contour shows viscosity structure. The presented range is horizontally $5,000 < x < 7,500$ [km] and vertically $0 < z < 1,250$ [km]. Red and blue dotted lines are clockwise ($\psi > 0$) and counterclockwise ($\psi < 0$) stream functions (10^{-4} [m^2/s] intervals), respectively. Dashed gray lines represent the 410-km and 660-km phase boundaries.

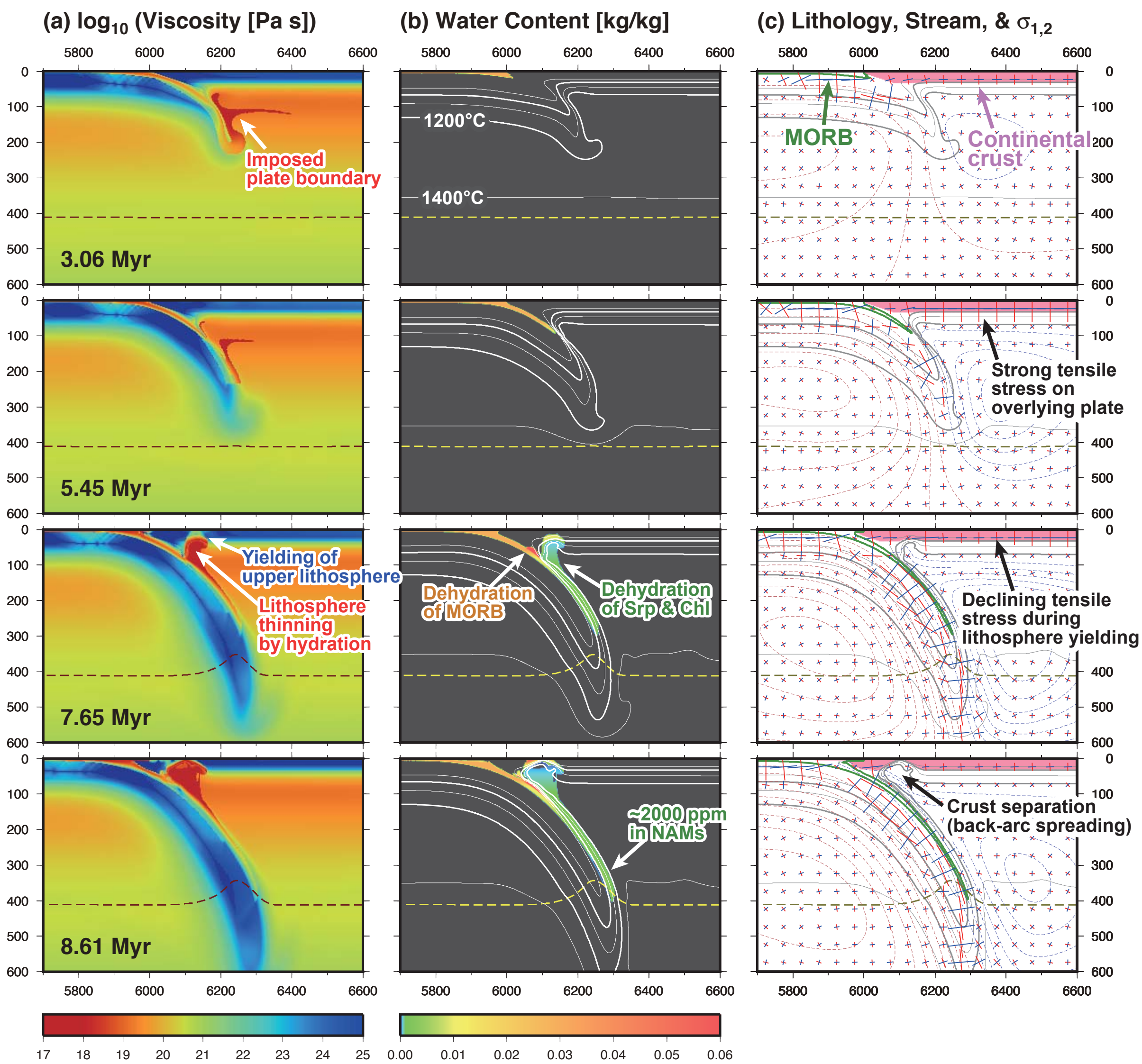

Figure 8: Initial evolution of run r1b1 ($r_{\mathrm{diff}} = 1.0, r_{\mathrm{disl}} = 1.2, \beta = 1$). The presented range is horizontally $5,750 < x < 6,800$ [km] and vertically $0 < z < 600$ [km]. (a) The colored contour shows viscosity structure. Dashed brown lines represent the 410-km phase boundary. (b) The colored contour shows the weight fraction of water in rocks. White lines represent isotherms (200°C intervals). Dashed yellow lines represent the 410-km phase boundary. (c) Pink and green areas show continental granite and oceanic basalt, respectively. Red and blue dotted lines are clockwise ($\psi > 0$) and counterclockwise ($\psi < 0$) stream functions (5×10^{-5} [m^2/s] intervals), respectively. Blue and red axes put at 50-km intervals represent the magnitude and directions of maximum principal stress σ_1 (tensile) and minimum principal stress σ_2 (compressive), respectively. Isotherms and the 410-km phase boundary are also shown.

$Chl+Cpx \rightarrow Ol+Opx \pm Pl/Sp/Gt \pm Cpx$) with the temperature increase owing to thermal conduction (7.65 Myr in Figure 8b). This reaction path is the same as that of southwest Japan simulated by Iwamori (2007) using a wedge flow model. After that, the water fraction equal to the water storage capacity of nominally anhydrous minerals (NAMs) in assemblage Ol + Opx ± Pl/Sp/Gt ± Cpx, around 2,000 ppm, is transported by advection of the solid phase into the mantle transition zone without dehydration (8.61 Myr of Figure 8b) because of the high water storage capacity of wadsleyite and ringwoodite (e.g., Inoue et al., 1995). These features were similarly reproduced by Horiuchi & Iwamori (2016), who considered the finite ascent velocity of aqueous fluid porous flow based on the same phase diagram and water storage capacity, which justifies the approximation of infinite ascent velocity in our model. In the case of $r_{\text{diff}} \leq 1.0, r_{\text{disl}} \leq 1.2$, despite hydrous weakening, the ultramafic hydrous layer is viscously coupled with the down-going slab without inducing wet plumes. This is in contrast to the results of Richard & Iwamori (2010), who considered the simple initial thermal structure of a slab. Excess water emitted from the ultramafic layer creates a low viscosity column from the slab surface to the shallow area (7.65 Myr in Figure 8a), which is consistent with previous numerical studies (e.g., "thermal erosion of the overlapping lithosphere" of Arcay et al., 2005). Thus, lithosphere thinning occurs in the continental margin. Because the thermal effects on the viscosity are stronger than the hydrous effect, the cold upper continental lithosphere is sufficiently viscous. As a result, strong tensile stress working on the overlying lithosphere (5.45 Myr in Figure 8c) induced by negative buoyancy of the subducting slab concentrates on the region of local erosion; correspondingly, the continental margin spreads by the yielding mechanism. While the yielding of the continental margin progresses, tensile stress working on the overlying lithosphere declines (5.45 Myr to 8.61 Myr in Figure 8c). After that, with the hot asthenosphere welling to the surface, the overlying plate and continental crust separate (8.61 Myr in Figure 8c). In this spreading mechanism, the stress concentration within the overlying lithosphere eroded by underlying hydration is the main cause for the back-arc opening. This differs from that proposed by Gerya & Meilick (2011), who argued for reduction of the yield strength of lithosphere owing to hydration. The gap enhances trench migration retreat or advance, depending on the parameter values, as will be discussed in the following sections.

3.2. Effects of viscosity reduction owing to hydration

Figure 9 shows snapshots of four runs with different hydrous weakening r and the same hydrous buoyancy β. In the cases of larger r (Figure 9a,b), erosion of the lower continental lithosphere hydrated through the porous flows from decomposed hydrous minerals plays an important role in causing the hot surrounding mantle to enter the shallower corner of the mantle wedge. As the slab reaches the 410-km phase boundary (i.e., the density of the slab increases due to the shallower phase change of olivine to wadsleyite), the continental margin is rapidly extended. This results in the intense trench retreat. Correspondingly, rapid flows are induced around the slab (i.e., closely plotted stream lines). Thereafter, a stagnant slab stably develops at the 660-km phase boundary. Although the scenarios of these two runs seem quite similar, evolution of run r2b0 is slightly faster than that of run r1b0 (Figure 10). This is because the less viscous the hydrous layer and column are, the lower the viscous resistance around the slab is. Besides, given larger r, the ultramafic hydrous layer becomes less viscous, helping the hydrous rocks to separate from the slab surface.

In the cases of smaller r (Figure 9c,d), although the hydrous layer and column also form, erosion of the lower continental lithosphere by hydration is slight or none. Such a thick continental margin prevents the concentration of tensile stress; therefore, neither back-arc spreading nor trench retreat occurs. The fixed trench causes slab penetration. The subduction rate in the case of lower r is much smaller (i.e., sparsely plotted stream lines) than that with larger r (Figure 10). Similar to the runs with the stagnant slab formation, the evolution and subduction rates of run r0.3b0 are slightly higher than those of run r0b0, although these two results seem broadly similar.

Thus, viscosity reduction due to large r enhances trench migration and affects slab morphology. Note that transition between the retreating trench (and the corresponding stagnant slab) and the stationary trench (and the corresponding slab penetration) is related to yielding of the thinned continental margin; therefore, it is controlled not only by r but also by the thermal structure (i.e., thickness of the plate) and yield strength of the overlying plate. Moreover, since the especially small yield strength of hydrous lithosphere, which mimics fault activation by pore fluids, is not imposed, continental margins in nature may be extendable. In other words, after reaching the 660-km phase boundary, the slab does not penetrate further into the lower mantle, but tends to release

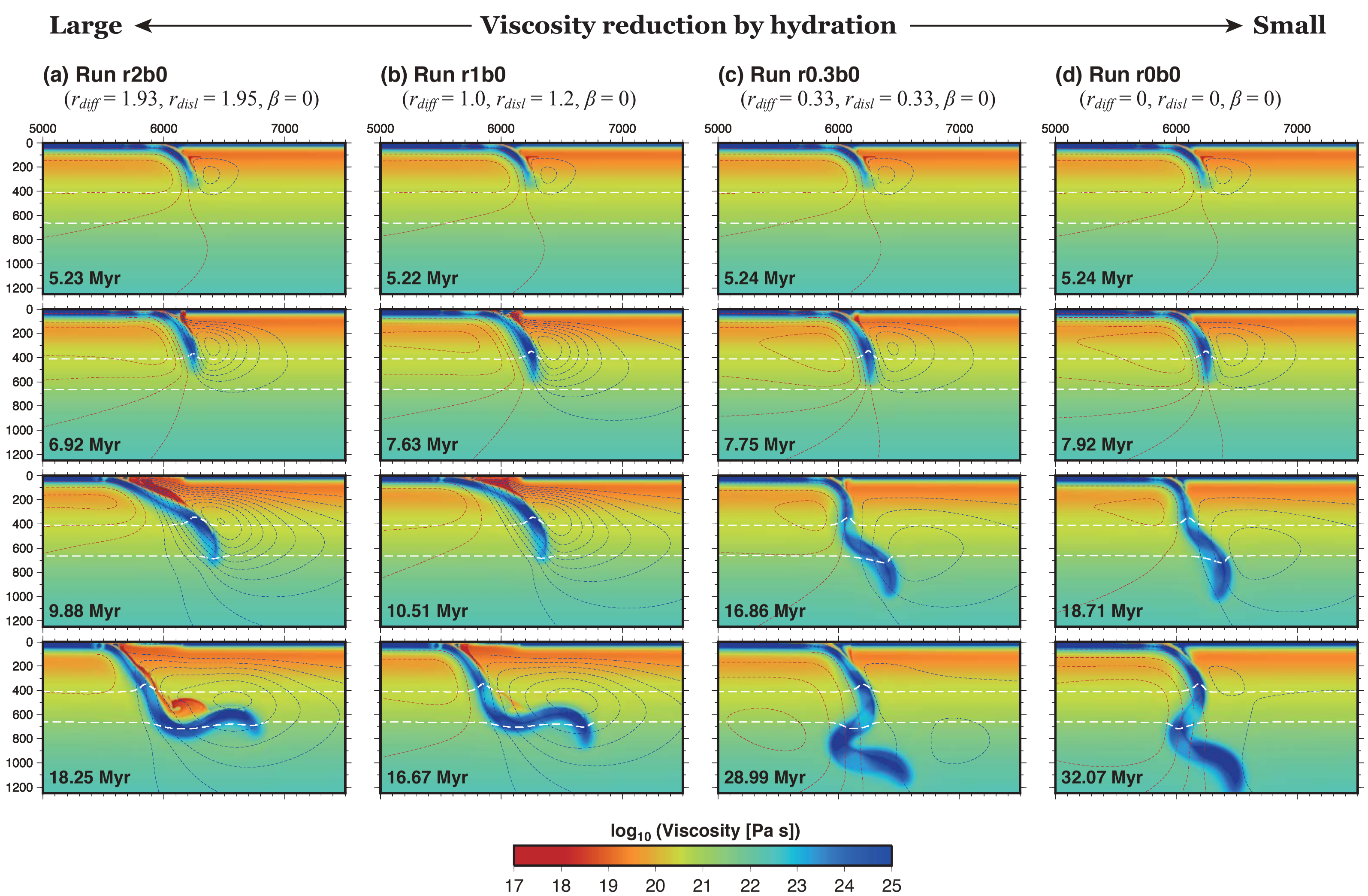

Figure 9: Comparison of evolution of four runs, where different r (viscosity reduction by hydration) and the same β (= 0; hydrous buoyancy) are given. Symbols are the same as those in Figure 7. (a) Evolution of run r2b0 ($r_{\rm diff} = 1.93, r_{\rm disl} = 1.95$). (b) Evolution of run r1b0 ($r_{\rm diff} = 1.0, r_{\rm disl} = 1.2$). (c) Evolution of r0.3b0 ($r_{\rm diff} = 0.33, r_{\rm disl} = 0.33$). (d) Evolution of r0.3b0 ($r_{\rm diff} = 0, r_{\rm disl} = 0$).

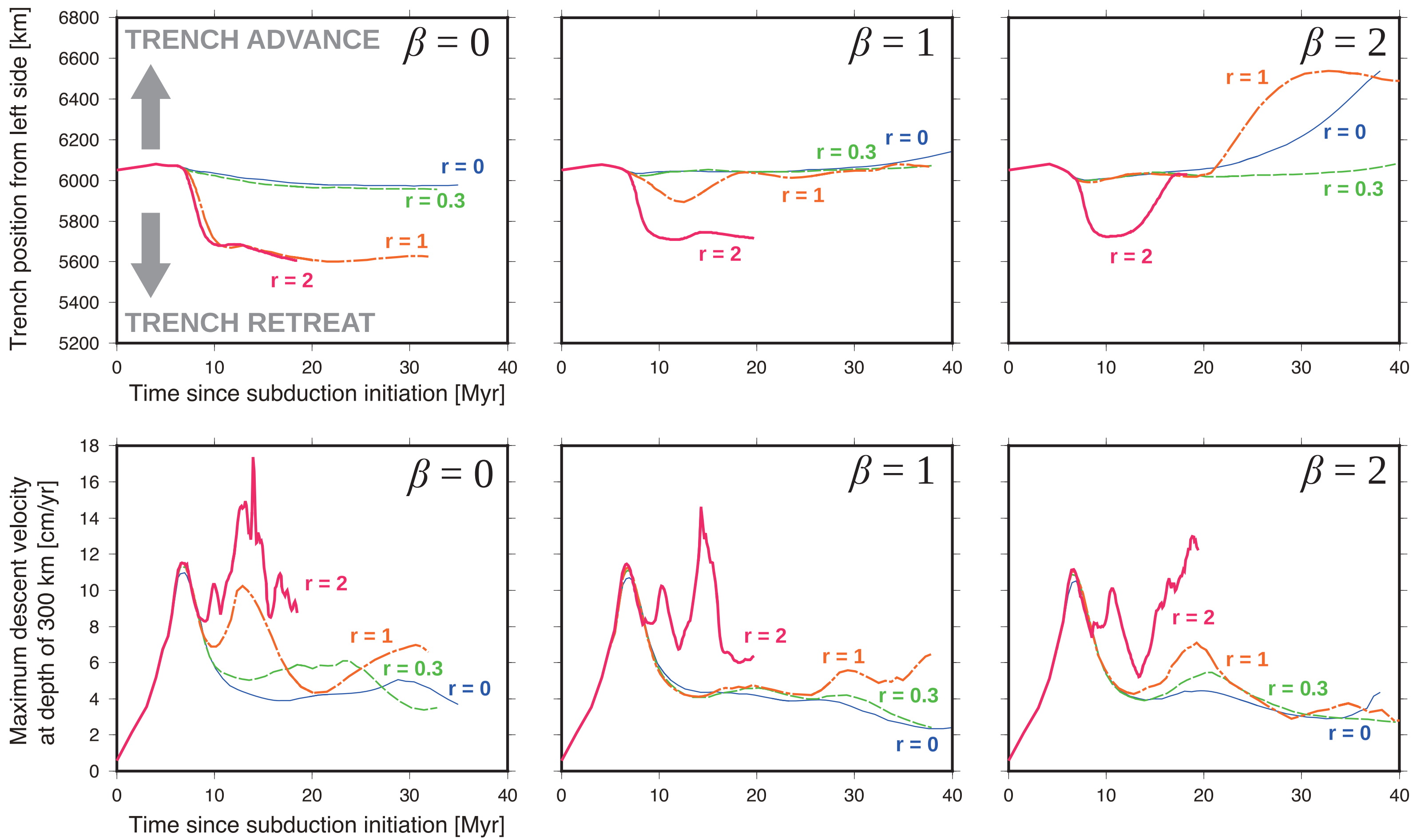

Figure 10: Top three graphs denoting time-dependent lateral positions of the trench of all 12 runs with different r (viscosity reduction by hydration) and β (density reduction by hydration), where the decline of the vertical value means trench retreat, and its increase means trench advance. The bottom three graphs similarly denote the maximum descent (vertical) velocity at a depth of 300 km.

its potential energy while the tip is anchored at the phase boundary owing to the higher viscosity of the lower mantle. This causes trench migration accompanied by extension of the deformable overriding plate due to a large r. Thus, we can consider that in runs with large r, slabs behave as if there is no overlying plate.

3.3. Effects of density reduction owing to hydration

Figure 11 shows snapshots of three runs with varying hydrous buoyancy β and fixed hydrous weakening r. The dynamic pressure (difference from lithostatic pressure) displayed in Figure 11 is solved using a SIMPLER algorithm (Patankar, 1981).

In the case of small β, Figure 11a shows the same case as that of Figure 9b, and we have already confirmed that tensile stress on the overlying plate, back-arc spreading, and trench retreat in run r1b0 are associated with a density increase in the slab due to Ol/Wd transition. During trench retreat and corresponding back-arc spreading, strong "downward" mantle flows (closely plotted stream functions) across the hydrous prism and layer in the edge of the mantle wedge are induced to compensate for the retreating slab (7.63 to 11.03 Myr of Figure 11a). Suction from the retreating slab induces negative dynamic pressure in the extending mantle wedge, and the overlying plate undergoes continuous tensile stress.

In the case of large β, as with run r1b0, back-arc spreading and trench retreat occur initially as the slab reaches the 410-km boundary. However, the retreat, induced corner flows, and subduction rate are less active than those in run r1b0 (Figure 11b,c). The reason for this is that the buoyant hydrous areas along the slab surface partially cancel out the driving force of slab subduction, preventing the concentration of tensile stress enough to cause continental margin extension. As a result, the slab dip remains steep. After the slab crosses the 660-km boundary (i.e., the driving force diminishes), strong lateral flows directed from the oceanic asthenosphere to the continental side predominate (19.71 Myr of Figure 11c) instead of the sub-continental "counterclockwise" streams that emerge in the trench retreat mode. This rightward flow compresses the hydrated mantle wedge and induces a correspondingly strong positive pressure. In contrast, the pressure at the rear of the advancing slab is negative, contributing to lifting of the tip of the slab in the lower mantle. The slab deformation causes maximum principal stress σ_1 (tensile axis) to turn along the slab in the lower mantle (19.71 Myr of Figure 11c). The

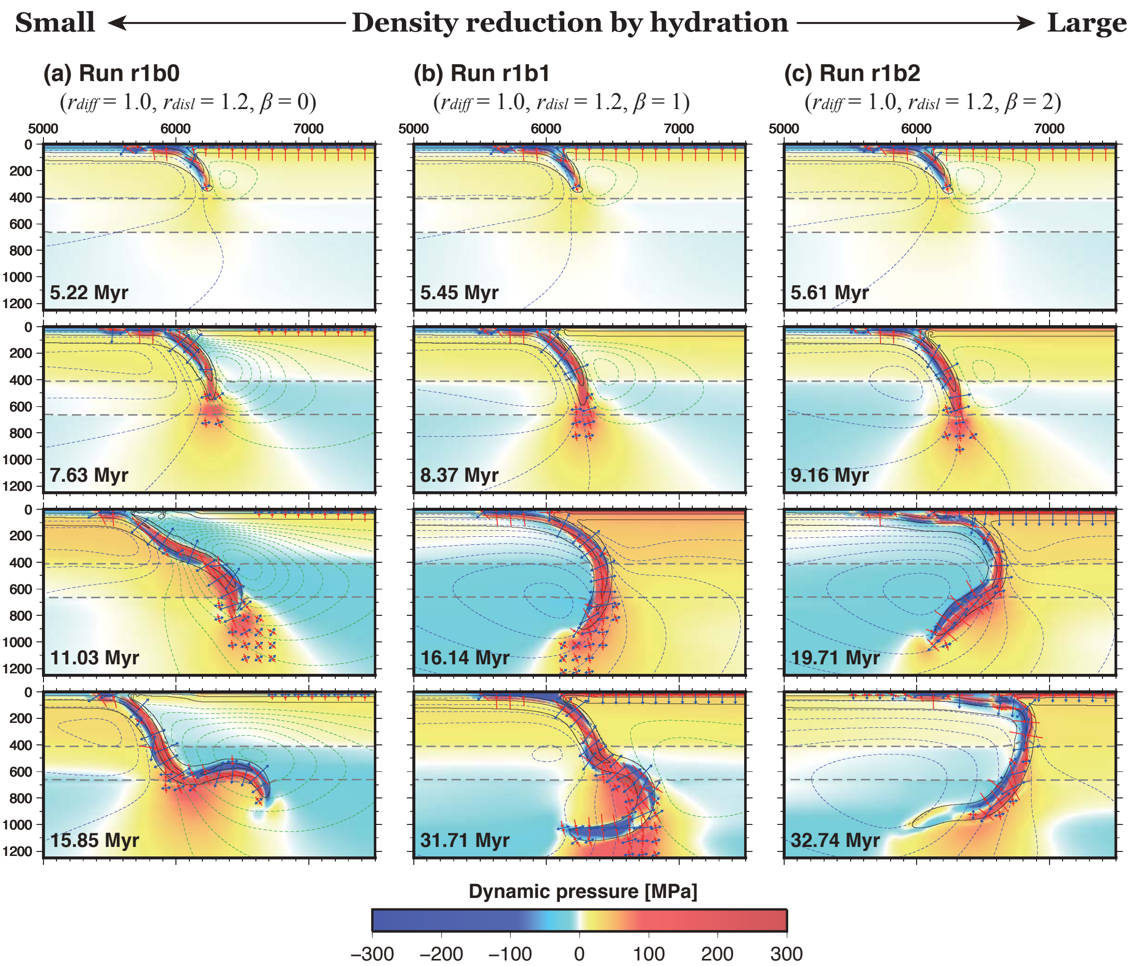

Figure 11: Comparison between evolution of three runs, where varying β (hydrous buoyancy) and fixed r $(= 1.0, 1.2$; viscosity reduction by hydration) are given. The presented horizontal range is $5000 < x < 7500$ [km] and the vertical range is $0 < z < 1250$ [km]. The colored contour shows dynamic overpressure, or difference from lithostatic pressure; red areas are compressed, and blue areas are decompressed. Solid black lines represent isotherms (400°C intervals). Purple and green dotted lines are clockwise ($\psi > 0$) and counterclockwise ($\psi < 0$) stream functions (10^{-4} [m^2/s] intervals), respectively. Blue and red arrows put at 150-km intervals represent magnitudes and directions of maximum principal stress σ_1 (tensile) and minimum principal stress σ_2 (compressive), respectively. Here we ignore arrows with small principal stress. Dashed gray lines represent 410- and 660-km phase boundaries. (a) Evolution of run r1b0 ($\beta = 0$). (b) Evolution of run r1b1 ($\beta = 1$). (c) Evolution of r1b2 ($\beta = 2$).

continuous-track-like shape accompanying trench advance occasionally emerges in previous laboratory and numerical experiments (e.g., Schellart, 2008; Stegman et al., 2010). This subduction structure would be the most efficient mode to release the potential energy of the cold slab so as to enable its descent into the deep mantle without dragging the buoyant hydrous rocks. In addition, the trench advance is also expected to be favorable to a small convergence rate owing to reduction of viscous dissipation by plate bending. These mechanisms to produce the trench motion are consistent with Royden & Husson (2006), who showed that the small buoyant "frontal prism" prevents the trench retreat and the formation of the gently-sloping slab.

Thus, hydrous buoyancy β contributes to slow subduction, slight back-arc spreading, compressive stress on the overlying plate associated with the 660-km-depth interaction, and the steep slab, all of which are roughly contrary to the effects of hydrous weakening r; however, the large (r, β) model, whose characteristics are the deforming continental margin and the movable trench (retreat to advance), is clearly different from the small (r, β) model, where both continental margin and trench are stationary.

3.4. Tensile stress acting on overlying plate

In the models described in the previous sections, yield strength is imposed on the lithosphere to provide the upper limit of the stress. This causes continental margin spreading, which induces the trench retreat and the slab stagnation. To quantify the potential for various r and β to generate tensile stress σ_{xx} in the overlying plate, we conducted a further simulation in which the yield strength was removed from the overriding lithosphere.

- (Procedure 1) Before the 3,001st step (< 9.73 Myr; after the tip of a slab enters the mantle transition zone; c.f., the second panel of Figure 9d), we conducted a common simulation employing the same method described in Section 2 using the same parameters as run r0b0.
- (Procedure 2) At the 3,001st step (9.73 Myr), we removed yielding behavior (Equation 13) from the overlying plate, and imposed 12 different (r, β) pairs on hydrous regions. Here we name them runs r0b0ny, r0b1ny, $\cdots$ r2b2ny. We then solved the stream and the accompanying stress field at the time step. We calculate average σ_{xx} of the continental margin ("area A"; 6,170$< x <$6,180 [km] and $2.5 < z < 10$ [km]) and the inland ("area B"; $6{,}250 < x < 6{,}300$ [km] and $2.5 < z < 10$ [km]).

The results are shown in Figure 12. Values of σ_{xx} for area A increase with r, whereas σ_{xx} of area B is scarcely affected, suggesting that viscosity reduction by hydration, which competes with cooling of the plate, brings stress concentration. On the other hand, given reasonably larger hydrous buoyancy β, σ_{xx} on the overlying plate (both areas A and B) is diminished by several tens of percent. These features emerge significantly after the slab reaches the mantle transition zone.

In run r0.3b0ny, in which r and β are similar to runs without back-arc spreading (run r0.3b0; Figure 9c), σ_{xx} on area A is much larger than yield strength ($50 < \sigma_{\mathrm{Y}} < 130$ [MPa]). This means that positive feedback between tensile stress concentration and lithosphere extension contribute significantly to back-arc spreading.

4. Discussion

4.1. Interpretation of subduction velocity change

We can easily understand how hydrous rock controls the subduction rate by quantifying the one-dimensional force balance around a slab

$$\int \{f_{\mathrm{T}}(l) \pm f_{\mathrm{P}}(l) - f_{\mathrm{H}}(\beta, l)\} \sin\theta dl + F_{\mathrm{top}} - \int \eta(r, l) \frac{du_{\mathrm{sp}}(h)}{dh} dl = 0 \tag{24}$$

where θ is the slab dip, and l and h are coordinates parallel/perpendicular to slab subduction. The first term is slab buoyancy controlled by heat (f_{T}), phase change (f_{P}), and hydration (f_{H}). The second term F_{top} represents the force acting on the top of the slab associated with ridge push. The third term is the viscous resistance acting along the slab. The subduction rate along the slab u_{sp} in the third term is controlled so as to be balanced with other forces. Given large hydrous weakening r, large u_{sp} is required to compensate for the reduction of $\eta(r)$ along a hydrous peridotite layer just above a slab (i.e., to keep the viscous resistance term). In contrast, given large hydrous buoyancy β, small u_{sp} is required to compensate for the reduction of the negative buoyancy. Thus, r and β play opposite roles in determining the subduction rate.

Initially, ($<$ 7 Myr) the effects of f_{T} and f_{P} are dominant, whereas the effects of water are small. Thus, the acceleration of subduction in both cases is similar (Figure 10). Deceleration after the first peak around 7 Myr corresponds to the contact between the slab tip and the 660-km phase boundary. Subsequently, a large subduction rate peak around 13 Myr in runs with large r corresponds to slab bending during trench retreat.

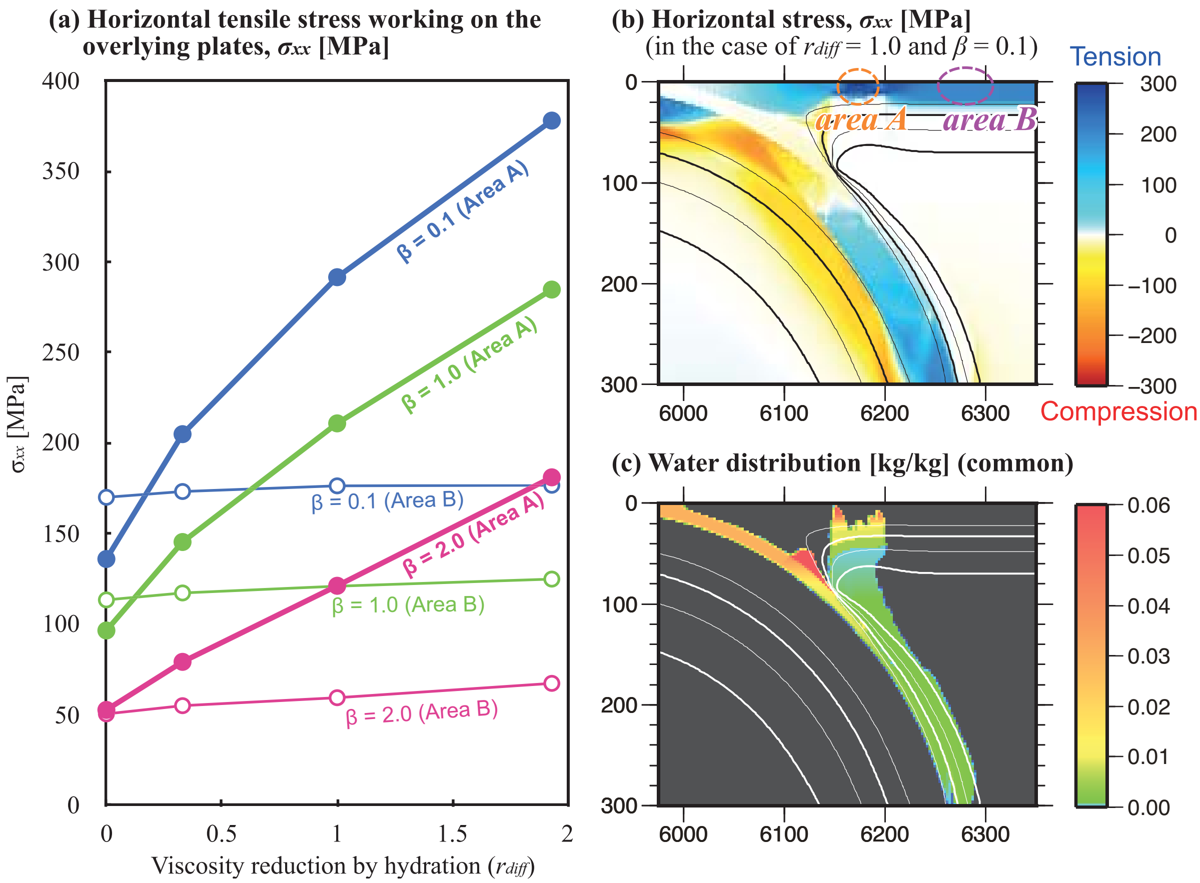

Figure 12: (a) Horizontal tensile stress working on the overlying plates at 9.73 Myr (3,001st step). Results of all 12 runs are plotted here. Areas A (spreading region) and B (inland) are shown in (b). (b) Horizontal stress field at 9.73 Myr (3001st step) in run r1b0ny ($r_{\mathrm{diff}} = 1.0, r_{\mathrm{disl}} = 1.2, \beta = 0.1$). Positive values (cool color) mean laterally tensile and negative values (warm color) mean laterally compressive. Solid black lines represent 600, 800, 1,000, and 1,200°C isotherms. (c) Water distribution at 9.73 Myr (3001st step) in the cases of all runs.

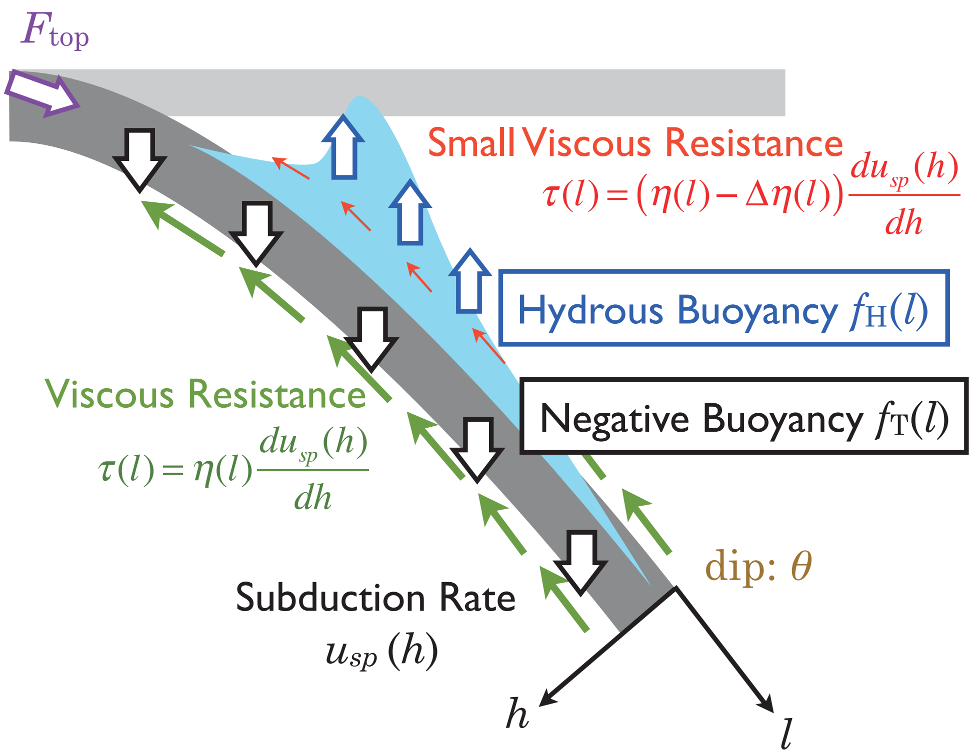

Figure 13: A schematic of the one-dimensional force valance discussed in Section 4.1.

In run r2b2, significant acceleration after 14 Myr would be caused by the collapse of a stagnant slab and/or thickened hydrous low-viscosity layer. After slab penetration, in runs with a semi-stationary trench (runs r1b1, r0.3b1, r0b1), the r effect emerges during semi-constant subduction (> 15 Myr).

4.2. Insights into slab deformation and plate velocity

According to observations of plate motions and slab geometries, subduction styles in nature vary between two extreme modes (e.g., Schellart, 2011): one characterized by a rapid convergence rate, rapid trench retreat, and slab stagnation at the 660-km phase boundary, and the other by a slow convergence rate, a slightly advancing or stationary trench, and slab penetration into the lower mantle with steep dip. We can regard the Tonga and Mariana subduction zones as representatives of the end members. Figure 14 shows the relationship between the convergence rate and trench migration of the global subduction zones (after Lallemand et al., 2008). Subduction zones with rapid convergence rates due to rapid trench retreat are observed where slabs make contact with the 660-km phase boundary (Tonga type). In contrast, the slab penetrating into the lower mantle has a noticeably slow convergence rate with advancing or stationary trench migration (Mariana type). The plate motions calculated in this study are consistent with the observational range, as shown in Figure 14. The temporal variations of the convergence rate versus trench migration rate reproduce the observed variations depending on the (r, β) set (except for the slab rollover mode as will be described later), exhibiting a broad correlation between the trench migration and the convergence rate both in the natural and simulation systems.

4.2.1. Forces and conditions controling subduction mode

The set of these features are reproduced in both numerical and laboratory experiments for "natural" or "forced" convection models (e.g., Schellart, 2011). This implies that the subduction mode is controlled by both "internal" and "external" forces. The tendency of dense slabs toward the Tonga-type mode and that of buoyant slabs toward the Mariana-type or rollover mode can be cited as instances of the influence of internal forces (Stegman et al., 2010). The results obtained in this study by varying β are in agreement with this. Slab suction or pressure force induced by overriding plate motion or asthenospheric flow change (Čížková & Bina, 2015; Heuret & Lallemand, 2005; Torii & Yoshioka, 2007) can

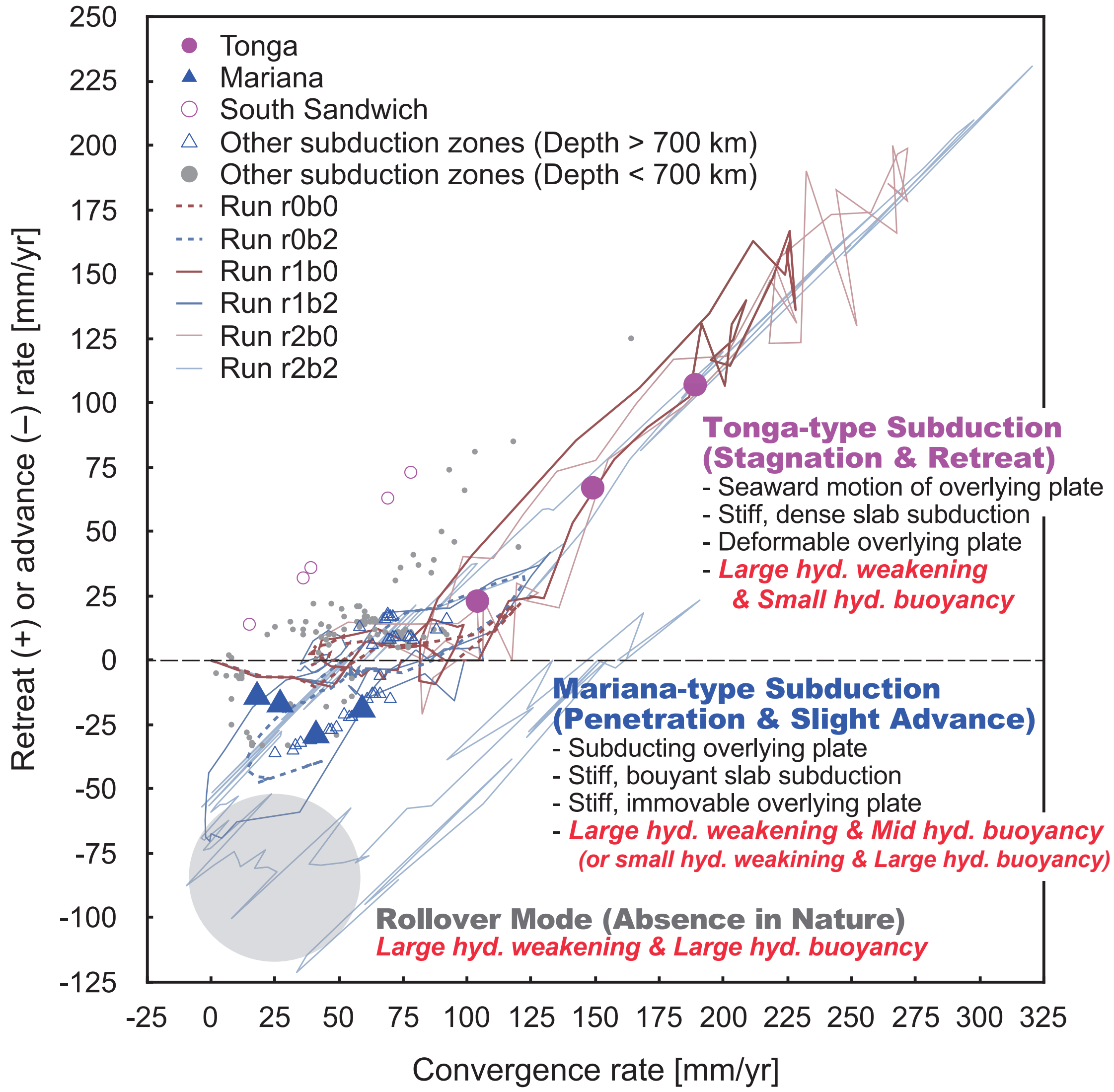

Figure 14: Observed plate motions along subduction zones in the world. Data sets are referred from Lallemand et al. (2008) and are based on the plate model of Steinberger et al. (2004). The lateral axis indicates convergence rates between an oceanic plate and an overlying plate along a trench. The vertical axis indicates rates of trench motion; positive and negative values correspond to retreat and advance, respectively, and the horizontal dashed line represents the static trench. Large pink dots and large blue triangles represent the Tonga and Mariana regions, respectively. The South Sandwich subduction zone, where rapid trench retreat with slow subduction is exhibited by way of exception, is indicated by pinkish open circles. Data of other subduction zones are symbolized as small gray dots (slabs shallower than the 660-km phase boundary) and small blue opened triangles (slabs penetrating at the boundary). Possible tectonic forces and conditions that contribute to Tonga- and Mariana-type subduction are added to the figure. Convergence rates and trench movements of six runs (r2b0, r2b2, r1b0, r1b2, r0b0, and r0b2) are presented as tracks. The rollover mode with slow subduction and rapid trench advance, such as run r1b2 (Figure 11c), is not observed in nature.

be cited as candidates for the external force. In addition, trench mobility is necessary to enable these internal and external forces to change the slab morphology (e.g., Christensen, 1996; Nakakuki & Mura, 2013; Čížková & Bina, 2013). The viscosity reduction measured by r performs this conversion of the forces to motion: if r is low and lithospheric weakening does not occur, the trench is highly immobile to constrain the subduction velocity, whereas, if r is large, the trench is movable to allow a variable convergence rate (i.e., either advance or retreat) with variable slab morphology.

4.2.2. Outliers of the velocity trend

One of the outliers to the correlation in Figure 14 is run r2b2: after the collapse of a folded stagnant slab, rapid convergence with the advancing trench appears. This would be attributed to a release of its accumulated potential energy by the sudden slab penetration. Another outlier is the rapid trench retreat associated with slow convergence as is observed at the South Sandwich Islands. The deformable overlying Scotia plate because of the developed back-arc basin seems to contribute to the rapid retreat of the trench. Except for these cases, a dynamic pressure change in the asthenospheric mantle induced by trench movement primarily controls the velocity of the corresponding induced flows, resulting in the variation of the subduction rate.

4.2.3. Hydrous wedge mantle systematically accounts for some subduction zones —Mariana as an example

The external force is not incorporated into our models, and the deformation of continental margins is also controlled by other factors such as the thickness of the continental lithosphere; therefore, our results cannot be applied to predict unique slab geometries for specific (r, β) pairs. We should, however, note that if r is large, the observed broad variations can be explained by the variation in β. Given the practical meaning of β, i.e., buoyancy owing to the presence of water, a global variation in the water content specific to each subducting slab could account for the variations in Figure 14.

For example, numerous large non-volcanic seamounts occur along the Mariana forearc that originated from serpentinized diapirs produced by slab dehydration (Fryer et al., 1985; Ishiwatari & Tsujimoto, 2003). Seismic imaging by receiver functions also supports the widespread serpentinization in the Mariana forearc (Tibi et al., 2008). Thus, the Mariana slab contains abundant water owing to long-term lithosphere cooling, and the large hydrous buoyancy of the Mariana slab would contribute to its peculiar slab morphology and advancing trench. In addition, subduction of the overlying Philippine sea plate is also essential for both its back-arc spreading and the advancing Mariana trench (Čížková & Bina, 2015).

The buoyant mantle wedge favors focal mechanism of intra-slab earthquakes in the Mariana slab: down dip tension in intermediate depth earthquakes ($<$ 300 km) and down dip compression in deep earthquakes (300–660 km) (Seno & Yamanaka, 1998). Indeed such stress distribution is reproduced in large r – large β model (run r1b2; later stage of Figure 11c). The large buoyancy contrast between the shallower well-hydrous wedge mantle and the depth of less-hydrous subducting slab may arise down dip tension of the intermediate depth seismicity. On the other hand, down dip compression suggested by the deep seismology can be attributed to the resistance forces to the subducting slab from 660-km boundary.

The predominance of retreating slabs and the absence of extremely advancing slabs in actual subduction zones (Figure 14) imply that buoyant mantle such as serpentinite does not exist widely under the forearc and that less-buoyant hydrous NAMs primarily carry water into deeper mantle if the hydration sufficiently reduces the density of the mantle minerals, as shown by experimental studies (e.g., $\beta = 1.6$; Jacobsen et al., 2008).

4.3. Hydration physical parameters in terms of mineral physics

4.3.1. Theoretical background of hydrous weakening r

Traditional deformation experiments have shown that the strain rate $\dot{\varepsilon}$ of hydrous olivine is roughly proportional to the fugacity of water $f_{\mathrm{H_2O}}$, i.e., $r = 1$ (e.g., Hirth & Kohlstedt, 2003), which is consistent with the observation that hydrogen is primarily incorporated as OH^- into the metal sites (M) of olivine to maintain electrical neutrality (Kohlstedt et al., 1996), i.e., $\dot{\varepsilon} \propto [(2\mathrm{H})_{\mathrm{M}}^{\times}]$. On the other hand, recently Fei et al. (2013) revealed the small effect of water on olivine deformation ($r = 1/3$) based on the Si diffusion measurement and proposed that it is controlled by electrically charged vacancies at Si^{4+} and O^{2-} sites. Thus, the site in the olivine structure at which hydrogen is incorporated, which controls how the hydrous crystal deforms, is still being debated. This uncertainty exists because the ion exchange reactions predominant in olivine crystals depend on p-, T-, and $f_{\mathrm{H_2O}}$-conditions, and it is possible that the parameter r is a function of these conditions (e.g., Karato, 2008).

Moreover, Fei et al. (2013) attribute the extremely low viscosity of wet olivine observed in previous polycrystalline deformation experiments to excess grain boundary water, based on the correspondence between their measurement and a previous single crystalline deformation (Raterron et al., 2009). If their insistence is valid, the possible range of r in a mantle wedge is wide (i.e., $0.33 \leq r \leq 1.2$) and depends on whether aqueous fluid commonly flows through grain boundaries.

4.3.2. Theoretical background of hydrous buoyancy β

The uncertainty of hydrogen partitioning in NAMs also causes uncertainty about the hydrous buoyancy β as the point defects cause crystal mass loss. Quantification of β may be more complicated because it not only depends on the ionic exchange but also on the ratio of states of water in the mantle. If water is incorporated into dry olivine as fluid inclusions (FI; i.e., exterior to the crystal structure; $r_{\mathrm{diff}} = 0$), we rewrite the state equation (19) as

$$\frac{M_{\mathrm{Olv}} + M_{\mathrm{H_2O}}}{\dfrac{M_{\mathrm{Olv}}}{\rho_{\mathrm{Olv}}} + \dfrac{M_{\mathrm{H_2O}}}{\rho_{\mathrm{H_2O}}}} = \rho_{\mathrm{Olv}} \left(1 - \beta_{\mathrm{FI}} \frac{M_{\mathrm{H_2O}}}{M_{\mathrm{Olv}} + M_{\mathrm{H_2O}}}\right), \tag{25}$$

where M is mass and ρ is density. Considering the amount of water to be very small ($M_{\mathrm{H_2O}}/M_{\mathrm{Olv}} \approx 0$), we obtain

$$\beta_{\mathrm{FI}} \approx \frac{\rho_{\mathrm{Olv}}}{\rho_{\mathrm{H_2O}}} - 1 = 2.30, \tag{26}$$

implying that β_{FI} only depends on the density of the host mineral and fluid inclusions, ρ_{Olv} = 3,300 [kg/m^3] and $\rho_{\mathrm{H_2O}}$ = 1,000 [kg/m^3], and is much larger than that of synthesized wet olivine (e.g., $\beta = 1.6$; Jacobsen et al., 2008), suggesting that ionic exchange reactions cause β to become smaller.

Thus, the form of existence and the dissolution mechanism of H_2O and OH^- (e.g., metal sites in NAMs, grain boundary, or fluid inclusion) may be essential for the ratio of r and β.

4.3.3. Estimation of water content in actual mantle wedge

Based on the comparison between our numerical results (Sections 3.2 and 3.3) and subduction behavior in nature (Section 4.2), we can roughly constrain water content in the actual mantle wedge through viscosity and density reduction owing to hydration. The hydration physical parameters (r, β) and water content are tradeoff through the relations $\eta \propto C_{\mathrm{OH}}^{-r}$ and $\rho \propto \beta C_{\mathrm{H2O}}$. Therefore we should pay attention to their uncertainty discussed in the previous subsections.

It is difficult to derive water content in the mantle wedge from the relation $\eta \propto C_{\mathrm{OH}}^{-r}$ because the deformation of continental margin is controlled by plural factors including thickness of continental plate margins (i.e., temperature structure of the overlying lithosphere), yield strength reduction owing to hydration or melting (e.g., Gerya & Meilick, 2011), and pre-existent fault zones. We only can conclude that large hydration weakening r or large water content under the continental margin favors the variety of the subduction style (Figure 14).

The relation $\rho \propto \beta C_{\mathrm{H2O}}$ may be useful if thermal effects of subducting oceanic plates are ignored. Our results show that given $\beta_{\mathrm{simu}} = 2$, the slab behavior absence in nature (rapid advance and rollover), is reproduced, while $\beta_{\mathrm{simu}} = 1$ gives the possible slab behavior in nature. Therefore $\beta_{\mathrm{simu}} \approx 1.5$ may give the upper limit for the reasonable subduction style in the setting of our simulation. Then the water content in the mantle wedge NAMs is around 0.2 wt.% (2,000 ppm) according to the employed phase diagram (Iwamori, 2007). Hence the upper limit of the density "contrast" between the well-hydrous wedge mantle and the less-hydrous surrounding mantle reduction for the actual mantle wedge is $d\rho/\rho = -\beta dC_{\mathrm{H2O}} = -1.5 \times 0.2\,\mathrm{wt.\%} = -0.3\%$ (note that we consider completely dry mantle at the initial condition of the numerical model). If the actual density reduction for olivine hydration $\beta_{\mathrm{Olv}} = 1.6$–$2.3$ (Subsection 4.3.2) is applied, the contrast of the water content dC_{H2O} becomes 1300–1880 ppm. Given the water content of surrounding mantle 130 ppm (estimated from the post-seismic deformation of the suboceanic asthenospheric mantle; Masuti et al., 2016), the upper limit of C_{H2O} of the hydrous mantle wedge and the slab surface is 1430–2010 ppm, which is consistent with the water storage capacity of olivine (about 1500 ppm; Kohlstedt et al., 1996). Maximum density reduction $d\rho/\rho = -0.3$ wt.% justifies our results that serpentinite, which is more buoyant, are not so dominant in the mantle wedge.

4.4. Constraints on water transportation in big mantle wedges

There are some hypotheses on the origin of interplate volcanism such as the Changbaishan ("big mantle wedge"; Zhao et al., 2009). One of these invokes upwellings of buoyant hydrous rocks from the stagnant slab known as wet plumes (e.g., Richard & Iwamori, 2010). Richard & Iwamori (2010) assume that water initially exists directly above the stagnant slab, in contact with the surrounding hotter mantle. However, our simulation shows that, to some extent, the hydrous layer is mechanically coupled with the slab despite heating of the hydrous layer; therefore, a larger viscosity reduction due to hydration r would be necessary for the separation of the plumes. Moreover, large hydrous buoyancy β is required for upwellings of the plumes; however, our simulation shows that large β prevents back-arc spreading, trench retreat, and slab stagnation (Figure 11). The spontaneous realization of back-arc spreading, stagnant slab, and wet plumes would require some special conditions such as (a) extremely small yield strength along continental margins, which can be split even by a buoyant slab, (b) large negative buoyancy by slab cooling against positive buoyancy of a hydrous layer, and/or (c) extremely localized wet plumes which do not prevent corner flows in a mantle wedge. Testing these conditions would require more detailed 3-D numerical subduction modeling to take into account the toroidal effects during slab stagnation (Schellart & Moresi, 2013). Another explanation is that (d) coincidentally, a stagnant slab and wet plumes are observed simultaneously in spite of a time lag between them. Indeed, our simulation in the case of the large (r, β) pair, such as run r2b2, where wet plumes arise, initially shows slab stagnation at the 660-km phase boundary.

Another hypothesis pertaining to the big mantle wedge invokes aqueous porous flows originating from the dehydration of the stagnant slab (e.g., Ohtani & Zhao, 2009). Porous flows from dehydrated wadsleyite or ringwoodite of the stagnant slab do not affect the solid state flow, rendering it reasonable that a stagnant slab, back-arc spreading (i.e., small β), and water transportation are realized spontaneously. However, dehydration of these minerals may be impossible due to their high water storage capacities (e.g., up to 3.1 wt.%H_2O; Inoue et al., 1995) because the amount of water transported into the mantle transition zone is strictly limited at the "choke point" (Kawamoto et al., 1996). In our runs, the temperature of the hydrous peridotite layers far exceeds this point, and wadsleyite and ringwoodite on the stagnant slab would contain only $\sim$0.2 wt.%H_2O.

5. Conclusions

We have demonstrated that hydrous rocks have multiple effects on subduction dynamics. If hydrous rocks are less viscous (large r), they cause rapid subduction, deformable continental margins, strong trench retreat, and slab stagnation. In contrast, if the hydrous rocks are buoyant (large β), they cause slow subduction, compressional stress on overlying continental plates, trench advance, and slab penetration, all of which are opposite to the effects of r. In other words, the buoyancy of hydrous rocks inhibits subduction by partially canceling out the negative thermal buoyancy of the slab, whereas the low viscosity of hydrous rocks causes the driving force to be transferred to the motion of the mantle by decoupling the slab from the overlying plate and the surrounding mantle. These features are a result of the whole mantle natural convection model. These interesting results arise because water exists in cold regions in the mantle while heat and water have similar effects on fluid dynamics. Thus, water is important for geodynamics, not only in the hot, deep mantle but also in cold regions such as the slab surface and the lower continental lithosphere. Our results are consistent with observations of plate motions and slab geometry in natural subduction zones; large r contributes to the diversity of actual subduction zones, whereas β controls the subduction mode including Tonga-type subduction (retreat and stagnation) and Mariana-type subduction (slight advance and penetration) in the case of large r. Thus, the influence of hydrous rocks on subduction dynamics is comparable to that of tectonic forces such as overlying plate motions.

Chapter III.

A new mechanism to produce chemical heterogeneity of Earth's mantle: Slab dehydration at 660-km phase boundary

1. Introduction

1.1. Chemical heterogeneity of mantle and its origin

In order to investigate the chemistry of the Earth's mantle, many researchers have analyzed isotopic ratio of mantle-derived basalts, i.e., mid-ocean ridge basalts (MORB) and oceanic island basalts (OIB). As the isotopic ratio does not fractionate upon melting below mid-ocean ridges or oceanic islands, it directly reflects the history of mantle convection including partial melting, dehydration/hydration, mantle–core interaction, aging, and mixing. Isotopic records are consequences of different behaviors of parent and daughter nuclides in these events through partition coefficients between multiple phases such as solid, melt, and aqueous fluid. Therefore, by combining several isotopic systems, e.g., ^{87}Rb-^{87}Sr, ^{147}Sm-^{143}Nd, ^{238}U-^{206}Pb, ^{235}U-^{207}Pb, and ^{232}Th-^{208}Pb, more detailed mantle evolution can be unraveled. Based on these data sets, geochemists have attributed the variation in the chemistry of the present mantle to the mixing of several distinct reservoirs (e.g., Hart et al., 1986), including Depleted MORB Mantle (DMM), Enriched Mantle I, II (EM I, EMII), High-μ (High U/Pb; HIMU). Although the origin of these reservoirs are still controversial, the HIMU component is widely regarded as ancient dehydrated oceanic crust (Chase, 1981; Chauvel et al., 1992; Hauri et al., 1993; Tatsumi, 2005). High p–T dehydration experiments (Kogiso et al., 1997; Kessel et al., 2005) have demonstrated that Pb is more dissolved from oceanic crust into genered aqueous fluid than U, supporting the hypothesis for the HIMU origin.

1.2. Distribution of the heterogeneity and dynamics suggested by ICA

A recent independent component analysis (ICA) of mantle-derived basalts (Iwamori et al., 2010; Iwamori & Nakamura, 2015) has also concluded that only two fractional processes are sufficient conditions for mantle chemical heterogeneity: melting and dehydration/hydration. The analytical result showed that the component indicating fluid addition ("IC2+"; Iwamori & Nakamura, 2012, 2015) are distributed in the eastern hemisphere rather than southern hemisphere (Dupré & Allègre, 1983; Hart, 1984). They pointed out the correspondence between the hemispherical chemical structure in mantle and the seismological degree-one structure in the inner core (Tanaka & Hamaguchi, 1997; Cao & Romanowicz, 2004). They suggested that in the eastern hemisphere, subduction zones were once confined around the supercontinent (Pangea), and that fluid-related components were concentrated beneath the supercontinent. At the same time, the eastern hemisphere of the inner core would be cooled due to cold oceanic slabs extended to the core-mantle boundary. This "top-down hemispherical dynamics" hypothesis invokes the whole mantle water circulation processes (surface to bottom of the mantle).

Thus dehydration and hydration have been regarded as one of essential processes for the mantle chemical evolution, and now in order to discuss it in detail, we should pay attention to the stability of hydrous phases at lower mantle pressure as well as dehydration of MORB and hydrous peridotite in mantle wedges.

1.3. Recent high p-T experiments on hydrous phases in lower mantle

In the lower mantle, phase H, which was once predicted by a first-principles calculation (Tsuchiya, 2013) and was recently discovered by high pressure experiments (Nishi et al., 2014), is regarded as a possible water reservoir ($\sim$15 wt.%). Phase H is stable at relatively low temperature and expected to be formed in slabs penetrating into the lower mantle. Although phase H would decompose in the mid lower mantle pressure with the pyrolite composion (>40–50 GPa; Tsuchiya, 2013; Ohira et al., 2016), in the Al-rich composition, the stability p-T range would be extended as the phase H – phase δ solid solution (aluminous phase H; Ohira et al., 2014). Therefore, Ohira et al. (2016) predict that aqueous fluid released owing to decomposition of phase H in the cold core of subducting slabs in the mid lower mantle would be re-captured in the surface of the slab (i.e., Al-rich crustal composition) by forming the aluminous phase H.

In the hotter lower mantle, water storage capacity of bridgemanite is one of recent controversial topics. Experimental studies have leaded variable results: almost dry (1–2 ppm; Bolfan-Casanova et al., 2003); small amount (<220 ppm; Panero et al., 2015); larger amount (1,900–2,400 ppm; Murakami et al., 2002); and much large amount (8,000 ppm as $(Mg_{0.97},Al_{0.01})(Si_{0.92},Al_{0.08})H_{0.09}O_3$; Inoue et al., 2016). Panero et al. (2015) attribute the variable results to differences in total composition including Al content, synthesis conditions, and interpretation of the spectroscopy of the synthesized materials as either bound water.

1.4. Seismic evidences of dehydration in lower mantle

Even if the water storage capacity of bridgmanite is higher (e.g., 1,900–2,400 ppm; Murakami et al., 2002), it is much smaller than that of ringwoodite in the transition zone (up to 2.2 wt.%, Kohlstedt et al., 1996), which is regarded to be a major water reserver in the Earth's mantle (Karato, 2011; Maruyama & Okamoto, 2007). If hydrous ringwoodite as discovered in a natural diamond ($\sim$1.0 wt.%H_2O; Pearson et al., 2014) descends near subducting slabs into lower mantle, it would produce much aqueous fluids.

By receiver function imaging, Schmandt et al. (2014) discovered seismic low velocity anomalies at the top of the lower mantle ($\sim$ 690–750 km depth) where downward flows cross the 660-km boundary beneath the North American continent. They attribute the low velocity to partial melting caused by dehydration of ringwoodite. As the aqueous fluid and melt phases are completely miscible under the lower mantle p-T conditions (Bureau & Keppler, 1999; Mibe et al., 2007), the low velocity patch can reflect the aqueous fluid itself. Such signatures are also observed just beneath the stagnant slab in the Japan-China subduction zones but are not universally distributed (Liu et al., 2016). Unlike America and Japan regions, however, no obvious low velocity anomaly is observed beneath west Antarctica, where the transition zone mantle seems hydrous (Emry et al., 2015).

Thus, although some uncertainty remains, recent experimental and seismological studies propose at least two possible dehydration/hydration processes in the lower mantle, which have not been considered in the previous mantle mixing model including the HIMU origin (e.g., Tatsumi, 2005).

1.5. Why is geodynamical simulation essential for chemical evolution?

These dehydration processes indicate that the production rate of chemical reservoirs are not constant throughout the mantle evolution because present-day mantle convection is between one and two layered (i.e., intermittent slab penetration) based on Rayleigh number and the 660-km depth Clapeyron slope (Fukao et al., 2009). High pressure experiments also indicate that dehydration would occur in both hotter and colder regions of the lower mantle. Since partition coefficients of trace elements between rocks and aqueous fluids strongly depend on temperature (Kessel et al., 2005), we should pay attention to mantle dynamics including energy transportation. Dehydration/hydration processes also affect the transportation of the generated heterogeneity because hydrous rocks are expected to enhance the advection of the chemical component due to its lower viscosity. Contrary, through the active energy release from a planet owing to less viscous hydrous rocks, the mantle convection becomes extremely weaken at the late stage of the mantle evolution (Nakagawa et al., 2015). Thus, mantle dynamics closely participates in both the origin and mixing of the chemical reservoirs, and numerical simulation of the mantle convection is a powerful tool to discuss them.

There are some previous numerical simulations of mantle convection including element transportation. For example, Ikemoto & Iwamori (2014) simulate trace element transportation in the mantle wedge for the sake of the process of island arc magma generation, but subducting slab dynamics is not incorporated. Xie & Tackley (2004) simulate the evolution of U-Pb and Sm-Nd systems in the whole mantle domain, but their model targets melting processes and does not include water transportation. Thus whole mantle scale fluid dynamical simulation including water and trace elements that can be sufficiently compared with actual rock samples is not previously conducted.

1.6. Aim of Chapter III

The aim of this chapter is to discuss the origin and transportation mechanisms of the mantle chemical heterogeneity observed as isotopic data of mantle-derived basalts by using a numerical model including lower mantle dehydration/hydration processes and trace element transportation. The main target is how the slab geometry and aqueous fluid ascent affect the mantle chemical evolution. From the results, the author tries to decipher the global geochemical history and its relation to the supercontinental dynamics (Section 4.5) . For this sake, the numerical model in Chapter II is expanded in the next section.

2. Model setup and basic equations

2.1. Model design

The model setup is schematically shown in Figure 15. While the aim of Chapter II is to demonstrate the subduction dynamics mainly in the upper mantle at the initial stage (several tens of Myr), this chapter seeks for the chemical evolution over 100 Myr or more. Therefore the numerical model and physical parameters in Chapter III is based on those in Chapter II but is designed for such long term evolution.

Thermal age of subducting oceanic plate is initially 0 Ma at the top left (mid-ocean ridge) to 120 Ma at the top right (trench). Initial thermal age of overlying continental plate is uniformly 80 Ma. The thick continental margin prevents the occurrence of back-arc spreading (e.g., Run r1b0 in Chapter II), which prevents the fast corner flow and relaxes the Courant condition, resulting in numerical stabilization. As reaction p–T path of hydrous minerals and resulting water distribution in deeper mantle are less affected by the back-arc spreading as simulated in Chapter II, here in order to calculate long-term evolution, such thick continental lithosphere is incorporated. Constant temperature 4,300 K is imposed along the bottom boundary for solving the energy conservation equation for the long term evolution. Other thermal boundary conditions are the same as those of Chapter II.

The plate configuration is determined to produce stagnant slab stably. The right tip of the overlying continental plate is movable by putting soft material at the right wall of the model domain ($\eta = 10^{22}$; 500-km width $\times$ 300-km thick). Deformation of this soft material enables tensile stress on the overlying continental plate arising from the subducting oceanic plate to be released. Accordingly the trench continuously retreats and the subducted oceanic slab stably stagnates over the 660-km discontinuity. The initial dip of the plate boundary is 27°.

The surface 10 km of oceanic plate (7.5-km-thick MORB and 2.5-km-thick underlying peridotite) is initially contain 3 wt.%H_2O. The hydrous area is slightly extended to the core of the oceanic plate compared to Chapter II in order to investigate formation and decomposition of phase H, which is expected to be stable in the cold core of penetrating slab in lower mantle.

Parameters for viscosity and density reduction owing to hydration are fixed in this

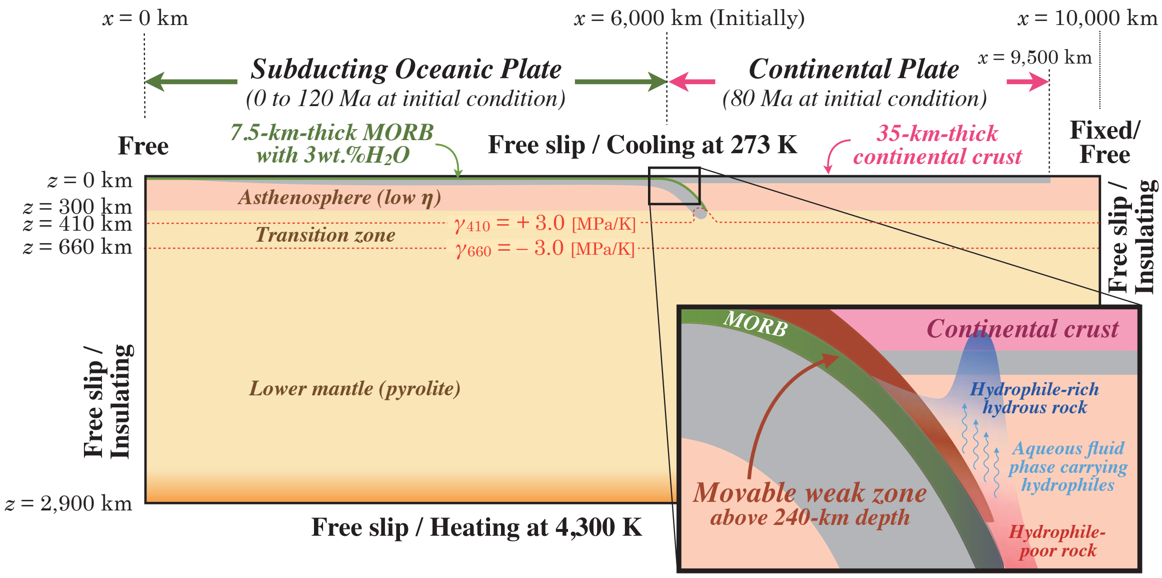

Figure 15: Schematic diagram of the 2-D convection model in Chapter III. Details are described in Section 2.1.

chapter: $r_{\mathrm{diff}} = 1.0$, $r_{\mathrm{disl}} = 1.2$ for upper mantle, transition zone, and lower mantle (Hirth & Kohlstedt, 2003); $\beta = 1.6$ for upper mantle (Jacobsen et al., 2008); $\beta = 1.3$ for transition zone (Mao et al., 2008; Inoue et al., 1998); $\beta = 1.0$ for lower mantle. Constitutive and state equations are the same as those in Chapter II.

In addition to these changes in the model setup, water and trace element transportation by two phases, solid and aqueous fluid phases, are incorporated into a Marker-in-Cell technique as follows.

2.2. Water transportation

Ascent velocity of aqueous fluids is much larger than the velocity of mantle convection in the upper mantle conditions; therefore, in Chapter II, the aqueous fluids are considered to exist instantaneously. However, in the lower mantle, the ascent velocity is expected to be small owing to the small fluid fraction and permeability. Besides, the aqueous fluid phase coexisting with the solid phase is necessary for calculation of the trace element partitioning between them. Then the author introduces the aqueous fluid phase with a finite ascent velocity as well as hydrous rock transportation:

- Equation of water transportation by mantle rocks:

$$\frac{\partial C_{\mathrm{H_2O}}^{\mathrm{sol}}}{\partial t} + \boldsymbol{v} \cdot \nabla C_{\mathrm{H_2O}}^{\mathrm{sol}} = \kappa_{\mathrm{H_2O}} \nabla^2 C_{\mathrm{H_2O}}^{\mathrm{sol}} - \dot{C}_{\mathrm{H_2O}}^{\mathrm{sol}\to\mathrm{aq}} \tag{27}$$

- Equation of water transportation by aqueous fluids:

$$\frac{\partial C_{\mathrm{H_2O}}^{\mathrm{aq}}}{\partial t} + \left(\boldsymbol{v} - \frac{k_{\phi_a}(1-\phi_a)\Delta\rho_a g}{\phi_a \eta_a} \boldsymbol{e}_z \right) \cdot \nabla C_{\mathrm{H_2O}}^{\mathrm{aq}} = \dot{C}_{\mathrm{H_2O}}^{\mathrm{sol}\to\mathrm{aq}} \tag{28}$$

$$k_{\phi_a} = \frac{R_g^2 \phi_a^n}{B} \tag{29}$$

$\kappa_{\mathrm{H_2O}} \nabla^2 C_{\mathrm{H_2O}}^{\mathrm{sol}}$ in Equation (27) is the diffusion term owing to hydrogen diffusion in hydrous minerals and is solved by a Moving Particle Semi-implicit method (Koshizuka & Oka, 1996). The detail of the method is shown in Appendix E. Although diffusion coefficient of hydrogen $\kappa_{\mathrm{H_2O}}$ strongly depends on temperature (Mackwell & Kohlstedt, 1990; Sun et al., 2015), a constant value is given in the simulation ($\kappa_{\mathrm{H_2O}} = 0, 10^{-9}, 10^{-6}$ $\mathrm{m^2/s}$; Table 6).

$\dot{C}_{\mathrm{H_2O}}^{\mathrm{sol}\to\mathrm{aq}}$ in Equations (27) and (28) is the amount of aqueous fluids released from decomposing hydrous minerals in a unit time estimated from phase relation diagrams. The generated fluids ascent at a velocity determined from the permeability k_{ϕ_a} and are absorbed into capable rocks. Similar to Chapter II, maximum water content for upper mantle peridotite and crust is based on Iwamori (2007). In the lower mantle, phase H (Nishi et al., 2014; Tsuchiya, 2013) is taken into account for water storage capacity: if a domain at the temperature of T and the depth of z satisfies the relation T [K] < 0.4545 [K/km] $\times$ z [km] + 900 [K], the maximum water content of the domain is 3 wt% (Figure 17). If not, the estimated maximum water content for bridgemanite is applied for the domain and is treated as a variable parameter (0.01, 0.1, or 0.21 wt%; Table 6).

The formula and the physical parameters of the finite upward velocity of the aqueous fluid in Equation (28) is based on Horiuchi & Iwamori (2016): k_{ϕ_a} is permeability, R_g is grain size (treated as a variable parameter; Table 6), ϕ_a is volume fraction of aqueous fluid, $n = 3$ is constant, $B = 10^3$ is permeability denominator, $\Delta\rho_a = 2.3 \times 10^3$ [kg/m^3] is density contrast between solid and aqueous fluid phases, $\eta_a = 1.0 \times 10^{-3}$ [Pa s] is aqueous fluid viscosity, and g is gravitational acceleration.

In the simulation, the advection term is solved by both markers and grids: (1) If hydration or dehydration occurs, aqueous fluid fraction at each node changes according

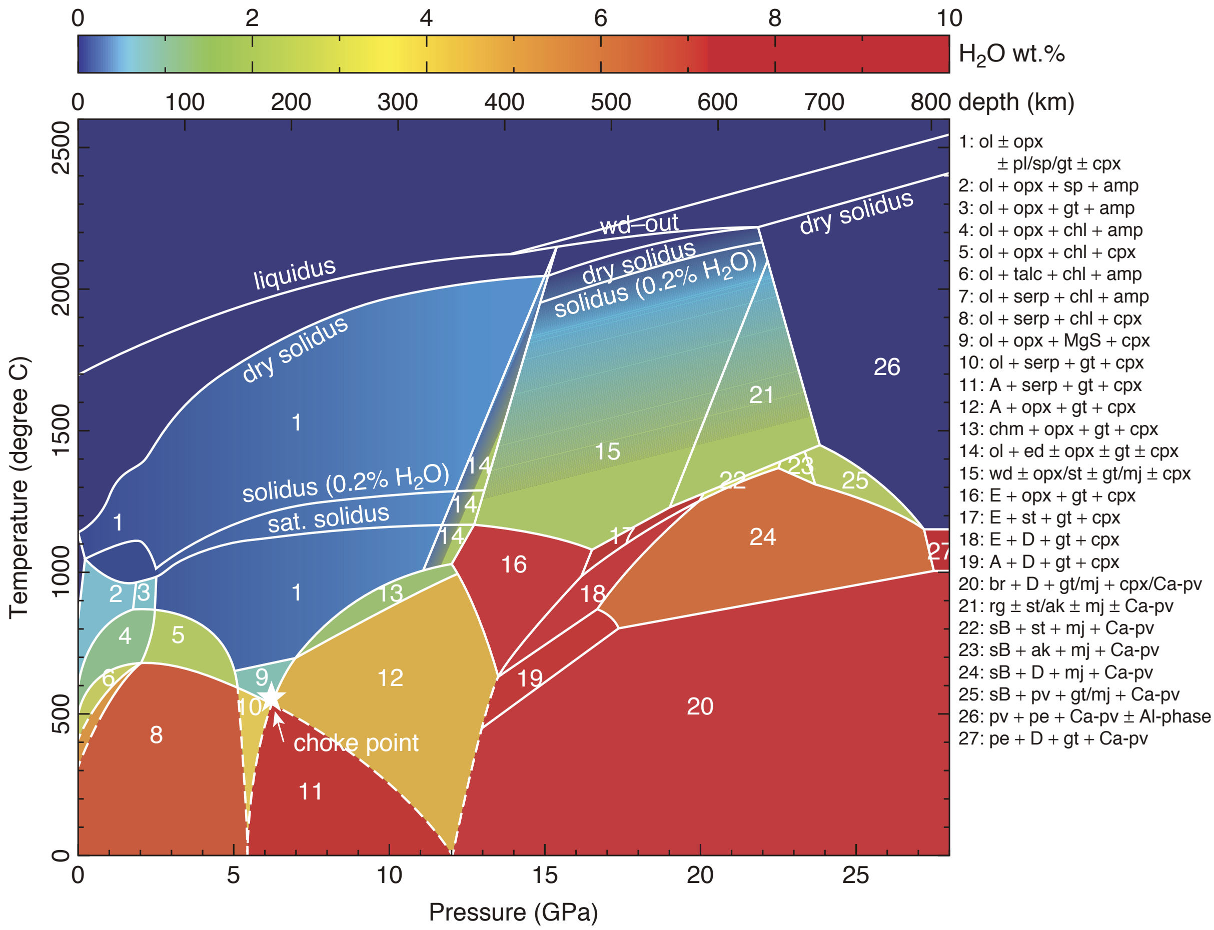

Figure 16: Phase diagram of hydrous peridotite in the simulation (Iwamori, 2007). ol = olivine; opx = orthopyroxene; cpx = clinopyroxene; pl = plagioclase; sp = spinel; gt = garnet; amp = amphibole; chl = chlorite; serp = serpentine; MgS = Mg-sursassite; A = phase A; chm = clinohumite; wd = wadsleyite; rg = ringwoodite; st = stishovite; mj = majorite; E = phase E; D = phase D; br = brucite; Ca-pv = Ca-perovskite; ak = akimotoite; sB = superhydrous phase B; pv = perovskite; pe = periclase (or magnesiowustite); Al-phase = Al-rich phase.

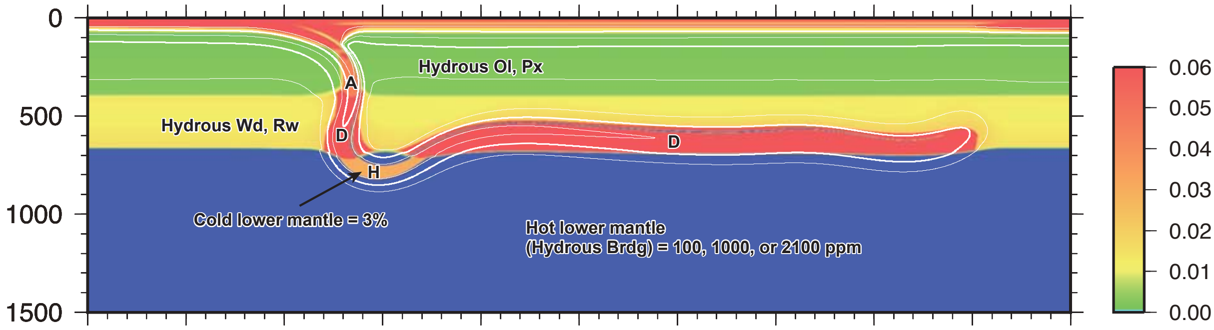

Figure 17: Maximum water content (weight fraction) based on Iwamori (2007) (Figure 16) and the stability field of phase H defined in Section 2.2. White lines are 600, 800, 1,000, 1,200, and 1,400°C isotherms.

to the phase diagrams. (2) The fluid ascent is solved by using a grid. (3) Grid values of aqueous fluid fraction are converted into marker values. (4) The marker values are transported along the solid flows. (5) Go to the next step and back to (1). In this cycle the Courant condition for solid phase is applied.

2.3. Trace element transportation

In order to produce isotopic evolution of U-Pb, Th-Pb, Rb-Sr, and Sm-Nd systems, 13 kinds of nuclides (plus 3 imaginary trace elements) listed in the Table 3 are transported in the simulation. Similar to water, each trace element is transported by two phases:

- Equation of trace element transportation in mantle rocks:

$$\frac{\partial W_{\mathrm{TE}}^{\mathrm{sol}}}{\partial t} + \boldsymbol{v} \cdot \nabla W_{\mathrm{TE}}^{\mathrm{sol}} = -\dot{W}_{\mathrm{TE}}^{\mathrm{sol}\to\mathrm{aq}} + \Lambda_{\mathrm{TE}}^{\mathrm{sol}} \tag{30}$$

- Equation of trace element transportation in aqueous fluids:

$$\frac{\partial W_{\mathrm{TE}}^{\mathrm{aq}}}{\partial t} + \left(\boldsymbol{v} - \frac{k_{\phi_a}(1-\phi_a)\Delta\rho_a g}{\phi_a \eta_a}\boldsymbol{e}_z\right) \cdot \nabla W_{\mathrm{TE}}^{\mathrm{aq}} = \dot{W}_{\mathrm{TE}}^{\mathrm{sol}\to\mathrm{aq}} + \Lambda_{\mathrm{TE}}^{\mathrm{aq}} \tag{31}$$

Where $W_{\mathrm{TE}}^{\mathrm{phase}}$ is abundance of a trace elements in solid or fluid phase. The way to solve advection terms are the same as that for water. The Marker in Cell enables the transportation of multiple elements. The right hands of the equations are discribed for in the following subsections.

Table 3: The list of isotopic tracers transported in the simulation. (a) Initial abundance in the numerical simulation relative to the reference stable nuclide (^{204}Pb, ^{86}Sr, ^{143}Nd). These values are estimated by tracing the present isotopic composition of Bulk Silicate Earth[b] back to 0.5 Gyr. (b) Isotopic compositions of present primitive mantle (Bulk Silicate Earth) referred from Kogiso et al. (1997) and based on McCulloch & Black (1984), Goldstein et al. (1984), Taylor & McLennan (1985), and Allègre et al. (1988). The isotopic ratio of uranium $(^{235}\mathrm{U}/^{238}\mathrm{U})_{\mathrm{present}} = 0.007257$ reported by IUPAC (Berglund & Wieser, 2011) is used to calculate $(^{235}\mathrm{U}/^{204}\mathrm{Pb})_{\mathrm{present}}$. (c) Decay constant and half-life referred from Turcotte & Schubert (2001) and based on Allègre et al. (1987).

Nuclide	**Type**	**Relative abundance**[a] (initial)	**Relative abundance**[b] (present)	**Decay const.**[c] λ [Gyr^{-1}]	**Half-life**[c] $T_{\frac{1}{2}}$ [Gyr]
^{238}U	Parent	8.86	8.2	1.551×10^{-1}	4.469
^{206}Pb	Daughter	17.14	17.8	–	–
^{235}U	Parent	0.097	0.0595	9.849×10^{-1}	0.704
^{207}Pb	Daughter	15.56	15.6	–	–
^{232}Th	Parent	35.0	34	4.948×10^{-2}	11.93
^{208}Pb	Daughter	37.20	38.2	–	–
^{204}Pb	Stable	1	1	–	–
^{87}Rb	Parent	0.0856	0.085	1.42×10^{-2}	48.8
^{87}Sr	Daughter	0.7041	0.7047	–	–
^{86}Sr	Stable	1	1	–	–
^{147}Sm	Parent	0.1972	0.1966	6.54×10^{-3}	106
^{143}Nd	Daughter	0.51200	0.51264	–	–
^{144}Nd	Stable	1	1	–	–
Imaginary 1	Stable	1	1	–	–
Imaginary 2	Stable	1	1	–	–
Imaginary 3	Stable	1	1	–	–

2.3.1. Non-equilibrium partitioning model

$\dot{W}_{\mathrm{TE}}^{\mathrm{sol}\to\mathrm{aq}}$ in Equations (30) and (31) is the flux of the trace element released from the solid phase into the aqueous fluid phase during dehydration (if plus) or that precipitated from the aqueous fluid phase into the solid phases during hydration (if munus). This study employs two different models for trace element partitioning: non-equilibrium (or fractional) and equilibrium models.

First, in the former model, the amount of trace element transferred between the phases during a time step Δt is calculated based on the analogies of fractional melting and the non-equilibrium crystallization:

- Dehydration ($\dot{C}_{\mathrm{H_2O}}^{\mathrm{sol}\to\mathrm{aq}} > 0$):

$$\dot{W}_{\mathrm{TE}}^{\mathrm{sol}\to\mathrm{aq}}\Delta t = \frac{\dot{C}_{\mathrm{H_2O}}^{\mathrm{sol}\to\mathrm{aq}}\Delta t}{\left(1 - \dot{C}_{\mathrm{H_2O}}^{\mathrm{sol}\to\mathrm{aq}}\Delta t\right) D_{\mathrm{TE}}^{\mathrm{sol/aq}} + \dot{C}_{\mathrm{H_2O}}^{\mathrm{sol}\to\mathrm{aq}}\Delta t} W_{\mathrm{TE}}^{\mathrm{sol}} \tag{32}$$

- Hydration ($\dot{C}_{\mathrm{H_2O}}^{\mathrm{sol}\to\mathrm{aq}} < 0$):

$$\dot{W}_{\mathrm{TE}}^{\mathrm{sol}\to\mathrm{aq}}\Delta t = \frac{\dot{C}_{\mathrm{H_2O}}^{\mathrm{sol}\to\mathrm{aq}}\Delta t}{C_{\mathrm{H_2O}}^{\mathrm{aq}}} W_{\mathrm{TE}}^{\mathrm{aq}} \quad \left(\dot{W}_{\mathrm{TE}}^{\mathrm{aq}\to\mathrm{sol}}\Delta t = \frac{\dot{C}_{\mathrm{H_2O}}^{\mathrm{aq}\to\mathrm{sol}}\Delta t}{C_{\mathrm{H_2O}}^{\mathrm{aq}}} W_{\mathrm{TE}}^{\mathrm{aq}}\right) \tag{33}$$

- No dehydration/hydration or fluid path ($\dot{C}_{\mathrm{H_2O}}^{\mathrm{sol}\to\mathrm{aq}} = 0$):

$$\dot{W}_{\mathrm{TE}}^{\mathrm{sol}\to\mathrm{aq}}\Delta t = 0. \tag{34}$$

$D_{\mathrm{TE}}^{\mathrm{sol/aq}}$ in Equation (32) is partition coefficient of the trace element between the residual rock and aqueous fluid phases generating at the time step defined by

$$D_{\mathrm{TE}}^{\mathrm{sol/aq}} = \frac{(W_{\mathrm{TE}}^{\mathrm{sol}} - \dot{W}_{\mathrm{TE}}^{\mathrm{sol}\to\mathrm{aq}}\Delta t)/(1 - \dot{C}_{\mathrm{H_2O}}^{\mathrm{sol}\to\mathrm{aq}}\Delta t)}{(\dot{W}_{\mathrm{TE}}^{\mathrm{sol}\to\mathrm{aq}}\Delta t)/(\dot{C}_{\mathrm{H_2O}}^{\mathrm{sol}\to\mathrm{aq}}\Delta t)}, \tag{35}$$

where $(W_{\mathrm{TE}}^{\mathrm{sol}} - \dot{W}_{\mathrm{TE}}^{\mathrm{sol}\to\mathrm{aq}}\Delta t)$ is the abundance of the element in the residual rock phase, $(1 - \dot{C}_{\mathrm{H_2O}}^{\mathrm{sol}\to\mathrm{aq}}\Delta t)$ is the weight fraction of the residual rock phase, $(\dot{W}_{\mathrm{TE}}^{\mathrm{sol}\to\mathrm{aq}}\Delta t)$ is the abundance of the element in the aqueous fluid phase generating during the time step, and $(\dot{C}_{\mathrm{H_2O}}^{\mathrm{sol}\to\mathrm{aq}}\Delta t)$ is the weight fraction of the aqueous fluid phase generating duing the time step. Equation (32) can be obtained by deforming Equation (35). $D_{\mathrm{TE}}^{\mathrm{sol/aq}}$ is defined in the Subsection 2.3.3.

This formularization means no element flux between the fluid and surrounding solid phases during fluid ascent and well accounts for the trace element compositions of volcanic rocks in island arcs (Ikemoto & Iwamori, 2014). Well penetrative fluid paths such as dikes is favorable to the non-equilibrium, or fractional partitioning.

2.3.2. Equilibrium partitioning model

However, such a fractional situation may be possible only in the shallower, colder regions such as brittle continental margins. This study also includes fluids in the lower mantle, and the dikes seem impossible. In addition, slow fluid ascent in the lower mantle due to the small fluid abundance enhances complete equilibrium of trace elements between rock and fluid phases. Therefore, the author also employs the equilibrium model for the trace element partitioning, in which the partition coefficient between the surrounding rock ascent fluid phases are expressed by

$$D_{\mathrm{TE}}^{\mathrm{sol/aq}} = \frac{\left(W_{\mathrm{TE}}^{\Sigma} - W_{\mathrm{TE}}^{\mathrm{aq}}\right) / \left(1 - C_{\mathrm{H_2O}}^{\mathrm{aq}}\right)}{W_{\mathrm{TE}}^{\mathrm{aq}} / C_{\mathrm{H_2O}}^{\mathrm{aq}}}, \tag{36}$$

where $W_{\mathrm{TE}}^{\Sigma} \equiv W_{\mathrm{TE}}^{\mathrm{sol(pre)}} + W_{\mathrm{TE}}^{\mathrm{aq(pre)}}$ is the sum of the element abundance just before the partition calculation, $\left(W_{\mathrm{TE}}^{\Sigma} - W_{\mathrm{TE}}^{\mathrm{aq}}\right)$ is the element abundance in the surrounding rock phase, $\left(1 - C_{\mathrm{H_2O}}^{\mathrm{aq}}\right)$ is the weight fraction of the surrounding rock phase, $W_{\mathrm{TE}}^{\mathrm{aq}}$ is the element abundance in the ascending fluid phase, and $C_{\mathrm{H_2O}}^{\mathrm{aq}}$ is the weight fraction of the ascending fluid phase. Similar to the fractional partitioning model, $D_{\mathrm{TE}}^{\mathrm{sol/aq}}$ is defined in the Subsection 2.3.3.

By deforming Equation (36), we can obtain the element abundance in each phase at the new time step:

$$W_{\mathrm{TE}}^{\mathrm{aq}} = \frac{C_{\mathrm{H_2O}}^{\mathrm{aq}}}{\left(1 - C_{\mathrm{H_2O}}^{\mathrm{aq}}\right) D_{\mathrm{TE}}^{\mathrm{sol/aq}} + C_{\mathrm{H_2O}}^{\mathrm{aq}}} W_{\mathrm{TE}}^{\Sigma} \tag{37}$$

$$\begin{aligned} W_{\mathrm{TE}}^{\mathrm{sol}} &= W_{\mathrm{TE}}^{\Sigma} - W_{\mathrm{TE}}^{\mathrm{aq}} \\ &= \frac{\left(1 - C_{\mathrm{H_2O}}^{\mathrm{aq}}\right) D_{\mathrm{TE}}^{\mathrm{sol/aq}}}{\left(1 - C_{\mathrm{H_2O}}^{\mathrm{aq}}\right) D_{\mathrm{TE}}^{\mathrm{sol/aq}} + C_{\mathrm{H_2O}}^{\mathrm{aq}}} W_{\mathrm{TE}}^{\Sigma}. \end{aligned} \tag{38}$$

Therefore the element flux in Equations (30) and (31) can be written as

$$\dot{W}_{\mathrm{TE}}^{\mathrm{sol \to aq}} = \frac{W_{\mathrm{TE}}^{\mathrm{sol(pre)}} - W_{\mathrm{TE}}^{\mathrm{sol}}}{\Delta t} = \frac{W_{\mathrm{TE}}^{\mathrm{aq}} - W_{\mathrm{TE}}^{\mathrm{aq(pre)}}}{\Delta t}. \tag{39}$$

In the equilibrium partition medel, the element partitioning is calculated at every time step as far as the aqueous fluid exists (i.e., $C_{\mathrm{H_2O}}^{\mathrm{aq}} > 0$).

2.3.3. Partition coefficients between solid and aqueous fluid phases

$D_{\mathrm{TE}}^{\mathrm{sol/aq}}$ values (defined in Subsections 2.3.1 and 2.3.2) of each element for the upper mantle conditions used in the simulation are referred from Kessel et al. (2005) and depend on temperature (Table 4, Figure 18). In the range of 700–1200°C, these values are logarithmically interpolated.

As far as the author knows, there is no experimental investigation into trace element partitioning between lower mantle minerals and fluids. Therefore $D_{\mathrm{TE}}^{\mathrm{sol/aq}}$ values for the lower mantle are constant and are treated as variable parameters (Table 5). The values are roughly determined on the basis of those at high temperature of Kessel et al. (2005). The difference in Models A and B in Table 5 is the hydrophilicity contrast between parent and daughter nuclides, which is essential for the isotopic evolution. Kessel et al. (2005) (Table 18) suggests small differences of hydrophilicity between U-Pb and Th-Pb pairs at the higher temperature, favoring Model B. On the other hand, as the aqueous fluid and melt phases are thought to be completely miscible under the lower mantle p-T conditions (Bureau & Keppler, 1999; Mibe et al., 2007), partition coefficient data between lower mantle minerals and partial melt phases may be helpful. Such experiments (Hirose et al., 2004; Corgne et al., 2005) suggest that incompatibility of Pb into Mg-perovskite is > 10 times as higher as that of U or Th in spite of high temperature (> 2400°C; Hirose et al., 2004), favoring Model A and significant differentiation in the lower mantle. Partial melting (i.e., presence of silica-rich supercritical fluids) under the p-T conditions of the top of the lower mantle (experimental part of Schmandt et al., 2014) justifies the assumption. Thus $D_{\mathrm{TE}}^{\mathrm{sol/aq}}$ values reflect uncertainty of the trace element behaviors.

2.3.4. Radioactive decay

$\Lambda_{\mathrm{TE}}^{\mathrm{sol}}$ in Equation (30) is the trece element decrease or increase owing to radioactive decay, i.e.,

$$\Lambda_{\mathrm{TE}}^{\mathrm{sol}} = \begin{cases} -\lambda_{\mathrm{TE}} W_{\mathrm{TE}}^{\mathrm{sol}} & \text{(Parent)} \\ \lambda_{\mathrm{PTE}} W_{\mathrm{PTE}}^{\mathrm{sol}} & \text{(Daughter)} \\ 0 & \text{(Stable)} \end{cases} \tag{40}$$

where the index PTE means the parent trace element, and λ_{TE} is decay constant. $\Lambda_{\mathrm{TE}}^{\mathrm{aq}}$ in Equation (31) is similarly calculated. Radioactive parameters used in the simulation is listed in Table 3.

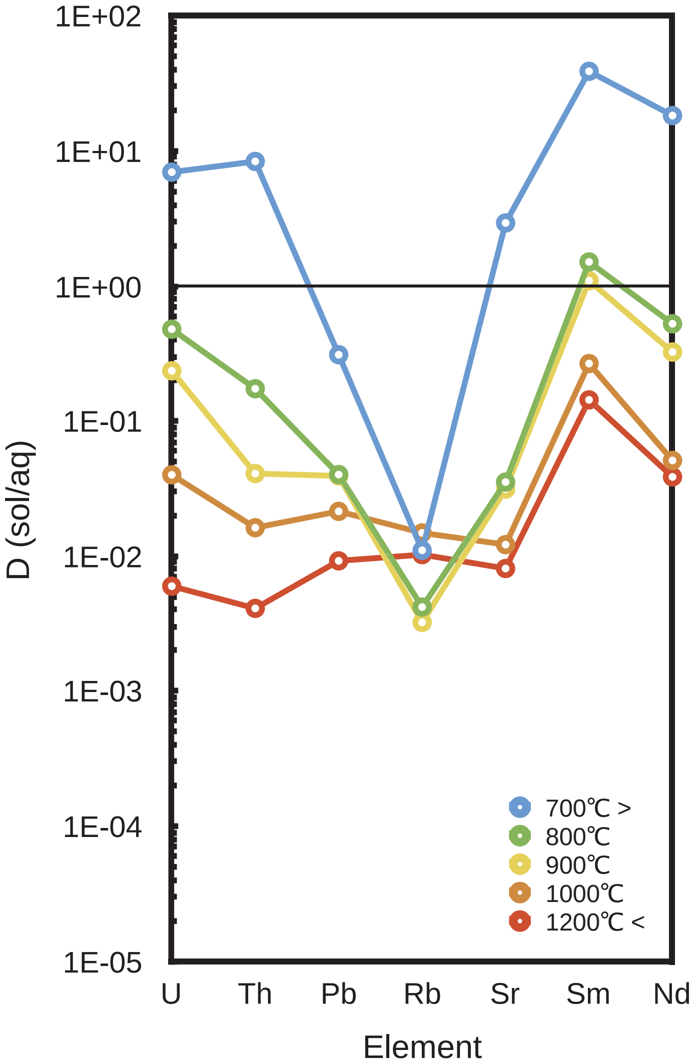

Figure 18: Partition coefficient of chemical tracers between rock and fluid, $D^{\mathrm{sol/aq}}$, for the upper mantle (Kessel et al., 2005, Table 4).

Table 4: Partition coefficient of chemical tracers between rock and fluid, $D^{\mathrm{sol/aq}}$, referred from Kessel et al. (2005). $D^{\mathrm{sol/aq}}$ is a function of temperature in the simulation while the effects of pressure and mineral composition are not considered.

Upper Mantle

Nuclide	**≤700°C**	**800°C**	**900°C**	**1,000°C**	**1,200°C≤**
^{238}U, ^{235}U	6.98	4.79×10^{-1}	2.36×10^{-1}	4.00×10^{-2}	5.99×10^{-3}
^{232}Th	8.37	1.74×10^{-1}	4.08×10^{-2}	1.62×10^{-2}	4.10×10^{-3}
^{204}Pb, ^{206}Pb, ^{207}Pb, ^{208}Pb	3.10×10^{-1}	4.02×10^{-2}	3.92×10^{-2}	2.14×10^{-2}	9.22×10^{-3}
^{87}Rb	1.10×10^{-2}	4.19×10^{-3}	3.23×10^{-3}	1.49×10^{-2}	1.02×10^{-2}
^{87}Sr, ^{86}Sr	2.93	3.53×10^{-2}	3.13×10^{-2}	1.22×10^{-2}	8.09×10^{-3}
^{147}Sm	3.89×10	1.51	1.10	2.66×10^{-1}	1.44×10^{-1}
^{143}Nd, ^{144}Nd	1.83×10	5.25×10^{-1}	3.25×10^{-1}	5.11×10^{-2}	3.86×10^{-2}
Imaginary 1	10^{-1}	10^{-1}	10^{-1}	10^{-1}	10^{-1}
Imaginary 2	10^{-2}	10^{-2}	10^{-2}	10^{-2}	10^{-2}
Imaginary 3	10^{-3}	10^{-3}	10^{-3}	10^{-3}	10^{-3}

Table 5: Partition coefficient of chemical tracers between rock and fluid, $D^{\mathrm{sol/aq}}$, for the lower mantle. Two models A and B are applied for the parameter study (Table 6).

Lower Mantle

Nuclide	**Model A**	**Model B**
^{238}U, ^{235}U	1×10^{-2}	1×10^{-2}
^{232}Th	1×10^{-2}	1×10^{-2}
^{204}Pb, ^{206}Pb, ^{207}Pb, ^{208}Pb	1×10^{-3}	5×10^{-3}
^{87}Rb	1×10^{-3}	5×10^{-3}
^{87}Sr, ^{86}Sr	1×10^{-2}	1×10^{-2}
^{147}Sm	1×10^{-1}	1×10^{-1}
^{143}Nd, ^{144}Nd	1×10^{-2}	5×10^{-2}
Imaginary 1	10^{-1}	10^{-1}
Imaginary 2	10^{-2}	10^{-2}
Imaginary 3	10^{-3}	10^{-3}

2.3.5. Initial abundance of trace elements

Abundance of trace elements for calculating isotopic evolution at the initial condition is estimated by tracing the present isotopic composition of Bulk Silicate Earth (Kogiso et al., 1997) 0.5 Gyr before present as shown in Table 3 and its caption. Isotopic heterogeneity is not considered at the initial condition due to the uncertainty of the Bulk Silicate Earth values, and we pay attention to relative isotopic evolution.

In contrast, three imaginary hydrophilic tracers with constant partition coefficients (10^{-1}, 10^{-2}, and 10^{-3}) have heterogeneity at the initial condition: 10 times concentration in a 7.5-km-thick MORB layer, and 10^{-2} times concentration in a 30-km-thick harzburgite layer just below the MORB layer, relative to the primitive value.

3. Results

Based on the above numerical scheme, 11 runs with different variable parameters are performed (Table 6) to discuss the effects of hydrogen diffusion (Section 3.2), upward velocity of aqueous fluids (Section 3.3), maximum water content of the lower mantle (Section 3.4), partition coefficients of trace elements (Section 3.5), equilibrium models for trace element partitioning (Section 3.6), and slab geometry (Section 3.7), on the production and transportation of the mantle chemical heterogeneities.

3.1. Evolution of subducting slab

Here the evolution of run stg2 from subduction initiation to 149 Myr after is descrived as shown in Figures 19 and 20.

3.1.1. Upper mantle process

The p–T path of hydrous oceanic crust and overlying hydrous peridotite in the upper mantle is the same as that described in Chapter II. Resultant water distribution in the solid phase in the upper mantle (12.16 Myr in the left of Figure 20) is also roughly similar to that of Chapter II although a finite upward velocity of aqueous fluids is introduced in run stg2. This correspondence justifies the approximation for the instantaneous aqueous flows with the infinite upward velocity under the upper mantle condition (i.e., large aqueous fluid fraction owing to dehydration of highly hydrous minerals). During the dehydration of MORB and overlying hydrous peridotite (e.g., serpentine and chlorite),

Table 6: All run IDs and corresponding parameters in Chapter III.

Run ID	Element partitioning model	Grain size R_g to calculate permeability of fluid [mm]	Diffution coefficient of hydrogen κ_{H_2O} [m^2/s]	Water storage capacity in LM [ppm]	$D^{\mathrm{sol/aq}}$ in LM (Table 5)	Plate configu-ration
stg1	Non-eq.	10^3	0	100	A	§2.1
stg2	Non-eq.	1	0	100	A	§2.1
stg3	Non-eq.	0.1	0	100	A	§2.1
stg2diff9	Non-eq.	1	10^{-9}	100	A	§2.1
stg2diff6	Non-eq.	1	10^{-6}	100	A	§2.1
stg2Pv1000	Non-eq.	1	0	1,000	A	§2.1
stg2Pv2100	Non-eq.	1	0	2,100	A	§2.1
stg2B	Non-eq.	1	0	100	B	§2.1
pnt1	Non-eq.	∞	0	100	–	Fig. 32
stg2eq	Eq.	1	0	100	A	§2.1
stg2Beq	Eq.	1	0	100	B	§2.1
(Formulas)	§2.3.1, §2.3.2	§2.2	Apx. E	§2.2	§2.3.3	§2.1
(Results)	§3.6	§3.3	§3.2	§3.4	§3.5	§3.7

hydrophilic trace elements are released with the aqueous fluid and incorporate into the bottom of the continental plate (12.16 Myr of Figure 21). Correspondingly the residual rock depleted in the elements is subducted with the slab. Thus the chemical heterogeneity generated in the shallow wedge mantle is well coupled with the plates or the slabs because of the high viscosity and is not advected widely in the mantle.

3.1.2. Transition zone process

On the other hand, underlying hydrous peridotite beneath the hydrous MORB is much colder, and phase A, a high water storage capacity mineral, is stably formed as the assemblage 11 and 12 in Figure 16 beneath the depth of the "choke point" (Kawamoto et al., 1996). Therefore, there is neither aqueous fluid generation nor element fractionation in this area even if oceanic plate contains much water (3 wt.%) at the initial condition. This high water content (3 wt.%) in the slab core is preserved in the transition zone by the phase change of A into D (Figures 16 and 17). This hydrous patch at the transition zone depth reduces the density of the subducting slab, preventing the slab from entering the lower mantle. As a result, after the slab reaches the bottom of the transition zone, it stagnates and the trench begins rapid retreat (29.11 Myr in Figures 19 and 20). Then the soft material at the top right corner of the model domain is extended and the continental plate is dragged leftwards.

3.1.3. Transition from stagnation to penetration

Although the trench continuously retreats, it stops at the middle of the model domain and correspondingly the stagnant slab begin collapsing to the lower mantle ($z \sim 4,000$ km; 61.75 Myr in Figure 19). As the oceanic plate continues retreat, the overlying continental plate to be dragged becomes larger, arising large viscous dissipation around the continental plate. If this viscous resistance around it exceeds the drag force by the slab subduction, the trench retreat is weakened.

3.1.4. Lower mantle process

After the slab penetration at the 660-km boundary, owing to the smaller water storage capacity in the lower mantle (100 ppm), the hydrous layer with about 2,000 ppm just above the subducted MORB dehydrates (100 Myr in the left of Figure 20). Aqueous fluids generated at the top of the lower mantle ascend to the mantle transition zone and

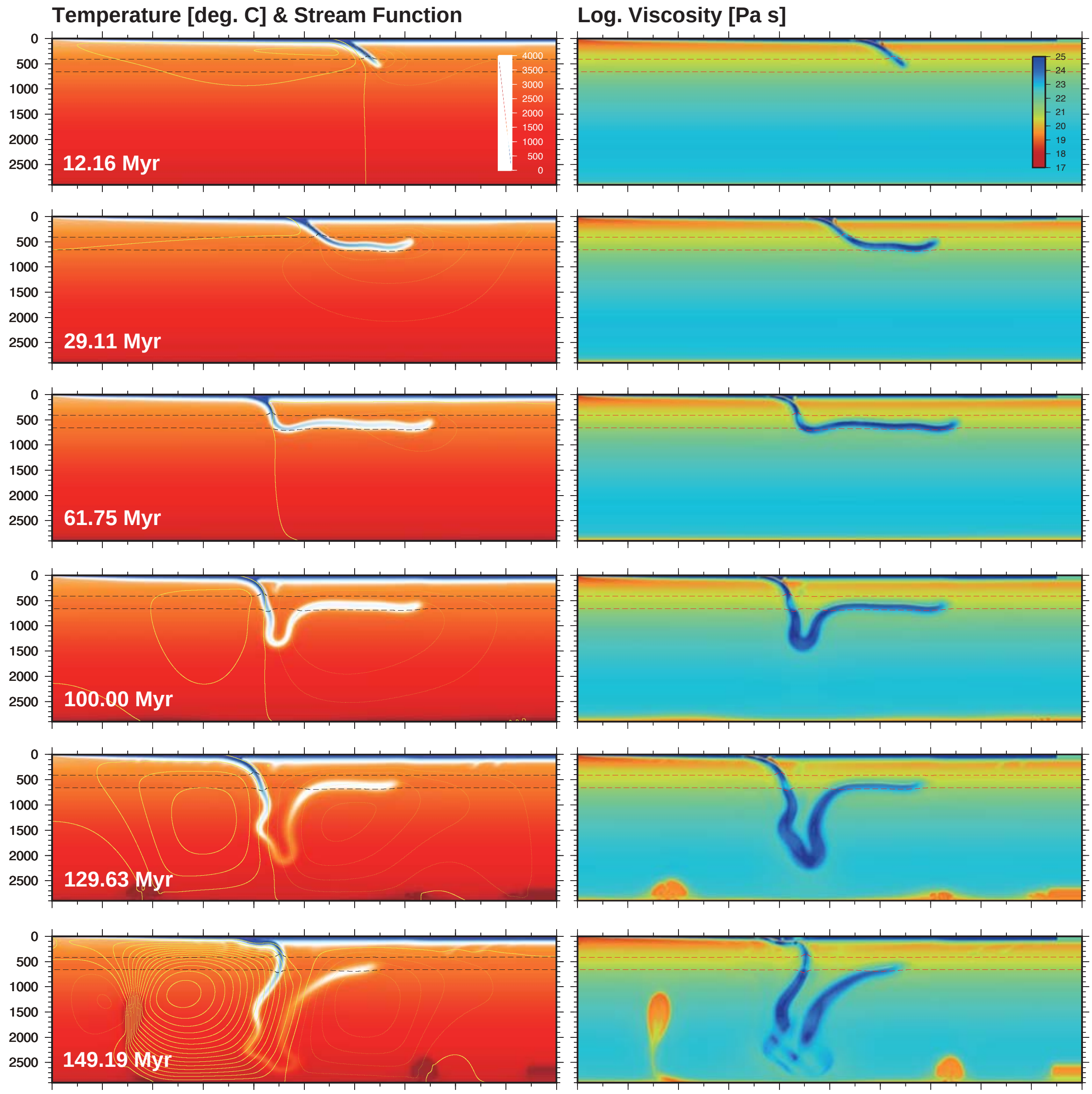

Figure 19: Evolution of run stg2. Whole model domain (10,000 km width × 2,900 km depth) is presented. Left boxes show temperature and stream function. Right boxes show viscosity.

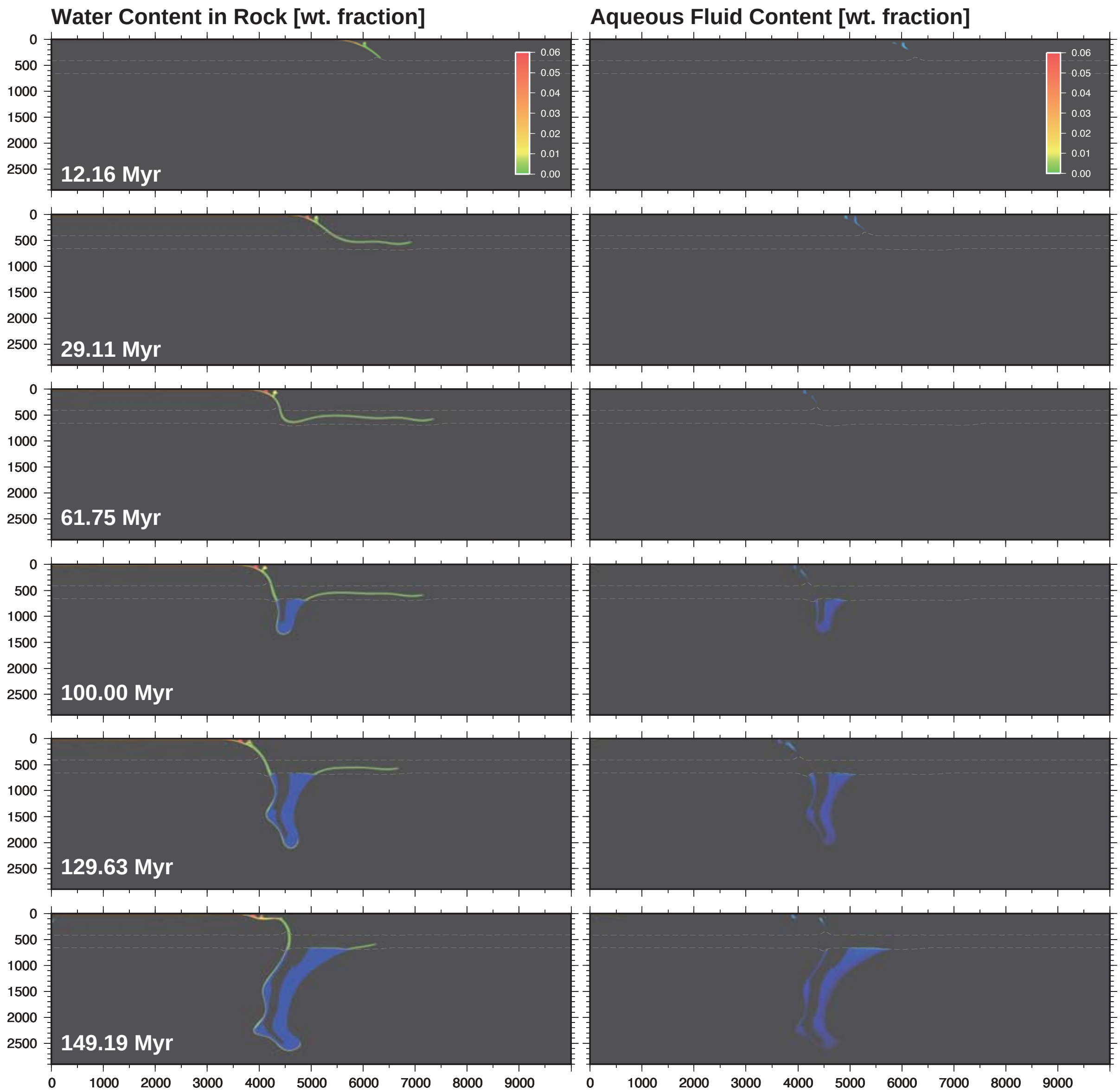

Figure 20: Evolution of run stg2 corresponding to Figure 19. Left boxes show water content of hydrous rocks, and right boxes show weight fraction of the aqueous fluid phase (dark gray = 0 ppm; blue = 100 ppm; cyan = 500 ppm; green = 1,000 ppm; yellow = 10,000 ppm; red = 60,000 ppm).

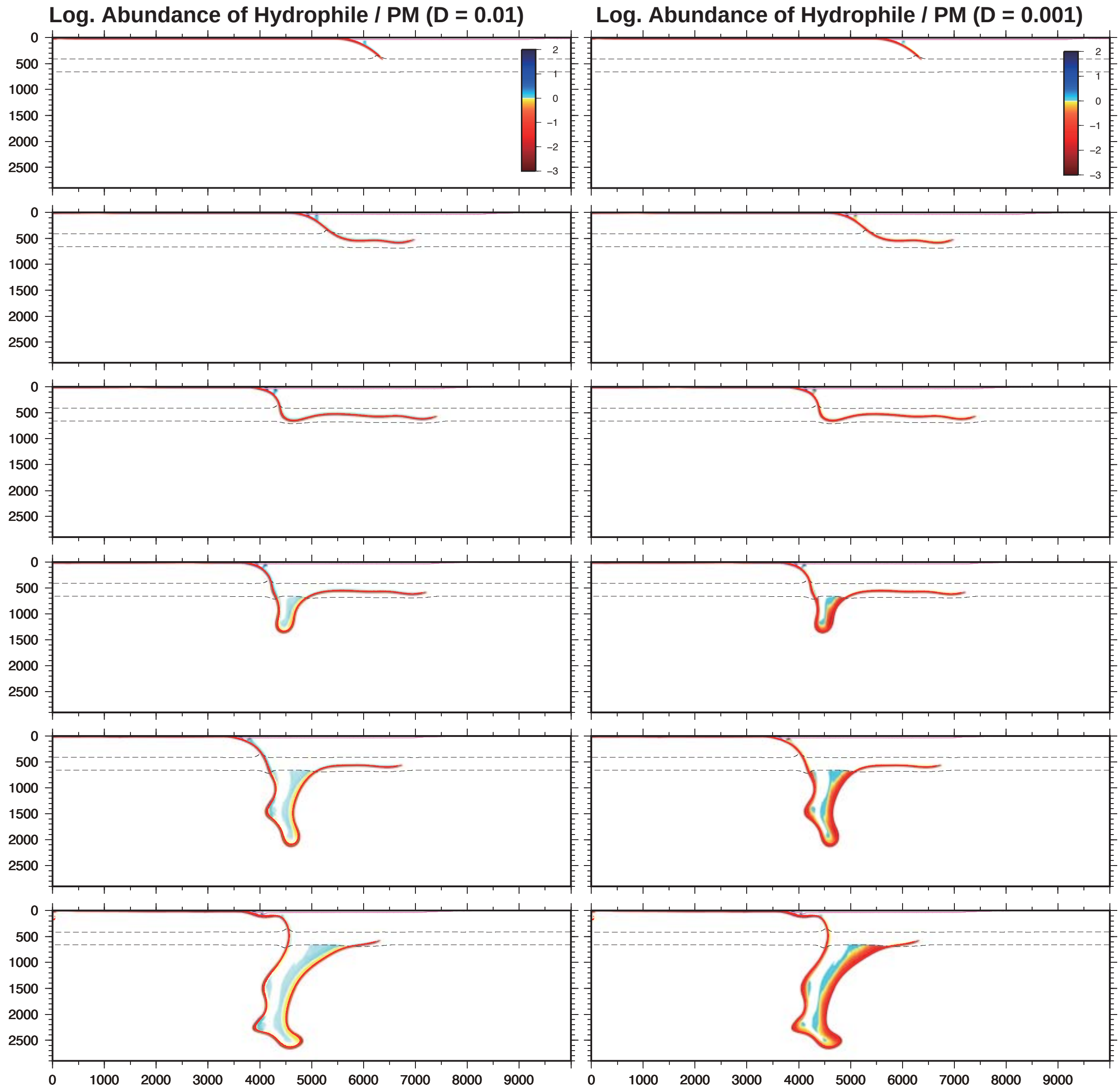

Figure 21: Evolution of run stg2 corresponding to Figures 19 and 20. Boxes show logarithmic abundance of an imaginal highly hydrophilic element with $D^{\mathrm{sol/aq}} = 10^{-2}$ (left boxes) and $D^{\mathrm{sol/aq}} = 10^{-3}$ (right boxes; listed in Table 3) normalized by that of the primitive mantle. White area is primitive, cooler color indicates its concentration, and warmer color indicates its depletion. Harzburgite (0.01 times concentration; red layer) and MORB (10 times concentration; blue) layers are considered as the initial chemical heterogeneity. Pink contours show the positions of continental crust.

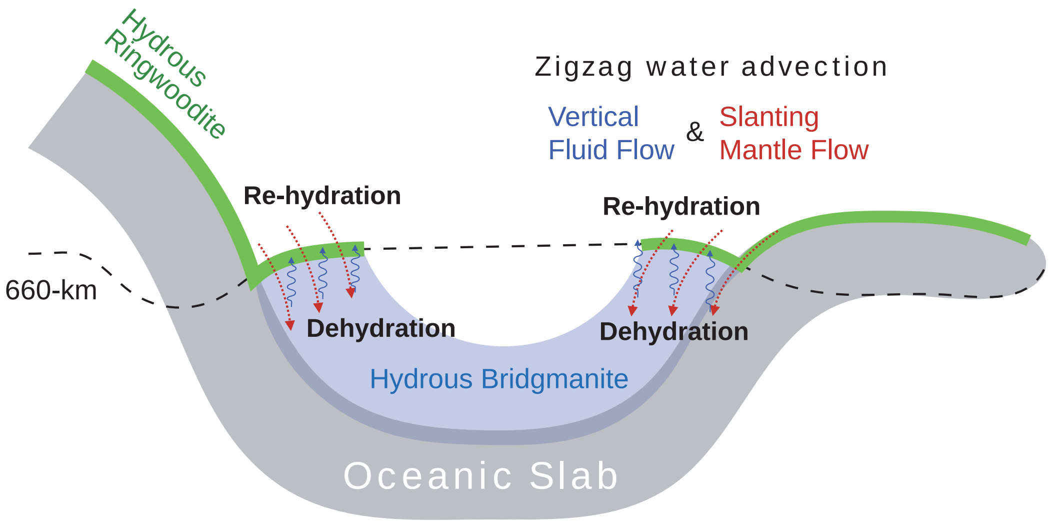

Figure 22: A schematic of the mechanism to transport water laterally along the 660-km depth boundary through the zigzag path (Iwamori & Nakakuki, 2013).

are re-captured into ringwoodite just above the 660-km depth boundary. The generated hydrous ringwoodite patch immediately descends into lower mantle owing the mantle flows induced by slab subduction, and it decomposes again. Thus the wet-Rw $\rightleftharpoons$ wet-Brdg + H_2O reaction is repeated along the 660-km boundary. In the process, the flows of hydrous ringwoodite are slanting, while the aqueous fluids ascend vertically. These two water transportation mechanisms make zigzag paths (Figure 22; Iwamori & Nakakuki, 2013), helping water advected laterally along the 660-km boundary. While the zigzag path extends, hydrous bridgmanite is continuously generated and flows into the lower mantle widely. In the cold core of the penetrating slab, phase H is formed after phase D decomposes. This hydrous layer becomes thin owing to the slab heating in the lower mantle. Then aqueous fluids are generated, producing hydrous bridgmanite.

In the repeated dehydration-hydration process along the 660-km boundary, hydrophilic elements are released with the aqueous fluids from the descending bridgmanite in the lower mantle and are concentrated into the hydrous ringwoodite piles at the bottom of the transition zone (100 Myr of Figure 21). After the sufficient zigzag water transportation, the hydrous ringwoodite piles enriched in the hydrophilic components gradually sink into the lower mantle (100–149 Myr of Figure 21). Thus there are both enriched and depleted components in the lower mantle. The chemical heterogeneity can be transported more widely because of the low viscosity (well detached from the subducting slab) than that produced in the shallow dehydration processes. In the following sections, we focus on the fractionation process along the 660-km.

3.2. Hydrogen diffusion

The diffusion coefficient of hydrogen κ_{H_2O} in hydrous NAMs strongly depends on temperature and it would be 10^{-8}–10^{-9} m^2/s (in hotter mantle) to 10^{-12}–0 m^2/s (in cold slabs) (e.g., Mackwell & Kohlstedt, 1990; Sun et al., 2015; Ohtani & Zhao, 2009). Figure 23 is the different results of water transportation corresponding to κ_{H_2O}=0, 10^{-9}, and 10^{-6} m^2/s. If large κ_{H_2O} ($= 10^{-6}$), the diffusion mechanism helps hydrous rock detached from cold slabs by softening the slab. Given the reasonable κ_{H_2O} ($= 10^{-9}$), the effect of hydrogen diffusion on water transportation is small. Therefore, it is ignored in the other runs in the following sections (Table 6).

3.3. Upward velocity of aqueous fluid

Figure 24 shows effects of upward velocity of aqueous fluid on the water and element transportation. As already described, the ascent velocity of aqueous fluids is fast enough in the upper mantle given a reasonable permeability so that we can treat it as an instantaneous process in Chapter II. However, in the case of the smaller permeability, the hydrous rock layer along the slab surface becomes thicker (run stg3 in Figure 24): the aqueous fluid generated due to serpentinite dehydration is dragged more deeply, and larger amount of water sinks into the transition zone. In the lower mantle, as the fraction of the aqueous fluid is smaller, approximation of the fluid ascent velocity to the infinite is not valid. With a reasonable permeability (Horiuchi & Iwamori, 2016; run stg2 in Figure 24), several tens ppm of aqueous fluids generated by hydrous ringwoodite decomposition sink together with fully hydrated bridgmanite (100 ppmH_2O in this run). The amount of the water as aqueous fluid phase in the lower mantle is also larger given the small permeability (run stg3 in Figure 24). In run stg2 (Fugure 20), the weight fraction of the free aqueous fluid in the lower mantle is larger just beneath the 660-km and where phase H is decomposing (both about several hundred ppm H_2O) and becomes smaller as the slab sinks into the depth; several ten (about 1,000 km depth) to several ppm H_2O (lowermost lower mantle), in the bridgmanite saturated in water. These aqueous fluids beneath the

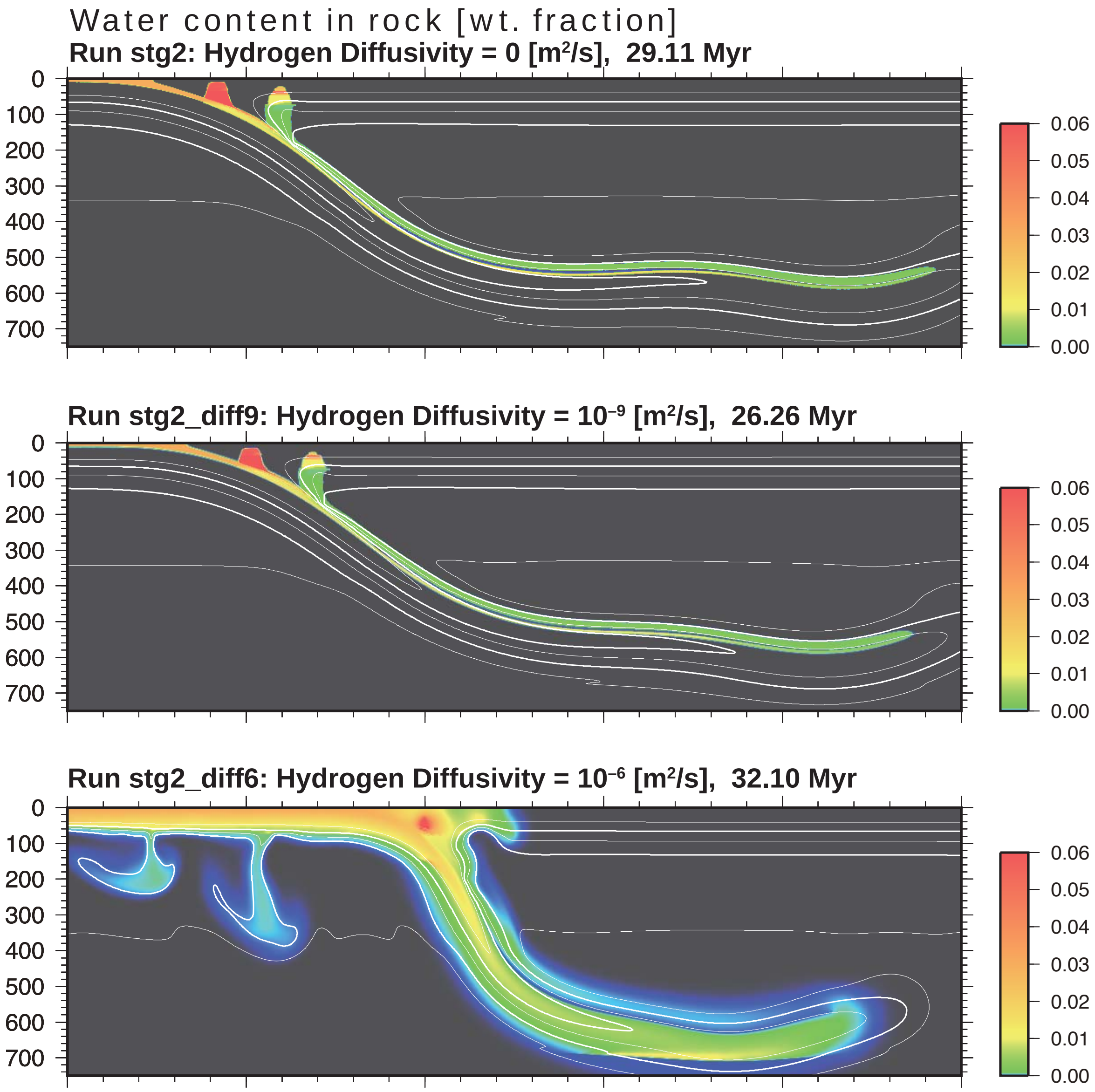

Figure 23: Effects of hydrogen diffusion. Comparison of water distribusion between runs stg2 at 29 Myr ($\kappa_{H_2O} = 0$ m^2/s), stg2diff9 at 26 Myr ($\kappa_{H_2O} = 10^{-9}$ m^2/s), and stg2diff6 at 32 Myr ($\kappa_{H_2O} = 10^{-6}$ m^2/s). The MPS method (Appendix E) is applied to only runs stg2diff9 and stg2diff6.

660-km depth boundary may be observed as the low seismic velocity anomalies near a penetrating slab (Schmandt et al., 2014; Liu et al., 2016).

3.4. Water storage capacity of lower mantle

The difference between the water content of the subducting hydrous layer and the water storage capacity of bridgmanite is essential for the zigzag water transportation (Figure 22). The smaller the lower mantle water storage capacity is, the more efficient the lateral water transportation becomes (top three boxes in Figure 25). Similarly it affects the spatial distribution of the heterogeneity of hydrophilic components (second line in the Figure 25). In addition, the generation rate of aqueous fluids $\dot{C}_{\mathrm{H_2O}}^{\mathrm{sol}\to\mathrm{aq}}$ controls chemical composition according to Equation (32). Figures 26a–c show the variation of $^{208}\mathrm{Pb}/^{204}\mathrm{Pb}$–$^{206}\mathrm{Pb}/^{204}\mathrm{Pb}$ isotopic diagrams of the whole model domain (correspond to the bottom six boxes in Figure 25). If the dehydration rate is small owing to a large lower mantle water storage capacity, the residual rocks sinking into the deeper lower mantle is not so depleted (Figure 26c). On the other hand, if much water is released during ringwood dehydration, the Pb isotopic ratios of the residual after some evolution diverge to infinite (Figure 26a) because of the extreme depletion of the residual rocks in the daughter (Pb) compared to the parent (U or Th). This tendency is also obtained from an analytical approach (Figure 27).

Two possible mechanisms would produce the wide range of the depleted components in run stg2 (Figure 26a). One of them is a large variation of water content of hydrous ringwoodite along the 660-km depth boundary (10^2–10^4 ppm). This variation causes the variation of the aqueous fluid emission (0–10^4 ppmH_2O as the aqueous fluid). As a result, a trend like Figure 27 can be drawn. Another one is the repeated hydration along the 660-km. In the zigzag process, hydrophile-rich ringwoodite repeatedly dehydrates; therefore, as the process progresses, the residual becomes enriched in the hydrophiles gradually. Similarly the weakening of the zigzag process causes gradation of the isotopic ratio from the depleted slab surface (early dehydration) to the enriched uppermost lower mantle (late dehydration) (the left bottom of Figure 25).

3.5. Partition coefficient in lower mantle

Partition coefficient $D^{\mathrm{sol/aq}}$ is also essential for the trend in the isotopic space. Figure 26d and the right of Figure 28 are the case of the smaller differences of hydrophilicity

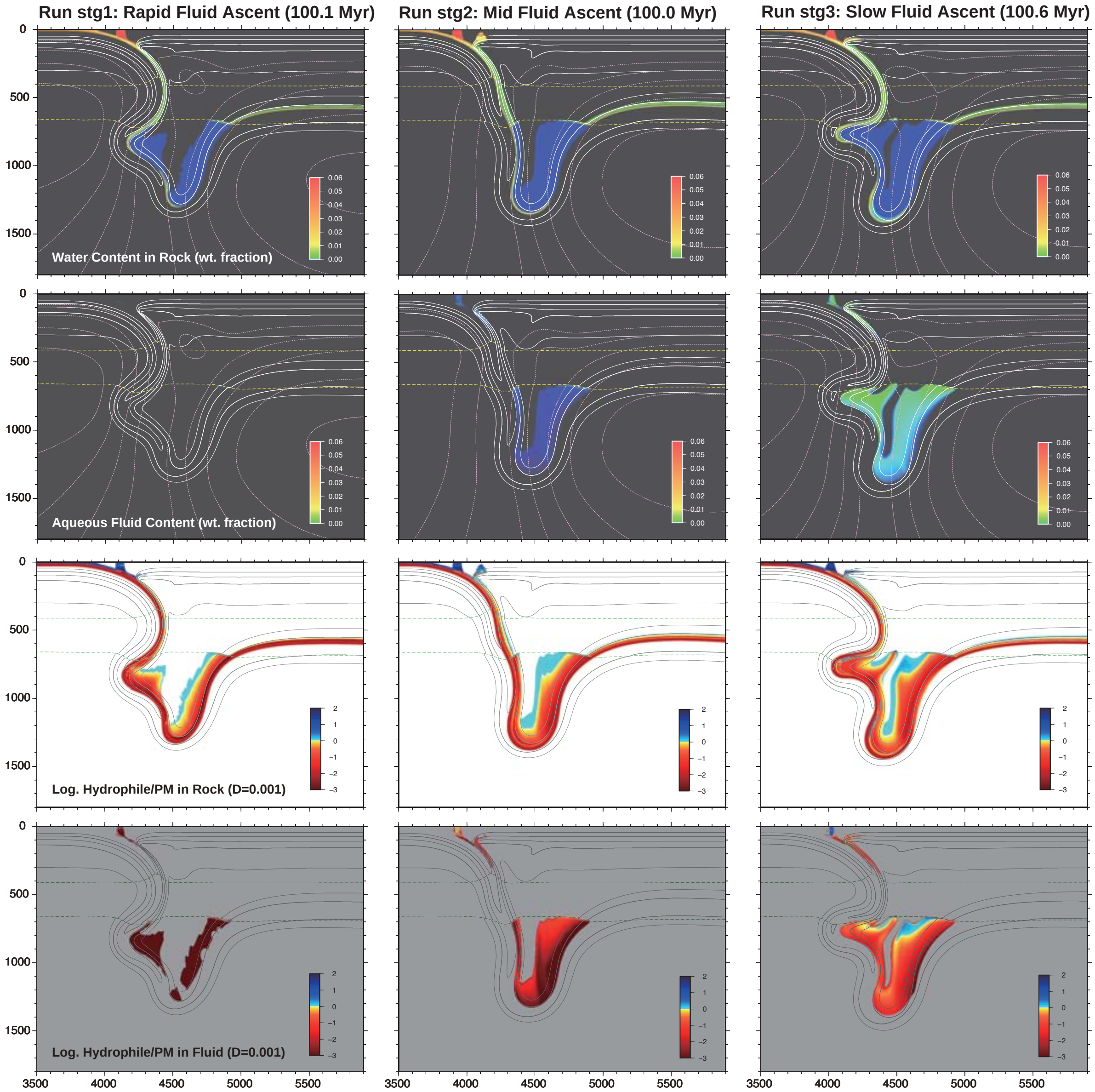

Figure 24: Effects of the permeability of ascentding aqueous fluids. Comparison between runs stg1 at 100 Myr (rapid fluid ascent; left), stg2 at 100 Myr (mid fluid ascent; center), and stg3 at 101 Myr(slow fluid ascent; right). Three boxes in the first line indecates water content of mantle rocks, isotherms (200°C intervals), the 410- and 660-km depth boundary, stream function. The second line shows aqueous fluid abundance. The third line show logarithmic abundance of an imaginal highly hydrophilic element ($D^{\mathrm{sol/aq}} = 10^{-3}$) in mantle rocks normalized by that of the primitive mantle. The bottom line show logarithmic abundance (not density) of the element in aqueous fluid normalized by that of the primitive mantle“rocks”. In gray areas aqueous fluids do not exist.

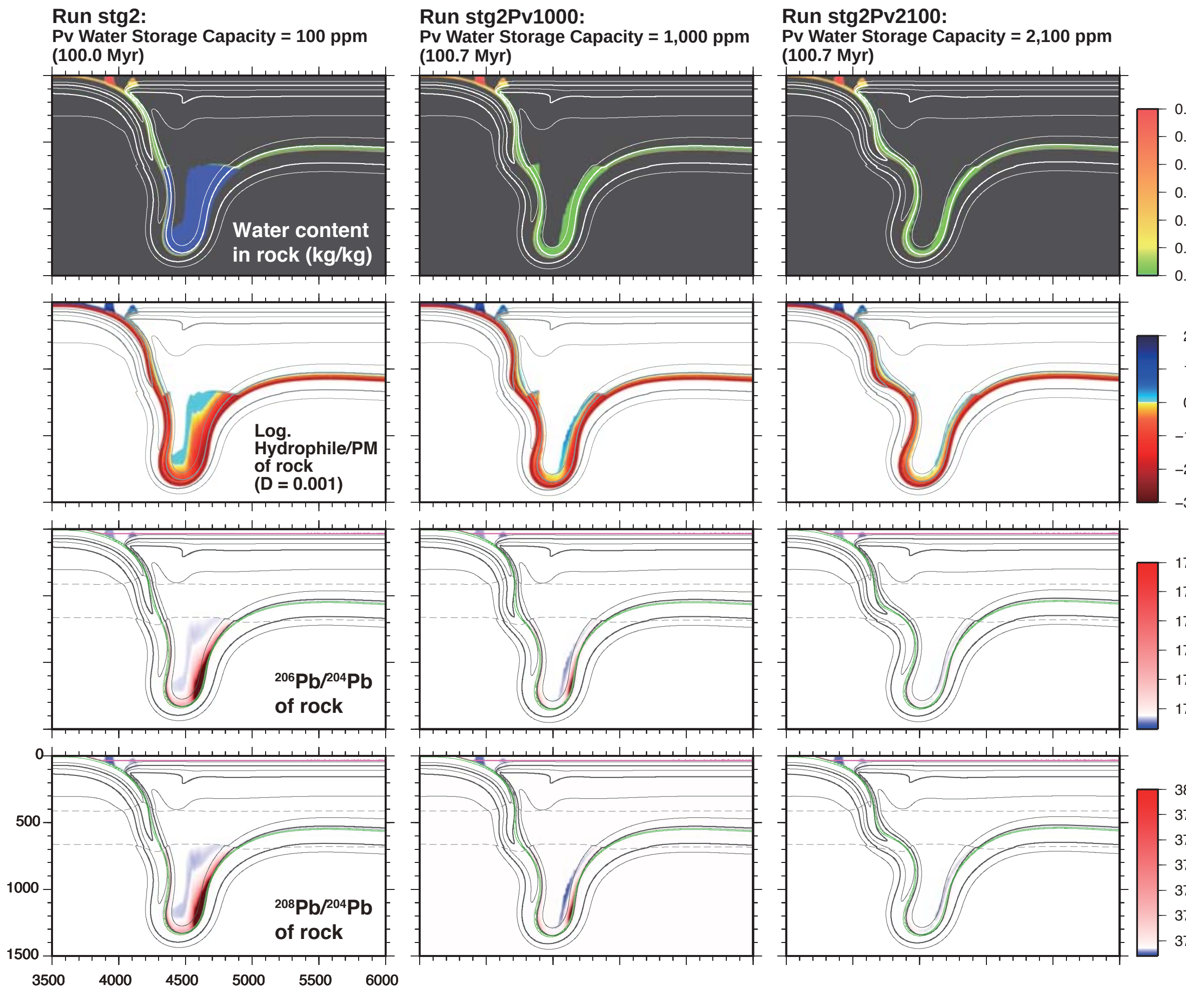

Figure 25: Effects of the maximum water content of the lower mantle on the distribution of water and chemical compositions. Comparison between runs stg2 at 100 Myr (100 ppm; left), stg2Pv1000 at 101 Myr (1,000 ppm; center), and stg2Pv2100 at 101 Myr(2,100 ppm; right). Three boxes in the first line indecates water content of mantle rocks. The second line show logarithmic abundance of an imaginal highly hydrophilic element ($D^{\mathrm{sol/aq}} = 10^{-3}$) in mantle rocks normalized by that of the primitive mantle. The third and bottom lines show maps of the $^{206}\mathrm{Pb}/^{204}\mathrm{Pb}$ and $^{208}\mathrm{Pb}/^{204}\mathrm{Pb}$ ratios of the mantle rocks, respectively. Blue areas indicate re-hydrated component, and red areas indicate dehydrated components. Pink and green lines show continental and oceanic crust, respectively.

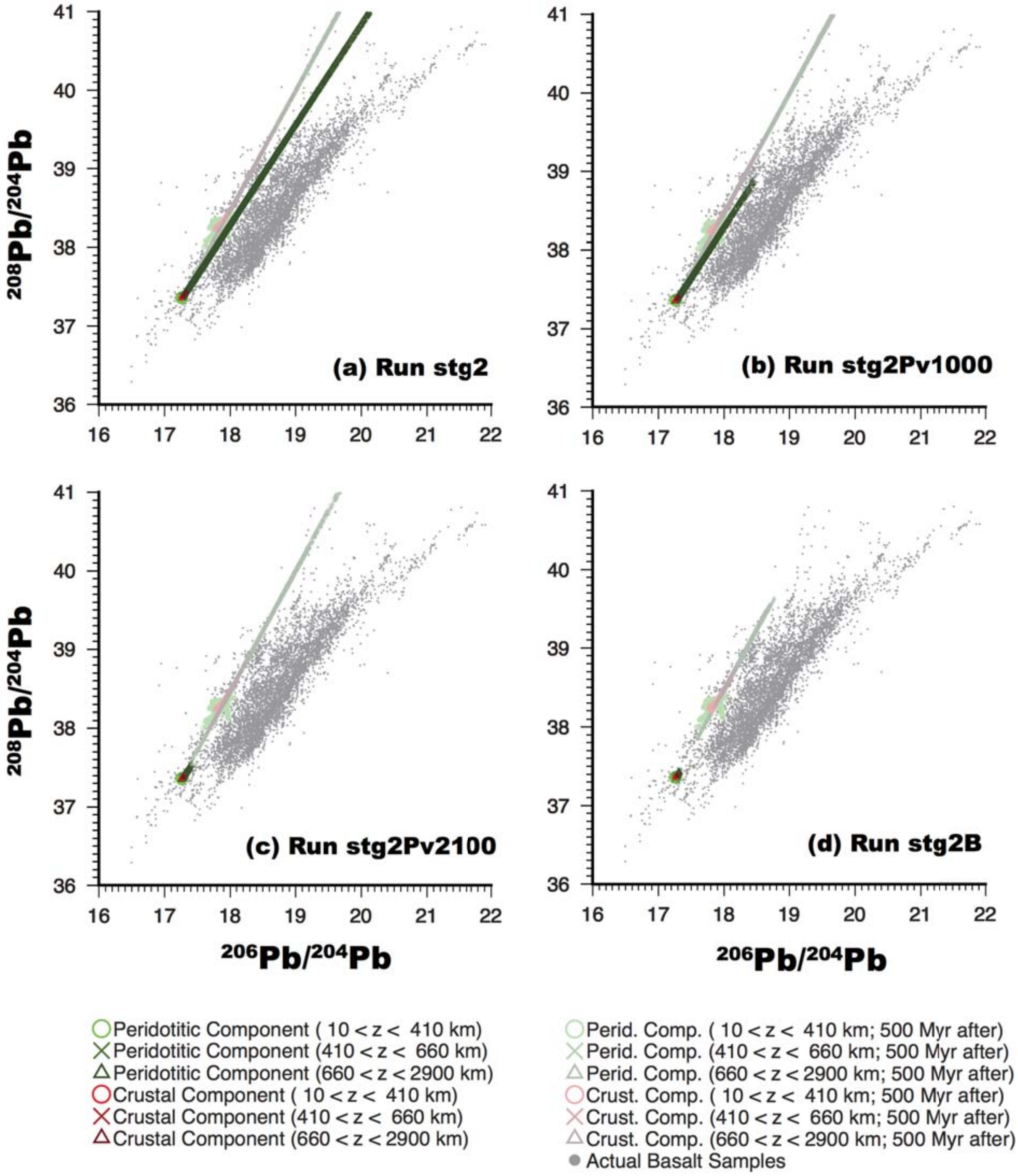

Figure 26: Comparison of the ^{206}Pb/^{204}Pb–^{208}Pb/^{204}Pb range between four runs. Dark green and dark red symbols indicates mantle and crustal isotope composition at about 100 Myr since the initial condition, respectively. Light green and light red symbols show analytical solutions of the evolved isotopic values after 500 Myr (i.e., 100 Myr by convection model + 500 Myr by analytical solution). All node values in the model domain are plotted in these figures. Gray dots indicates isotopic compositions of natural basalt (Iwamori & Nakamura, 2015)

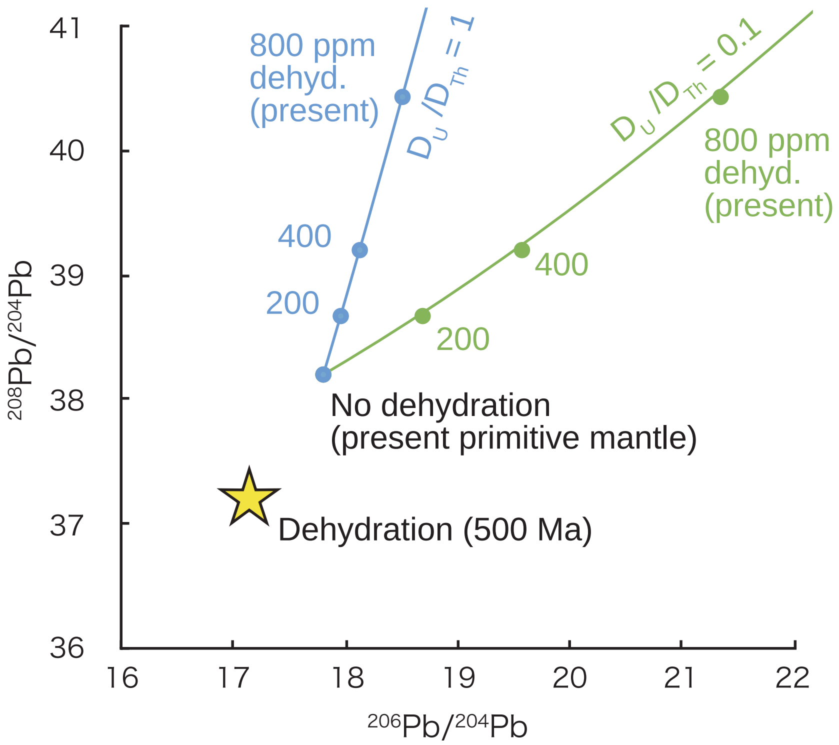

Figure 27: Analytical solution of isotopic compositions of dehydrated mantle rocks. The yellow star indicates the initial value at which the dehydration process occurs (500 Ma). Given $D_{\mathrm{U}}^{\mathrm{sol/aq}} = 10^{-2}$, $D_{\mathrm{Th}}^{\mathrm{sol/aq}} = 10^{-2}$, and $D_{\mathrm{Pb}}^{\mathrm{sol/aq}} = 10^{-3}$, isotopic compositions of the residual rocks at 500 Myr after the dehydration are plotted along the blue line. Given $D_{\mathrm{U}}^{\mathrm{sol/aq}} = 10^{-3}$, $D_{\mathrm{Th}}^{\mathrm{sol/aq}} = 10^{-2}$, and $D_{\mathrm{Pb}}^{\mathrm{sol/aq}} = 10^{-3}$, that are plotted along the green line. The larger the amount of aqueous fluids generated in the dehydration process is, the larger the isotopic ratios become.

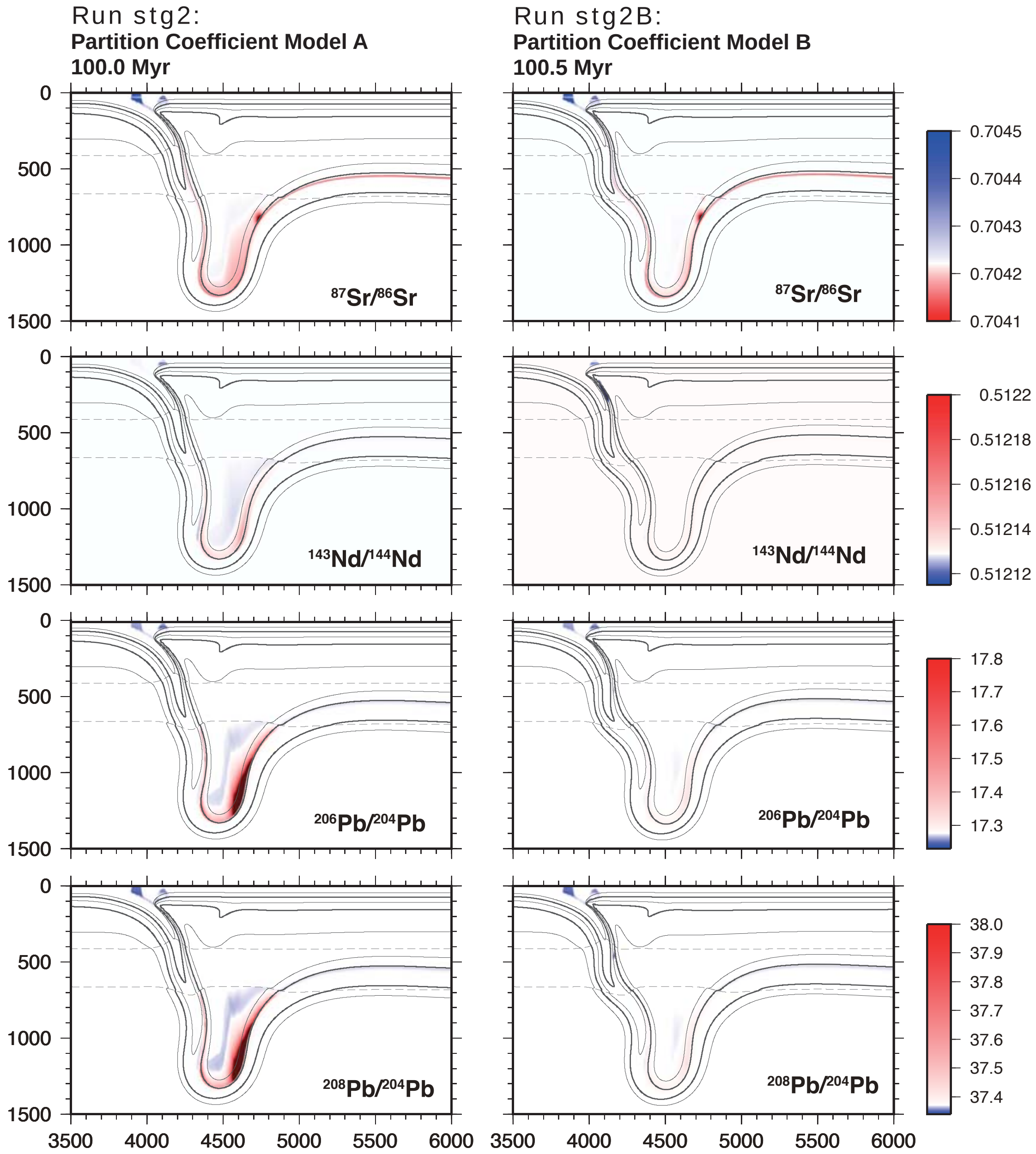

Figure 28: Effects of partition coefficient between rocks and fluids in the lower mantle. Comparison of chemical compositions between runs stg2 at 100 Myr (partition model A in Table 5; left) and stg2B at 101 Myr (partition model B in Table 5; right). Blue areas indicate re-hydrated component, and red areas indicate dehydrated components for each isotope map.

between the daughters (Pb, Sr, Nd) and the parents (U, Th, Rb, Sm) in the lower mantle (run stg2B, Model B of Table 5). The fractionation during the zigzag process is smaller than that in run stg2. The slope of the trend in the isotopic ratio diagrams depend on the hydrophilicity relationship between the parents. The slopes reproduced in the simulation roughly consistent with that of the actual basalt (Figure 26), justifying the assumption of $D_{\mathrm{U}}^{\mathrm{sol/aq}}/D_{\mathrm{Th}}^{\mathrm{sol/aq}}$ in Table 5. If U is more hydrophilic than Th, the slop in the ^{206}Pb/^{204}Pb–^{208}Pb/^{204}Pb diagram becomes gentle (green line in Figure 27).

3.6. Effects of equilibrium model for trace elements partitioning

So far we have examined the results of the non-equilibrium (fractional) element partitioning model (Subsection 2.3.1), and here we also check the equilibrium partitioning model (Subsection 2.3.2; Figures 29, 31).

3.6.1. Depletion of eclogitic layer

In the non-equilibrium model (run stg2), depletion of the residual owing to MORB dehydration (HIMU-like layer) is significant (10^{-3} times concentration) because the dehydrated rocks are isolated from the reacting zone one after another, causing strong contrast of the elemental abundance between the eclogitic depleted layer and the above adjoining fluid-added peridotitic layer (around the depth of 100 km in the upper box of Figure 29). The extreme depletion would be caused by the formularization that the element flux from the dehydrating rock phase into the generating aqueous fluid phase does not depend on the elemental abundance of the fluid phase (Equation 32).

On the other hand, such strong contrast or layered structure is not reproduced in the equilibrium model (lower box of Figure 29; run stg2eq) because the dehydrated layer remaines still capable of the incompatible elements as far as the aqueous fluids exist, or because the aqueous fluid phase along the MORB layer enriched in the incompatible elements restrict the extraction of them from the dehydrating MORB layer into the fluid phase unlike Equation (32).

3.6.2. Element extraction during fluid ascending

In the equilibrium model, as far as the aqueous fluid exist at each node, the elemental partitioning for the node is calculated at every time step. Therefore, the fluid path penetrating the surrounding mantle rock is mode depleted (e.g., a red vertical column

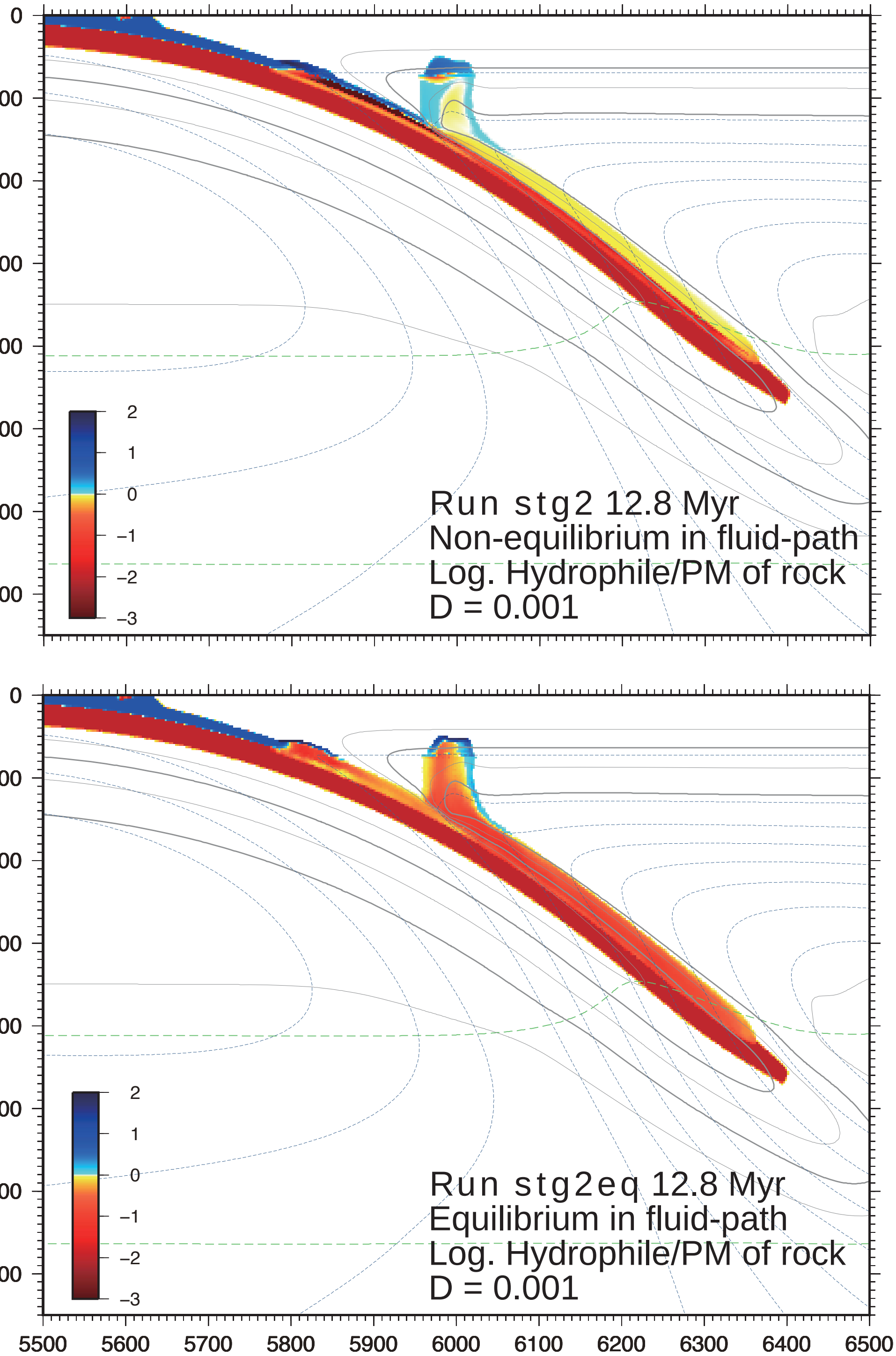

Figure 29: Effects of the fractional or equilibrium model for the trace element partitioning (Subsections 2.3.1 and 2.3.2) on chemical compositions. Comparison between runs stg2 at 12.8 Myr (left) and stg2eq at 12.8 Myr (right). Colored contours show logarithmic abundance of an imaginal highly hydrophilic element ($D^{\mathrm{sol/aq}} = 10^{-3}$) in mantle rocks normalized by that of the primitive (non-reacted) mantle.

around x = 6,000 km in the lower box in Figure 29), and the hydrophiles are more partitioned into the aqueous fluid phase. Although the depletion grade of residual rocks of run stg2eq is smaller for the reasons stated in Subsection 3.6.1, the distribution of the residues are wider due to the fluid ascending compared to those of the fractional partitioning model (run stg2), in which there is no elemental extraction during the fluid ascending (Equation 34).

3.6.3. Element precipitation during re-hydration

In the fractional model (run stg2), when the aqueous fluid is incorporated into capable less-hydrous rocks, concentration of the precipitating elements is assumed to be the same as that in the aqueous fluid (Equation 33), like rapid cooling of magma (i.e., no elemental fractionation in the crystallization process). Therefore the enriched rocks pile up on the fluid column around x = 6,000 km in the upper box of Figure 29.

On the other hand, the equilibrium model (run stg2eq) is an analogy of concentration of volatiles and incompatible elements in silicic magma, not in the crystallizing minerals. Therefore, the hydrophiles tend to remain in the aqueous fluid during re-hydration, causing more element concentration in the solid phase in a limited area beneath the continental lithosphere (about 50-km depth in the box of Figure 29).

This tendency is also recognized in isotopic ratios (Figure 30). Fractionation between Rb and Sr and the resultant wide range of ^{87}Sr/^{86}Sr are mainly caused the shallower processes in the simulation, and the equilibrium partitioning model is more favorable to reproduce such wide range observed in actual basalt samples, especially enriched (high-^{87}Sr/^{86}Sr) components. Contrary, the fractional partitioning model is more favorable to reproduce extremely depleted component (e.g., high ^{208}U/^{204}U) as discussed in Subsection 3.6.1.

3.6.4. Element partitioning around the 660-km

Similar to the above description of the mantle wedge dehydration processes, the 660-km dehydration also causes both widespread depleted residues and re-hydrated rocks with well-concentrated hydrophiles (i.e., enriched hydrous ringwoodite piles along the 660-km and resultant enriched hydrous bridgmanite in the latest stage of the zigzag water transportation; deep blue areas in the lower mantle in the bottom right box of Figure 31). Since the equilibrium partitioning model would be more reasonable in the lower mantle conditions (Subsection 2.3.2), the hydrophilic trace elements concentrate more efficiently during the 660-km dehydration.

3.7. Wet plumes from the 660-km boundary

In the zigzag water transport process (Figure 22), the hydrophile-rich hydrous ringwoodite piles continuously develop at the bottom of the transition zone. In the run stg2, the piles are finally absorbed into the lower mantle because of the fast downward mantle flows induced by the slab collapse. On the other hand, some runs show continuous growth of the hydrous piles, and they ascend as hydrous plumes (not upward aqueous fluid flows) due to the low density and viscosity (run pnt1; Figure 32; Parameters used in this run is shown in the caption). Although the requirement for the wet plume generation is somewhat unclear, slow mantle wedge flows seem essential. Therefore, static or slightly advancing trench modes discussed in the Chapter II are favorable for the generation of the plumes (see slow wedge flows of run r1b2 in Figure 11c). The lateral water transportation by the zigzag process is also important to put the hydrous piles away from the descending slab in terms of the plume ascent although inefficient lateral water transport is favorable for the growth of the hydrous piles. In run pnt1 (Figure 32), plumes seem to ascend when the slab migrates leftward in the transition zone. Thus slab wandering would be important for the expanding the chemical heterogeneity.

When the wet plumes from the 660-km boundary ascent across the 410-km boundary, decomposition of hydrous wadsleyite into olivine and much aqueous fluid occurs. Then the fractionation of hydrophilic components occurs. However, the enriched plume head and the depleted plume tail still ascend together and are not well separated mechanically (upper mantle at 71.33 Myr of Figure 32). Therefore, the fractionation at the 410-km boundary seems less influential in the global mantle chemical heterogeneity than that at the 660-km in the numerical setting. Further discussion on the 410-km fractionation processes is described in Section 4.3.

4. Discussion

4.1. Interpretation of isotopic data of mantle-derived basalt

Traditionally geochemists have considered that the mantle chemical heterogeneity is a result of mixing of distinct chemical end-members (e.g., Hart et al., 1986). HIMU,

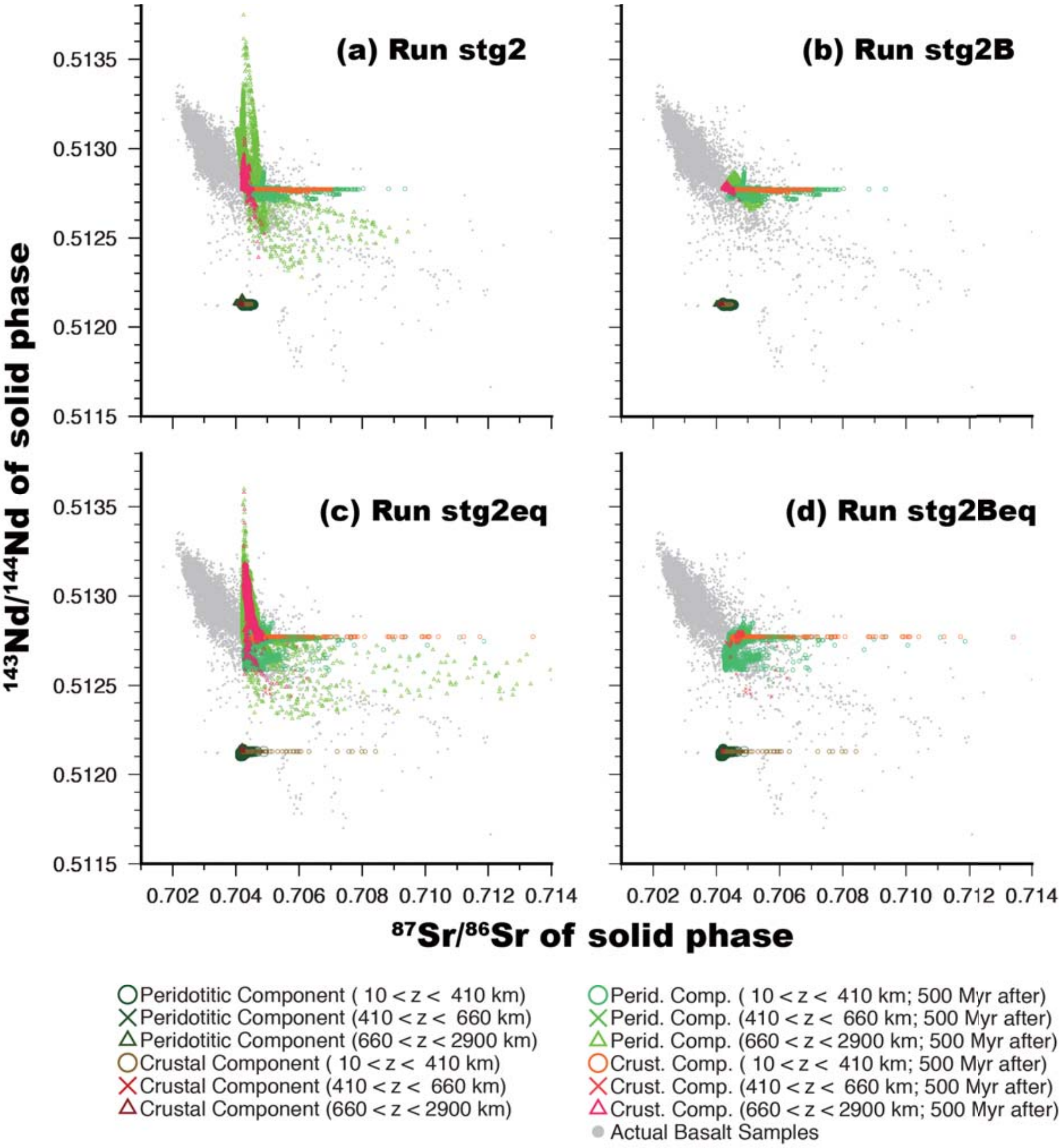

Figure 30: Comparison of the $^{87}Sr/^{86}Sr$–$^{143}Nd/^{144}Nd$ range between four runs. The symbols are almost the same as those in Figure 26

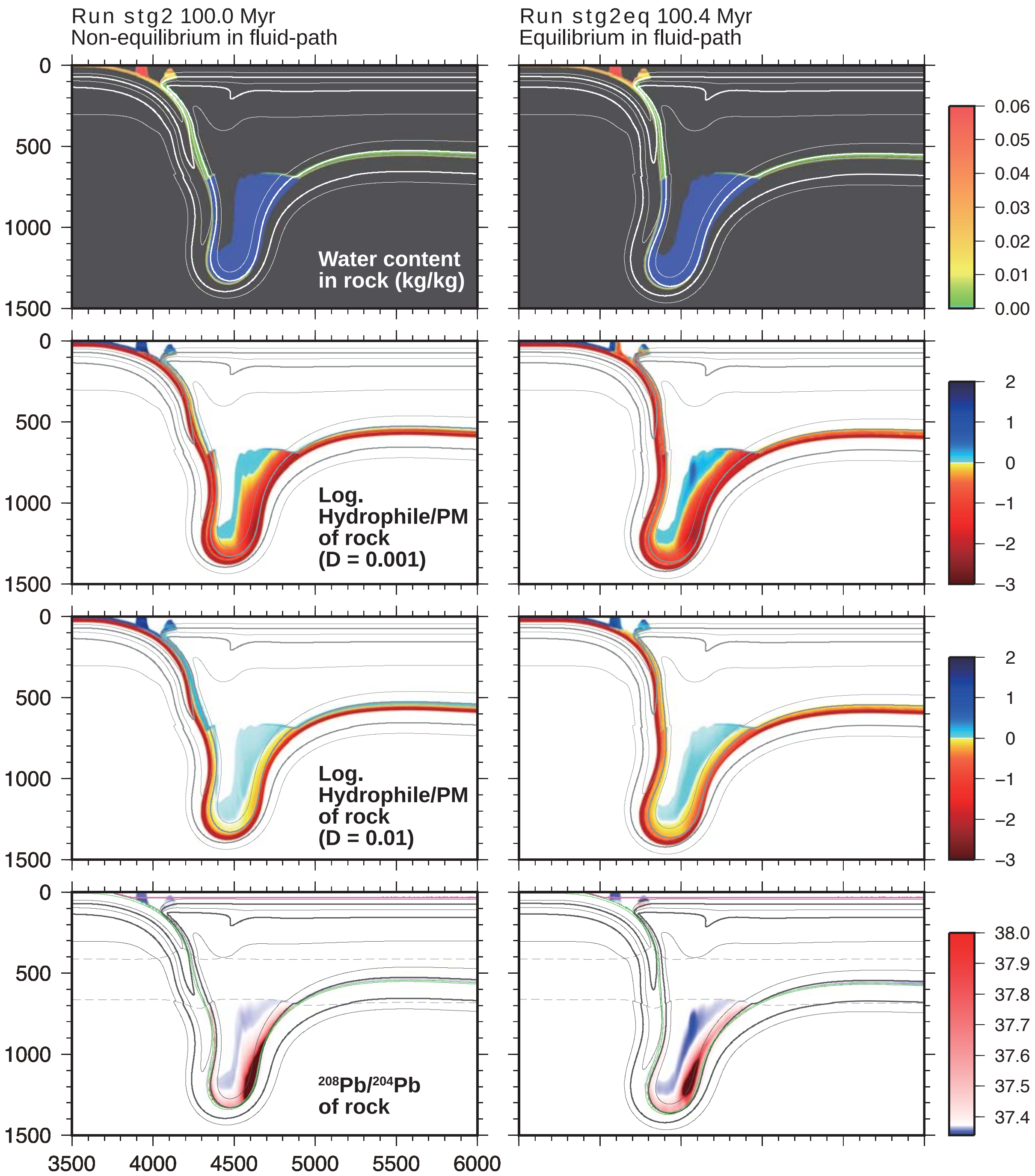

Figure 31: Effects of the equilibrium model for the trace element partitioning on chemical compositions. Comparison between runs stg2 at 100.0 Myr (left) and stg2eq at 100.4 Myr (right). Colored contours are almost the same as those in Figure 25.

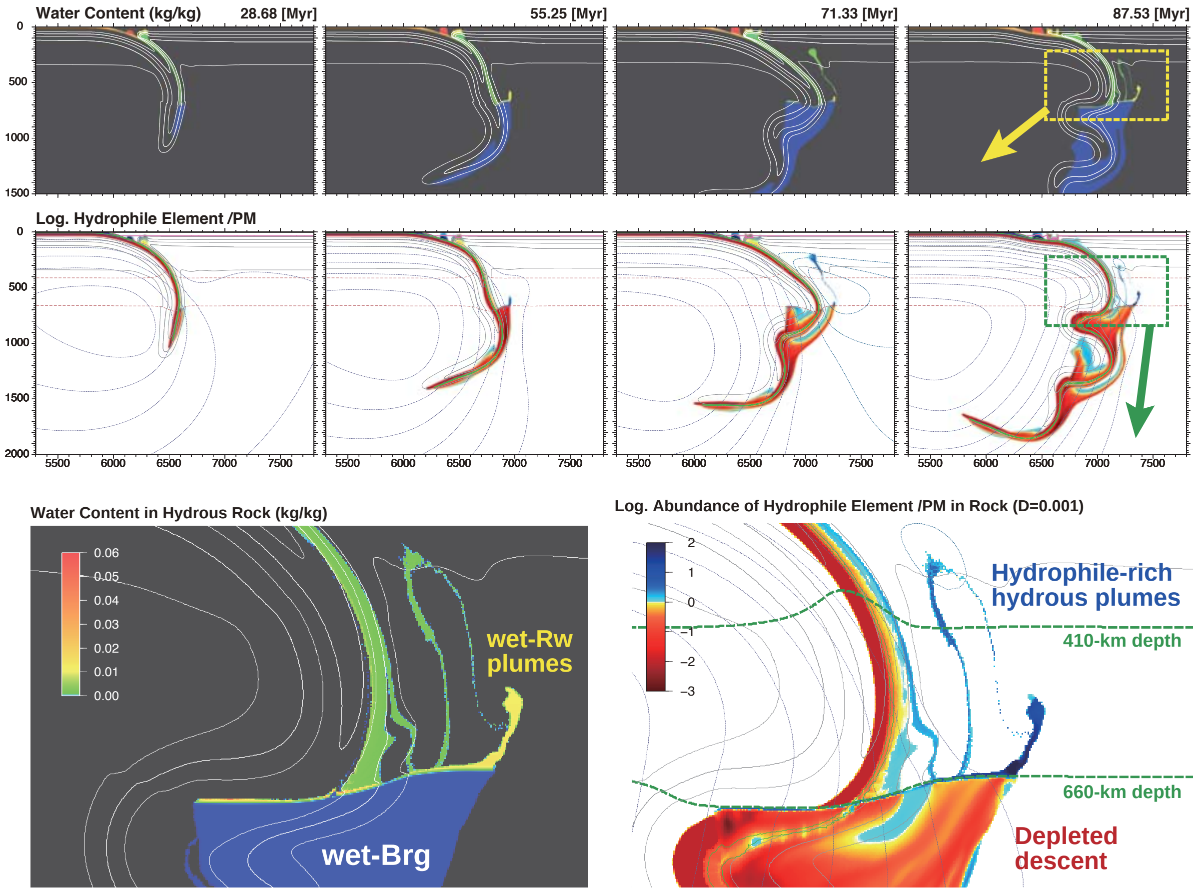

Figure 32: Evolution of run pnt1. Boxes in the first lines show water content in rocks. Second lines show logarithmic abundance of an imaginal highly hydrophilic element ($D^{\mathrm{sol/aq}} = 10^{-3}$) in mantle rocks normalized by that of the primitive mantle. Bottom two boxes are the enlarged views around the mantle transition zone at 87.53 Myr. The water transportation in this run is based on Chapter II (i.e., the infinite ascent velocity of aqueous fluids). There is no hydrous slab core that generates phases A and D; therefore, the slab penetrates at the 660-km because of small hydrous buoyancy in the transition zone. Phase H is not considered. The initial ages of oceanic and continental plates are 0–120 Myr and 50 Myr, respectively. No heat flux boundary condition is imposed at the bottom of the model domain. Maximum yield strength is 180 MPa. Hydrous buoyancy parameter $\beta = 1$ is applied.

one of these extreme components, is widely regarded as ancient subducted oceanic crust: Tatsumi (2005) states that it has been reserved in the deep mantle for 2 Gyr since its subduction and has contributed to the heterogeneity through convective mixing. Such a long term evolution is favorable for the efficient mixing because subducted slabs can assimilate thermally into the surrounding mantle.

The dehydration process at the 660-km boundary demonstrated in this study would cause wide Pb isotopic ranges (Figures 26 and 30) within shorter period (about 100–200 Myr) by repeating dehydration/hydration of various degrees (i.e., 0 to 1 wt.%H_2O dehydration). The produced heterogeneity is released to the hotter mantle as well as the slab surface, allowing itself to be redistributed widely (detached from the cold slab). Such active chemical advection is consistent with the hypothesis that the mantle chemical heterogeneity has been produced within a supercontinental cycle (i.e., within several hundreds of Myr; Iwamori & Nakamura, 2015).

However, the fractionation process proposed here strongly depends on the bridgmanite water storage capacity, which is still controversial. The dehydration process well works if the capacity is smaller (e.g., $<$ 240 ppm; Panero et al., 2015). A noticeable topic is how much the slight aluminous bridgmanite with 8,000 ppmH_2O (Inoue et al., 2016) forms in the peridotitic composition. Dehydration experiments for trace element behavior at the uppermost lower mantle conditions are also expected. An experiment of MORB dehydration (Kessel et al., 2005) indicates that the hydrophilicity contrast between the daughter (Pb) and the parent (U or Th) becomes much smaller (or rather than reversed) under high temperature. The p-T- dependent $D^{\mathrm{sol/aq}}$ data will be helpful for discussing the lower mantle dehydration because its temperature range is wide (900–1500°C from the simulation).

4.2. Seismic observations of uppermost lower mantle

Here the author reviews two different cases on the 660-km dehydration processes, both of which are proposed by receiver function imaging beneath the United States and Japan, and discusses the possibility of further detection of similar signatures.

4.2.1. Penetrating slab beneath America

The position of the sub-660 "low" Ps/P anomalies observed by Schmandt et al. (2014) are consistent with a local "positive" P-wave velocity anomaly across the 660-km boundary around longitude 100°W beneath the United States imaged by a seismic tomography inversion by Sigloch et al. (2008). Sigloch et al. (2008) proposes that the penetrating high-velocity zone material is connected to the Cascadian trench, along the West Coast. If true, the downgoing rocks across the 660-km are hydrous because its origin is oceanic plate, supporting the possibility of water transportation simulated in this study. The sub-660 negative anomalies are distributed at the depth of ~700 km (Schmandt et al., 2014), and are consistent with the simulation result that the aqueous fluid is concentrated just below the 660-km and becomes less-concentrated as the slab descent (Figure 24). Moreover, the width of the detected sub-660 low velocity zone (about 500 km) is much larger than the typical oceanic slab thickness and is consistent with the lateral range of the hydrous ringwoodite piles over the 660-km reproduced in the simulation, implying the efficient zigzag water transportation (Figure 22, Subsection 3.1.4) is possible in nature. The depth of the slab tip is ~1500 km (Sigloch et al., 2008), and sufficient water to form such widespread water filter seems to have been supplied.

4.2.2. Stagnant slab beneath Japan to China

Liu et al. (2016) also discovers the low velocity anomaly beneath the Japan-China stagnant slab by the receiver function imaging. The observation implies that the patches of pre-existent hydrous wadsleyite or ringwoodite were pushed out into the lower mantle due to slab intrusion into the transition zone. High electrical conductivity of the transition zones in this area (Karato, 2011) supports this hypothesis. In this case, the low velocity jumps are distributed at the depth of ~770 km (Liu et al., 2016) and are consistent with the depression of the 660-km boundary owing to the stagnant slab. However, the low velocity anomalies are not universally distributed, and their formation seems to depend on the distribution the pre-existent hydrous transition zone minerals.

4.2.3. Expectation for signature of lower mantle dehydration

Thus the position, depth, and width of the sub-660 low velocity zone seem to be related to the slab geometry and subduction history. The sub-660 discontinuity seems much thin and may be detected in limited regions by using receiver function imaging. In order to judge whether detected low velocity anomalies are true of artificial, we should compare them with the structure of subducting slab obtained from tomographic results, i.e., near penetrating slabs and the base of stagnant slabs.

Schmandt et al. (2014) state that 0.68 to 1% partial melt (or silicic supercritical fluid) explains the shear velocity reduction induced by negative Ps conversions beneath the 660-km. Our simulation exhibits that the amount of water in hydrous ringwoodite is restricted by the choke point (Kawamoto et al., 1996), and is $\sim$2,000 ppmH_2O according to the employed phase diagram (Figure 16; Iwamori, 2007). Therefore, if the water storage capacity of the lower mantle is 0–1,000 ppm, the fraction of aqueous fluid generated due to ringwoodite dehydration is 0.1–0.2 wt.%, which seems impossible to be detected as such a remarkable signature. Therefore silica solution from lower mantle minerals into the supercritical fluid seems necessary for its observability. Large silica solubility is possible only in the hot surrounding mantle (i.e., where the horizontal zigzag process works), and the partial melting signature may be detectible with some distance from penetrating cold slabs.

Another hypothesis for the significant velocity reduction is that much hydrous pre-existent ringwoodite ($\sim$1 wt.%H_2O) before the stagnant slab intrusion causes significant aqueous fluid fraction due to its decomposition in the lower mantle. This hypothesis, however, requires the origin of the well-hydrated ringwoodite piles and a reason for their staying against their gravitational instability. In this case, the sub-660 low velocity anomalies are expected to be detected where high electrical conductivity is observed in the transition zone.

4.3. How does the 410-km boundary work?

4.3.1. 410-km melting proposed by experiments and seismology

The simulation has demonstrated that the 410-km boundary is not so influential on the global chemical heterogeneities (Section 3.7). However, solidus temperature just above the 410-km boundary is extremely lower than that of the transition zone (Kawamoto, 2004; Figure 16), and the wet plumes with much higher water content (about 1%) across the boundary may cause significant aqueous fluid generation and widespread partial melting. The density of the melt along the 410-km boundary is larger than that of the solid phase and smaller than that of the top of the transition zone mantle rocks (Sakamaki et al., 2006). Therefore the partial melt is gravitationally stable and is expected to exist as horizontal sheets just above the 410-km. Actually seismic observations by receiver functions suggest that such structures are more universally distributed, e.g., Tasman and

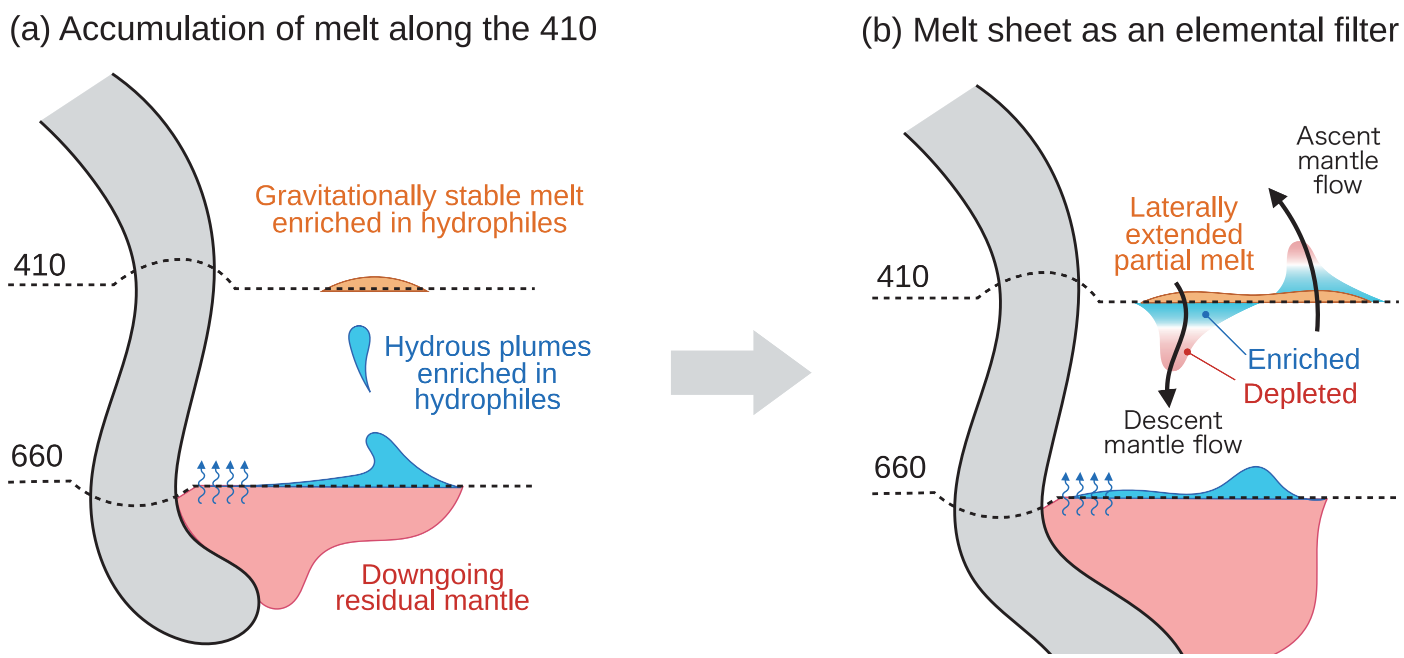

Figure 33: A schematic of a possible scenario if the partial melt is gravitationally stable in the lowermost transition zone (Sakamaki et al., 2006) in Section 4.3. (a) Wet plumes from the 660-km boundary (blue areas) are potent suppliers for the melt sheets (orange area) observed as low seismic velocity anomalies (e.g., Liu et al., 2016). (b) The hydrous dense melt extends horizontally along the 410-km. If the vertical flow of the solid phase go across the melt layer, incompatible trace elements are more partitioned into the melt phase, and the solid phase is depleted in the elements.

Coral Seas (Courtier & Revenaugh, 2007), Canada (Schaeffer & Bostock, 2010), Japan (Liu et al., 2016), and so on, compared to the sub-660 low velocity anomalies. Thus Bercovici & Karato (2003) predicted that the "transition zone water filter" has significant influences on the trace element partitioning.

4.3.2. Possible roles of 410-km melting as elemental filter

The wet plumes from the 660-km are a potent factor in the melt sheets (Figure 33a). If the wet plumes are trapped into them, the expansion of the hydrous rocks enriched in the hydrophilic elements would be limited. Or, contrary, the horizontal sheet may work as an efficient elemental filter for the ascending or descending mantle rocks as well as the 660-km (Figure 33b): If the induced vertical mantle flows across the laterally extended partial melt along the 410-km, incompatible or hydrophilic trace elements are extracted from the flowing rock phase into the partial melt phase, causing depleted residual rocks in a laterally wide range (red areas around the 410-km in Figure 33b). However, since the melt is originally much enriched in the incompatible elements due to the supply from the wet plumes from the 660-km, if the part of the melt is diminishing, finally the enriched rocks are produced (blue areas around the 410-km in Figure 33b) like the 660-km process as simulated.

By introducing solidus (or silica solubility in the supercritical fluid phase) and melt phase transportation into the simulation, the formation and stabiliry of the filter just above the transition zone and their effects on the chemical distribution should be inspected in the near future.

4.4. Possible scenario for the India-Himalaya collision

The 660-km dehydration process may efficiently work beneath the India-Himalaya collision belt. Although the tectonic history before the continental collision is somewhat controversial, several seismologists consider that older subducted Neo-Tethyan slab(s) is widely distributed in the lower mantle beneath India and now newer Neo-Tethyan slab is penetrating the 660-km phase boundary beneath the collision belt to islands in the southeast Asia (Van der Voo et al., 1999; Replumaz et al., 2004; Hafkenscheid et al., 2006). The discussion in this section is based on the plate history proposed by Stampfli & Borel (2004) and Hafkenscheid et al. (2006):

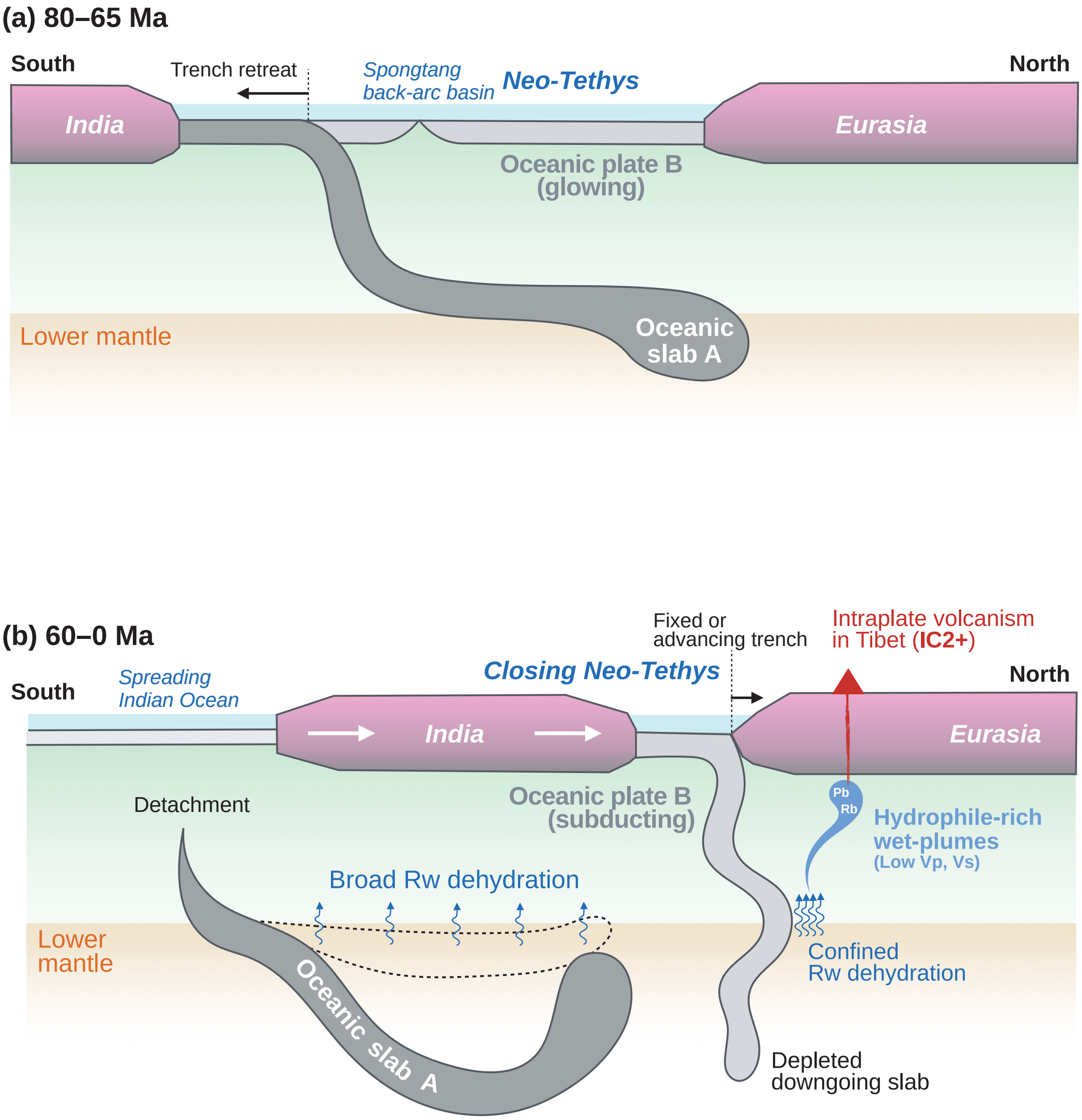

Figure 34: A possible plate-slab dynamics and chemical evolution around the India-Himalaya collision belt based on Hafkenscheid et al. (2006). Details are described in the main text in Section 4.4.

4.4.1. Tectonic history proposed previously

Around 100 Ma, an older Neo-Tethyan slab ('Oceanic slab A' in Figure 34) began subducting and correspondingly Indean Spontang Ocean opened due to the slab retreat. Thus the slab A was laterally extended over the transition zone (Figure 34a). Around 60 Ma, slab A was detached from the Indian continental plate. After that, slab A began sinking into the lower mantle. At the same time, newly generated Spongtang oceanic plate ('Oceanic plate B' in Figure 34) started to subduct near the Eurasian plate. The subduction of plate B caused the rapid northward migration of the Indian plate (Figure 34b). Then Neo-Tethys was closing, and finally the continents collided. While the sea was closing, Plate B vertically penetrated the 660-km phase boundary.

4.4.2. Dehydration patterns of Neo-Tethyan slabs

In this process, the collapse of slab A into the lower mantle would cause wide dehydration due to the decomposition of hydrous ringwoodite as simulated in run stg2. As water was not concentrated, hydrous piles did not grow well over the 660-km boundary and much water would sink into lower mantle with slab A. On the other hand, plate B is penetrating at the 660-km boundary: During continental collision, a trench is fixed or slightly advancing, and such a situation favors its slab penetration as discussed in Section 4.2 in Chapter II. Then the slab B is dehydrating in the limited area at the 660-km. Because of the confined water distribution, hydrous piles would grow enough to produce hydrous plume enriched in the hydrophilic components as simulated in run pnt1. Although the hydrous plumes from the 660-km would trapped over the 410-km boundary (Section 4.3), but much water supply would disturb the stability of the supercritical fluid sheets along the 410-km, causing further upwellings.

4.4.3. Cenozoic Tibetan volcanism

Actually the transition zone mantle around the penetrating young slab (plate B) seems to be observed as seismic low velocity anomalies that extend to Tibetan inter-continent volcanoes (Replumaz et al., 2004; Hafkenscheid et al., 2006), which are continuously active through the Cenozoic (Ding et al., 2003). Ding et al. (2003) attribute the post-collision volcanoes (17 Ma to present) in the Songpan-Ganzi terrane, northern Tibet, to induced hot asthenospheric mantle flows due to southward subduction of the Eurasian continental plate (Kind et al., 2002) or heating due to thinning of the continental lithosphere (Turner et al., 1996); however, they do not mention whether the heat source or fluid addition due to the "continent" subduction is sufficient for the partial melting under Songpan-Ganzi. Contrary the wet plume model of our simulation favors the active volcanism in terms of the sufficient volatile supply. Then the continental thinning (Turner et al., 1996) may also be important for the partial melting owing to the fluid addition. Consistently the Quaternary volcanic rocks in Tibet have high IC2+ value (i.e., highly re-hydrated signature) according to the independent component analysis (Iwamori & Nakamura, 2015).

Thus by interpreting results of the present simulation, we can relates both dynamic and chemical processes consistently.

4.5. Implication for global chemical heterogeneity

Here the author describes a possible scenario for the global chemical evolution for several billions of years on the basis of the numerical results.

4.5.1. Generation of heterogeneity: Continent gathering

Repeatedly IC2+, an independent component of the mantle isotopic composition indicating aqueous fluid addition, is distributed where once the supercontinent Pangea has formed (Iwamori & Nakamura, 2015). The mechanism to produce the hemispherical chemical structure is also explainable by the 660-km dehydration as well as the India-Himalaya region (Section 4.4).

While continents are gathering, considerable amount of oceanic slabs are subducting at the same time: inland sea plates and those around the supercontinent. Therefore much water would be transported beneath the supercontinent. In this situation, most trenches are advancing toward the center of the supercontinent. As discussed in Chapter II, the trench advance contributes to the slab penetration (Figure 14). In addition, the advancing oceanic slab induces positive dynamic pressure beneath the supercontinent as simulated in run r1b2 (Figure 11c) and Appendix B, preventing slab stagnation. In other words, in order to meet the equation of continuity for mantle rock flows beneath the super continent, massive downward mantle rocks equivalent to the influx of the advancing continent, slabs and underlying asthenosphere flow across the 660-km beneath the supercontinent in the gathering process. Then significant dehydration at the 660-km would progress, and IC2+ (hydrophile-rich) hydrous plumes ascend from there. The IC2+ plumes would circulate by the combined effects of its ascent due to hydrous buoyancy and the downward slab drag, contaminating the upper mantle beneath the supercontinent like Figure 32 (Section 3.7).

Chemical heterogeneities generated during the mantle wedge dehydration (e.g., extremely high U/Pb ratio) are not so widely distributed compared to those generated by the 660-km process and are menacingly coupled with subducting slabs. They sink into the great depth of the mantle and pile up at the bottom of the lower mantle for a long time (probably >1 Gyr) owing to their large density and viscosity. After the thermal assimilation into the surrounding mantle, the depleted crustal component would be advected again, causing the mantle component with a high Pb isotopic ratio, as proposed by Tatsumi (2005).

4.5.2. Welling up and mixing of heterogeneity: After supercontinent

Since the author does not simulate the latter stage of the elemental transportation, note that the following discussion includes much speculation.

While a supercontinent breaks up, the surrounding trenches tend to retreat because of the seaward motion of supercontinent fragments. Such plate geometry induces predominancy of global slab stagnation (Figure 11c, Appendix B). In other words, in order to meet the equation of continuity for mantle rock flows beneath the super continent, lateral outward (seaward) mantle flows should arises equivalent to massive upward mantle rocks filling up the gaps between the supercontinent fragments. Thus the oceanic slabs hardly penetrate beneath the separating supercontinent due to the predominance of negative dynamic pressure in the sub-continental mantle. In this era, therefore, the 660-km dehydration and the corresponding elemental fractionation are diminishing. Hydrophilic components once distributed commonly beneath Pangea have welled up from the transition zone in the upper mantle and Earth's surface and are now observed as enriched MORB and OIB (e.g., low Pb isotopic ratio) in the Indian Ocean ("Dupal anomaly" of Dupré & Allègre, 1983; Hart, 1984; or "IC2+ hemisphere" of Iwamori & Nakamura, 2015), along which Pangea has broken up.

4.5.3. Fractionation versus mixing

Since the generation rate of chemical heterogeneities is much small during and after the break up, simple mixing theories (Table 7) are useful for the chemical evolution in

Table 7: Mixing time estimation for Earth's mantle convection summarized by Tackley (2009).

Study	τ_{mix}	**Length scale**	**Note**	**Rescaled** τ_{mix}
Gurnis & Davies (1986)	2.4 Gyr	Visible clumps	Survival time of clumps	
Olson et al. (1984)	10 Gyr	Diffusion	Laminar stretching	
Christensen (1989)	1.5–2.0 Gyr	$\sim$100 m (1/50)	stretching of MORB	3–4 Gyr
Hoffman & McKenzie. (1985)	1.0 Gyr	3 km	$\eta_{\mathrm{LM}}/\eta_{\mathrm{UM}} = 3$	>3 Gyr
	1.5 Gyr	3 m	η increases with depth	
Kellogg & Turcotte (1990)	0.96 Gyr	Diffusive	50% homogenized	$\sim$3 Gyr

this stage. Our simulation exhibits that both depleted and enriched components are hydrous and buoyant. Although transportation of buoyant or dense materials is somewhat complicated, here we ignore the buoyancy effects because of their small density reduction ($d\rho/\rho = 0.01$–0.3%), because the well-hydrated transition zone minerals are unstable for a long time and soon decompose into hydrous olivine or hydrous bridgmanite due to its buoyant flows or slab-induced flows in our simulation. The mixing times for mantle convection estimated by theoretical and numerical background, e.g. laminar stretching of chemical heterogeneity until the fluid either can be homogenized by diffusion, is summarized in Table 7 (Tackley, 2009). Although the estimated values are diverse and strongly depend on the numerical settings, Tackley (2009) concludes that it requires 3–4 Gyr for stretching MORB (i.e., chemical heterogeneity with length scale of several km) to the sub-meter length scale.

On the other hand, a supercontinental cycle is about 0.6 Gyr (e.g., Nance et al., 2014), much smaller than the estimated mixing time; therefore, heterogeneity with the kilometer length scale seems to remain during one supercontinental cycle. For example, OIB samples of the South Polynesian islands have a large variety of IC2 in the limited range (around several to several tens kilometer; Iwamori & Nakamura, 2015). After Rodinia broke up (about 0.8 Gyr ago), the interior ocean closed again, and Pangea is formed (e.g. Li et al., 2008; "introversion", Murphy & Nance, 2003) without significant changes in the continent configuration. This plate history suggests that the hyrophilic heterogeneity generated beneath Rodinia remains to some extent (not disturbed) even in the Pangea re-gathering process. Indeed Iwamori & Nakamura (2012) consider IC2+ of Pacific OIBs to be related to fluid addition beneath Rodinia. Thus the present global heterogeneity observed as the Dupal anomaly (Dupré & Allègre, 1983; Hart, 1984) or the IC2+ hemisphere (Iwamori &

Nakamura, 2015) may be a result of at least two supercontinent processes.

Contrary “extroversion” of plate re-configuration (closure of the exterior ocean) may bring more disturbance of the heterogeneity. Since both introversion and extroversion are considered to have occurred in the past (e.g., Murphy & Nance, 2003), the present global hydrophilic heterogeneity may not be the summation (or accumulation) throughout the whole Earth’s history of 4.6 Gyr.

Chapter IV.

Integration of geodynamics and geochemistry in the future

Summary of the roles of hydrous weakening

This study has demonstrated that aqueous fluids released from the subducting slab cause plate segmentation during back-arc spreading by eroding the bottom of the continental plate (Section 3.2 in Chapter II). This segmentation and the resultant movable trench promotes efficient potential energy release of each oceanic slab, and rapid subduction occurs intermittently. Thus, the diverse characteristics of the subducting slab are reproduced (Section 4.2 in Chapter II). Slab wandering related to trench migration may contribute to the ascent of wet plumes enriched in hydrophilic elements (Section 3.7 in Chapter III), which indicates the importance of a free convection setup to evaluate the chemical evolution of the mantle. Hydrous weakening of the slab surface also helps detach fractionated components from the subducting slab and transport these components widely. Thus, viscosity reduction caused by hydration undoubtedly enhances subduction zone evolution and trace element circulation in the mantle.

Summary of the roles of hydrous buoyancy

Careful evaluation is required of the effects of density reduction from hydration on dynamics and chemistry. This density reduction effectively carries water and hydrophile heterogeneity from the deeper zones as a driving force of wet plumes (3.7 in Chapter III), whereas a buoyant mantle wedge prevents active subduction (i.e., slow trench retreat and corner flows; Section 3.3 in Chapter II). This conflict is strongly related to the amount of water in the rocks that can be transported into the mantle transition zone. Therefore, water distribution within the oceanic plate before subduction and the temperature structure of the subducting plate, both of which control the stability of hydrous minerals within the slab, influence the characteristics of the dynamics and chemistry of the subduction zone.

(Perspective 1) 3-D spherical modeling

In the future, it is expected that a 3-D spherical simulation with sufficiently high resolution will be able to resolve water transportation and related dynamics. Three-dimensionality is essential to represent slab dynamics including the subduction rate, slab geometry, and the occurrence of back-arc spreading (e.g., Schellart & Moresi, 2013); therefore, our conclusions, especially the conflict between mantle wedge flow and plume ascent, should be reevaluated in the future. Such a simulation may resolve the enigma of formation of the big mantle wedge (Zhao et al., 2009; Section 4.4 in Chapter II).

A 3-D spherical model is also important for generating patterns of chemical heterogeneity. It has been well established that such a simulation exhibits 2-D sheets of descent flows and 1-D plumes of ascent flows (e.g., Bercovici et al., 1989), which differ greatly from the flow pattern of a 2-D box model, in which descent and ascent are equivalent. In a 3-D setting, the 660-km zig-zag process (Subsection 3.1.4 in Chapter III) extends two-dimensionally, which causes 3-D generation of chemical heterogeneity, whereas the mantle wedge process causes 2-D distribution. In contrast, it should be investigated whether 1-D wet plumes from 660 km depth (Section 3.7 in Chapter III) are an important factor in the observed widespread hydrophilic enrichment in the upper mantle referred to as the Dupal or IC2+ anomaly (Dupré & Allègre, 1983; Hart, 1984; Iwamori & Nakamura, 2015). If not, more attention should be given to roles of the 410-km elemental filter (Bercovici & Karato, 2003; Section 4.3 in Chapter III), which also generates 3-D heterogeneity.

Moreover, 3-D flows enhance mixing of chemical components because the Lyapunov exponent, a quantity that characterizes the rate of separation of infinitesimally close trajectories, is much larger in 3-D because of toroidal motion (e.g., Ferrachat & Ricard, 1998), which makes flows more chaotic. Also of interest are how the mixing of chemical heterogeneities is affected by "introversion" and "extroversion" (Murphy & Nance, 2003) of supercontinental cycles in a 3-D spherical settings, and the stability of the global chemical structure.

(Perspective 2) Supercritical fluid composition

The amount of silica in lower mantle minerals that can be dissolved into supercritical fluid is also important. If the supercritical fluid is melt-like, we can apply the partition coefficient between lower mantle minerals and melt phases (e.g., Hirose et al., 2004; Section

2.3.3 in Chapter III). In addition, based on combining fluid composition data with the position and amplitude of the sub-660-km low-velocity anomaly (Schmandt et al., 2014; Liu et al., 2016), we further constrain water transportation mechanisms around 660 km depth (Section 4.2 in Chapter III). Melting behavior is also expected be introduced in future simulations to investigate the formation of the 410-km-depth melt sheets and their effects (Section4.3; Chapter III).

(Perspective 3) Paradigm shift from "continental drift"

Traditionally, continents have been regarded as floating on the Earth's surface following mantle convection ("continental drift"; e.g., Turcotte & Schubert, 2001). However, our simulation presented in Chapter II and Appendix B demonstrates that mantle convection, including oceanic slab subduction, is strongly affected by the rheological structure (i.e., the effects of hydration on both viscosity and yield strength) and motions of the overlying plate. Correspondingly, the generation patterns of hydrophilic components around 660 km are affected (Chapter III) by flow changes in the deep mantle. These results indicate that the continents should not be considered passive components in whole-mantle dynamics and geochemistry, and that supercontinental processes may control the input of oceanic slabs and volatiles to the deep mantle.

(Perspective 4) Integration of experiments, observation, and simulation

Laboratory experiments are essential for investigating aspects of both geodynamic and geochemical evolution, e.g., the water storage capacity of hydrous phases in the lower mantle, partition coefficients under lower mantle conditions, and state and constitutive parameters. In addition, detailed seismological observations focused on heterogeneity around the 660-km phase boundary (Schmandt et al., 2014; Liu et al., 2016) may contribute to constraining the scenario proposed in this study. Probing the ocean floor is also important to constrain water input into the deep mantle (e.g., the formation of phases A, D, and H). By combining progress in each of these research fields, we will better understand the multi-sphere system of the water planet.

Acknowledgements

The author would like to express the deepest appreciation to the supervisors; Dr. Hikaru Iwamori (Japan Agency for Marine-Earth Science and Technology; JAMSTEC) and Dr. Tomoeki Nakakuki (Hiroshima University) for their continuous and warm guidances, suggestions, discussions. The author is deeply grateful to the referees in Tokyo Tech; Dr. Jun-ichi Nakajima, Dr. Tetsuya Yokoyama, Dr. Yuichiro Ueno, and Dr. Kenji Ohta; for their thorough reading and valuable comments on this thesis. Present and previous members of Iwamori laboratory in Tokyo Tech and JAMSTEC; Dr. Hitomi Nakamura, Dr. Kenta Ueki, Dr. Takeshi Matsuyama, and other colleagues; are also greatly appreciated. Chapter II was improved through the constructive peer review of Nakao et al. (2016) provided by Dr. Bruce A. Buffett (editor of *Earth and Planetary Science Letters*), Dr. Hana Čížková (Charles University Prague), and an anonymous reviewer. Numerical simulations were conducted by TSUBAME 2.5 of Tokyo Tech and JAMSTEC SC System. Some figures were produced using Generic Mapping Tools (Wessel & Smith, 1998). This work was supported by JSPS KAKENHI Grant Number 26010035.

Appendix A: Discretization of equation of motion

The equation of motion in the main text (Equation 1),

$$\left(\frac{\partial^2}{\partial x^2}-\frac{\partial^2}{\partial z^2}\right)\left[\eta\left(\frac{\partial^2\psi}{\partial x^2}-\frac{\partial^2\psi}{\partial z^2}\right)\right]+4\frac{\partial^2}{\partial x\partial z}\left(\eta\frac{\partial^2\psi}{\partial x\partial z}\right)=\frac{\partial\rho}{\partial x}g,$$

is discretized by a finite volume method after nondimensionalization in order to solve the stream function ψ. Because the discretized equation is linear, the simultaneous equations for all n nodes in the model domain can be expressed by using a coefficient matrix A ($n \times n$; known), a stream function vector $\mathbf{\Psi}$ ($n \times 1$; unknown), and a buoyancy term vector $\mathbf{B}$ ($n \times 1$; known) as

$$A\mathbf{\Psi}=\mathbf{B}. \tag{41}$$

Because the matrix A is symmetric, the modified Cholesky decomposition algorithm can be applied for solving $\mathbf{\Psi}$. The matrix (41) for 5×5 nodes around (i, j) as shown in Figure 35 (i.e., 25 simultaneous equations with 25 unknown parameters ψ), for example, can be written as follows:

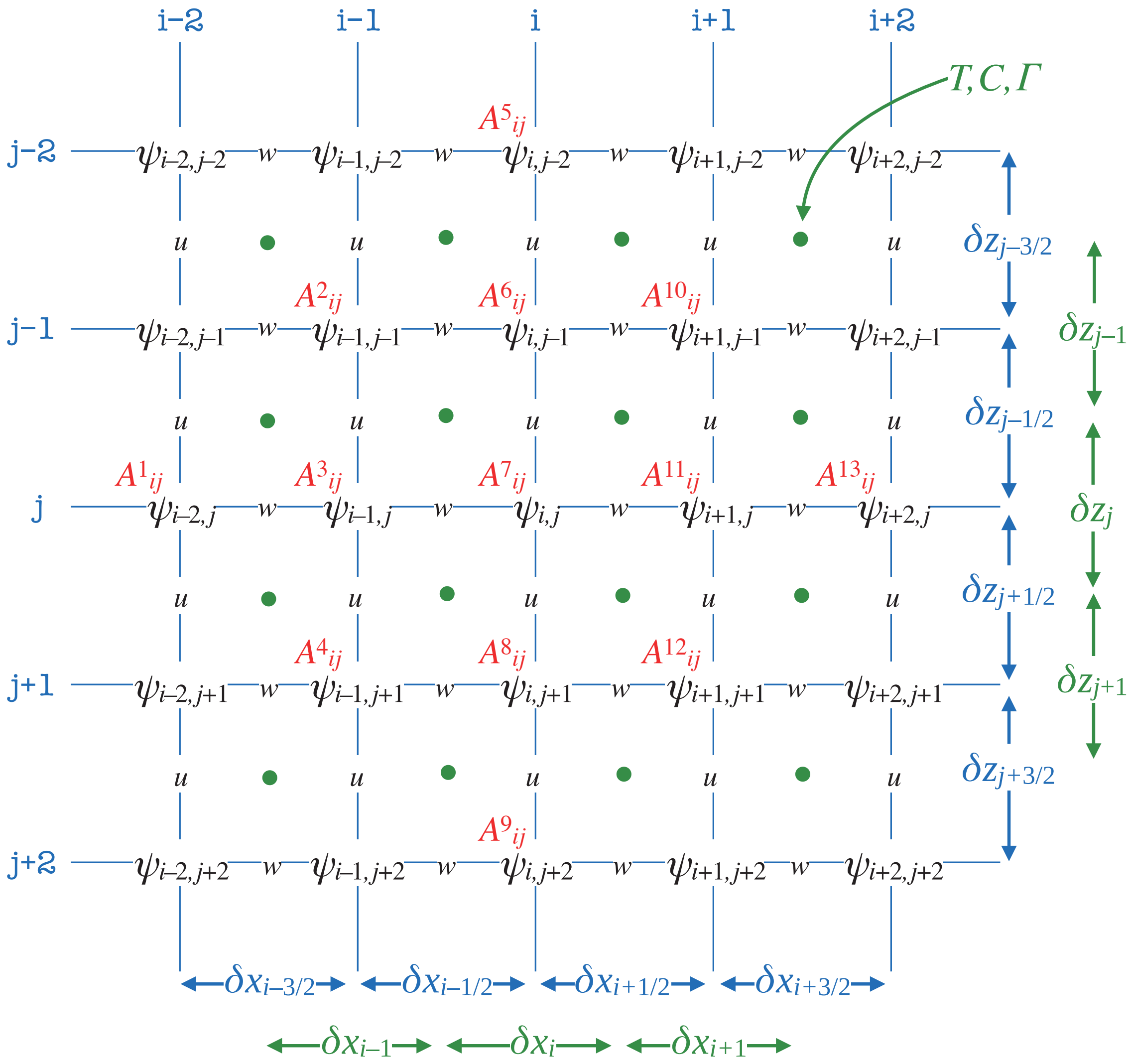

Figure 35: Staggered grid for discretizing the equation of motion.

$$
\left(\begin{matrix}
A^{7}_{i-2,j-2} & A^{8}_{i-2,j-2} & A^{9}_{i-2,j-2} & 0 & 0 & A^{11}_{i-2,j-2} & A^{12}_{i-2,j-2} & 0 \\
A^{6}_{i-2,j-1} & A^{7}_{i-2,j-1} & A^{8}_{i-2,j-1} & A^{9}_{i-2,j-1} & 0 & A^{10}_{i-2,j-1} & A^{11}_{i-2,j-1} & A^{12}_{i-2,j-1} \\
A^{5}_{i-2,j} & A^{6}_{i-2,j} & A^{7}_{i-2,j} & A^{8}_{i-2,j} & A^{9}_{i-2,j} & 0 & A^{10}_{i-2,j} & A^{11}_{i-2,j} \\
0 & A^{5}_{i-2,j+1} & A^{6}_{i-2,j+1} & A^{7}_{i-2,j+1} & A^{8}_{i-2,j+1} & 0 & 0 & A^{10}_{i-2,j+1} \\
0 & 0 & A^{5}_{i-2,j+2} & A^{6}_{i-2,j+2} & A^{7}_{i-2,j+2} & 0 & 0 & 0 \\
A^{3}_{i-1,j-2} & A^{4}_{i-1,j-2} & 0 & 0 & 0 & A^{7}_{i-1,j-2} & A^{8}_{i-1,j-2} & A^{9}_{i-1,j-2} \\
A^{2}_{i-1,j-1} & A^{3}_{i-1,j-1} & A^{4}_{i-1,j-1} & 0 & 0 & A^{6}_{i-1,j-1} & A^{7}_{i-1,j-1} & A^{8}_{i-1,j-1} \\
0 & A^{2}_{i-1,j} & A^{3}_{i-1,j} & A^{4}_{i-1,j} & 0 & A^{5}_{i-1,j} & A^{6}_{i-1,j} & A^{7}_{i-1,j} \\
0 & 0 & A^{2}_{i-1,j+1} & A^{3}_{i-1,j+1} & A^{4}_{i-1,j+1} & 0 & A^{5}_{i-1,j+1} & A^{6}_{i-1,j+1} \\
0 & 0 & 0 & A^{2}_{i-1,j+2} & A^{3}_{i-1,j+2} & 0 & 0 & A^{5}_{i-1,j+2} \\
A^{1}_{i,j-2} & 0 & 0 & 0 & 0 & A^{3}_{i,j-2} & A^{4}_{i,j-2} & 0 \\
0 & A^{1}_{i,j-1} & 0 & 0 & 0 & A^{2}_{i,j-1} & A^{3}_{i,j-1} & A^{4}_{i,j-1} \\
0 & 0 & A^{1}_{i,j} & 0 & 0 & 0 & A^{2}_{i,j} & A^{3}_{i,j} \\
0 & 0 & 0 & A^{1}_{i,j+1} & 0 & 0 & 0 & A^{2}_{i,j+1} \\
0 & 0 & 0 & 0 & A^{1}_{i,j+2} & 0 & 0 & 0 \\
0 & 0 & 0 & 0 & 0 & A^{1}_{i+1,j-2} & 0 & 0 \\
0 & 0 & 0 & 0 & 0 & 0 & A^{1}_{i+1,j-1} & 0 \\
0 & 0 & 0 & 0 & 0 & 0 & 0 & A^{1}_{i+1,j} \\
0 & 0 & 0 & 0 & 0 & 0 & 0 & 0 \\
0 & 0 & 0 & 0 & 0 & 0 & 0 & 0 \\
0 & 0 & 0 & 0 & 0 & 0 & 0 & 0 \\
0 & 0 & 0 & 0 & 0 & 0 & 0 & 0 \\
0 & 0 & 0 & 0 & 0 & 0 & 0 & 0 \\
0 & 0 & 0 & 0 & 0 & 0 & 0 & 0 \\
0 & 0 & 0 & 0 & 0 & 0 & 0 & 0
\end{matrix}\right.
$$

$$
\begin{array}{ccccccccc}
0 & 0 & A^{13}_{i-2,j-2} & 0 & 0 & 0 & 0 & 0 & 0 \\
0 & 0 & 0 & A^{13}_{i-2,j-1} & 0 & 0 & 0 & 0 & 0 \\
A^{12}_{i-2,j} & 0 & 0 & 0 & A^{13}_{i-2,j} & 0 & 0 & 0 & 0 \\
A^{11}_{i-2,j+1} & A^{12}_{i-2,j+1} & 0 & 0 & 0 & A^{13}_{i-2,j+1} & 0 & 0 & 0 \\
A^{10}_{i-2,j+2} & A^{11}_{i-2,j+2} & 0 & 0 & 0 & 0 & A^{13}_{i-2,j+2} & 0 & 0 \\
0 & 0 & A^{11}_{i-1,j-2} & A^{12}_{i-1,j-2} & 0 & 0 & 0 & A^{13}_{i-1,j-2} & 0 \\
A^{9}_{i-1,j-1} & 0 & A^{10}_{i-1,j-1} & A^{11}_{i-1,j-1} & A^{12}_{i-1,j-1} & 0 & 0 & 0 & A^{13}_{i-1,j-1} \\
A^{8}_{i-1,j} & A^{9}_{i-1,j} & 0 & A^{10}_{i-1,j} & A^{11}_{i-1,j} & A^{12}_{i-1,j} & 0 & 0 & 0 \\
A^{7}_{i-1,j+1} & A^{8}_{i-1,j+1} & 0 & 0 & A^{10}_{i-1,j+1} & A^{11}_{i-1,j+1} & A^{12}_{i-1,j+1} & 0 & 0 \\
A^{6}_{i-1,j+2} & A^{7}_{i-1,j+2} & 0 & 0 & 0 & A^{10}_{i-1,j+2} & A^{11}_{i-1,j+2} & 0 & 0 \\
0 & 0 & A^{7}_{i,j-2} & A^{8}_{i,j-2} & A^{9}_{i,j-2} & 0 & 0 & A^{11}_{i,j-2} & A^{12}_{i,j-2} \\
0 & 0 & A^{6}_{i,j-1} & A^{7}_{i,j-1} & A^{8}_{i,j-1} & A^{9}_{i,j-1} & 0 & A^{10}_{i,j-1} & A^{11}_{i,j-1} \\
A^{4}_{i,j} & 0 & A^{5}_{i,j} & A^{6}_{i,j} & A^{7}_{i,j} & A^{8}_{i,j} & A^{9}_{i,j} & 0 & A^{10}_{i,j} \\
A^{3}_{i,j+1} & A^{4}_{i,j+1} & 0 & A^{5}_{i,j+1} & A^{6}_{i,j+1} & A^{7}_{i,j+1} & A^{8}_{i,j+1} & 0 & 0 \\
A^{2}_{i,j+2} & A^{3}_{i,j+2} & 0 & 0 & A^{5}_{i,j+2} & A^{6}_{i,j+2} & A^{7}_{i,j+2} & 0 & 0 \\
0 & 0 & A^{3}_{i+1,j-2} & A^{4}_{i+1,j-2} & 0 & 0 & 0 & A^{7}_{i+1,j-2} & A^{8}_{i+1,j-2} \\
0 & 0 & A^{2}_{i+1,j-1} & A^{3}_{i+1,j-1} & A^{4}_{i+1,j-1} & 0 & 0 & A^{6}_{i+1,j-1} & A^{7}_{i+1,j-1} \\
0 & 0 & 0 & A^{2}_{i+1,j} & A^{3}_{i+1,j} & A^{4}_{i+1,j} & 0 & A^{5}_{i+1,j} & A^{6}_{i+1,j} \\
A^{1}_{i+1,j+1} & 0 & 0 & 0 & A^{2}_{i+1,j+1} & A^{3}_{i+1,j+1} & A^{4}_{i+1,j+1} & 0 & A^{5}_{i+1,j+1} \\
0 & A^{1}_{i+1,j+2} & 0 & 0 & 0 & A^{2}_{i+1,j+2} & A^{3}_{i+1,j+2} & 0 & 0 \\
0 & 0 & A^{1}_{i+2,j-2} & 0 & 0 & 0 & 0 & A^{3}_{i+2,j-2} & A^{4}_{i+2,j-2} \\
0 & 0 & 0 & A^{1}_{i+2,j-1} & 0 & 0 & 0 & A^{2}_{i+2,j-1} & A^{3}_{i+2,j-1} \\
0 & 0 & 0 & 0 & A^{1}_{i+2,j} & 0 & 0 & 0 & A^{2}_{i+2,j} \\
0 & 0 & 0 & 0 & 0 & A^{1}_{i+2,j+1} & 0 & 0 & 0 \\
0 & 0 & 0 & 0 & 0 & 0 & A^{1}_{i+2,j+2} & 0 & 0
\end{array}
$$

$$
\left.\begin{matrix}
0 & 0 & 0 & 0 & 0 & 0 & 0 & 0 \\
0 & 0 & 0 & 0 & 0 & 0 & 0 & 0 \\
0 & 0 & 0 & 0 & 0 & 0 & 0 & 0 \\
0 & 0 & 0 & 0 & 0 & 0 & 0 & 0 \\
0 & 0 & 0 & 0 & 0 & 0 & 0 & 0 \\
0 & 0 & 0 & 0 & 0 & 0 & 0 & 0 \\
0 & 0 & 0 & 0 & 0 & 0 & 0 & 0 \\
A^{13}_{i-1,j} & 0 & 0 & 0 & 0 & 0 & 0 & 0 \\
0 & A^{13}_{i-1,j+1} & 0 & 0 & 0 & 0 & 0 & 0 \\
0 & 0 & A^{13}_{i-1,j+2} & 0 & 0 & 0 & 0 & 0 \\
0 & 0 & 0 & A^{13}_{i,j-2} & 0 & 0 & 0 & 0 \\
A^{12}_{i,j-1} & 0 & 0 & 0 & A^{13}_{i,j-1} & 0 & 0 & 0 \\
A^{11}_{i,j} & A^{12}_{i,j} & 0 & 0 & 0 & A^{13}_{i,j} & 0 & 0 \\
A^{10}_{i,j+1} & A^{11}_{i,j+1} & A^{12}_{i,j+1} & 0 & 0 & 0 & A^{13}_{i,j+1} & 0 \\
0 & A^{10}_{i,j+2} & A^{11}_{i,j+2} & 0 & 0 & 0 & 0 & A^{13}_{i,j+2} \\
A^{9}_{i+1,j-2} & 0 & 0 & A^{11}_{i+1,j-2} & A^{12}_{i+1,j-2} & 0 & 0 & 0 \\
A^{8}_{i+1,j-1} & A^{9}_{i+1,j-1} & 0 & A^{10}_{i+1,j-1} & A^{11}_{i+1,j-1} & A^{12}_{i+1,j-1} & 0 & 0 \\
A^{7}_{i+1,j} & A^{8}_{i+1,j} & A^{9}_{i+1,j} & 0 & A^{10}_{i+1,j} & A^{11}_{i+1,j} & A^{12}_{i+1,j} & 0 \\
A^{6}_{i+1,j+1} & A^{7}_{i+1,j+1} & A^{8}_{i+1,j+1} & 0 & 0 & A^{10}_{i+1,j+1} & A^{11}_{i+1,j+1} & A^{12}_{i+1,j+1} \\
A^{5}_{i+1,j+2} & A^{6}_{i+1,j+2} & A^{7}_{i+1,j+2} & 0 & 0 & 0 & A^{10}_{i+1,j+2} & A^{11}_{i+1,j+2} \\
0 & 0 & 0 & A^{7}_{i+2,j-2} & A^{8}_{i+2,j-2} & A^{9}_{i+2,j-2} & 0 & 0 \\
A^{4}_{i+2,j-1} & 0 & 0 & A^{6}_{i+2,j-1} & A^{7}_{i+2,j-1} & A^{8}_{i+2,j-1} & A^{9}_{i+2,j-1} & 0 \\
A^{3}_{i+2,j} & A^{4}_{i+2,j} & 0 & A^{5}_{i+2,j} & A^{6}_{i+2,j} & A^{7}_{i+2,j} & A^{8}_{i+2,j} & A^{9}_{i+2,j} \\
A^{2}_{i+2,j+1} & A^{3}_{i+2,j+1} & A^{4}_{i+2,j+1} & 0 & A^{5}_{i+2,j+1} & A^{6}_{i+2,j+1} & A^{7}_{i+2,j+1} & A^{8}_{i+2,j+1} \\
0 & A^{2}_{i+2,j+2} & A^{3}_{i+2,j+2} & 0 & 0 & A^{5}_{i+2,j+2} & A^{6}_{i+2,j+2} & A^{7}_{i+2,j+2}
\end{matrix}\right)
$$

$$\times \begin{pmatrix} \psi_{i-2,j-2} \\ \psi_{i-2,j-1} \\ \psi_{i-2,j} \\ \psi_{i-2,j+1} \\ \psi_{i-2,j+2} \\ \psi_{i-1,j-2} \\ \psi_{i-1,j-1} \\ \psi_{i-1,j} \\ \psi_{i-1,j+1} \\ \psi_{i-1,j+2} \\ \psi_{i,j-2} \\ \psi_{i,j-1} \\ \psi_{i,j} \\ \psi_{i,j+1} \\ \psi_{i,j+2} \\ \psi_{i+1,j-2} \\ \psi_{i+1,j-1} \\ \psi_{i+1,j} \\ \psi_{i+1,j+1} \\ \psi_{i+1,j+2} \\ \psi_{i+2,j-2} \\ \psi_{i+2,j-1} \\ \psi_{i+2,j} \\ \psi_{i+2,j+1} \\ \psi_{i+2,j+2} \end{pmatrix} = \begin{pmatrix} B_{i-2,j-2} \\ B_{i-2,j-1} \\ B_{i-2,j} \\ B_{i-2,j+1} \\ B_{i-2,j+2} \\ B_{i-1,j-2} \\ B_{i-1,j-1} \\ B_{i-1,j} \\ B_{i-1,j+1} \\ B_{i-1,j+2} \\ B_{i,j-2} \\ B_{i,j-1} \\ B_{i,j} \\ B_{i,j+1} \\ B_{i,j+2} \\ B_{i+1,j-2} \\ B_{i+1,j-1} \\ B_{i+1,j} \\ B_{i+1,j+1} \\ B_{i+1,j+2} \\ B_{i+2,j-2} \\ B_{i+2,j-1} \\ B_{i+2,j} \\ B_{i+2,j+1} \\ B_{i+2,j+2} \end{pmatrix} \qquad (42)$$

where

$$A^1_{i,j} = \frac{\eta_{i-1,j}\delta z_j}{\delta x_{i-\frac{1}{2}}\delta x_{i-1}\delta x_{i-\frac{3}{2}}} \qquad (43)$$

$$A^2_{i,j} = \frac{4\eta_{i-\frac{1}{2},j-\frac{1}{2}} - \eta_{i-1,j} - \eta_{i,j-1}}{\delta x_{i-\frac{1}{2}}\delta z_{j-\frac{1}{2}}} \qquad (44)$$

$$A^3_{i,j} = -\frac{4\eta_{i-\frac{1}{2},j-\frac{1}{2}}}{\delta x_{i-\frac{1}{2}}\delta z_{j-\frac{1}{2}}} - \frac{4\eta_{i-\frac{1}{2},j+\frac{1}{2}}}{\delta x_{i-\frac{1}{2}}\delta z_{j+\frac{1}{2}}}$$

$$
\begin{aligned}
& - \quad \frac{\eta_{i-1,j}}{\delta x_{i-\frac{1}{2}}}\left[\left(\frac{1}{\delta x_{i-\frac{3}{2}}}+\frac{1}{\delta x_{i-\frac{1}{2}}}\right)\frac{\delta z_j}{\delta x_{i-1}}-\left(\frac{1}{\delta z_{j-\frac{1}{2}}}+\frac{1}{\delta z_{j+\frac{1}{2}}}\right)\right] \\
& - \quad \frac{\eta_{i,j}}{\delta x_{i-\frac{1}{2}}}\left[\left(\frac{1}{\delta x_{i-\frac{1}{2}}}+\frac{1}{\delta x_{i+\frac{1}{2}}}\right)\frac{\delta z_j}{\delta x_{i}}-\left(\frac{1}{\delta z_{j-\frac{1}{2}}}+\frac{1}{\delta z_{j+\frac{1}{2}}}\right)\right] \qquad (45)\\
A^4_{i,j} &= \frac{4\eta_{i-\frac{1}{2},j+\frac{1}{2}}-\eta_{i-1,j}-\eta_{i,j+1}}{\delta x_{i-\frac{1}{2}}\delta z_{j+\frac{1}{2}}} \qquad (46)\\
A^5_{i,j} &= \frac{\eta_{i,j-1}\delta x_i}{\delta z_{j-\frac{1}{2}}\delta z_{j-1}\delta z_{j-\frac{3}{2}}} \qquad (47)\\
A^6_{i,j} &= -\frac{4\eta_{i-\frac{1}{2},j-\frac{1}{2}}}{\delta x_{i-\frac{1}{2}}\delta z_{j-\frac{1}{2}}}-\frac{4\eta_{i+\frac{1}{2},j-\frac{1}{2}}}{\delta x_{i+\frac{1}{2}}\delta z_{j-\frac{1}{2}}} \\
& - \quad \frac{\eta_{i,j-1}}{\delta z_{j-\frac{1}{2}}}\left[\left(\frac{1}{\delta z_{j-\frac{3}{2}}}+\frac{1}{\delta z_{j-\frac{1}{2}}}\right)\frac{\delta x_i}{\delta z_{j-1}}-\left(\frac{1}{\delta x_{i-\frac{1}{2}}}+\frac{1}{\delta x_{i+\frac{1}{2}}}\right)\right] \\
& - \quad \frac{\eta_{i,j}}{\delta z_{j-\frac{1}{2}}}\left[\left(\frac{1}{\delta z_{j-\frac{1}{2}}}+\frac{1}{\delta z_{j+\frac{1}{2}}}\right)\frac{\delta x_i}{\delta z_{j}}-\left(\frac{1}{\delta x_{i-\frac{1}{2}}}+\frac{1}{\delta x_{i+\frac{1}{2}}}\right)\right] \qquad (48)\\
A^7_{i,j} &= \frac{\eta_{i-1,j}\delta z_j}{(\delta x_{i-\frac{1}{2}})^2\delta x_{i-1}}+\frac{\eta_{i+1,j}\delta z_j}{(\delta x_{i+\frac{1}{2}})^2\delta x_{i+1}}+\frac{\eta_{i,j-1}\delta x_i}{(\delta z_{j-\frac{1}{2}})^2\delta z_{j-1}}+\frac{\eta_{i,j+1}\delta x_i}{(\delta z_{j+\frac{1}{2}})^2\delta z_{j+1}} \\
& + \quad \frac{4\eta_{i-\frac{1}{2},j-\frac{1}{2}}}{\delta x_{i-\frac{1}{2}}\delta z_{j-\frac{1}{2}}}+\frac{4\eta_{i-\frac{1}{2},j+\frac{1}{2}}}{\delta x_{i-\frac{1}{2}}\delta z_{j+\frac{1}{2}}}+\frac{4\eta_{i+\frac{1}{2},j-\frac{1}{2}}}{\delta x_{i+\frac{1}{2}}\delta z_{j-\frac{1}{2}}}+\frac{4\eta_{i+\frac{1}{2},j+\frac{1}{2}}}{\delta x_{i+\frac{1}{2}}\delta z_{j+\frac{1}{2}}} \\
& + \quad \eta_{i,j}\left[\left(\frac{1}{\delta z_{j-\frac{1}{2}}}+\frac{1}{\delta z_{j+\frac{1}{2}}}\right)\frac{\delta x_i}{\delta z_j}-\left(\frac{1}{\delta x_{i-\frac{1}{2}}}+\frac{1}{\delta x_{i+\frac{1}{2}}}\right)\right]\left(\frac{1}{\delta z_{j-\frac{1}{2}}}+\frac{1}{\delta z_{j+\frac{1}{2}}}\right) \\
& + \quad \eta_{i,j}\left[\left(\frac{1}{\delta x_{i-\frac{1}{2}}}+\frac{1}{\delta x_{i+\frac{1}{2}}}\right)\frac{\delta z_j}{\delta x_i}-\left(\frac{1}{\delta z_{j-\frac{1}{2}}}+\frac{1}{\delta z_{j+\frac{1}{2}}}\right)\right]\left(\frac{1}{\delta x_{i-\frac{1}{2}}}+\frac{1}{\delta x_{i+\frac{1}{2}}}\right) \qquad (49)\\
A^8_{i,j} &= A^6_{i,j+1} \\
&= -\frac{4\eta_{i-\frac{1}{2},j+\frac{1}{2}}}{\delta x_{i-\frac{1}{2}}\delta z_{j+\frac{1}{2}}}-\frac{4\eta_{i+\frac{1}{2},j+\frac{1}{2}}}{\delta x_{i+\frac{1}{2}}\delta z_{j+\frac{1}{2}}} \\
& - \quad \frac{\eta_{i,j}}{\delta z_{j+\frac{1}{2}}}\left[\left(\frac{1}{\delta z_{j-\frac{1}{2}}}+\frac{1}{\delta z_{j+\frac{1}{2}}}\right)\frac{\delta x_i}{\delta z_{j}}-\left(\frac{1}{\delta x_{i-\frac{1}{2}}}+\frac{1}{\delta x_{i+\frac{1}{2}}}\right)\right] \\
& - \quad \frac{\eta_{i,j+1}}{\delta z_{j+\frac{1}{2}}}\left[\left(\frac{1}{\delta z_{j+\frac{1}{2}}}+\frac{1}{\delta z_{j+\frac{3}{2}}}\right)\frac{\delta x_i}{\delta z_{j+1}}-\left(\frac{1}{\delta x_{i-\frac{1}{2}}}+\frac{1}{\delta x_{i+\frac{1}{2}}}\right)\right] \qquad (50)\\
A^9_{i,j} &= A^5_{i,j+2} = \frac{\eta_{i,j+1}\delta x_i}{\delta z_{j+\frac{1}{2}}\delta z_{j+1}\delta z_{j+\frac{3}{2}}} \qquad (51)
\end{aligned}
$$

$$
\begin{aligned}
A^{10}_{i,j} &= A^{4}_{i+1,j-1} = \frac{4\eta_{i+\frac{1}{2},j-\frac{1}{2}} - \eta_{i+1,j} - \eta_{i,j-1}}{\delta x_{i+\frac{1}{2}} \delta z_{j-\frac{1}{2}}} &(52)\\
A^{11}_{i,j} &= A^{3}_{i+1,j} \\
&= -\frac{4\eta_{i+\frac{1}{2},j-\frac{1}{2}}}{\delta x_{i+\frac{1}{2}} \delta z_{j-\frac{1}{2}}} - \frac{4\eta_{i+\frac{1}{2},j+\frac{1}{2}}}{\delta x_{i+\frac{1}{2}} \delta z_{j+\frac{1}{2}}} \\
&- \frac{\eta_{i,j}}{\delta x_{i+\frac{1}{2}}} \left[\left(\frac{1}{\delta x_{i-\frac{1}{2}}} + \frac{1}{\delta x_{i+\frac{1}{2}}} \right) \frac{\delta z_j}{\delta x_i} - \left(\frac{1}{\delta z_{j-\frac{1}{2}}} + \frac{1}{\delta z_{j+\frac{1}{2}}} \right) \right] \\
&- \frac{\eta_{i+1,j}}{\delta x_{i+\frac{1}{2}}} \left[\left(\frac{1}{\delta x_{i+\frac{1}{2}}} + \frac{1}{\delta x_{i+\frac{3}{2}}} \right) \frac{\delta z_j}{\delta x_{i+1}} - \left(\frac{1}{\delta z_{j-\frac{1}{2}}} + \frac{1}{\delta z_{j+\frac{1}{2}}} \right) \right] &(53)\\
A^{12}_{i,j} &= A^{2}_{i+1,j+1} = \frac{4\eta_{i+\frac{1}{2},j+\frac{1}{2}} - \eta_{i+1,j} - \eta_{i,j+1}}{\delta x_{i+\frac{1}{2}} \delta z_{j+\frac{1}{2}}} &(54)\\
A^{13}_{i,j} &= A^{1}_{i+2,j} = \frac{\eta_{i+1,j} \delta z_j}{\delta x_{i+\frac{1}{2}} \delta x_{i+1} \delta x_{i+\frac{3}{2}}} &(55)\\
B_{i,j} &= -\frac{\mathrm{Ra}_T}{2} \left[\left(T_{i+\frac{1}{2},j-\frac{1}{2}} - T_{i-\frac{1}{2},j-\frac{1}{2}} \right) \delta z_{j-\frac{1}{2}} \right. \\
&\qquad \left. + \left(T_{i+\frac{1}{2},j+\frac{1}{2}} - T_{i-\frac{1}{2},j+\frac{1}{2}} \right) \delta z_{j+\frac{1}{2}} \right] \\
&\quad -\frac{\mathrm{Rb}_W}{2} \left[\left(C_{\mathrm{H_2O}i+\frac{1}{2},j-\frac{1}{2}} - C_{\mathrm{H_2O}i-\frac{1}{2},j-\frac{1}{2}} \right) \delta z_{j-\frac{1}{2}} \right. \\
&\qquad \left. + \left(C_{\mathrm{H_2O}i+\frac{1}{2},j+\frac{1}{2}} - C_{\mathrm{H_2O}i-\frac{1}{2},j+\frac{1}{2}} \right) \delta z_{j+\frac{1}{2}} \right] + \quad \cdots\cdots &(56)\\
\mathrm{Ra}_T &= \frac{\rho_0 \alpha \Delta T g h^3}{\eta_0 \kappa} &(57)\\
\mathrm{Rb}_W &= \frac{\rho_0 \beta g h^3}{\eta_0 \kappa} &(58)
\end{aligned}
$$

$\delta x_{i+\frac{1}{2}}$ is a lateral grid spacing beween i-th and $(i+1)$-th nodes. $\delta z_{j+\frac{1}{2}}$ is a vertical grid spacing beween j-th and $(j+1)$-th nodes. $\eta_{i,j}$, located at both the nodes and the centers of the control volumes, is dimensionless viscosity at (i,j). $T_{i+\frac{1}{2},j+\frac{1}{2}}$ and $C_{\mathrm{H_2O}i+\frac{1}{2},j+\frac{1}{2}}$ is dimensionless temperature and water content at the center of the control volumes $(i+\frac{1}{2}, j+\frac{1}{2})$ to calculate the buoyancy terms, respectively. $\kappa = k/(\rho_0 C_p)$ is thermal diffusivity. ΔT is temperature difference between the top and the bottom of the fluid layer with the thickness h. η_0 is reference viscosity.

Appendix B: Influences of "external forces" on subduction mode

How to involve artificail velocity

Here, the author notes a way to involve artificial velocity in the model domain for the forced convection. In following, symbols are the same as those in Appendix A and Figure 35. As shown in Equation (2), stream function is defined as

$$\boldsymbol{v} = (u, w) \equiv \left(\frac{\partial \psi}{\partial z}, -\frac{\partial \psi}{\partial x} \right),$$

and can be discriminated as

$$u_{i,j-\frac{1}{2}} = \frac{\psi_{i,j} - \psi_{i,j-1}}{\delta z_{j-\frac{1}{2}}} \tag{59}$$

$$w_{i-\frac{1}{2},j} = -\frac{\psi_{i,j} - \psi_{i-1,j}}{\delta x_{i-\frac{1}{2}}}. \tag{60}$$

These equations can be deformed into

$$A^6_{i,j}\psi_{i,j-1} = A^6_{i,j}\psi_{i,j} - \delta z_{j-\frac{1}{2}} u_{i,j-\frac{1}{2}} A^6_{i,j} \qquad \text{for} \quad (i,j) \tag{61}$$

$$A^8_{i,j-1}\psi_{i,j} = A^8_{i,j-1}\psi_{i-1,j} + \delta z_{j-\frac{1}{2}} u_{i,j-\frac{1}{2}} A^8_{i,j-1} \qquad \text{for} \quad (i,j-1) \tag{62}$$

$$A^3_{i,j}\psi_{i-1,j} = A^3_{i,j}\psi_{i,j} + \delta x_{i-\frac{1}{2}} w_{i-\frac{1}{2},j} A^3_{i,j} \qquad \text{for} \quad (i,j) \tag{63}$$

$$A^{11}_{i-1,j}\psi_{i,j} = A^{11}_{i-1,j}\psi_{i-1,j} - \delta x_{i-\frac{1}{2}} w_{i-\frac{1}{2},j} A^{11}_{i-1,j} \qquad \text{for} \quad (i-1,j). \tag{64}$$

By substituting the right sides of Equations (61) to (64) for $A^6_{i,j}\psi_{i,j-1}$, $A^8_{i,j-1}\psi_{i,j}$, $A^3_{i,j}\psi_{i-1,j}$, and $A^{11}_{i-1,j}\psi_{i,j}$ in simultaneous equations of motion for (i,j)-th, $(i,j-1)$-th, and $(i-1,j)$-th nodes, the solution $\boldsymbol{\Psi}$ affected by imposed velocity $u_{i,j-\frac{1}{2}}$ and $w_{i-\frac{1}{2},j}$ can be obtained. For example, the coefficient matrix A and the buoyancy term vector $\mathbf{B}$ in Equation (42) can be partially modified as

$$
\begin{pmatrix}
\ddots & & & & & & \vdots & \\
& A^{7}_{i-1,j} + A^{11}_{i-1,j} & A^{8}_{i-1,j} & A^{9}_{i-1,j} & 0 & A^{10}_{i-1,j} & 0 & \\
& A^{6}_{i-1,j+1} & A^{7}_{i-1,j+1} & A^{8}_{i-1,j+1} & 0 & 0 & A^{10}_{i-1,j+1} & \\
& A^{5}_{i-1,j+2} & A^{6}_{i-1,j+2} & A^{7}_{i-1,j+2} & 0 & 0 & 0 & \\
& 0 & 0 & 0 & A^{7}_{i,j-2} & A^{8}_{i,j-2} & A^{9}_{i,j-2} & \\
& A^{4}_{i,j-1} & 0 & 0 & A^{6}_{i,j-1} & A^{7}_{i,j-1} + A^{8}_{i,j-1} & 0 & \\
\cdots & 0 & A^{4}_{i,j} & 0 & A^{5}_{i,j} & 0 & A^{7}_{i,j} + A^{3}_{i,j} + A^{6}_{i,j} & \cdots \\
& & & & & & \vdots & \ddots
\end{pmatrix}
$$

$$
\times \begin{pmatrix} \vdots \\ \psi_{i-1,j} \\ \psi_{i-1,j+1} \\ \psi_{i-1,j+2} \\ \psi_{i,j-2} \\ \psi_{i,j-1} \\ \psi_{i,j} \\ \vdots \end{pmatrix} = \begin{pmatrix} \vdots \\ B_{i-1,j} + \delta x_{i-\frac{1}{2}} w_{i-\frac{1}{2},j} A^{11}_{i-1,j} \\ B_{i-1,j+1} \\ B_{i-1,j+2} \\ B_{i,j-2} \\ B_{i,j-1} - \delta z_{j-\frac{1}{2}} u_{i,j-\frac{1}{2}} A^{8}_{i,j-1} \\ B_{i,j} - \delta x_{i-\frac{1}{2}} w_{i-\frac{1}{2},j} A^{3}_{i,j} + \delta z_{j-\frac{1}{2}} u_{i,j-\frac{1}{2}} A^{6}_{i,j} \\ \vdots \end{pmatrix} \tag{65}
$$

The matrix elements colored with dark gray have been replaced according to Equations (61) to (64), and those colored with light gray are diagonal elements of the matrix A. This deformation obviously keeps the symmetry of the matrix A; therefore, the modified Cholesky decomposition can also be applied for solving Equation (65).

Model setup for forced convection

Next, the author investigates the effects of "external forces" on subduction dynamics as discussed in Section 4.2 by performing further numerical simulations that are the same as those in Section 2, except for the following points.

- After the spontaneous subduction has initiated, constant horizontal velocity u is artificially incorporated at the depth of 11.25 km along migrating oceanic plate or

Table 8: All run IDs and corresponding parameters in this appendix. † Continentward motion contributing trench advance. †† Seaward motion contributing trench retreat.

Run ID	Viscosity reduction due to hydration r_{diff}	Viscosity reduction due to hydration r_{disl}	Density reduction due to hydration β	Imposed velocity along oceanic plate u_{OP}	Imposed velocity along continental plate u_{CP}
r1b1_free	1.0	1.2	1	Not imposed	Not imposed
r1b1_O20	1.0	1.2	1	Not $\rightarrow$ 20 mm/yr	Not imposed
r1b1_O120	1.0	1.2	1	Not $\rightarrow$ 120 mm/yr	Not imposed
r1b1_C50	1.0	1.2	1	Not imposed	Not $\rightarrow$ 50 mm/yr†
r1b1_C-100	1.0	1.2	1	Not imposed	Not $\rightarrow$ -100 mm/yr††

continental plate by partially modifying the equations of motion as described above. All run IDs and the corresponding u values are listed in Table 8.

- The top right corner of the model domain (i.e., the right end of the continental plate) is set to be free by imposing 500-km width $\times$ 300-km thick low viscosity zone (10^{22} Pa s), which stably enables continental drift and resulting trench migration.
- The thermal age of the continental plate is set to be 100 Ma instead of 20 Ma. The old overlying plate is expected not to cause back-arc spreading because of its thickness. By removing the effects of back-arc deformation, interpretation of the numerical results can be simplified because trench migration is the sum of the rates of continental drift (i.e., deformation within the imposed weak zone in this case) and extension/compression of the overlying plate.

Results

The evolution of each run in Table 8 is shown in Figures 36 to 42. Details are described in the captions.

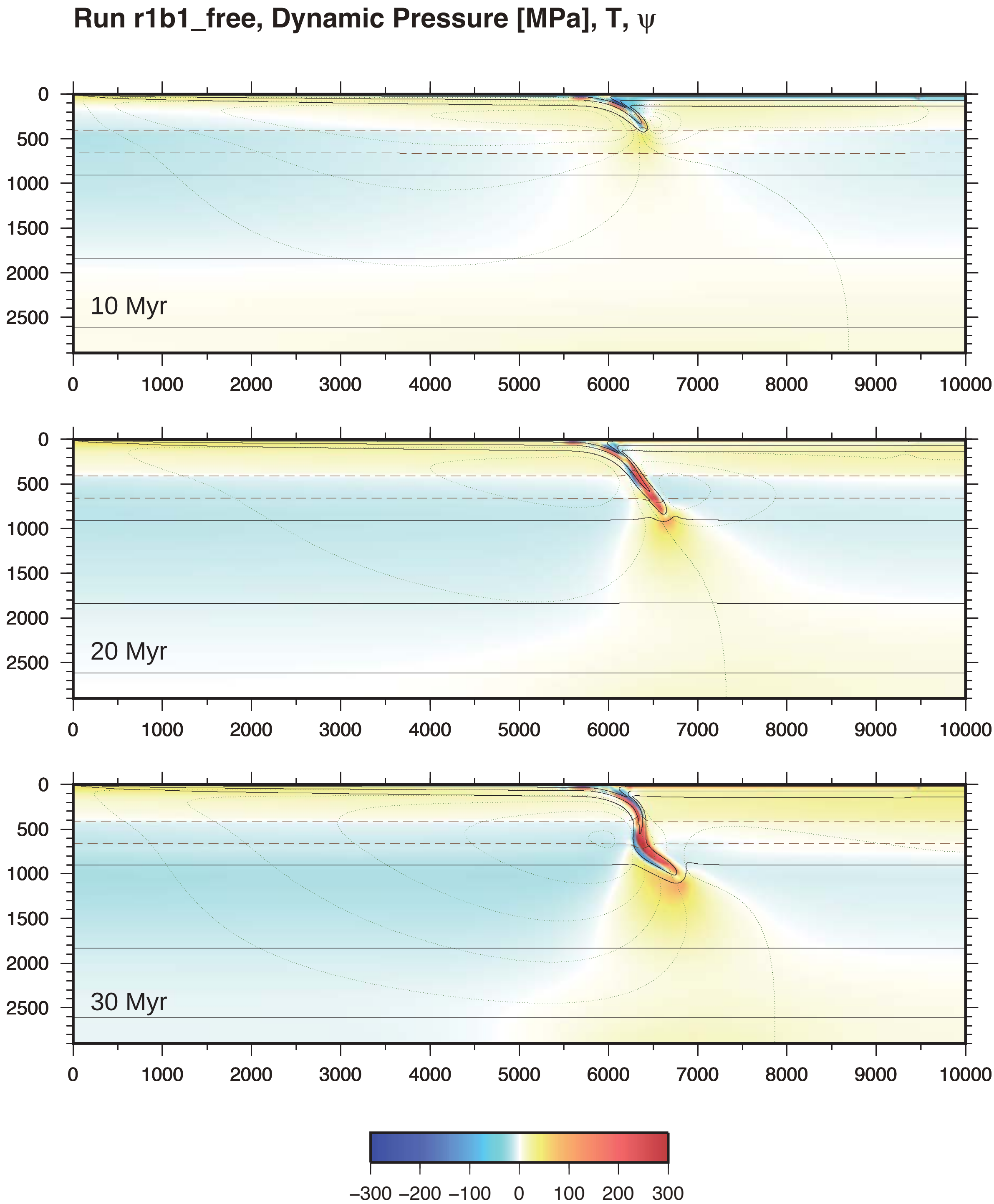

Figure 36: Evolution of the run without fixed-boundary conditions. Colored contour indicates dynamic pressure solved by SIMPLER (Patankar, 1981; Appendix D). Solid lines are isotherms of 400, 800, and 1,200°. Dotted lines are stream functions. This subduction evolution is the standard of the following results.

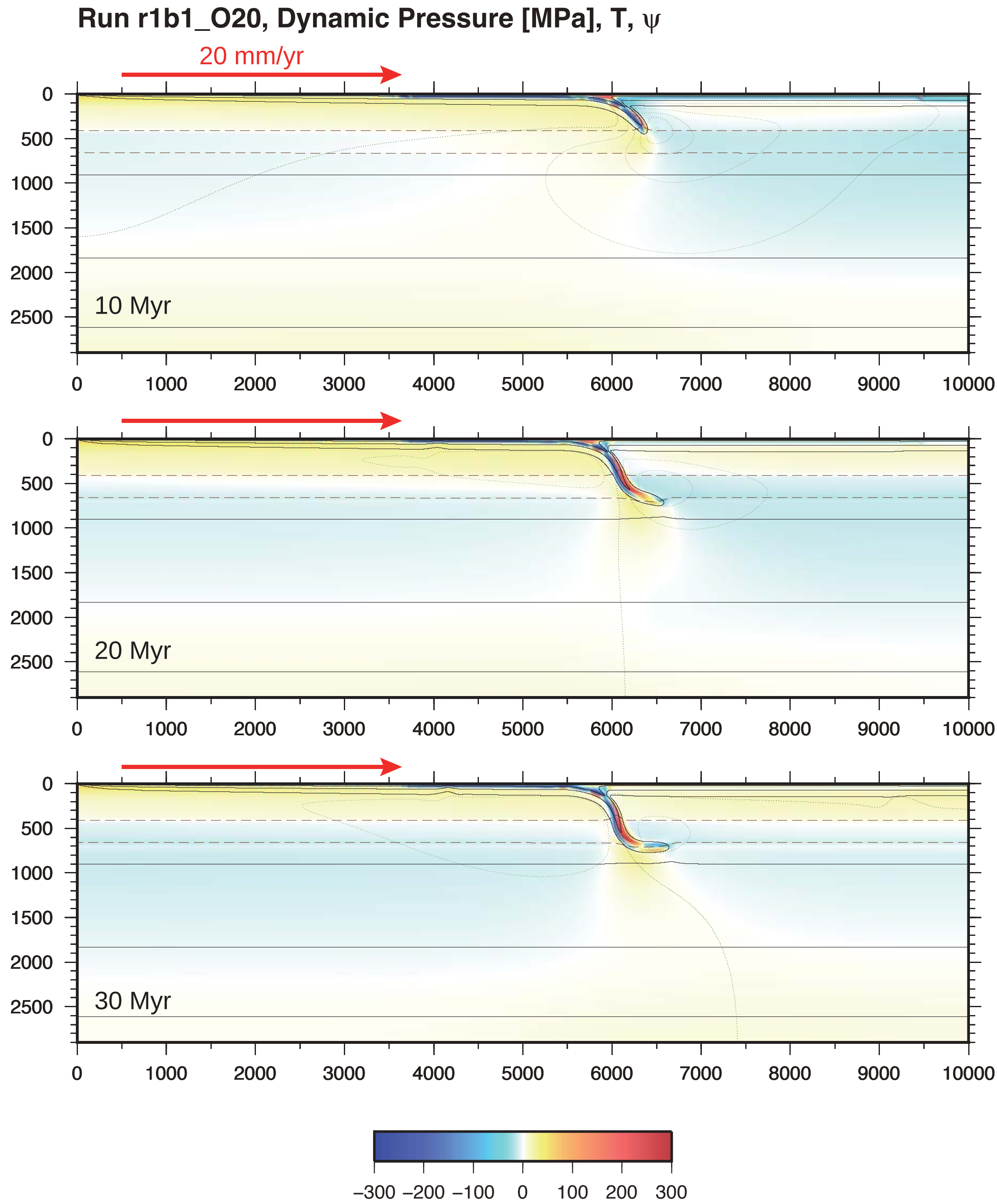

Figure 37: Evolution of the run with a brake on the oceanic plate subduction. The stagnant slabs is more stable over the 660-km boundary compared to the free convection (Figure 36). The retreat mechanism is similar to Schellart (2005).

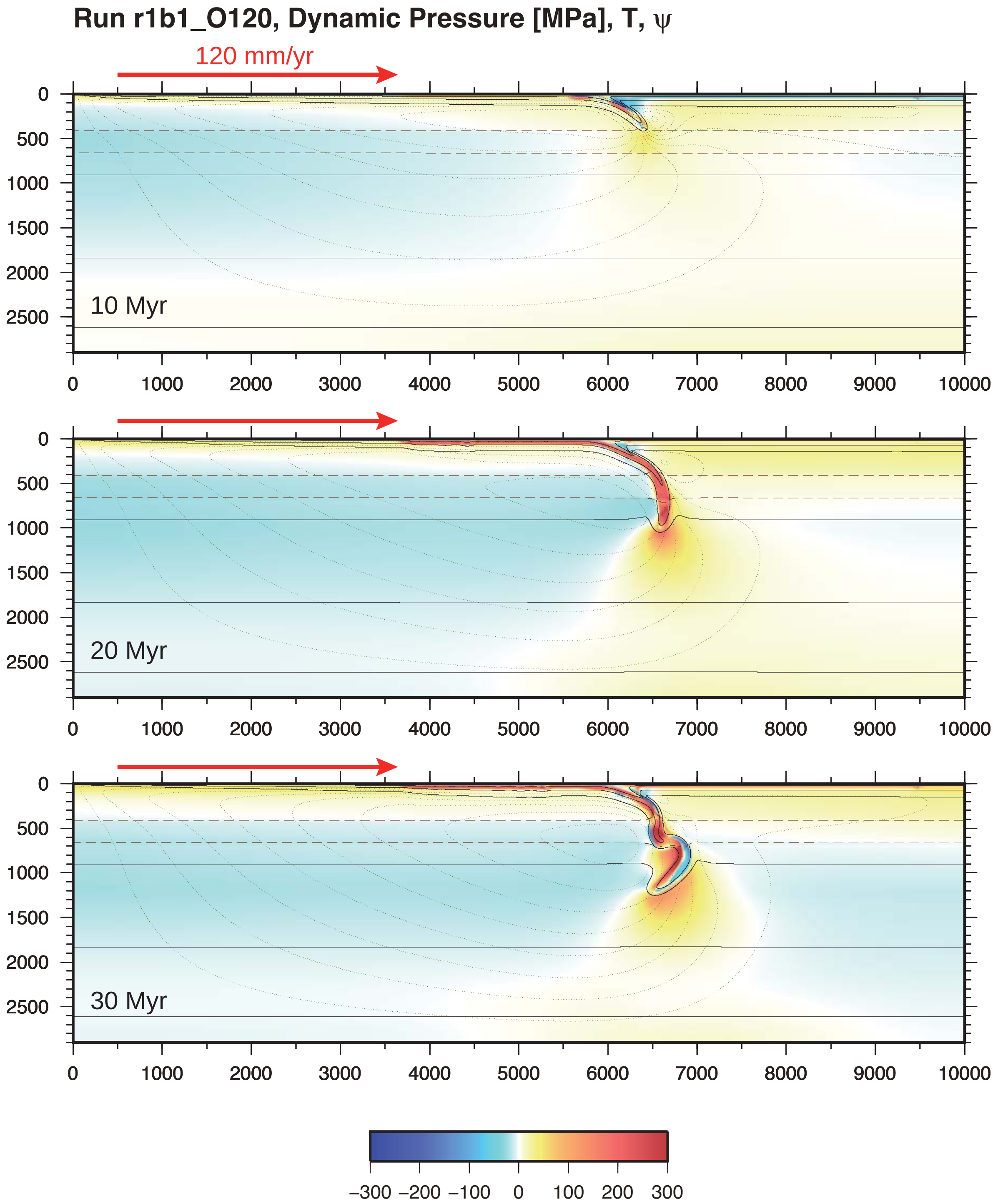

Figure 38: Evolution of the run with a large forced velocity along the subducting oceanic plate. The trench slightly advances, the dynamic pressure of wedge mantle is higher, and induced corner flows are weaker compared to the free convection (Figure 36). The mechanism of slight advancing trench with the slab folding over the 660-km phase boundary is similar to Schellart (2005).

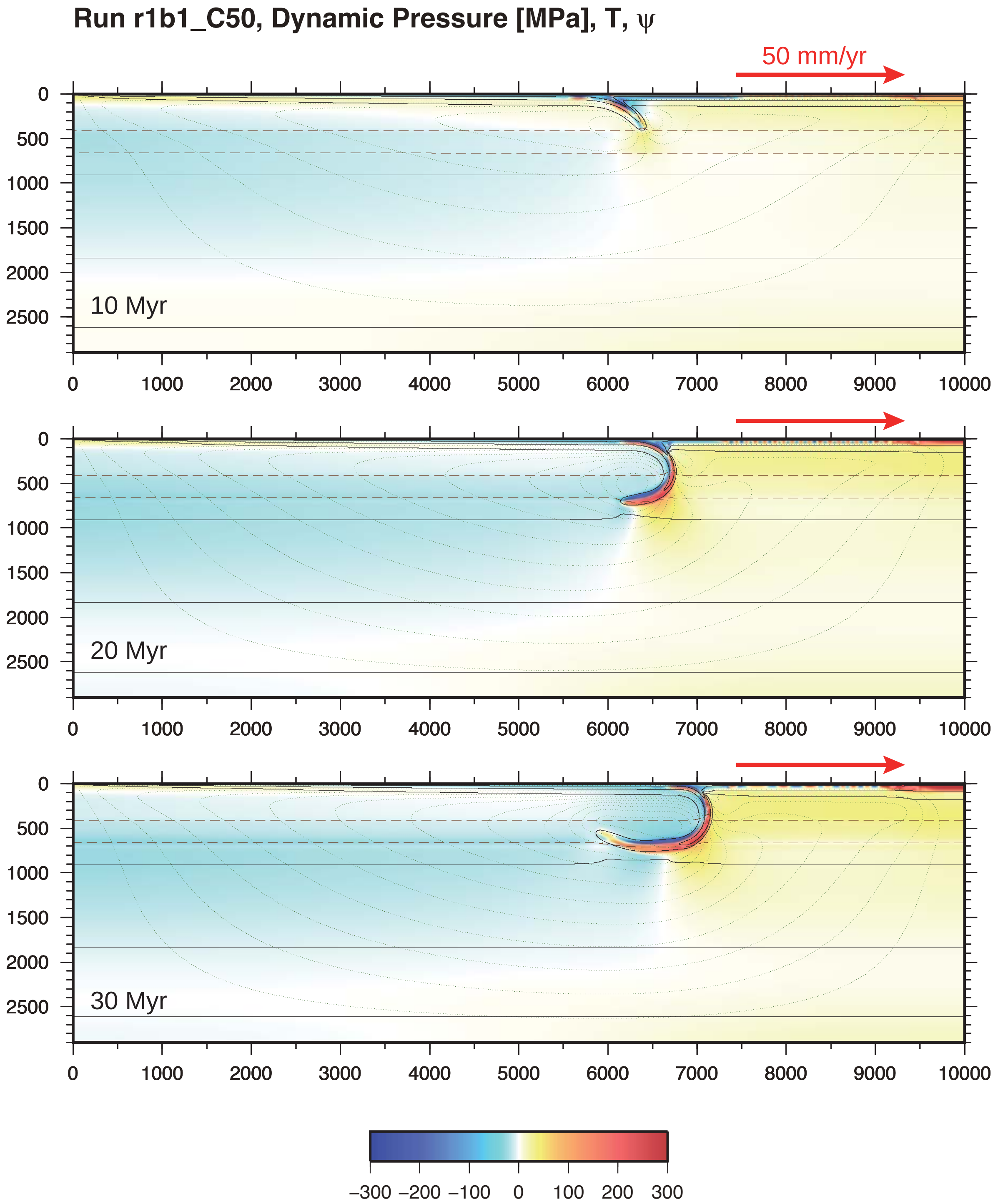

Figure 39: Evolution of the run with the continent migration away from the oceanic plate. The trench rapidly advances and the dynamic pressure of wedge mantle is higher. The mechanism to bring the peculiar slab morphology is discussed in Čížková & Bina (2015) and would work in the Mariana slab.

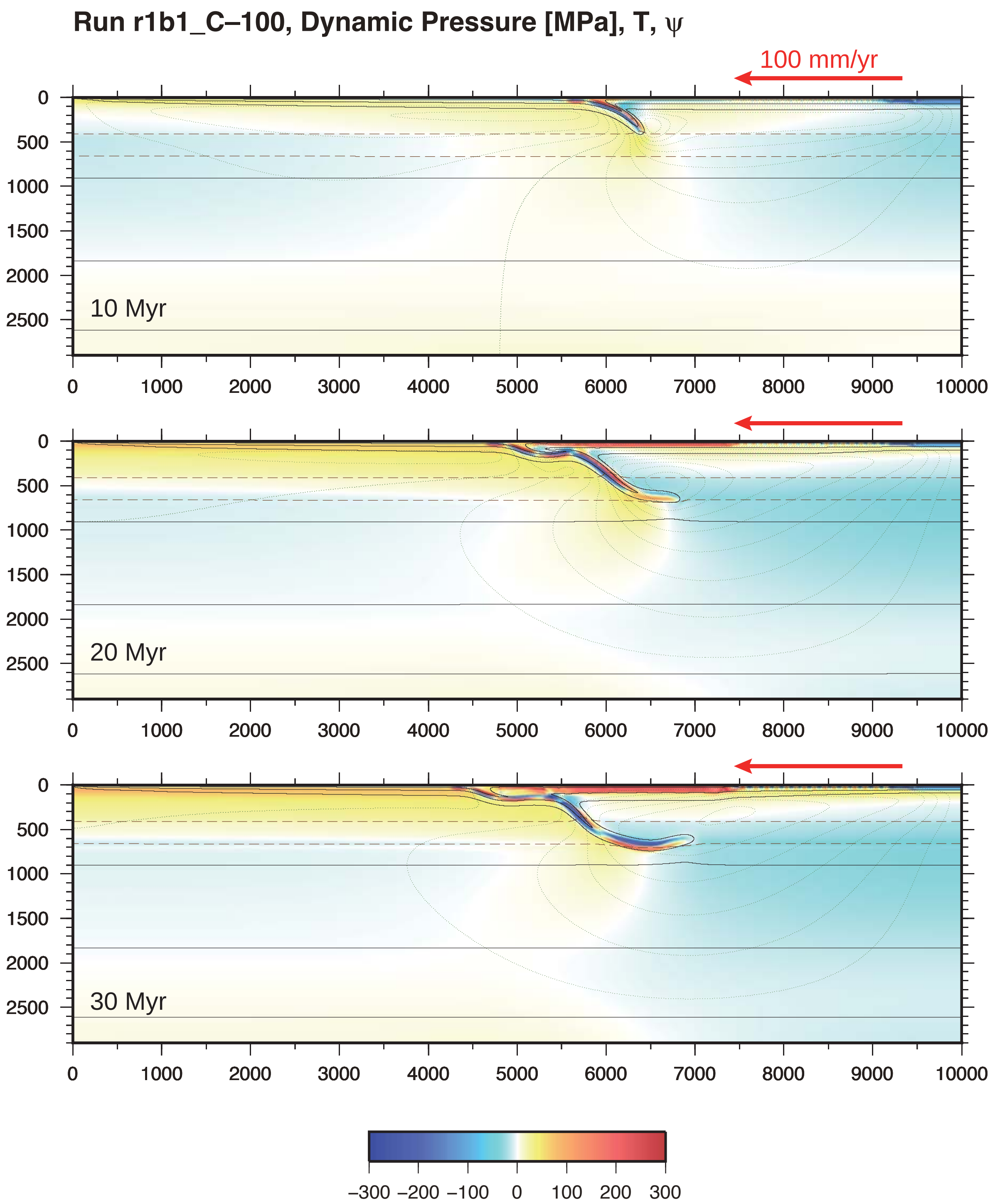

Figure 40: Evolution of the run with the continent migration toward the oceanic plate. The dynamic pressure of wedge mantle is higher, while the overlying plate is compressive. The stagnant slab is stable over the 660-km phase boundary. The mechanism to produce the stagnant slab is similar to Torii & Yoshioka (2007).

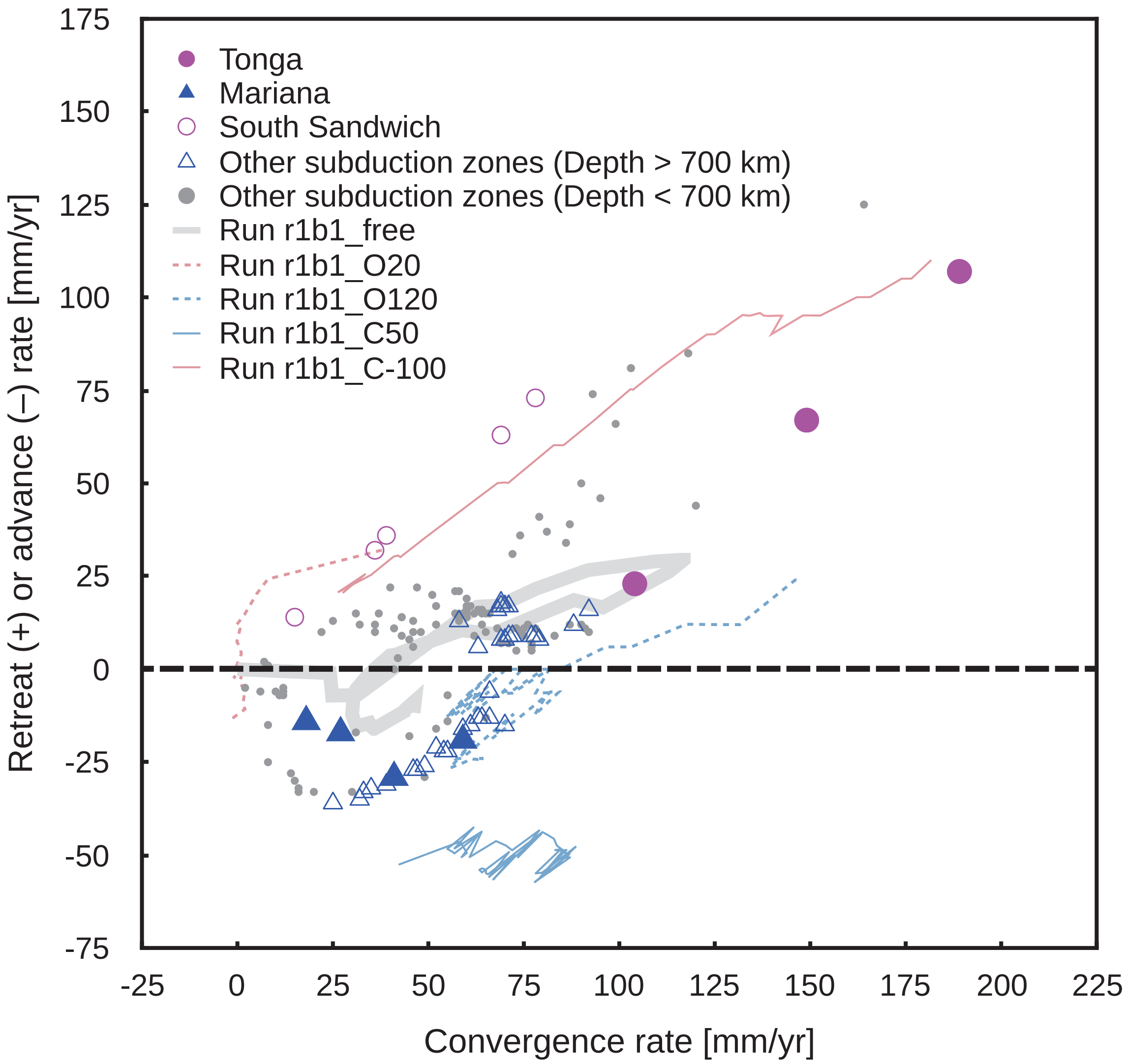

Figure 41: Tracks of convergence rates and trench migration rates of 5 runs in Table 8. The observational data is the same as that in Figure 14 in Chapter II (Lallemand et al., 2008). Compared to the free convection model (Figure 14), the correlation between convergence rates and trench migration rates is smaller. For example, run r1b1_O20 would explain the rapid trench retreat with the slow convergence rate of the South Sandwich subduction zone: the Pacific plate, which is much larger than South Sandwich slab, may work as a brake of rapid subduction (rapid plate convergence).

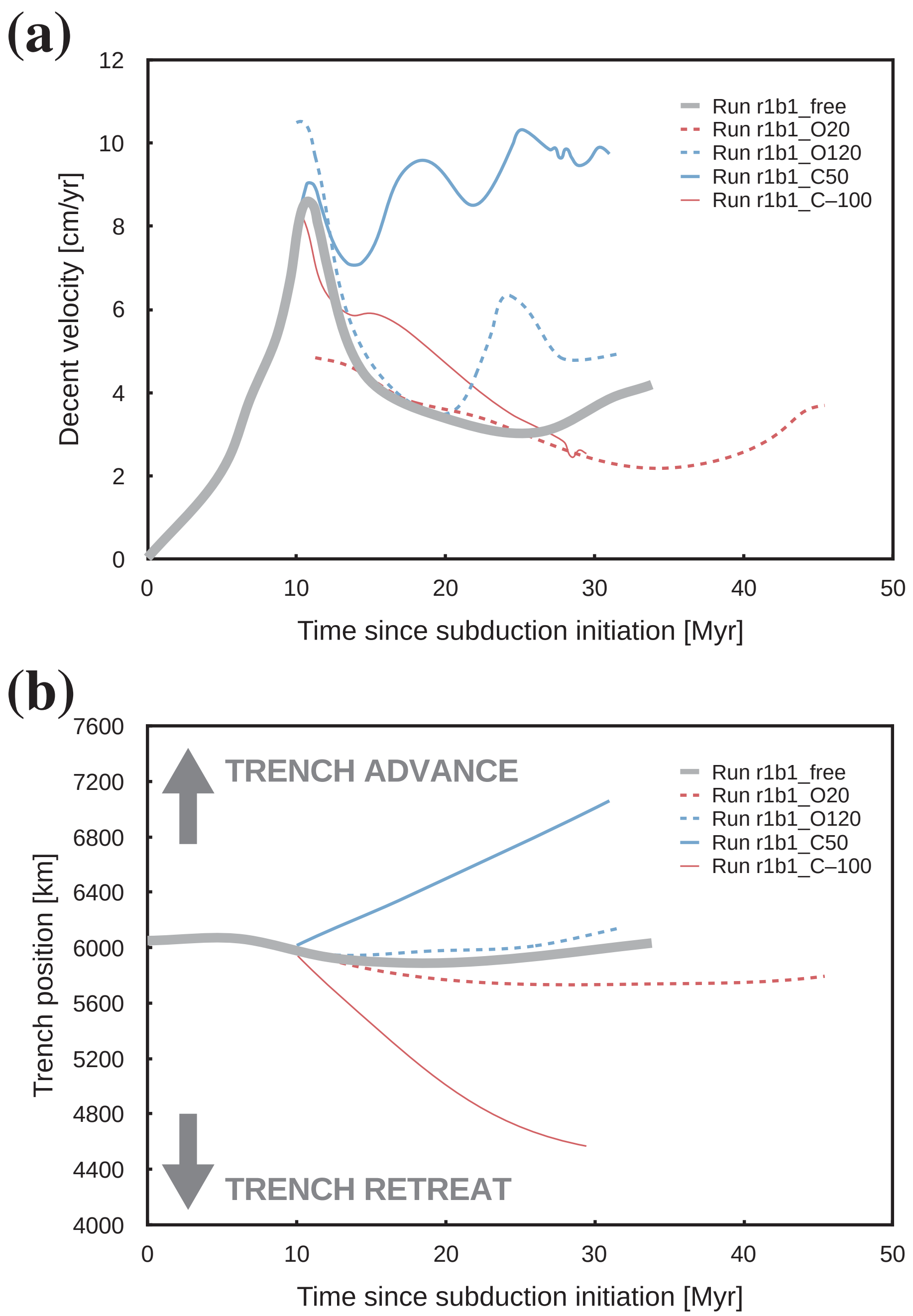

Figure 42: Time-dependent decent velocity and trench position of 5 runs in Table 8 (similar to Figure 10 in Chapter II).

Appendix C: Parameter tests for slab stagnation and penetration[2]

Here, the author checks the effects on trench retreat and advance of: Clapeyron slopes; the amount and distribution of water within the subducting oceanic crust (MORB); and the maximum yield strength of both overlying and subducting lithosphere. All parameters and settings are based on runs r1b0 (trench retreat and slab stagnation mode; Figure 43i) and r1b2 (trench advance and slab rollover mode; Figure 44i), both of which are discussed in detail in the main text. Run IDs in the following discussion and the corresponding parameter changes are listed in Table 9.

Clapeyron slope for olivine/wadsleyite transition

While the author applies a relatively gentle 410-km-depth Clapeyron slope $\gamma_{410} = +3$ [MPa/K] (e.g., Katsura & Ito, 1989) in Equation (4) to calculate the state equation (19) in the main text, a slightly steeper value has also been suggested (+4 MPa/K; Katsura et al., 2004). Here, the author imposes $\gamma_{410} = +4$ [MPa/K] instead of +3 [MPa/K]. In the case of trench retreat (r1b0_g410+4 in Figure 43ii), as the steeper slope contributes to negative buoyancy of the subducting slab, the subduction rate is higher than that of run r1b0 (Figure 43i). Accordingly, the development of slab stagnation is more rapid. Such rapid evolution is also reproduced in the case of trench advance (r1b2_g410+4 in Figure 44ii), and a density increase around the 410-km phase boundary does not slow trench advance.

Clapeyron slope for ringwoodite/bridgmanite transition

The 660-km-depth Clapeyron slope is still debated. The author applies a relatively strong value $\gamma_{660} = -3$ [MPa/K] (e.g., Akaogi & Ito, 1993) in the main text, while Katsura et al. (2003) suggest a weaker one, $-2 < \gamma_{660} < -0.4$ [MPa/K]. Here, the author imposes $\gamma_{660} = -1$ [MPa/K] instead of -3 [MPa/K]. In the case of trench retreat (r1b0_g660–1 in Figure 43iii), as weaker γ_{660} reduces resistance to slab subduction in the lower mantle, the subduction rate is higher, as with the case of steeper γ_{410}. Despite the small resistance, a stagnant slab develops, and the evolution is rapid compared to run r1b0 (Figure 43i).

[2]This appendix is based on the author's published paper: Nakao, A., Iwamori, H., and Nakakuki, T. (2016). Effects of water transportation on subduction dynamics: Roles of viscosity and density reduction. *Earth Planet. Sci. Lett.*, **454**, 178–191.

Table 9: All run IDs and corresponding parameters in this appendix.

Run ID	Viscosity reduction due to hydration r_{diff}	Viscosity reduction due to hydration r_{disl}	Density reduction due to hydration β	Clapeyron slope at 410-km [MPa/K] γ_{410}	Clapeyron slope at 660-km [MPa/K] γ_{660}	Thickness of hydrous MORB [km]	Water content of MORB [wt%]	Maximum yield strength [MPa] σ_{Ymax}
r1b0	1.0	1.2	0	+3	–3	7.5	3.0	200
r1b0_g410+4	1.0	1.2	0	+4	–3	7.5	3.0	200
r1b0_g660–1	1.0	1.2	0	+3	–1	7.5	3.0	200
r1b0_2.5km6%	1.0	1.2	0	+3	–3	2.5	6.0	200
r1b0_Y500MPa	1.0	1.2	0	+3	–3	7.5	3.0	500
r1b2	1.0	1.2	2	+3	–3	7.5	3.0	200
r1b2_g410+4	1.0	1.2	2	+4	–3	7.5	3.0	200
r1b2_g660–1	1.0	1.2	2	+3	–1	7.5	3.0	200
r1b2_2.5km6%	1.0	1.2	2	+3	–3	2.5	6.0	200
r1b2_Y500MPa	1.0	1.2	2	+3	–3	7.5	3.0	500

The rapid evolution and small effect on the slab morphology are also reproduced in the case of trench advance (r1b2_g660–1 in Figure 44iii), although both stagnant slabs and "continuous track" slabs are somewhat unstable at the 660-km boundary.

Amount and distribution of water within MORB

While my model assumes that a 7.5-km-thick MORB contains a uniform amount of water of 3 wt% (e.g., Rüpke et al., 2004), some previous models assume fully hydrated surface MORB and less hydrated lower MORB and gabbro (e.g., Faccenda et al., 2012; Quinquis & Buiter, 2014). Therefore, the author conducts two runs to analyze trench motion in which only one grid of the surface of the subducting oceanic plate is fully hydrated (2.5 km thick with 6 wt%H_2O). In the case of trench retreat (r1b0_2.5km6% in Figure 43iv), as the amount of water subducting into the deeper mantle decreases, more time is required to sufficiently hydrate the mantle wedge in order to thin the overlying lithosphere. Accordingly, trench retreat due to back-arc spreading and the resultant acceleration of slab descent are somewhat delayed (about 4 Myr). A similar delay is seen in runs for trench advance (r1b2_2.5km6% in Figure 44iv). In this case, more time is required to achieve sufficient hydrous buoyancy for the subducting slab to become upward convex, as well as for the overlying lithosphere to experience sufficient viscosity reduction. Its peculiar slab shape at 30.07 Myr is a result of slab advance in the upper mantle with a semi-fixed deeper slab in the lower mantle. Thus, descent and trench migration rate alternate, but transition of the subduction mode (e.g., stagnant or penetrating slab) is not observed.

Maximum yield strength

the author applies an experimentally quantified maximum yield strength to the subducting and overlying lithosphere, $\sigma_{\mathrm{Ymax}} = 200$ [MPa] (Kohlstedt et al., 1995), in Equation (15), but some numerical studies suggest higher σ_{Ymax} ($>$ 500 MPa; e.g., Billen, 2010). Therefore, here the author analyzes the effects of higher yield strength (500 MPa). In the case of trench retreat (r1b0_Y500MPa in Figure 43v), after the tip of the subducting slab cuts into the lower mantle, back-arc spreading is complete, and the resultant trench retreat occurs with a delay of ~7 Myr compared to run r1b0 (Figure 43i). The author attributes the delay to the stiff overlying plate; more water would be required to erode the continental margin sufficiently to concentrate tensional stress comparable to the increased yield strength, and/or the positive feedback between concentration of tensional stress and thinning of the overlying lithosphere would be weakened. Without a stiff overlying plate, a stiff slab would retreat and stagnate at the 660-km boundary instead (e.g., Stegman et al., 2010). A similar slight delay of trench migration is seen in the case of trench advance (r1b2_Y500MPa in Figure 44v). In this case, the curvature of the subducting slab becomes larger due to its larger yield strength, but both trench advance and an upward convex slab also develop in run r1b2 (Figure 44i).

Summary of the parameter checks

The author has confirmed that steeper γ_{410} and weaker γ_{660} contribute to rapid slab evolution, and that both smaller water contents of subducting MORB and larger σ_{Ymax} delay trench migration. However, subduction modes remain essentially the same, i.e., stagnant slab with retreating trench; penetrating slab with stationary trench; or rollover slab with advancing trench. Therefore, the author considers that the parameters used in the main simulations and subsequent discussions are reasonable.

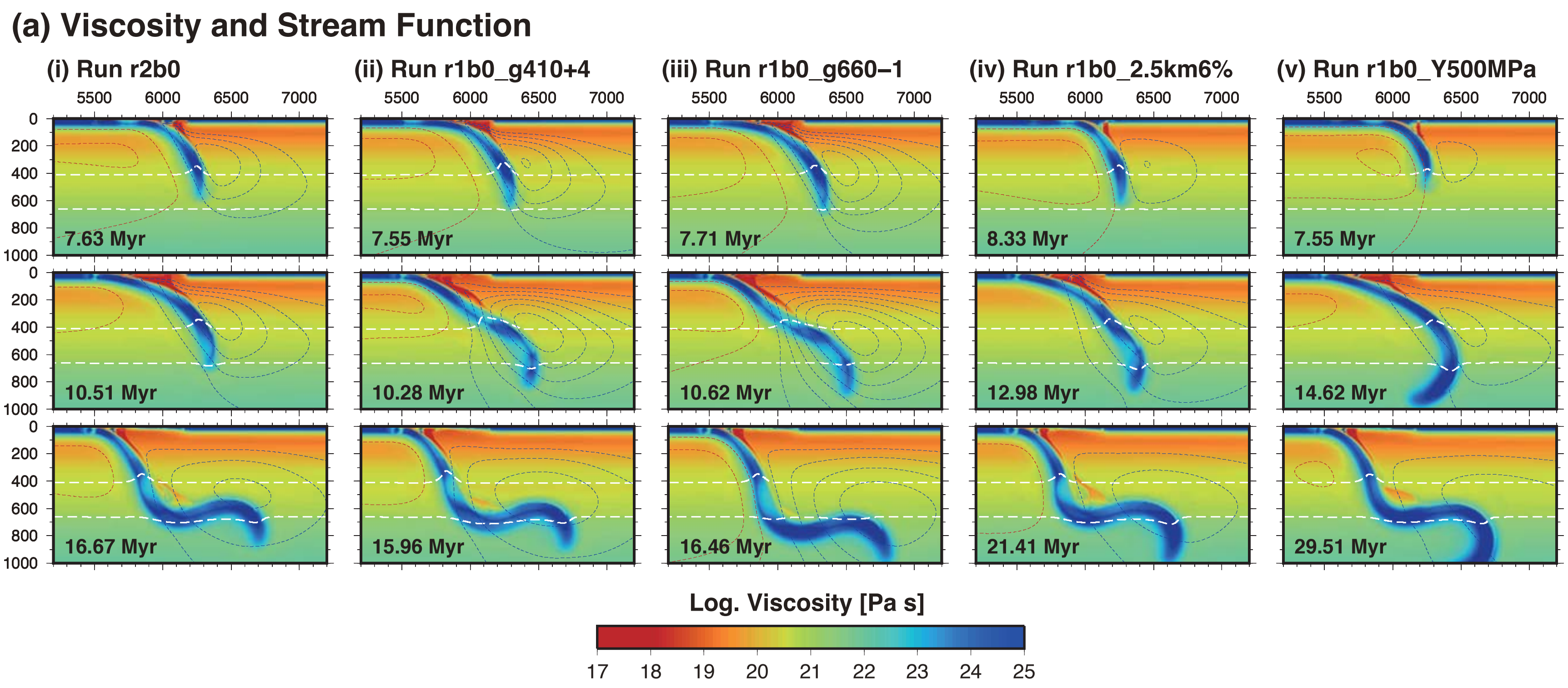

Figure 43: Analysis of trench retreat and slab stagnation based on run r1b0. (a) Evolution of 5 runs. The colored contours show the viscosity structure. The horizontal and vertical ranges are $5{,}200 < x < 7{,}200$ [km] and $0 < z < 1{,}000$ [km], respectively. Red and blue dotted lines are clockwise ($\psi > 0$) and counterclockwise ($\psi < 0$) stream functions (2×10^4 [m^2/s] intervals), respectively. Dashed white lines represent the 410-km and 660-km phase boundaries. Time since subduction initiation, i.e., initial condition, is indicated in bottom left of each panel.

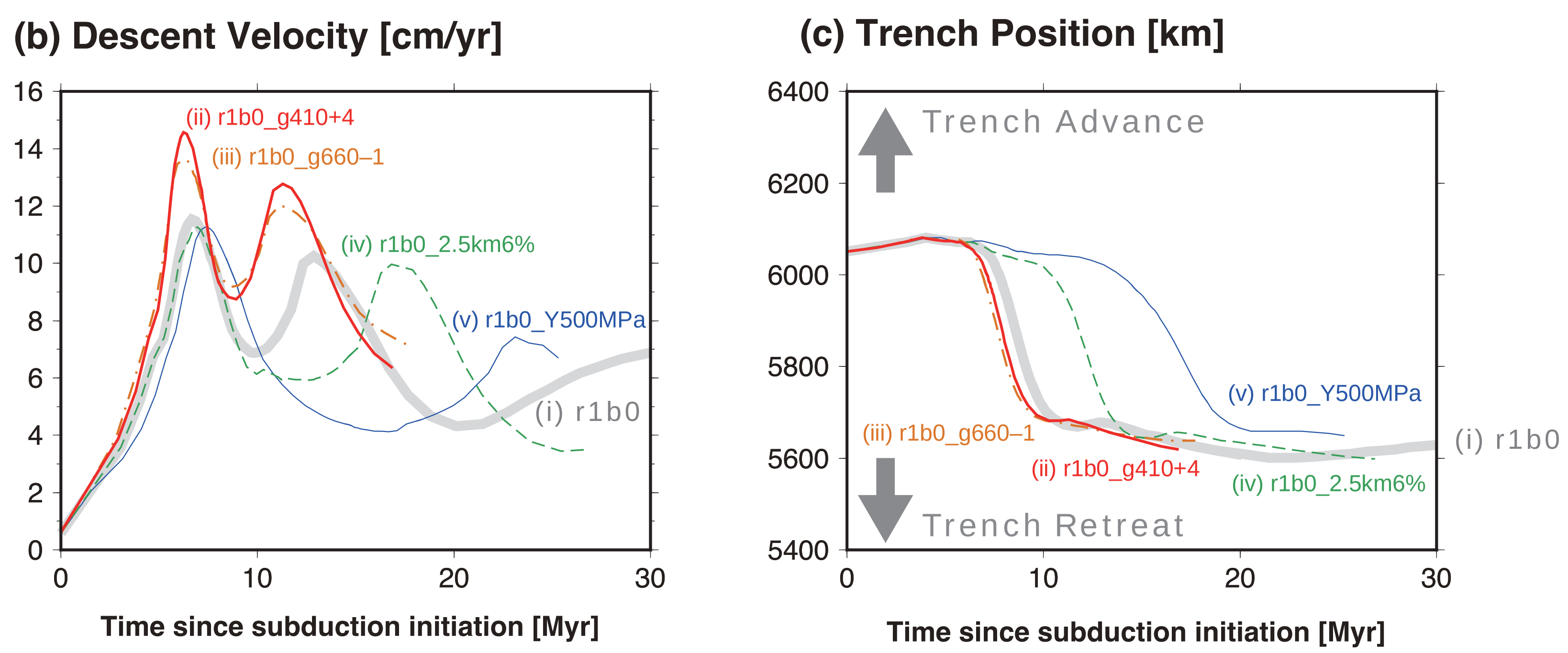

Figure 43 (contiuned): (b) Time-dependent maximum descent (vertical) velocity at a depth of 300 km for the 5 runs displayed in (a). (c) Time-dependent lateral positions of the trench for 5 runs displayed in (a). A decline of the vertical value represents trench retreat, and an increase represents trench advance.

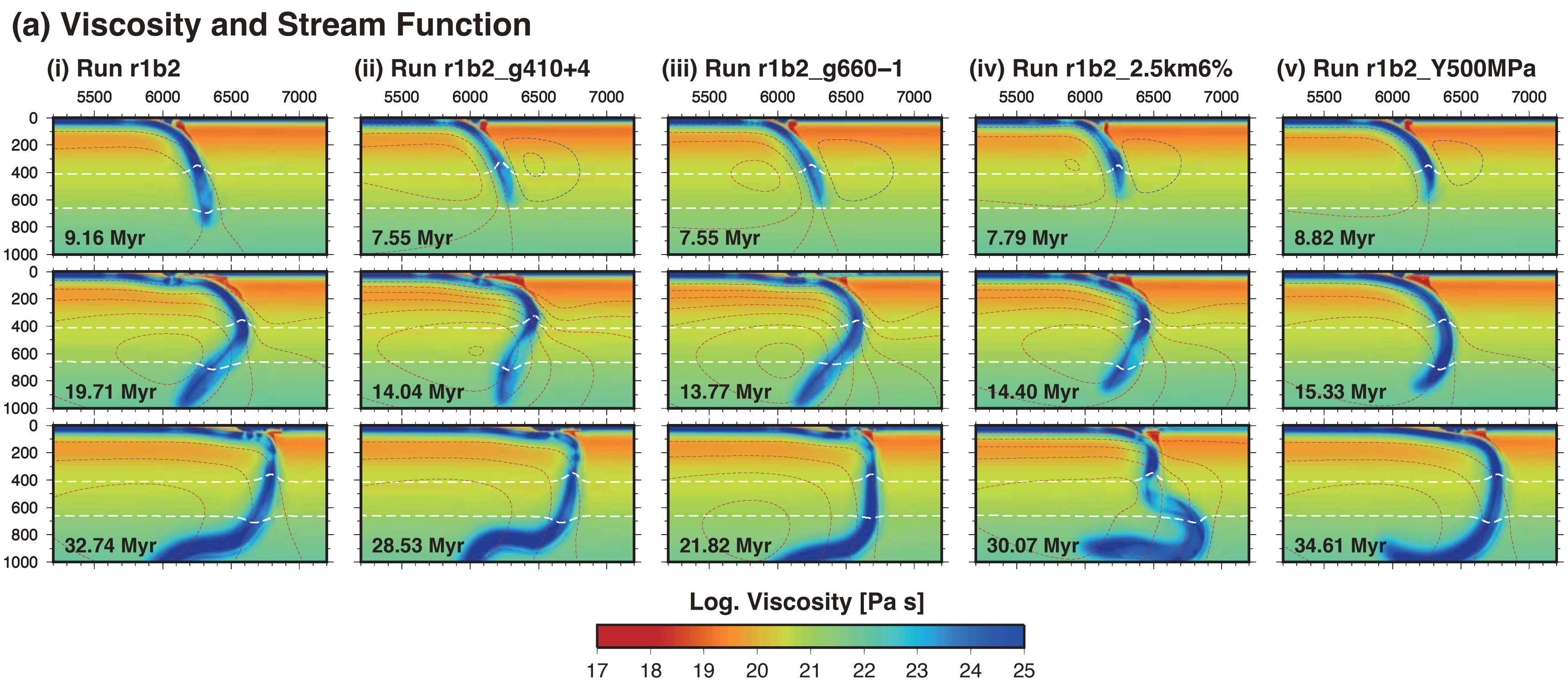

Figure 44: Analysis of trench advance and slab rollover based on run r1b2. Symbols are the same as those in Figure 43.

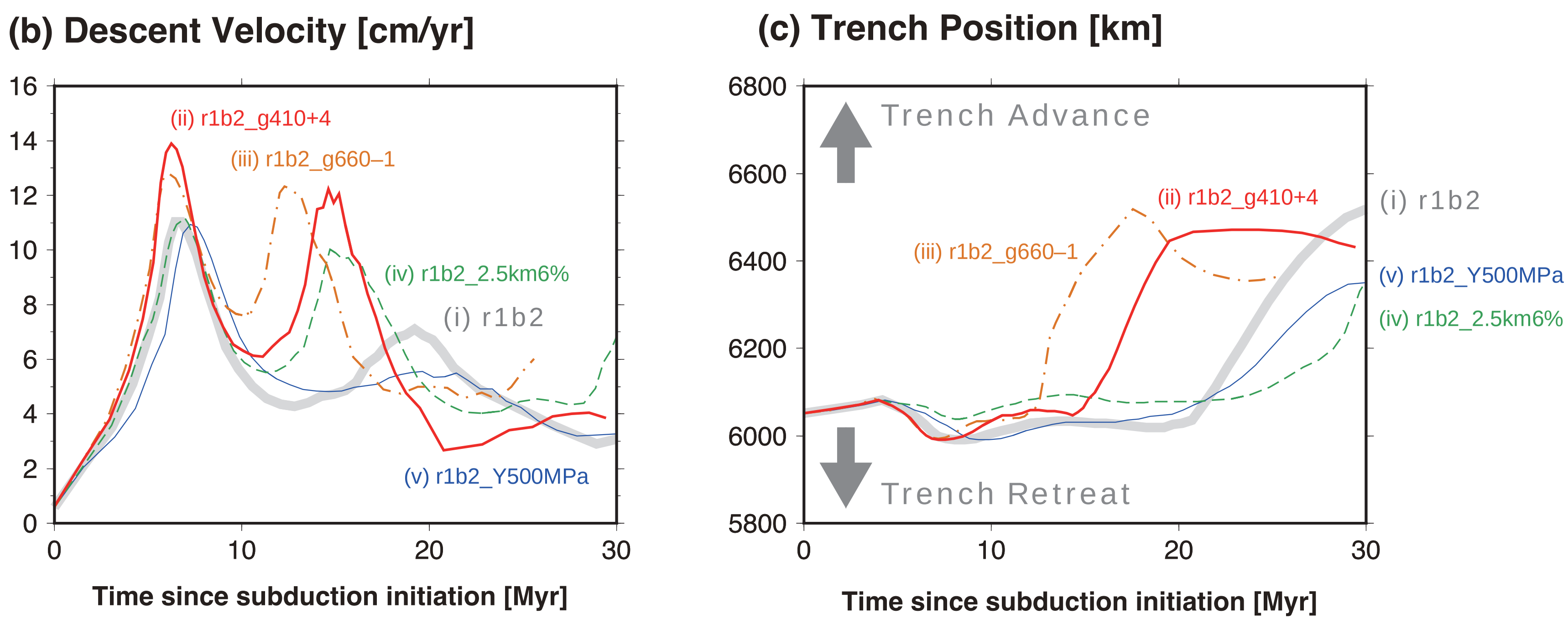

Figure 44 (contiuned).

Appendix D: Approach to solving dynamic pressure (SIMPLER)

The vectorial momentum equation for much viscous, incompressible fluid can be described as

$$\begin{aligned} \nabla p &= \nabla \cdot \sigma + \rho g \boldsymbol{e}_z \\ &= \nabla \cdot \eta \left[\nabla \boldsymbol{v} + (\nabla \boldsymbol{v})^T \right] + \rho g \boldsymbol{e}_z. \end{aligned} \tag{66}$$

If velocity $\boldsymbol{v}$, viscosity η (or stress tensor σ), and density ρ are given, dynamic pressure p can be obtained. However, linear integral of Equation (66) is known to provide a noisy solution. Therefore, we apply SIMPLER (Semi-Implicit Method for Pressure-Linked Equations, Revised; e.g., Patankar, 1981). The method is originally used for having unknown parameters p and $\boldsymbol{v}$ converge by the iteration. Given true velocity field $\boldsymbol{v}$, we can obtain true p without the iteration. The concept of the method is to solve simultaneous equations including the Laplacian of dynamic pressure $\nabla^2 p$, i.e.,

$$\begin{aligned} \left(\frac{\partial^2}{\partial x^2} + \frac{\partial^2}{\partial z^2} \right) p &= \frac{\partial^2 \sigma_{xx}}{\partial x^2} + \frac{\partial^2 \sigma_{zz}}{\partial z^2} + 2 \frac{\partial^2 \sigma_{xz}}{\partial x \partial z} + \frac{\partial}{\partial z} \rho g \\ &= \frac{\partial^2}{\partial x^2} \left(2\eta \frac{\partial u}{\partial x} \right) + \frac{\partial^2}{\partial z^2} \left(2\eta \frac{\partial w}{\partial z} \right) \\ &\quad + \frac{\partial^2}{\partial x \partial z} \left[\eta \left(\frac{\partial w}{\partial x} + \frac{\partial u}{\partial z} \right) \right] + \frac{\partial}{\partial z} \rho g. \end{aligned} \tag{67}$$

Because the discretized equation of (67) is linear of p, the simultaneous equations for all n control volumes in the model domain can be expressed in the same way as Appendix A by using a coefficient matrix C ($n \times n$; known), a dynamic pressure vector $\mathbf{p}$ ($n \times 1$; unknown), and a constant term vector $\mathbf{D}$ (the sum of viscous stress and buoyancy terms; $n \times 1$; known) as

$$C\mathbf{p} = \mathbf{D}. \tag{68}$$

The elements of matrixes in Equation (68) around the (I, J)-th control volumes (Figure 45; 3×3 simultaneous equations related to 3×3 unknown parameters $p_{I,J}$) can be expressed as follows (note that $p_{I,J}$ is located at the centers of control volumes; therefore, the coordinates (I, J) are discriminated from (i, j) to express nodes for stream functions, $\psi_{i,j}$, in Appendix A):

$$
\begin{pmatrix}
 & & & & & \vdots & & & & & \\
 & C^3_{I-1,J-1} & C^4_{I-1,J-1} & 0 & C^5_{I-1,J-1} & 0 & 0 & 0 & 0 & 0 & \\
 & C^2_{I-1,J} & C^3_{I-1,J} & C^4_{I-1,J} & 0 & C^5_{I-1,J} & 0 & 0 & 0 & 0 & \\
 & 0 & C^2_{I-1,J+1} & C^3_{I-1,J+1} & 0 & 0 & C^5_{I-1,J+1} & 0 & 0 & 0 & \\
 & C^1_{I,J-1} & 0 & 0 & C^3_{I,J-1} & C^4_{I,J-1} & 0 & C^5_{I,J-1} & 0 & 0 & \\
\cdots & 0 & C^1_{I,J} & 0 & C^2_{I,J} & C^3_{I,J} & C^4_{I,J} & 0 & C^5_{I,J} & 0 & \cdots \\
 & 0 & 0 & C^1_{I,J+1} & 0 & C^2_{I,J+1} & C^3_{I,J+1} & 0 & 0 & C^5_{I,J+1} & \\
 & 0 & 0 & 0 & C^1_{I+1,J-1} & 0 & 0 & C^3_{I+1,J-1} & C^4_{I+1,J-1} & 0 & \\
 & 0 & 0 & 0 & 0 & C^1_{I+1,J} & 0 & C^2_{I+1,J} & C^3_{I+1,J} & C^4_{I+1,J} & \\
 & 0 & 0 & 0 & 0 & 0 & C^1_{I+1,J+1} & 0 & C^2_{I+1,J+1} & C^3_{I+1,J+1} & \\
 & & & & & \vdots & & & & &
\end{pmatrix}
\times
\begin{pmatrix}
\vdots \\ p_{I-1,J-1} \\ p_{I-1,J} \\ p_{I-1,J+1} \\ p_{I,J-1} \\ p_{I,J} \\ p_{I,J+1} \\ p_{I+1,J-1} \\ p_{I+1,J} \\ p_{I+1,J+1} \\ \vdots
\end{pmatrix}
=
\begin{pmatrix}
\vdots \\ D_{I-1,J-1} \\ D_{I-1,J} \\ D_{I-1,J+1} \\ D_{I,J-1} \\ D_{I,J} \\ D_{I,J+1} \\ D_{I+1,J-1} \\ D_{I+1,J} \\ D_{I+1,J+1} \\ \vdots
\end{pmatrix}
\tag{69}
$$

where

$$C^1_{I,J} = -\frac{(\delta z_J)^2}{a^{up}_{I-\frac{1}{2},J}} \tag{70}$$

$$C^2_{I,J} = -\frac{(\delta x_I)^2}{a^{wp}_{I,J-\frac{1}{2}}} \tag{71}$$

$$C^3_{I,J} = \frac{(\delta z_J)^2}{a^{up}_{I+\frac{1}{2},J}} + \frac{(\delta z_J)^2}{a^{up}_{I-\frac{1}{2},J}} + \frac{(\delta x_I)^2}{a^{wp}_{I,J+\frac{1}{2}}} + \frac{(\delta x_I)^2}{a^{wp}_{I,J-\frac{1}{2}}} \tag{72}$$

$$C^4_{I,J} = C^2_{I,J+1} = -\frac{(\delta x_I)^2}{a^{wp}_{I,J+\frac{1}{2}}} \tag{73}$$

$$C^5_{I,J} = C^1_{I+1,J} = -\frac{(\delta z_J)^2}{a^{up}_{I+\frac{1}{2},J}} \tag{74}$$

$$D_{I,J} = -\left(\hat{u}_{I+\frac{1}{2},J} - \hat{u}_{I-\frac{1}{2},J}\right)\delta z_J - \left(\hat{w}_{I,J+\frac{1}{2}} - \hat{w}_{I,J-\frac{1}{2}}\right)\delta x_I \tag{75}$$

$$\hat{u}_{I+\frac{1}{2},J} = \frac{\begin{pmatrix} a^{u\rightarrow}_{I+\frac{1}{2},J} u_{I+\frac{3}{2},J} + a^{u\leftarrow}_{I+\frac{1}{2},J} u_{I-\frac{1}{2},J} \\ +a^{u\downarrow}_{I+\frac{1}{2},J} u_{I+\frac{1}{2},J+1} + a^{u\uparrow}_{I+\frac{1}{2},J} u_{I+\frac{1}{2},J-1} \\ +\eta_{I+\frac{1}{2},J+\frac{1}{2}} \left(w_{I+1,J+\frac{1}{2}} - w_{I,J+\frac{1}{2}} \right) \\ -\eta_{I+\frac{1}{2},J-\frac{1}{2}} \left(w_{I+1,J-\frac{1}{2}} - w_{I,J-\frac{1}{2}} \right) \end{pmatrix}}{a^{up}_{I+\frac{1}{2},J}} \tag{76}$$

$$\hat{w}_{I,J+\frac{1}{2}} = \frac{\begin{pmatrix} a^{w\rightarrow}_{I,J+\frac{1}{2}} w_{I+1,J+\frac{1}{2}} + a^{w\leftarrow}_{I,J+\frac{1}{2}} w_{I-1,J+\frac{1}{2}} \\ +a^{w\downarrow}_{I,J+\frac{1}{2}} w_{I,J+\frac{3}{2}} + a^{w\uparrow}_{I,J+\frac{1}{2}} w_{I,J-\frac{1}{2}} \\ +\eta_{I+\frac{1}{2},J+\frac{1}{2}} \left(u_{I+\frac{1}{2},J+1} - u_{I+\frac{1}{2},J} \right) \\ -\eta_{I-\frac{1}{2},J+\frac{1}{2}} \left(u_{I-\frac{1}{2},J+1} - u_{I-\frac{1}{2},J} \right) + B'_{I,J+\frac{1}{2}} \end{pmatrix}}{a^{wp}_{I,J+\frac{1}{2}}} \tag{77}$$

$$\begin{aligned} B'_{I,J+\frac{1}{2}} &= -\frac{\mathrm{Ra}_T}{2} \left(T_{I,J+1} \delta z_{J+1} + T_{I,J} \delta z_J \right) \delta x_I \\ &\quad -\frac{\mathrm{Rb}_W}{2} \left(C_{\mathrm{H_2O}I,J+1} \delta z_{J+1} + C_{\mathrm{H_2O}I,J} \delta z_J \right) \delta x_I + \cdots \end{aligned} \tag{78}$$

$$a^{up}_{I+\frac{1}{2},J} = a^{u\rightarrow}_{I+\frac{1}{2},J} + a^{u\leftarrow}_{I+\frac{1}{2},J} + a^{u\downarrow}_{I+\frac{1}{2},J} + a^{u\uparrow}_{I+\frac{1}{2},J} \tag{79}$$

$$a^{wp}_{I,J+\frac{1}{2}} = a^{w\rightarrow}_{I,J+\frac{1}{2}} + a^{w\leftarrow}_{I,J+\frac{1}{2}} + a^{w\downarrow}_{I,J+\frac{1}{2}} + a^{w\uparrow}_{I,J+\frac{1}{2}} \tag{80}$$

$$a^{u\rightarrow}_{I+\frac{1}{2},J} = 2\eta_{I+1,J} \frac{\delta z_J}{\delta x_{I+1}} \tag{81}$$

$$a^{u\leftarrow}_{I+\frac{1}{2},J} = 2\eta_{I,J} \frac{\delta z_J}{\delta x_I} \tag{82}$$

$$a^{u\downarrow}_{I+\frac{1}{2},J} = \eta_{I+\frac{1}{2},J+\frac{1}{2}} \frac{\delta x_{I+\frac{1}{2}}}{\delta z_{J+\frac{1}{2}}} \tag{83}$$

$$a^{u\uparrow}_{I+\frac{1}{2},J} = \eta_{I+\frac{1}{2},J-\frac{1}{2}} \frac{\delta x_{I+\frac{1}{2}}}{\delta z_{J-\frac{1}{2}}} \tag{84}$$

$$a^{w\rightarrow}_{I,J+\frac{1}{2}} = \eta_{I+\frac{1}{2},J+\frac{1}{2}} \frac{\delta z_{J+\frac{1}{2}}}{\delta x_{I+\frac{1}{2}}} \tag{85}$$

$$a^{w\leftarrow}_{I,J+\frac{1}{2}} = \eta_{I-\frac{1}{2},J+\frac{1}{2}} \frac{\delta z_{J+\frac{1}{2}}}{\delta x_{I-\frac{1}{2}}} \tag{86}$$

$$a^{w\downarrow}_{I,J+\frac{1}{2}} = 2\eta_{I,J+1} \frac{\delta x_I}{\delta z_{J+1}} \tag{87}$$

$$a^{w\uparrow}_{I,J+\frac{1}{2}} = 2\eta_{I,J} \frac{\delta x_I}{\delta z_J} \tag{88}$$

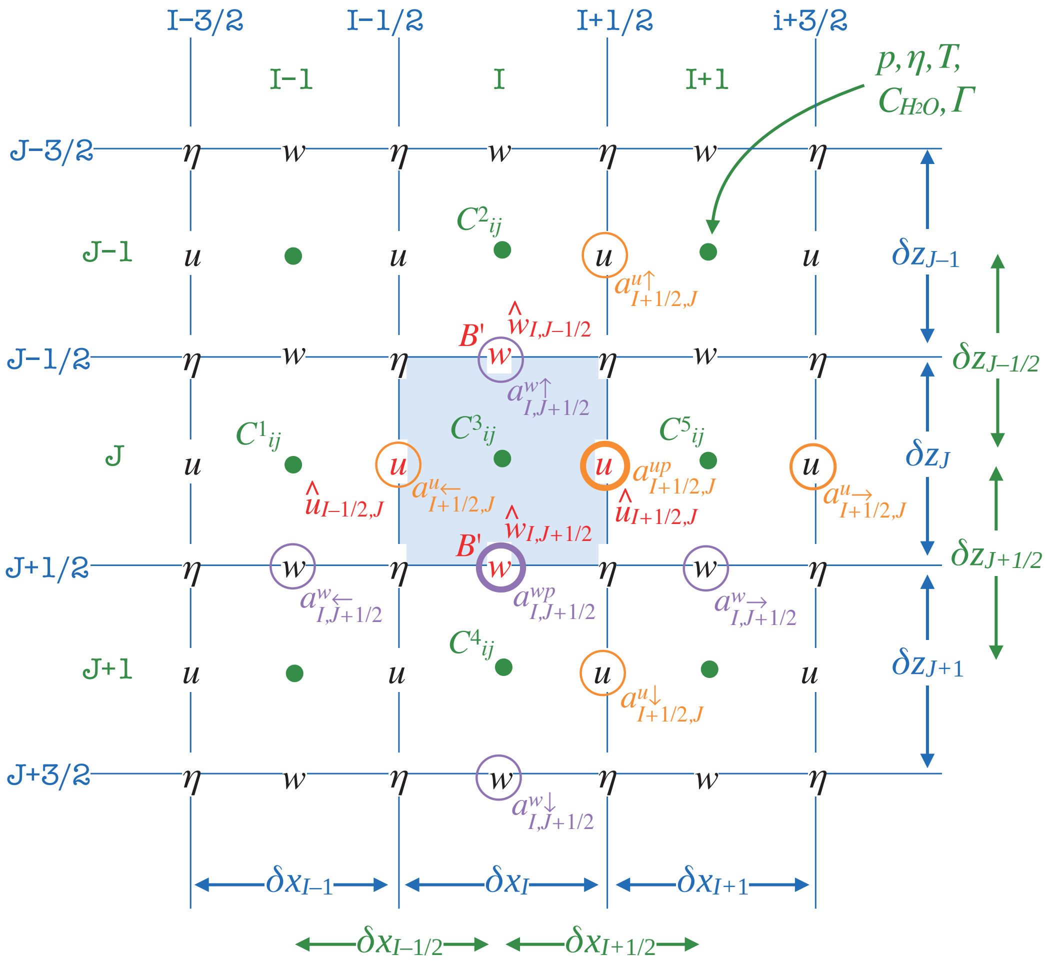

Figure 45: Staggered grid for solving dynamic pressure.

The modified Cholesky decomposition can be applied for solving this simultaneous equations because the matrix C is symmetric. Examples of the solution of this method are shown in Figures 11, 36, 37, 38, 39, and 40.

Appendix E: How to solve diffusion of hydrogen

Water in hydrous rock is transported not only advection of mantle but also hydrogen diffusion, i.e.,

$$\frac{DC_{\mathrm{H_2O}}}{Dt} = \kappa_{\mathrm{H_2O}} \nabla^2 C_{\mathrm{H_2O}}, \tag{89}$$

where D/Dt means a Lagrangian differentiation operator. Calculating diffusion term ($\kappa_{\mathrm{H_2O}} \nabla^2 C_{\mathrm{H_2O}}$) by using an Eulerian grid is simple. However, because water transportation is calculated by Lagrangian markers in this study, converting water content between nodes and markers at every time step leads to a severe numerical diffusion. To avoid it, the author introduces the moving-particle semi-implicit method (MPS; e.g., Koshizuka & Oka, 1996) only to calculate hydrogen diffusion term. The method is similar to the smoothed particle hydrodynamics (SPH; e.g., Gingold & Monaghan, 1982) in terms of using weight function, or kernel function, to calculate interaction between particles. While SPH can be applied for compressible fluid, MPS can be applied for incompressible fluid and is suitable for our simulation.

In the MPS method, the laplacian of a physical parameter ϕ of the i-th particle can be expressed as

$$\langle \nabla^2 \phi \rangle_i = \frac{2d}{\lambda n_0} \sum_j \Big[(\phi_j - \phi_i)\, w\left(|\mathbf{r}_j - \mathbf{r}_i|\right) \Big]. \tag{90}$$

d is the dimension of the numerical model ($d = 2$ in this study). j is the index of other particles around the particle i. $|\mathbf{r}_i - \mathbf{r}_j|$ is the distance between the i-th and j-th particles. $w(r)$ is a weight function depending on the particle distance r, usually defined by

$$w(r) = \begin{cases} \dfrac{R_e}{r} - 1 & (0 \le r \le R_e) \\ \quad 0 & (R_e < r), \end{cases} \tag{91}$$

and is shown in Figure 46. Statistical coefficient λ in (90) is defined by

$$\lambda = \frac{\sum_j |\mathbf{r}_j - \mathbf{r}_i|^2 w\left(|\mathbf{r}_j - \mathbf{r}_i|\right)}{\sum_j w\left(|\mathbf{r}_j - \mathbf{r}_i|\right)}. \tag{92}$$

n_0 in (90) is the density of the particles,

$$n_i = \sum_j w\left(|\mathbf{r}_j - \mathbf{r}_i|\right) = n_0, \tag{93}$$

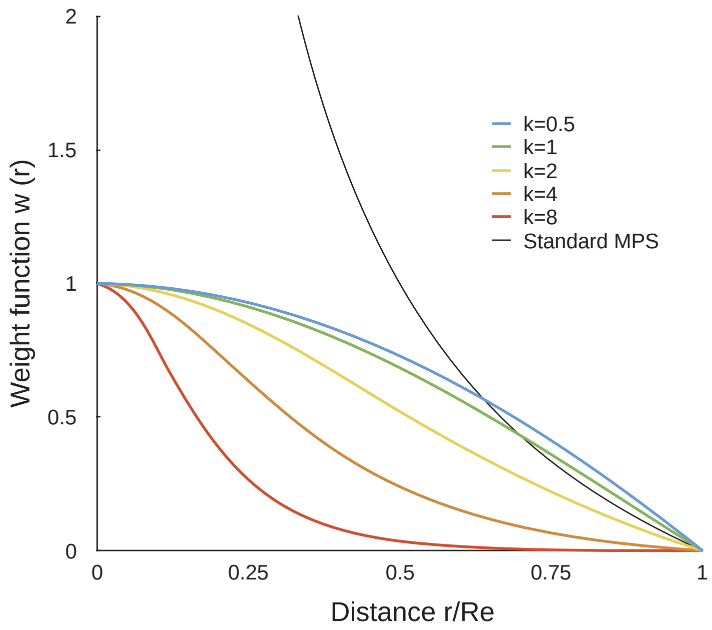

Figure 46: Weight function $w(r)$ to calculate interaction between markers with a distance of r in a MPS method. Black line shows standard-type $w(r)$ defined in Equation (91), and colored lines show hyperbolic-type $w(r)$ with different k in Equation (94).

and is constant in the compressible fluid.

Essentially, Gaussian-type weight function $w(r)$ gives the true value of the laplacian; however, it requires calculation of the interaction between far distant particles. To save computational time, $w(r)$ defined in Equation (91) is generally used in MPS, and interaction between particles with a distance larger than an effective radius R_e is ignored. Even if $w(r)$ is not Gaussian, the solution would converge to gaussian distribution as the time steps progress according to the central limit theorem.

In this study, searching particle pairs requires much computational time because of the huge number of Marker-in-Cell particles ($\sim 10^8$). In order to save the searching time, node values around i-th particle are adopted as the values of j-th particles (Figure 47). In this case, $w(r)$ may diverges to infinity where the i-th particle is near one of the j-th nodes because there is no repulsive force between them. Therefore the author applies hyperbolic-type weight function (Kakuda et al., 2014), which does not diverge at $r = 0$,

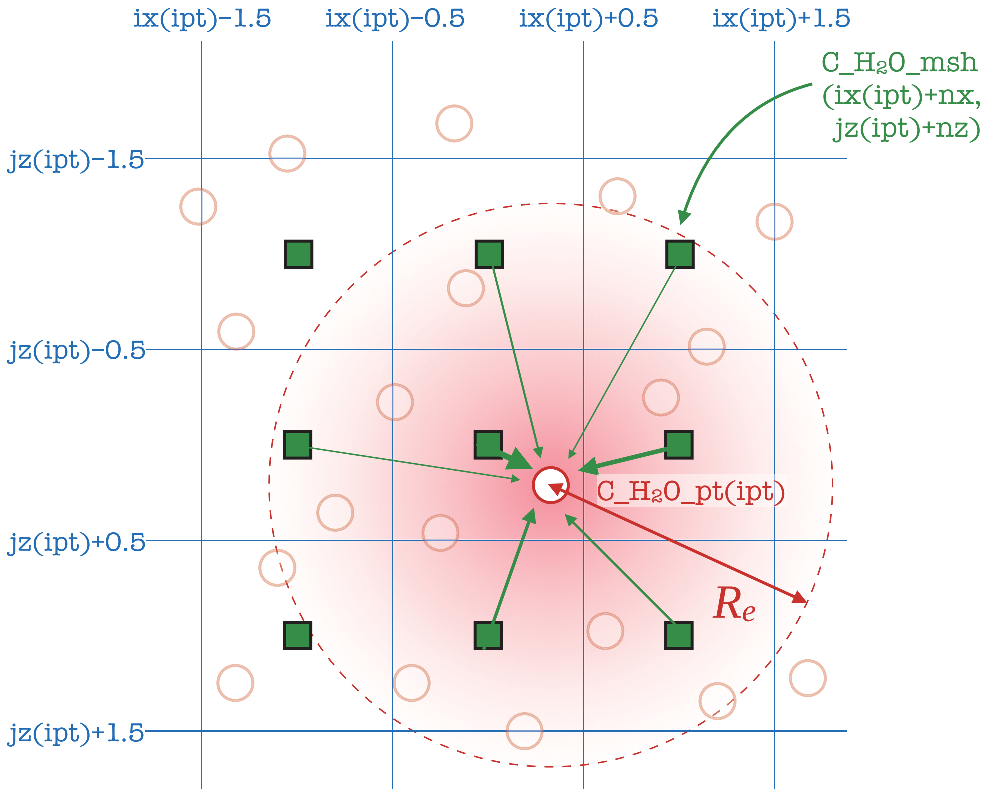

Figure 47: Schematic of grid-marker relation to calculate laplacian of water content by using a MPS method. Water content change at a marker (red circle) is the sum of water flux from green squares located at the centers of nodes within a dashed red line ($r < R_e$).

defined by

$$w(r) = \begin{cases} \dfrac{\mathrm{sech}^2 \dfrac{kr}{R_e} - \mathrm{sech}^2 k}{1 - \mathrm{sech}^2 k} & (0 \leq r \leq R_e) \\ 0 & (R_e < r). \end{cases} \tag{94}$$

The graph of the function is shown in Figure 46. The author uses $k = 2$ and $R_e = 3.75$ [km] for the simulation in Chapter III.

Appendix F: Effects of olivine metastability on subduction dynamics

Metastable olivine, which may exist around the 410-km phase boundary in the core of a subducting old oceanic plate, is a possible factor in changes of subduction rates and slab shapes due to its buoyancy (Schmeling et al., 1999; Tetzlaff & Schmeling, 2000). Here the author introduces the olivine metastability as shown in Figure 48 according to Schmeling et al. (1999) and Tetzlaff & Schmeling (2000):

$$\Gamma_{410}, \Gamma_{660} = \begin{cases} 0 & (T < 873\,\mathrm{K}) \\ 0.01 \times T - 873 & (873\,\mathrm{K} \leq T \leq 973\,\mathrm{K}) \\ 1 & (973\,\mathrm{K} < T) \end{cases} \tag{95}$$

where T is absolute temperature, and Γ_{410} (Γ_{660}) is phase change function for the Ol/Wd (Ol/Brdg) transition, which reflects on density increase in Equation (19) and adiabatic heating in Equation (3). Compared with Γ_{410} (Γ_{660}) calculated by Equation (4), the smaller one is adopted for each node.

Other settings are the same as those of run r1b0 (Chapter II). The initial thermal age of the subducting plate is 100 Ma at the trench (Figure 3). High p–T experiments have shown that water enhances the transition of metastable olivine into wadsleyite (e.g., Hosoya et al., 2005), but the effect is not considered in the simulation because the slab core where metastable olivine is expected to exist does not contain water in the numerical setting (Figure 49b). If the depth of the oceanic lithosphere is more hydrous, we should incorporate the effect.

The results of the further run are shown in Figures 49 and 50. At the initial stage (7.29 Myr of Figure 49), the slab tip is hot so that the metastable olivine is not generated. Some time is required for the generation of metastable olivine (11.25 Myr of Figure 49) and then trench retreat has already begun; therefore, the retreat rate and timing are scarcely affected (Figure 50b). Slab descent rate is also scarcely affected even if the metastable olivine exists (after 10 Myr; Figure 50a); probably because, the second peak of the descent velocity is induced by slab bending into downward convex at the depth of 200–300 km, and the metastable olivine wedge at the depth of 410 km hardly contributes to the bending, compared to the buoyancy of the hydrous wedge mantle as discussed in Chapter II.

Thus our results show that the influences of metastable olivine wedge in the slab core

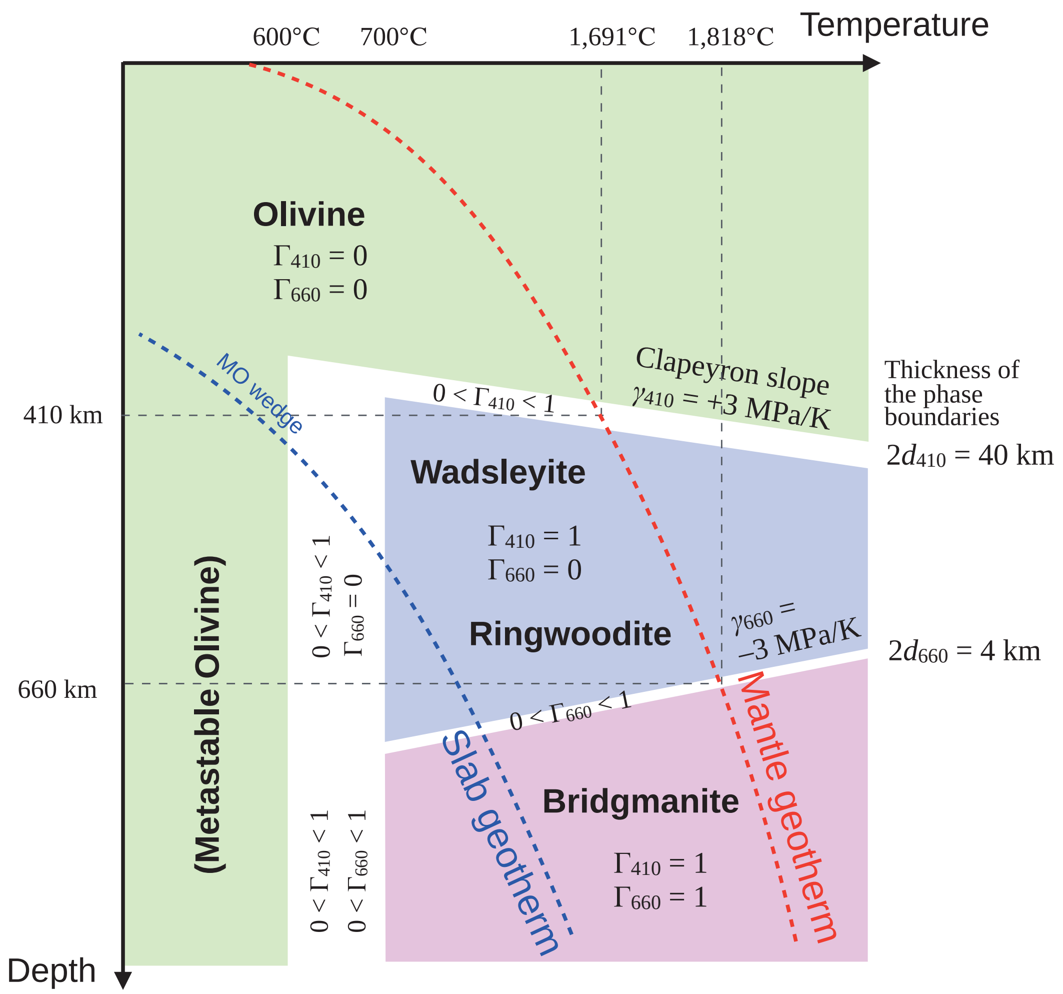

Figure 48: A schematic phase relation diagram in this appendix to calculate phase functions Γ_{410} and Γ_{660}, which affect density increase in Equation (19) and adiabatic heating in Equation (3). Not colored (white) areas indicate gradual phase changes ($0 < \Gamma_i < 1$). Around the depth of 410 km, cold slab core is capable of metastable olivine (blue dashed line), while surrounding hot mantle is not (red dashed line).

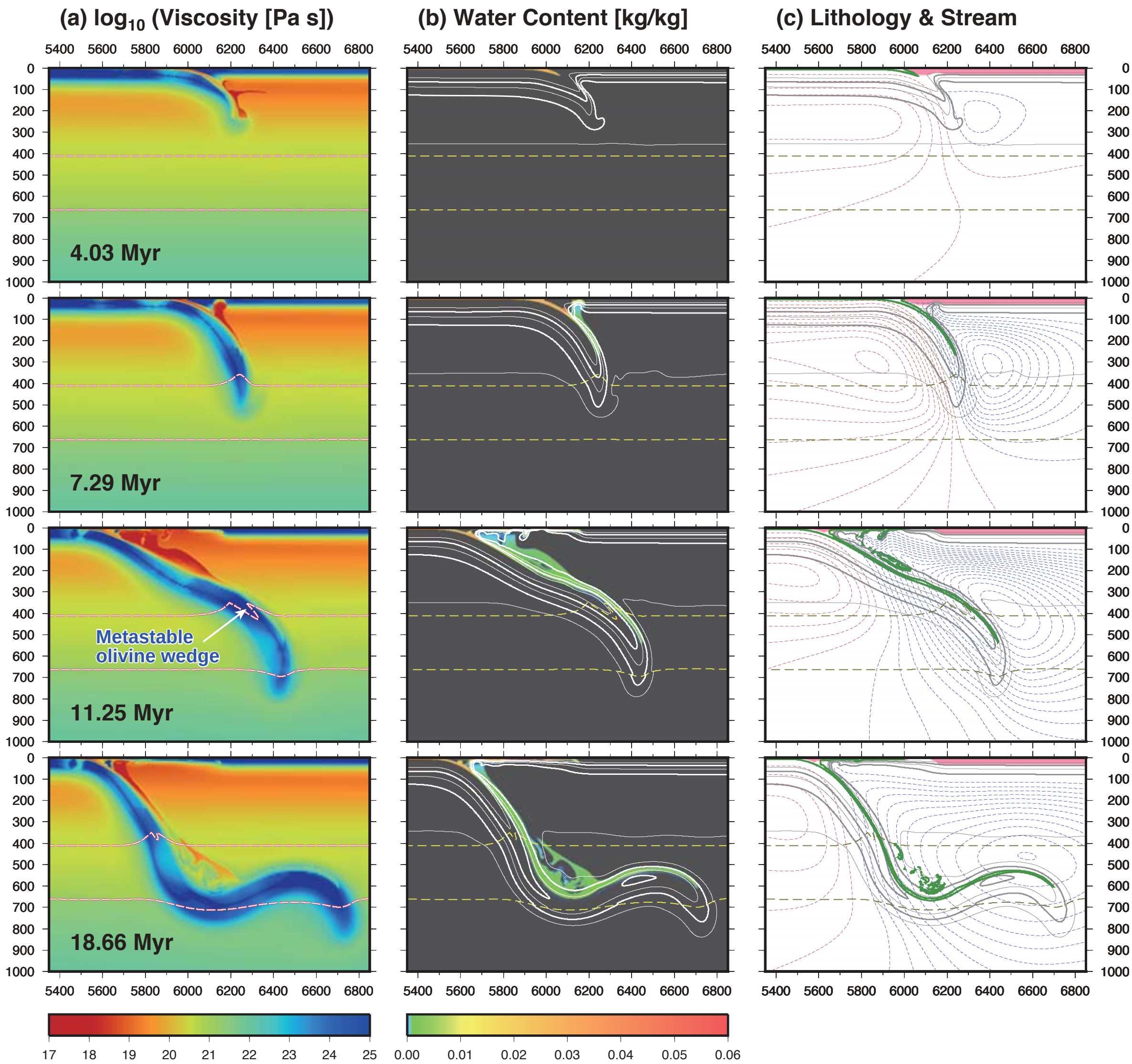

Figure 49: Evolution of run r1b0 with metastable olivine. (a) The colored contour shows viscosity structure. Dashed red lines represent the 410- and 660-km phase boundaries. (b) The colored contour shows the weight fraction of water in rocks. White lines represent isotherms (200°C intervals). (c) Pink and green areas show continental granite and oceanic basalt, respectively. Red and blue dotted lines are clockwise ($\psi > 0$) and counterclockwise ($\psi < 0$) stream functions (5×10^{-5} [m^2/s] intervals), respectively.

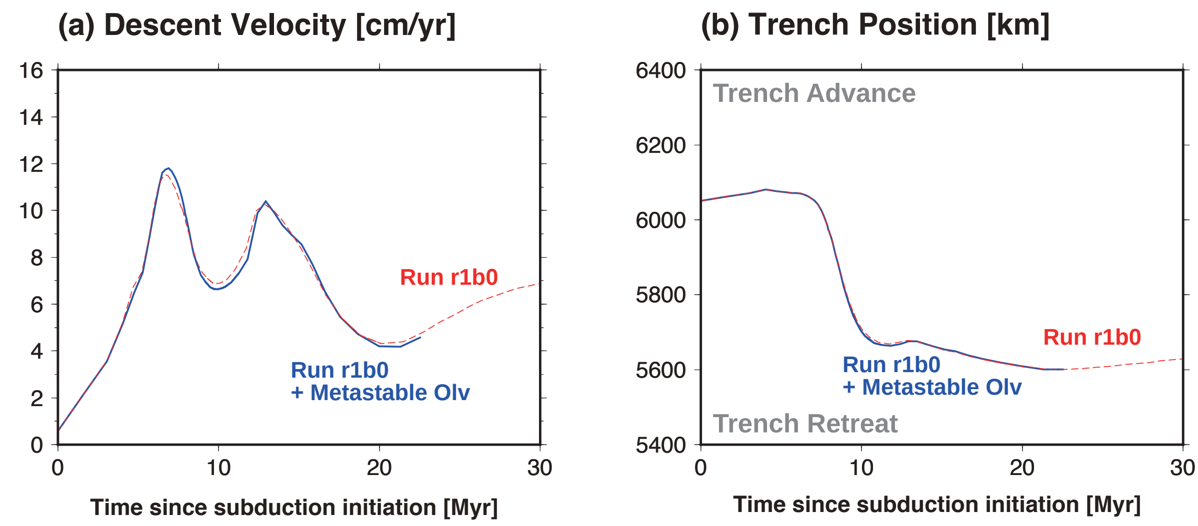

Figure 50: Time-dependent maximum descent (vertical) velocity at a depth of 300 km for Run r1b0 (No metastable olivine; red dashed lines) in Chapter II and Run r1b0 with metastable olivine (blue solid line). (c) Time-dependent lateral positions of the trench for the runs. A decline of the vertical value represents trench retreat, and an increase represents trench advance.

is much small on the subduction rate and the slab shape in the case of the oceanic plate age of 100 Myr. Contrary, if the oceanic slab is older than 100 Myr, subduction becomes much slow (Schmeling et al., 1999; Tetzlaff & Schmeling, 2000) because the stability range of metastable olivine is extended. Our result with the smaller stability field of metastable olivine favors the estimation of the slab temperature of Yamasaki & Seno (2003), who attribute double seismic zones at the depth of 70–300 km to decomposition of hydrous minerals (e.g., serpentine) at $\sim 600°$C

References

Akaogi, M., & Ito, E. (1993). Refinement of enthalpy measurement of $MgSiO_3$ perovskite and negative pressure-temperature slopes for Perovskite-forming reactions. *Geophys. Res. Lett.*, *20*, 1839–1842.

Allègre, C. J., Lewin, E., & Dupré, B. (1988). A coherent crust-mantle model for the uranium-thorium-lead isotopic system. *Chemical Geology*, *70*, 211–234.

Allègre, C. J., Staudacher, T., & Sarda, P. (1987). Rare gas systematics: formation of the atmosphere, evolution and structure of the Earth's mantle. *Earth and Planetary Science Letters*, *81*, 127–150.

Arcay, D., Tric, E., & Doin, M. P. (2005). Numerical simulations of subduction zones: effect of slab dehydration on the mantle wedge dynamics. *Phys. Earth Planet. Inter.*, *149*, 133–153.

Barker, D. S. (1983). *Igneous rocks*. Prentice Hall.

Bercovici, D., & Karato, S. (2003). Whole-mantle convection and the transition-zone water filter. *Nature*, *425*, 39–44.

Bercovici, D., Schuber, G., & Glatzmaier, G. A. (1989). Three-dimensional spherical models of convection in the Earth's mantle. *Science*, *244*, 950–955.

Berglund, M., & Wieser, M. E. (2011). Isotopic Compositions of the Elements 2009 (IUPAC Technical Report). *Pure Appl. Chem.*, *83*, 397–420.

Billen, M. I. (2010). Slab dynamics in the transition zone. *Physics of the Earth and Planetary Interiors*, *183*, 296–308.

Bizzarri, A., & Cocco, M. (2006). A thermal pressurization model for the spontaneous dynamic rupture propagation on a three-dimensional fault: 1. Methodological approach. *J. Geophys. Res.*, *111*, B05303.

Bolfan-Casanova, N., Keppler, H., & Rubie, D. C. (2003). Water partitioning at 660 km depth and evidence for very low water solubility in magnesium silicate perovskite. *Geophysical Research Letters*, *30*, 1905.

Buiter, S., & Ellis, S. (2012). Sulec: Benchmarking a new ale finite-element code. *EGU General Assembly*, (p. 7528).

Bureau, H., & Keppler, H. (1999). Complete miscibility between silicate melts and hydrous fluids in the upper mantle: experimental evidence and geochemical implications. *Earth and Planetary Science Letters*, *165*, 187–196.

Byerlee, J. (1978). Friction of rocks. *Pure Appl. Geophys.*, *116*, 615–626.

Cao, A., & Romanowicz, B. (2004). Hemispherical transition of seismic attenuation at the top of the earth's inner core. *Earth and Planetary Science Letters*, *228*, 243–253.

Chase, C. G. (1981). Oceanic island Pb: Two-stage histories and mantle evolution. *Earth and Planetary Science Letters*, *52*, 277–284.

Chauvel, C., Hofmann, A. W., & Vidal., P. (1992). HIMU-EM: the French Polynesian connection. *Earth and Planetary Science Letters*, *110*, 99–119.

Christensen, U., & Harder, H. (1991). 3-d convection with variable viscosity. *Geophysical Journal International*, *104*, 213–226.

Christensen, U. R. (1984). Convection with pressure- and temperature-dependent non-Newtonian rheology. *Geophys. J.: R. Astron. Soc.*, *77*, 343–384.

Christensen, U. R. (1989). Mixing by time-dependent convection. *Earth and Planetary Science Letters*, *95*, 382–394.

Christensen, U. R. (1996). The influence of trench migration on slab penetration into the lower mantle. *Earth and Planetary Science Letters*, *140*, 27–39.

Christensen, U. R., & Yuen, D. A. (1985). Layered convection induced by phase transitions. *J. Geophys. Res.*, *90*, 10291–10300.

Čížková, H., & Bina, C. R. (2013). Effects of mantle and subduction-interface rheologies on slab stagnation and trench rollback. *Earth and Planetary Science Letters*, *379*, 95–103.

Čížková, H., & Bina, C. R. (2015). Geodynamics of trench advance: Insights from a Philippine-Sea-style geometry. *Earth and Planetary Science Letters*, *430*, 408–415.

Clauser, C., & Huenges, E. (1995). Thermal conductivity of rocks and minerals. *Rock physics and phase relations: a handbook of physical constants*, (pp. 105–126).

Clauser, C., & Kiesner, S. (1987). A conservative, unconditionally stable, second-order three-point differencing scheme for the diffusion−convection equation. *Geophys. J. Int.*, *91(3)*, 557–568.

Conrad, C. P., & Lithgow-Bertelloni, C. (2007). Faster seafloor spreading and lithosphere production during the mid-Cenozoic. *Geology*, *35:1*, 29–32.

Corgne, A., Liebske, C., Wood, B. J., Rubie, D. C., & Frost, D. J. (2005). Silicate perovskite-melt partitioning of trace elements and geochemical signature of a deep perovskitic reservoir. *Geochimica et Cosmochimica Acta*, *69*, 485–496.

Courtier, A. M., & Revenaugh, J. (2007). Deep upper-mantle melting beneath the Tasman and Coral Seas detected with multiple *ScS* reverberations. *Earth and Planetary Science Letters*, *259*, 66–76.

Cserepes, L. (1982). Numerical studies of non-Newtonian mantle convection. *Physics of the Earth and Planetary Interiors*, *30*, 49–61.

Ding, L., Kapp, P., Zhong, D., & Deng, W. (2003). Cenozoic Volcanism in Tibet: Evidence for a Transition from Oceanic to Continental Subduction. *J. Petrol.*, *44*, 1833–1865.

Dupré, B., & Allègre, C. J. (1983). Pb–Sr isotope variation in Indian Ocean basalts and mixing phenomena. *Nature*, *303*, 142–146.

Dziewonski, A. M., & Anderson, D. L. (1981). Preliminary reference Earth model. *Physics of the Earth and Planetary Interiors*, *25*, 297–356.

Emry, E. L., Nyblade, A. A., Julià, J., Anandakrishnan, S., Aster, R. C., Wiens, D. A., Huerta, A. D., & Wilson, T. J. (2015). The mantle transition zone beneath West Antarctica: Seismic evidence for hydration and thermal upwellings. *Geochem. Geophys. Geosyst.*, *16*, 40–58.

Faccenda, M., Gerya, T. V., Mancktelow, N. S., & Moresi, L. (2012). Fluid flow during slab unbending and dehydration: Implications for intermediate-depth seismicity, slab weakening and deep water recycling. *Geochem. Geophys. Geosyst.*, *13*, Q01010.

Fei, H., Wiedenbeck, M., Yamazaki, D., & Katsura, T. (2013). Small effect of water on upper-mantle rheology based on silicon self-diffusion coefficients. *Nature*, *498*, 213–215.

Ferrachat, S., & Ricard, Y. (1998). Regular vs. chaotic mantle mixing. *Earth and Planetary Science Letters*, *155*, 75–86.

Fryer, P., Ambos, E. L., & Hussong, D. M. (1985). Origin and emplacement of mariana forearc seamounts. *Geology*, *13*, 774–777.

Fujita, K., & Ogawa, M. (2013). A preliminary numerical study on water-circulation in convecting mantle with magmatism and tectonic plates. *Physics of the Earth and Planetary Interiors*, *216*, 1–11.

Fukao, Y., Obayashi, M., & Nakakuki, T. (2009). Stagnant slab: A review. *Annu. Rev. Earth Planet. Sci.*, *37*, 19–46.

Gerya, T. V., & Meilick, F. I. (2011). Geodynamic regimes of subduction under an active margin: effects of rheological weakening by fluids and melts. *J. metamorphic Geol.*, *29*, 7–31.

Gerya, T. V., & Yuen, D. A. (2007). Robust characteristics method for modelling multiphase visco-elasto-plastic thermo-mechanical problems. *Phys. Earth and Planet. Inter.*, *163*, 83–105.

Gingold, R. A., & Monaghan, J. J. (1982). Kernel estimates as a basis for general particle methods in hydrodynamics. *J. Comput. Phys.*, *46*, 429–.

Goldstein, S. L., O'Nions, R. K., & Hamilton, P. J. (1984). A Sm–Nd study of atmospheric dusts and particulates from major river systems. *Earth and Planetary Science Letters*, *70*, 221–236.

Gurnis, M., & Davies, G. F. (1986). Mixing in numerical models of mantle convection incorporating plate kinematics. *J. Geophys. Res.*, *91*, 6375–6395.

Hafkenscheid, E., Wortel, M. J. R., & Spakman, W. (2006). Subduction history of the Tethyan region derived from seismic tomography and tectonic reconstructions. *J. Geophys. Res.*, *111*, B08401.

Hart, S. R. (1984). A large-scale isotope anomaly in the Southern Hemisphere mantle. *Nature*, *309*, 753–757.

Hart, S. R., Gerlach, D. C., & White., W. M. (1986). A possible new Sr-Nd-Pb mantle array and consequences for mantle mixing. *Geochimica et Cosmochimica Acta*, *50*, 1551–1557.

Hart, S. R., Hauri, E. H., Oschmann, L. A., & Whitehead, J. A. (1992). Mantle Plumes and Entrainment: Isotopic Evidence. *Science*, *256*, 517–520.

Hauri, E. H., Shimizu, N., Dieu, J. J., & Hart, S. R. (1993). Evidence for hotspot-related carbonatite metasomatism in the oceanic upper mantle. *Nature*, *365*, 221–227.

Hebert, L. B., Antoshechkina, P., Asimow, P., & Gurnis, M. (2009). Emergence of a low-viscosity channel in subduction zones through the coupling of mantle flow and thermodynamics. *Earth and Planetary Science Letters*, *278*, 243–256.

Heuret, A., & Lallemand, S. (2005). Plate motions, slab dynamics and back-arc deformation. *Physics of the Earth and Planetary Interiors*, *149*, 31–51.

Hirose, K., Shimizu, N., van Westrenen, W., & Fei, Y. (2004). Trace element partitioning in Earth's lower mantle and implications for geochemical consequences of partial melting at the core–mantle boundary. *Phys. Earth and Planet. Inter.*, *146*, 249–260.

Hirth, G., & Kohlstedt, D. (2003). Rheology of the upper mantle and the mantle wedge: A view from the experimentalists. *Inside the Subduction Factory, edited by J. Eiler*, (pp. 83–105).

Hoffman, N. R. A., & McKenzie., D. P. (1985). The destruction of geochemical heterogeneities by differential fluid motions during mantle convection. *Geophys. J. Int.*, *82*, 163–206.

Horiuchi, S., & Iwamori, H. (2016). A consistent model for fluid distribution, viscosity distribution, and flow-thermal structure in subduction zone. *J. Geophys. Res. Solid Earth*, *121*, 3238–3260.

Hosoya, T., Kubo, T., Ohtani, E., Sano, A., & Funakoshi, K. (2005). Water controls the fields of metastable olivine in cold subducting slabs. *Geophys. Res. Lett.*, *32*, L17305.

Ikemoto, A., & Iwamori, H. (2014). Numerical modeling of trace element transportation in subduction zones: implications for geofluid processes. *Earth, Planets and Space*, *66:26*.

Inoue, T., Kakizawa, S., Fujino, K., Kuribayashi, T., Nagase, T., Greaux, S., Higo, Y., Sakamoto, N., Yurimoto, H., Hattori, T., & Sano, A. (2016). Hydrous bridgmanite: Possible water reservior in the lower mantle. *Goldschmidt 2016, Yokohama*, *Session 04c*.

Inoue, T., Weidner, D. J., Northrup, P. A., & Parise, J. B. (1998). Elastic properties of hydrous ringwoodite (γ-phase) in Mg_2SiO_4. *Earth Planet. Sci. Lett.*, *160*, 107–113.

Inoue, T., Yurimoto, H., & Kudoh, Y. (1995). Hydrous modified spinel, $Mg_{1.75}SiH_{0.5}O_4$: a new water reservoir in the mantle transition region. *Geophys. Res. Lett.*, *22*, 117–120.

Ishiwatari, A., & Tsujimoto, T. (2003). Paleozoic ophiolites and blueschists in Japan and Russian Primorye in the tectonic framework of East Asia: A synthesis. *Island Arc*, *12*, 190–206.

Iwamori, H. (1998). Transportation of H_2O and melting in subduction zones. *Earth and Planetary Science Letters*, *160*, 65–80.

Iwamori, H. (2007). Transportation of H_2O beneath the Japan arcs and its implications for global water circulation. *Chemical Geology*, *239*, 182–198.

Iwamori, H., Albarede, F., & Nakamura, H. (2010). Global structure of mantle isotopic heterogeneity and its implications for mantle differentiation and convection. *Earth and Planetary Science Letters*, *299*, 339–351.

Iwamori, H., & Nakakuki, T. (2013). Fluid Processes in Subduction Zones and Water Transport to the Deep Mantle. *Physics and Chemistry of the Deep Earth, First Edition*, (pp. 372–391).

Iwamori, H., & Nakamura, H. (2012). East-west mantle geochemical hemispheres constrained from Independent Component Analysis of basalt isotopic compositions. *Geochemical Journal*, *46*, e39–e46.

Iwamori, H., & Nakamura, H. (2015). Isotopic heterogeneity of oceanic, arc and continental basalts and its implications for mantle dynamics. *Gondwana Research*, *27*, 1131–1152.

Jacobsen, S. D., Jiang, F., Mao, Z., Duffy, T. S., Smyth, J. R., Holl, C. M., & Frost, D. J. (2008). Effects of hydration on the elastic properties of olivine. *Geophys. Res. Lett.*, *35*, L14303.

Kakuda, K., Hayashi, Y., & Toyotani, J. (2014). Particle-based Simulations of Flows with Free Surfaces Using Hyperbolic-type Weighting Functions. *Computer Modeling in Engineering and Sciences*, *103*, 229–249.

Karato, S. (2008). *Deformation of Earth Materials*. Cambridge University Press.

Karato, S. (2011). Water distribution across the mantle transition zone and its implications for global material circulation. *Earth and Planetary Science Letters*, *301*, 413–423.

Karato, S., & Jung, H. (1998). Water, partial melting and the origin of seismic low velocity and high attenuation zone in the upper mantle. *Earth and Planetary Science Letters*, *157*, 193–207.

Karato, S., & Jung, H. (2003). Effects of pressure on high-temperature dislocation creep in olivine. *Philosophical Magazine*, *83:3*, 401–414.

Karato, S., & Wu, P. (1993). Rheology of the Upper Mantle: A Synthesis. *Science*, *260*, 771–778.

Katsura, T., & Ito, E. (1989). The system Mg_2SiO_4-Fe_2SiO_4 at high pressures and temperatures: Precise determination of stabilities of olivine, modified spinel, and spinel. *J. Geophys. Res.*, *94*, 15663–15670.

Katsura, T., Yamada, H., Nishikawa, O., Song, M., Kubo, A., Shinmei, T., Yokoshi, S., Aizawa, Y., Yoshino, T., Walter, M. J., Ito, E., & Funakoshi, K. (2004). Olivine-wadsleyite transition in the system $(Mg,Fe)_2SiO_4$. *J. Geophys. Res.*, *109*, B02209.

Katsura, T., Yamada, H., Shinmei, T., Kubo, A., Ono, S., Kanzaki, M., Yoneda, A., Walter, M. J., Ito, E., Urakawa, S., Funakoshi, K., & Utsumi, W. (2003). Post-spinel transition in Mg_2SiO_4 determined by high P–T in situ X-ray diffractometry. *Phys. Earth and Planet. Inter.*, *136*, 11–24.

Kawamoto, T. (2004). Hydrous phase stability and partial melt chemistry in H_2O-saturated KLB-1 peridotite up to the uppermost lower mantle conditions. *Phys. Earth and Planet. Inter.*, *143-144*, 387–395.

Kawamoto, T., Herving, R. L., & Holloway, J. R. (1996). Experimental evidence for a hydrous transition zone in the early Earth's mantle. *Earth and Planetary Science Letters*, *142*, 587–592.

Kellogg, L. H., & Turcotte, D. L. (1990). Mixing and the distribution of heterogeneities in a chaotically convecting mantle. *J. Geophys. Res.*, *95*, 421–432.

Kessel, R., Schmidt, M. W., Ulmer, P., & Pettke, T. (2005). Trace element signature of subduction-zone fluids, melts and supercritical liquids at 120–180 km depth. *Nature*, *437*, 724–727.

Kimura, J.-i., Hacker, B. R., van Keken, P. E., Kawabata, H., Yoshida, T., & Stern, R. J. (2009). Arc Basalt Simulator version 2, a simulation for slab dehydration and fluidfluxed mantle melting for arc basalts: Modeling scheme and application. *Geochem. Geophys. Geosyst.*, *10*, Q09004.

Kind, R., Yuan, X., Saul, J., Nelson, D., Sobolev, S. V., Mechie, J., Zhao, W., Kosarev, G., Ni, J., Achauer, U., & Jiang, M. (2002). Seismic Images of Crust and Upper Mantle Beneath Tibet: Evidence for Eurasian Plate Subduction. *Science*, *298*, 1219–1221.

King, S. D., Raefsky, A., & Hager, B. H. (1990). ConMan: Vectorizing a finite element code for incompressible two-dimensional convection in the Earth's mantle. *Physics of the Earth and Planetary Interiors*, *59*, 195–207.

Kogiso, T., Tatsumi, Y., & Nakano, S. (1997). Trace element transport during dehydration processes in the subducted oceanic crust: 1. Experiments and implications for the origin of ocean island basalts. *Earth and Planetary Science Letters*, *148*, 193–205.

Kohlstedt, D. L., Evans, B., & Mackwell, S. J. (1995). Strength of the lithosphere: constraints provided by the experimental deformation of the rocks. *J. Geophys. Res.*, *100*, 17587–17602.

Kohlstedt, D. L., Keppler, H., & Rubie, D. C. (1996). Solubility of water in the α , β and γ phases of $(\mathrm{Mg}, \mathrm{Fe})_2\mathrm{SiO}_4$. *Contributions to Mineralogy and Petrology*, *123*, 345–357.

Korenaga, J., & Karato, S. (2008). A new analysis of experimental data on olivine rheology. *J. Geophys. Res.*, *113*, B02403.

Koshizuka, S., & Oka, Y. (1996). Moving-Particle Semi-Implicit Method for Fragmentation of Incompressible Fluid. *Nuclear Science and Engineering*, *123*, 421–434.

Lallemand, S., Heuret, A., & Boutelier, D. (2005). On the relationships between slab dip, back-arc stress, upper plate absolute motion, and crustal nature in subduction zones. *Geochem. Geophys. Geosyst.*, *6*, Q09006.

Lallemand, S., Heuret, A., Faccenna, C., & Funiciello, F. (2008). Subduction dynamics as revealed by trench migration. *Tectonics*, *27*, TC3014.

Van der Lee, S., Regenauer-Lieb, K., & Yuen, D. A. (2008). The role of water in connecting past and future episodes of subduction. *Earth Planet. Sci. Lett.*, *273*, 15–27.

Li, Z. X., Bogdanova, S. V., Collins, A. S., Davidson, A., De Waele, B., Ernst, R. E., Fitzsimons, I. C. W., Fuck, R. A., Gladkochub, D. P., Jacobs, J., Karlstrom, K. E., Lu, S., Natapov, L. M., Pease, V., Pisarevsky, S. A., Thrane, K., & Vernikovsky, V. (2008). Assembly, configuration, and break-up history of Rodinia: a synthesis. *Precambrian Research*, *160*, 179–210.

Liu, Z., Park, J., & Karato, S. (2016). Seismological detection of low-velocity anomalies surrounding the mantle transition zone in Japan subduction zone. *Geophys. Res. Lett.*, *43*.

Mackwell, S. J., & Kohlstedt, D. L. (1990). Diffusion of hydrogen in olivine: Implications for water in the mantle. *J. Geophys. Res.*, *95*, 5079–5088.

Mallard, C., Coltice, N., Seton, M., Müller, R. D., & Tackley, P. J. (2016). Subduction controls the distribution and fragmentation of Earth's tectonic plates. *Nature*, *535*, 140–143.

Mao, Z., Jacobsen, S. D., Jiang, F., Smyth, J. R., Holl, C. M., & Duffy, T. S. (2008).

Elasticity of hydrous wadsleyite to 12GPa: implications for Earth's transition zone. *Geophys. Res. Lett.*, *35*, L21305.

Maruyama, S., & Okamoto, K. (2007). Water transportation from the subducting slab into the mantle transition zone. *Gondwana Research*, *11*, 148–165.

Masuti, S., Barbot, S. D., i. Karato, S., Feng, L., & Banerjee, P. (2016). Upper-mantle water stratification inferred from observations of the 2012 Indian Ocean earthquake. *Nature*, *538*, 373–377.

McCulloch, M. T., & Black, L. P. (1984). Sm–Nd isotopic systematics of Enderby Land granulites and evidence for the redistribution of Sm and Nd during metamorphism. *Earth and Planetary Science Letters*, *71*, 46–58.

McKenzie, D. (1984). The generation and compaction of partially molten rock. *J. Petrol.*, *25*, 713–765.

Mével, C. (2003). Serpentinization of abyssal peridotites at mid-ocean ridges. *Comptes Rendus Geoscience*, *335*, 825–852.

Mibe, K., Kanzaki, M., Kawamoto, T., Matsukage, K. N., Fei, Y., & Ono, S. (2007). Second critical endpoint in the peridotite-H_2O system. *J. Geophys. Res.*, *112*, B03201.

Milne, G. A., Mitrovica, J. X., & Davis, J. L. (1999). Near-field hydro-isostacy: the implementation of a revised sea-level equations. *Geophys. J. Int.*, *139*, 464–482.

Miyamoto, H., Tachibana, S., Hirata, N., & Sugita, S. (2008). *Planetary Geology*. University of Tokyo Press.

Moresi, L., & Solomatov, V. (1998). Mantle convection with brittle lithosphere: thoughts on the global styles of the Earth and Venus. *Geophys. J. Int.*, *133*, 669–682.

Murakami, M., Hirose, K., Yurimoto, H., Nakashima, S., & Takafuji, N. (2002). Water in the Earth's lower mantle. *Science*, *295*, 1885–1887.

Murphy, J. B., & Nance, R. D. (2003). Do supercontinents introvert or extrovert?: Sm–Nd isotopic evidence. *Geology*, *31*, 873–876.

Nakagawa, T., Nakakuki, T., & Iwamori, H. (2015). Water circulation and global mantle dynamics: Insight from numerical modeling. *Geochem. Geophys. Geosyst.*, *16*, 1449–1464.

Nakagawa, T., & Tackley, P. J. (2005). Deep mantle heat flow and thermal evolution of the Earth's core in thermochemical multiphase models of mantle convection. *Geochem. Geophys. Geosyst.*, *6*, Q08003.

Nakakuki, T., & Mura, E. (2013). Dynamics of slab rollback and induced back-arc basin formation. *Earth and Planetary Science Letters*, *361*, 287–297.

Nakao, A., Iwamori, H., & Nakakuki, T. (2016). Effects of water transportation on subduction dynamics: Roles of viscosity and density reduction. *Earth Planet. Sci. Lett.*, *454*, 178–191.

Nance, R. D., Murphy, J. B., & Santosh, M. (2014). The supercontinent cycle: A retrospective essay. *Gondwana Research*, *25*, 4–29.

Nishi, M., Irifune, T., Tsuchiya, J., Tange, Y., Nishihara, Y., Fujino, K., & Higo, Y. (2014). Stability of hydrous silicate at high pressures and water transport to the deep lower mantle. *Nature Geoscience*, *7*, 224–227.

Ohira, I., Ohtani, E., Kamada, S., & Hirao, N. (2016). Formation of Phase H – δ-AlOOH solid solution in the lower mantle. *Goldschmidt 2016, Yokohama*, *Poster board 41, in Session 04c*.

Ohira, I., Ohtani, E., Sakai, T., Miyahara, M., Hirao, N., Ohishi, Y., & Nishijima, M. (2014). Stability of a hydrous δ-phase, AlOOH-$MgSiO_2(OH)_2$, and a mechanism for water transport into the base of lower mantle. *Earth and Planetary Science Letters*, *401*, 12–17.

Ohtani, E., & Zhao, D. (2009). The role of water in the deep upper mantle and transition zone: dehydration of stagnant slabs and its effects on the big mantle wedge. *Russian Geology and Geophysics*, *50*, 1073–1078.

Okuno, J., & Nakada, M. (2001). Effects of water load on geophysical signals due to glacial rebound and implication for mantle viscosity. *Earth Planets Space*, *53*, 1121–1135.

Olson, P., Yuen, D. A., & Balsiger, D. (1984). Mixing of passive heterogeneities by mantle convection. *J. Geophys. Res.*, *89*, 425–436.

Panero, W. R., Pigott, J. S., Reaman, D. M., Kabbes, J. E., & Liu, Z. (2015). Dry (Mg,Fe)SiO_3 perovskite in the Earth's lower mantle. *J. Geophys. Res. Solid Earth*, *120*, 894–908.

Patankar, S. V. (1981). A calculation procedure for two-dimensional elliptic situations. *Numerical Heat Transfer*, *4*, 409–425.

Peacock, S. M. (2001). Are the lower planes of double seismic zones caused by serpentine dehydration in subducting oceanic mantle? *Geology*, *29*, 299–302.

Pearson, D. G., Brenker, F. E., Nestola, F., McNeill, J., Nasdala, L., Hutchison, M. T., Matveev, S., Mather, K., Silversmit, G., Schmitz, S., Vekemans, B., & Vincze, L. (2014). Hydrous mantle transition zone indicated by ringwoodite included within diamond. *Nature*, *507*, 221–224.

Quinquis, M. E. T., & Buiter, S. J. H. (2014). Testing the effects of basic numerical implementations of water migration on models of subduction dynamics. *Solid Earth*, *5*, 537–555.

Ranalli (1995). *Rheology of the Earth*. Springer Science and Business Media.

Ranero, C., & Sallarès, V. (2004). Geophysical evidence for hydration of the crust and mantle of the Nazca plate during bending at the north Chile trench. *Geology*, *32*, 549–552.

Raterron, P., Amiguet, E., Chen, J., Li, L., & Cordier, P. (2009). Experimental deformation of olivine single crystals at mantle pressures and temperatures. *Physics of the Earth and Planetary Interiors*, *172*, 74–83.

Regenauer-Lieb, K., Yuen, D. A., & Branlund, J. (2001). The initiation of subduction: criticality by addition of water? *Science*, *294*, 578–580.

Replumaz, A., Kárason, H., van der Hilst, R. D., Besse, J., & Tapponnier, P. (2004). 4-D evolution of SE Asia's mantle from geological reconstructions and seismic tomography. *Earth and Planetary Science Letters*, *221*, 103–115.

Richard, G. C., & Iwamori, H. (2010). Stagnant slab, wet plumes and Cenozoic volcanism in East Asia. *Physics of the Earth and Planetary Interiors*, *183*, 280–287.

Royden, L. H., & Husson, L. (2006). Trench motion, slab geometry and viscous stresses in subduction systems. *Geophys. J. Int.*, *167*, 881–905.

Rüpke, L. H., Morgana, J. P., Hortb, M., & Connolly, J. A. D. (2004). Serpentine and the subduction zone water cycle. *Earth and Planetary Science Letters*, *223*, 17–34.

Sakamaki, T., Suzuki, A., & Ohtani, E. (2006). Stability of hydrous melt at the base of the Earth's upper mantle. *Nature*, *439*, 192–194.

Schaber, G. G., Strom, R. G., Moore, H. J., Soderblom, L. A., Kirk, R. L., Chadwick, D. J., Dawson, D. D., Gaddis, L. R., Boyce, J. M., & Russell, J. (1992). Geology and distribution of impact craters on Venus: What are they telling us? *J. Geophys. Res.*, *97*, 13257–13301.

Schaeffer, A. J., & Bostock, M. G. (2010). A lowvelocity zone atop the transition zone in northwestern Canada. *J. Geophys. Res.*, *115*, B06302.

Schellart, W. P. (2005). Influence of the subducting plate velocity on the geometry of the slab and migration of the subduction hinge. *Earth and Planetary Science Letters*, *231*, 197–219.

Schellart, W. P. (2008). Kinematics and flow patterns in deep mantle and upper mantle subduction models: Influence of the mantle depth and slab to mantle viscosity ratio. *Geochem. Geophys. Geosyst.*, *9*, Q03014.

Schellart, W. P. (2011). A subduction zone reference frame based on slab geometry and subduction partitioning of plate motion and trench migration. *Geophys. Res. Lett.*, *38*, L16317.

Schellart, W. P., & Moresi, L. (2013). A new driving mechanism for backarc extension and backarc shortening through slab sinking induced toroidal and poloidal mantle flow: Results from dynamic subduction models with an overriding plate,. *J. Geophys. Res. Solid Earth*, *118*, 3221–3248.

Schmandt, B., Jacobsen, S. D., Becker, T. W., Liu, Z., & Dueker, K. G. (2014). Dehydration melting at the top of the lower mantle. *Science*, *344*, 1265–1268.

Schmeling, H., Marquart, G., & Ruedas, T. (2003). Pressure- and temperature-dependent thermal expansivity and the effect on mantle convection and surface observables. *Geophys. J. Int.*, *154*, 224–229.

Schmeling, H., Monz, R., & Rubie, D. C. (1999). The influence of olivine metastability on the dynamics of subduction. *Earth and Planetary Science Letters*, *165*, 55–66.

Seno, T., & Yamanaka, Y. (1998). Arc stresses determined by slabs: Implications for mechanisms of back-arc spreading. *Geophys. Res. Lett.*, *25*, 3227–3230.

Sigloch, K., McQuarrie, N., & Nolet, G. (2008). Two-stage subduction history under North America inferred from multiple-frequency tomography. *Nature Geoscience*, *1*, 458–462.

Stampfli, G. M., & Borel, G. D. (2004). The TRANSMED transects in space and time: Constraints on the paleotectonic evolution of the Mediterranean domain. *in The TRANSMED Atlas: The Mediterranean Region From Crust to Mantle, edited by W. Cavazza et al.*, (pp. 53–80).

Stegman, D. R., Farrington, R., Capitanio, F. A., & Schellart, W. P. (2010). A regime diagram for subduction styles from 3-D numerical models of free subduction. *Tectonophysics*, *483*, 29–45.

Steinberger, B., Sutherland, R., & O'Connell, R. J. (2004). Prediction of Emperor-Hawaii seamount locations from a revised model of global plate motion and mantle flow. *Nature*, *430*, 167–173.

Strom, R. G., Schaber, G. G., & Dawson, D. D. (1994). The global resurfacing of Venus. *J. Geophys. Res.*, *99*, 10899–10926.

Sun, T., Wang, K., Iinuma, T., Hino, R., He, J., Fujimoto, H., Kido, M., Osada, Y., Miura, S., Ohta, Y., & Hu, Y. (2014). Prevalence of viscoelastic relaxation after the 2011 Tohoku-oki earthquake. *Nature*, *514*, 84–87.

Sun, W., Yoshino, T., Sakamoto, N., & Yurimoto, H. (2015). Hydrogen self-diffusivity in single crystal ringwoodite: Implications for water content and distribution in the mantle transition zone. *Geophys. Res. Lett.*, *42*, 6582–6589.

Tackley, P. J. (2000). Self-consistent generation of tectonic plate in time-dependent, three-dimensional mantle convection simulations 1. Pseudoplastic yielding. *Geochem. Geophys. Geosyst.*, *1*.

Tackley, P. J. (2008). Modelling compressible mantle convection with large viscosity contrasts in a three-dimensional spherical shell using the yin-yang grid. *Phys. Earth and Planet. Inter.*, *171*, 7–18.

Tackley, P. J. (2009). Mantle Geochemical Geodynamics. *Treatise on geophysics 7: Mantle Dynamics*, *Chapter 10*, 437–505.

Tagawa, M., Nakakuki, T., Kameyama, M., & Tajima, F. (2007). The role of history-dependent rheology in plate boundary lubrication for generating one-sided subduction. *Pure and Applied Geophysics*, *164*, 1–29.

Tanaka, S., & Hamaguchi, H. (1997). Degree one heterogeneity and hemispherical variation of anisotropy in the inner core from *PKP* (BC)–*PKP* (DF) times. *J. Geophys. Res.*, *102*, 2925–2938.

Tatsumi, Y. (2005). The subduction factory: how it operates in the evolving Earth. *GSA today*, *15*, 4–10.

Taylor, S. R., & McLennan, S. M. (1985). *The Continental Crust: its Composition and Evolution*. Blackwell Oxford.

Tetzlaff, M., & Schmeling, H. (2000). The influence of olivine metastability on deep subduction of oceanic lithosphere. *Phys. Earth Planet. Inter.*, *120*, 29–38.

Tibi, R., Wiens, D. A., & Yuan, X. (2008). Seismic evidence for widespread serpentinized forearc mantle along the Mariana convergence margin. *Geophys. Res. Lett.*, *35*, L13303.

Torii, Y., & Yoshioka, S. (2007). Physical conditions producing slab stagnation: Constraints of the Clapeyron slope, mantle viscosity, trench retreat, and dip angles. *Tectonophysics*, *445*, 200–209.

Tsuchiya, J. (2013). First principles prediction of a new high-pressure phase of dense hydrous magnesium silicates in the lower mantle. *Geophys. Res. Lett.*, *40*, 4570–4573.

Turcotte, D. L., & Schubert, G. (2001). *Geodynamics*. Cambridge University Press.

Turner, S., Arnaud, N., Liu, L., Rogers, N., Hawkesworth, C., Harris, N., Kelley, S., Van Calsteren, P., & Deng, W. M. (1996). Post-collision, Shoshonitic Volcanism on the Tibetan Plateau: Implications for Convective Thinning of the Lithosphere and the Source of Ocean Island Basalts. *J. Petrol.*, *37*, 45–71.

Ulmschneider, P. (2005). *Intelligent life in the universe: principles and requirements behind its emergence*. Springer Science and Business Media.

Van der Voo, R., Spakman, W., & Bijwaard, H. (1999). Tethyan subducted slabs under India. *Earth and Planetary Science Letters*, *171*, 7–20.

Wannamaker, P. E., Caldwell, T. G., Jiracek, G. R., Maris, V., Hill, G. J., Ogawa, Y., Bibby, H. M., Bennie, S. L., & Heise, W. (2009). Fluid and deformation regime of an advancing subduction system at Marlborough, New Zealand. *Nature*, *460*, 733–736.

Waples, D. W., & Waples, J. S. (2004). A Review and Evaluation of Specific Heat Capacities of Rocks, Minerals, and Subsurface Fluids. Part 1: Minerals and Nonporous Rocks. *Natural Resources Research*, *13*, 97–122.

Wessel, P., & Smith, W. H. F. (1998). New, improved version of the Generic Mapping Tools released. *EOS Trans. Am. Geophys. Union*, *79*, 575–579.

White, R. S., McKenzie, D., & O'Nions, R. K. (1992). Oceanic crustal thickness from seismic measurements and rare earth element inversions. *Journal of Geophysical Research: Solid Earth*, *97*, 19683–19715.

Xie, S., & Tackley, P. J. (2004). Evolution of U-Pb and Sm-Nd systems in numerical models of mantle convection and plate tectonics. *J. Geophys. Res.*, *109*, B11204.

Yagi, Y., Nakao, A., & Kasahara, A. (2012). Smooth and rapid slip near the Japan Trench during the 2011 Tohoku-oki earthquake revealed by a hybrid back-projection method. *Earth and Planetary Science Letters*, *355*, 94–101.

Yamasaki, T., & Seno, T. (2003). Double seismic zone and dehydration embrittlement of the subducting slab. *J. Geophys. Res.*, *108(B4)*, 2212.

Zhao, D., Tian, Y., Lei, J., Liu, L., & Zheng, S. (2009). Seismic image and origin of the Changbai intraplate volcano in East Asia: Role of big mantle wedge above the stagnant Pacific slab. *Physics of the Earth and Planetary Interiors*, *173*, 197–206.